TRANSIENT ANALYSIS AND OPTIMIZATION OF FIXED-BED REGENERATORS FOR HVAC APPLICATIONS

A Thesis Submitted to the
College of Graduate and Postdoctoral Studies
In Partial Fulfillment of the Requirements
For the Degree of Doctor of Philosophy
In the Department of Mechanical Engineering
University of Saskatchewan
Saskatoon

By

Hadi Ramin

2021

PERMISSION TO USE

In presenting this thesis in partial fulfillment of the requirements for a Postgraduate degree from the University of Saskatchewan, I agree that the Libraries of this University may make it freely available for inspection. I further agree that permission for copying of this thesis in any manner, in whole or in part, for scholarly purposes may be granted by the professor or professors who supervised my thesis work or, in their absence, by the Head of the Department or the Dean of the College in which my thesis work was done. It is understood that any copying or publication or use of this thesis or parts thereof for financial gain shall not be allowed without my written permission. It is also understood that due recognition shall be given to me and to the University of Saskatchewan in any scholarly use which may be made of any material in my thesis.

DISCLAIMER

Reference in this thesis/dissertation to any specific commercial products, process, or service by trade name, trademark, manufacturer, or otherwise, does not constitute or imply its endorsement, recommendation, or favoring by the University of Saskatchewan. The views and opinions of the author expressed herein do not state or reflect those of the University of Saskatchewan, and shall not be used for advertising or product endorsement purposes.

Requests for permission to copy or to make other uses of materials in this thesis in whole or part should be addressed to:

Head of the Department of Mechanical Engineering
University of Saskatchewan
Saskatoon, Saskatchewan S7N 5A9
Canada
OR

Dean of College of Graduate and Postdoctoral Studies
University of Saskatchewan
116 Thorvaldson Building, 110 Science Place
Saskatoon, Saskatchewan S7N 5C9
Canada.

ABSTRACT

Air-to-air energy exchangers (AAEEs) recover energy from the exhaust airstream to precondition the supply airstream into buildings. In a fixed-bed regenerator (FBR), a type of AAEE, energy from the exhaust airstream is stored in the exchanger over a period; then, the energy is transferred to the supply airstream flowing through the same exchanger in the next period. Due to the storage and release of energy in consequent periods, the temperature and humidity of the airstreams at the outlet of the FBR vary with time. This variation poses difficulties for experimental testing and effectiveness evaluation of the FBR because of the slow response of sensors. The primary goal of this thesis is to develop and validate transient numerical models to accurately predict the transient characteristics of FBRs (sensible and desiccant-coated) and their sensors (temperature and humidity).

A numerical model consisting of an exchanger model and sensor models is developed to capture the transient characteristics of FBRs and their sensors. The developed model is validated using experimental results and can distinguish the actual FBR performance from the performance that is measured by the sensors in an experiment. The results show that the configuration of the FBR, and the sensors' location influence the measurement of the outlet air properties and, thus, the calculated effectiveness (effectiveness error). In addition, for the desiccant-coated FBRs, the effectiveness error depends on the operating condition of an experiment. This thesis also provides recommendations to improve North American testing standards (ASHRAE 84 and CSA C439-18) for FBRs. The results show that measurement requirements in the testing standards are conservative and can be relaxed for many designs and operating conditions. Furthermore, this thesis provides insights on optimizing sensible FBRs considering their transient characteristics.

ACKNOWLEDGMENT

Throughout my PhD studies, I have received a great deal of support and assistance from many great minds and kind hearts that I will be indebted to forever.

First and foremost, I wish to express my sincere appreciation to my supervisor, Professor Carey Simonson, for his infinite guidance, encouragement, and consistent supports throughout my studies. Without his persistent help, the goal of this thesis would not have been realized.

I cannot express enough thanks to my Advisory Committee members for their continued support and encouragement: Prof. D. Bergstrom, Prof. D. Sumner, Prof. D. Torvi, and Prof. O. D. Baik. I offer my sincere appreciation for the learning opportunities provided by my committee.

I would also like to take this opportunity to thank Professor Linda Xiao Fu, my external examiner from Hongkong Polytechnic University, for her willingness to read my thesis and for her insightful comments and suggestions.

Special thanks go to Mr. Easwaran N. Krishnan for the great discussions and communications during this research. Having you on the team was a matter of privilege for me. I also would like to thank HVAC research group members and postdoctoral fellows: Dr. A. Gurubalan, Dr. Wahab O. Alabi, Mr. Mehrdad Torabi, Mr. Alireza Razmavar, Mr. Teddy Okolo, and Mr. Mostafa Mostafavi Sani.

Special thanks are extended to Mr. Andy Kebernik and Mr. Jeff Goertzen from Tempeff for their support, great discussions, and valuable feedback during our monthly meetings.

I want to acknowledge the financial assistance from the Department of Mechanical Engineering at the University of Saskatchewan, Natural Science and Engineering Research Council (NSERC), Tempeff (Project No: 533225-18), the American Society of Heating, Refrigerating and Air-Conditioning Engineers (ASHRAE) graduate Grant-In-Aid, member

education grant of APEGS, George Carter Scholarships, Fredeen Scholarship in Engineering, Toyota Automotive Engineering and Safety Scholarships, Parya Scholarships, and Russell (Russ) William Haid Memorial Awards.

Writing a thesis is not an easy task, and I am grateful for receiving valuable assistance from our group members, especially Dr. A. Gurubalan. He spent countless hours reading my thesis and providing me with great comments that enhanced my thesis readability. I spent a great deal of time preparing my thesis, and I am happy that my thesis was well written, as mentioned by my committee members.

Finally, to my caring, loving, and supportive wife, Sirwa Padash: my deepest gratitude. Your encouragement when the times got rough is much appreciated and noted. It was a great comfort and relief to know you were here when I completed my PhD work. My heartfelt thanks.

DEDICATION

This thesis is dedicated to my wife Sirwa and our families for their endless love and supports.

TABLE OF CONTENTS

PERMISSION TO USE ..... **i**

DISCLAIMER ..... **i**

ABSTRACT ..... **ii**

ACKNOWLEDGMENT ..... **iii**

DEDICATION ..... **v**

TABLE OF CONTENTS ..... **vi**

LIST OF FIGURES ..... **x**

LIST OF TABLES ..... **xvii**

NOMENCLATURE ..... **xx**

CHAPTER 1: INTRODUCTION **1**

1.1 Motivation 1

1.2 Background 4

1.2.1 HVAC systems with energy recovery exchangers 4
1.2.2 Fixed-bed regenerators 5

1.3 Literature review 7

1.3.1 Energy recovery regenerators 7
1.3.2 Optimization of regenerators 10

1.4 Research objectives 11

1.5 Publications 12

1.5.1 Peer-reviewed journal papers 12
1.5.2 Conference papers and poster presentations 13

1.6 Thesis overview 14

CHAPTER 2: TRANSIENT NUMERICAL MODEL FOR SENSIBLE FBRs **18**

2.1 Overview 18

2.2 Abstract 19

2.3 Introduction 20

2.4 Numerical model for the FBR and temperature sensor 24

2.4.1 Exchanger (FBR) model 24
2.4.2 Temperature sensor model 29
2.4.3 Combined FBR and sensor model 30

2.4.4 Numerical solution for the FBR model 31
2.4.5 FBR model validation 33
2.4.6 Validation of the combined FRB and sensor model 37
2.5 Sensible effectiveness 44
2.5.1 Effect of non-instantaneous movement of exchanger between ducts on the predicted effectiveness 45
2.6 Applications of the combined FBR and sensor model 47
2.6.1 Quasi-steady-state temperature and effectiveness of a balanced FBR 47
2.6.2 Unbalanced flow rate 49
2.6.3 Hot and cold periods (with balanced flow rate) 51
2.7 Summary and conclusions 53
CHAPTER 3: TRANSIENT SENSOR ERRORS AND THEIR IMPACT ON TESTING STANDARDS FOR SENSIBLE FIXED-BED REGENERATOR (FBR) 55
3.1 Overview 55
3.2 Abstract 56
3.3 Introduction 58
3.4 FBR configurations and their outlet temperature profiles 61
3.5 Numerical model and experimental test facility 64
3.5.1 Performance parameters 64
3.5.2 Governing equations 65
3.5.3 FBR small-scale test facility 69
3.5.4 Validation of the results 71
3.6 Results and discussion 72
3.6.1 FBRs with a sawtooth profile 73
3.6.2 FBRs with a semi-sawtooth profile 75
3.6.3 Testing standards 79
3.7 Summary and conclusions 80
CHAPTER 4: OPTIMIZATION OF SENSIBLE FIXED-BED REGENERATORS (FBRs) CONSIDERING THEIR TRANSIENT CHARACTERISTICS 83
4.1 Overview 83
4.2 Abstract 84
4.3 Introduction 85
4.4 Thermal and operational modeling for optimization of FBRs 88

4.4.1 Effectiveness 88
4.4.2 Temperature swing (TS) 90
4.4.3 Pressure drop and fan energy consumption 93
4.4.4 Payback period 95
4.5 Multi-objective optimization and multi-criteria decision-aid procedure 99
4.5.1 Multi-objective optimization 99
4.5.2 Integration of optimization and MCDA 102
4.6 Results and discussion 104
4.6.1 Sensitivity of objective functions to the decision variables 104
4.6.2 Optimization of FBRs with/without temperature swing (TS) 105
4.7 Summary and conclusions 118
CHAPTER 5: A TRANSIENT NUMERCIAL MODEL FOR DESICCANT COATED FIXED-BED REGENERATORS 120
5.1 Overview 120
5.2 Abstract 121
5.3 Introduction 122
5.4 FBR configurations and outlet property profiles 125
5.5 Performance parameters 128
5.6 Numerical model for exchanger (FBR) and measurement sensors 129
5.6.1 FBR model 129
5.6.2 Temperature sensor model 135
5.6.3 Humidity sensor model-capacitive relative humidity sensor model 135
5.6.4 Numerical solution procedure 140
5.7 FBR small-scale test facility 142
5.7.1 Bag sampling method 145
5.8 Validation of results 145
5.8.1 Validation under isothermal conditions ($H^*=\infty$ or $\Delta T_{inlet}=0$, $\Delta W_{inlet}\neq 0$) 146
5.8.2 Validation under non-isothermal conditions ($H^*=0.85$ or $\Delta T_{inlet}\neq 0$, $\Delta W_{inlet}\neq 0$) 148
5.8.3 Effectiveness comparison for the FBR model 151
5.9 Applications of the combined FBR and sensor model 152
5.9.1 FBRs with a semi-sawtooth profile 153
5.9.2 FBRs with a sawtooth profile 156
5.9.3 Impact of operating condition factor (H^*) on latent effectiveness error 158
5.9.4 Testing standards 161
5.10 Summary and conclusions 162

CHAPTER 6: SUMMARY, CONCLUSIONS, CONTRIBUTIONS AND FUTURE WORK 165

6.1 Summary and conclusions 165

6.1.1 Objective 1: To develop and validate a transient numerical model for sensible FBR (addressed in Chapter 2) 165
6.1.2 Objective 2: To quantify sensor errors over a wide range of design and operating conditions of sensible FBRs and make recommendations for testing standards (addressed in Chapter 3) 166
6.1.3 Objective 3: To optimize sensible FBRs considering transient characteristics (addressed in Chapter 4) 167
6.1.4 Objective 4: To develop and validate a transient numerical model for desiccant-coated FBRs and quantify sensor errors (addressed in Chapter 5) 168

6.2 Contributions 170

6.3 Future work 170

6.3.1 Optimization of FBRs considering transient characteristics 170
6.3.2 Modeling and optimization of energy transfer enhancement methods 171
6.3.3 Measurement sensor requirements for desiccant-coated FBRs with semi-sawtooth outlet air properties profile 171
6.3.4 Experiment duration before reaching quasi-steady-state conditions 172
6.3.5 Condensation and frosting in FBRs 172

REFERENCES 173

APPENDIX A: COPYRIGHT PERMISSIONS 180

A.1. PERMISSION FOR MANUSCRIPTS USED IN CHAPTER 2 181
A.2. PERMISSION FOR MANUSCRIPTS USED IN CHAPTER 3 182
A.3. PERMISSION FOR MANUSCRIPTS USED IN CHAPTER 4 184
A.4. PERMISSION FOR MANUSCRIPTS USED IN CHAPTER 5 185

APPENDIX B: EFFECTIVENESS ERROR FROM THE TRANSIENT RESPONSE OF SENSORS AT DIFFERENT OPERATING CONDITIONS 188

APPENDIX C: THERMODYNAMICS AND PROPERTIES EQUATIONS FOR THE FBR MODEL OF THE DESICCANT-COATED EXCHANGER IN CHAPTER 5 196

LIST OF FIGURES

Figure 1.1. A schematic of an HVAC system with an air-to-air energy exchanger (AAEE). 4

Figure 1.2. A schematic showing the operation of an FBR for energy recovery in buildings. Schematics (a) and (b) represent the two periods of operations. 5

Figure 1.3. Papers published on FBRs and wheels between 1950 and 2020. 8

Figure 1.4. Classification of studies on FBRs and wheels. 9

Figure 1.5. Published papers (85) on optimization of regenerators between 1950 and 2020 from Engineering Village and ASME database. 10

Figure 1.6. Classification of studies on optimization of regenerators between 1950 and 2020. .. 11

Figure 1.7. Overview of this PhD thesis structure representing thesis objectives and chapters... 15

Figure 2.1. A schematic of an HVAC system with FBRs for heat recovery. 21

Figure 2.2. A schematic of alternate heating and cooling periods of FBRs and the corresponding temperature profile for temperature measurement sensors..... 22

Figure 2.3. (a) A picture of the small-scale FBR, and (b) the proposed geometrical configuration for numerical modeling. 25

Figure 2.4. A schematic showing the heat transfer process in the representative channel of FBR. 27

Figure 2.5. Numerical flowchart. 33

Figure 2.6. Comparison of results of the FBR model and the literature [19,41] for balanced and unbalanced flow conditions λ=0.04 and 0.24. 37

Figure 2.7. A schematic of the test section and thermocouples to measure the air temperature. . 39

Figure 2.8. Transient outlet temperature profile of FBR, a comparison between combined FBR and sensor model and experimental results from exchanger sensors (NTU_o=2.4, face velocity=2.0 m/s, sensor time constant=1.5 s). 41

Figure 2.9. Quasi-steady-state temperature profile from the experiment with duct sensors, FBR model, and combined FBR and sensor model as well as the inlet temperatures (NTU=2.4, face velocity=2.0 m/s, sensor time constant=1.5 s). 42

Figure 2.10. Quasi-steady-state temperature profile from the experiment with exchanger sensors, FBR model, and combined FBR and sensor model as well as the inlet temperatures (NTU=2.4, face velocity=2.0 m/s, sensor time constant=1.5 s). 43

Figure 2.11. Quasi-steady-state temperature profile from the experiment with duct and exchanger sensors, FBR model, as well as the inlet temperatures (NTU_o=2.4, face velocity=2.0 m/s, sensor time constant=1.5 s). 44

Figure 2.12. FBR effectiveness from the experiment and the FBR model (NTU_o=2.4, face velocity=2.0 m/s, sensor time constant=1.5 s). 45

Figure 2.13. Velocity profiles corresponding to the instantaneous and non-instantaneous movement of exchanger between the airflow ducts. 46

Figure 2.14. Changes in effectiveness when exchanger movement time is included in the model ($\Delta\varepsilon=\varepsilon_{movement}-\varepsilon_{instantaneous\ movement}$). 47

Figure 2.15. Comparison of temperature profiles from the FBR and combined FBR and sensor model (time constant=1.5 s) at P=120 and15 s (NTU=2.4, face velocity=2.0 m/s, time constant=1.5. s). 48

Figure 2.16. Effectiveness error ($\Delta\varepsilon$) for the duct and exchanger sensors for a balanced flow rate (NTU=2.4, face velocity=2.0 m/s) at different cycle times (time constant=1.5 s)... 49

Figure 2.17. Comparison of temperature profiles from the FBR and combined FBR and sensor model for balanced and unbalanced flow exchanger at 120 s cycle duration (face velocity=2.0 m/s, time constant=1.5 s). 50

Figure 2.18. Effectiveness error ($\Delta\varepsilon$) of balanced and unbalanced FBR from the duct and exchanger sensors at different cycle times (face velocity=2.0 m/s, time constant=1.5 s). 50

Figure 2.19. Air temperature profile from the FBR model and the combined FBR and sensor model for the equal and unequal hot and cold period duration at 120s cycle duration (NTU=2.4, face velocity=2.0 m/s, and time constant =1.5 s). 51

Figure 2.20. Comparison of effectiveness error (Δε) of equal and unequal hot and cold period for the duct and exchanger sensors at the different cycle times ((NTU=2.4, face velocity=2.0 m/s, and time constant=1.5 s). 52

Figure 3.1. A schematic of inlet and outlet temperatures during alternate hot and cold periods of FBRs. 59

Figure 3.2. Outlet air temperatures of positive/negative sawtooth ((a) & (b)) and the semi-sawtooth ((c) & (d)) profile and their corresponding sensor measurements with τ_s^*=0.2 (NTU_o=1.0, Cr^*=1.0, and λ=0). 68

Figure 3.3. A schematic of the small-scale test facility. 69

Figure 3.4. A schematic of the small-scale exchanger..... 70

Figure 3.5. (a) Numerical and experimental temperature comparison from the beginning of the experiment (NTU_o=2.4, Cr^*=1.2-8, λ=0.3) and (b) comparison of sensible effectiveness from experiment and numerical model. 72

Figure 3.6. (a) Quasi-steady-state temperature profile and sensor measurements with two dimensionless time constant of τ_s^*=0.2 and 0.5, and (b) $\Delta T_{sensor}/\Delta T_{actual}$ for FBR with sawtooth temperature (NTU_o=1, Cr^*=1, and λ=0)..... 74

Figure 3.7. The required dimensionless sensor time constant ($\tau s*$) to capture 80% and 90% of the actual temperature swing ($\Delta T_{sensor}/\Delta T_{actual}$ =80% and $\Delta T_{sensor}/\Delta T_{actual}$=90% for λ=0 (solid), 0.04 (dashed), NTU_o=1-10 and Cr^*=1,3,5 and10..... 75

Figure 3.8. Quasi-steady-state temperature profile and sensor measurements with two dimensionless time constant of τ_s^*=0.2 and 0.5, and (b) effectiveness error (Δε) for FBR with semi-sawtooth temperature (NTU_o=1, Cr1, and λ=0)..... 76

Figure 3.9. Effectiveness error as a function of τ_s^* at different design parameters of NTU_o and Cr^* (λ=0, and 0.04)..... 77

Figure 3.10. Required dimensionless sensor time constant (τ_s^*) that results in effectiveness error less than 1%, 2% and 3% for NTUo=1-10 and Cr*=1, 3, 5, and 10 for FBR with semi-sawtooth outlet profile. 78

Figure 3.11. (a) Maximum effectiveness error versus dimensionless time constant over the range of $1<NTU_o<10$ and $1<Cr^*<10$ for FBR with semi-sawtooth profile (b) closer look at the smaller values of τ_s^*. 79

Figure 4.1. A schematic of FBR and the representative parallel plates channel for optimization.88

Figure 4.2. Dimensionless temperature profile at the outlet of FBR in (a) hot and (b) cold periods. 91

Figure 4.3. Comparison of prediction of the temperature profile slopes (m_T) from (a) the correlation in Eqn. (4.11) and (b) the neural network with the simulation results. 93

Figure 4.4. Variation of m_T versus (a) NTU_o and (b) Cr^* at different conduction parameters of λ=0, 0.04 and 0.08. 94

Figure 4.5. (a) A schematic of an HVAC system with FBRs for sensible energy recovery (b) distribution of outdoor air temperature, the temperature at the outlet of FBR and energy recovered with FBR, and additional energy required to condition the ventilation air. 98

Figure 4.6. Multi-objective optimization and ranking process flowchart. 103

Figure 4.7. Variation of ε, Δp, M_{FBR} (left Y-axis) and PBP and TS (right Y-axis) with (a) h_c (b) t_p, (c) P, and (d) L. 105

Figure 4.8. (a)-(c) Pareto fronts for the optimization problem in Eqn. (4.22) and (d) variation of exchangers mass on the Pareto fronts versus effectiveness. 108

Figure 4.9. (a-c) Variation of the decision variables with effectiveness on the Pareto front for the optimization problem in Eqn. (4.22). 109

Figure 4.10. Pareto fronts for the optimization problem in Eqn. (4.22) at three different face velocities of V, 0.8V and 1.2V with and without TS. 111

Figure 4.11. (a)-(c) Pareto fronts for the optimization problem in Eqn. (4.23) and (d)-(f) exchanger mass versus effectiveness, temperature swing, and payback period for the Pareto fronts. 112

Figure 4.12. Comparison of Pareto fronts for the optimization problem in Eqn. (4.24) with (hexagonal)/without (circles) temperature swing. 114

Figure 4.13. Comparison of Pareto fronts for optimization of FBRs in Eqn. (4.24) with (hexagonal)/without (circles) temperature swing. 115

Figure 4.14. Comparison of Pareto fronts for the optimization of FBRs in Eqn. (4.25) with (hexagonal)/without (circles) temperature swing. 117

Figure 5.1. A schematic of single-core FBR and the variation of air properties during discharge and regeneration periods for winter climatic conditions. 123

Figure 5.2. A schematic of the numerical domain for heat and mass transfer in a representative channel of desiccant-coated FBR. 130

Figure 5.3. Lines of H^* on the psychrometric chart for supply condition of 23°C and 50% RH. 134

Figure 5.4. Negative and positive step changes in humidity ratio at constant temperature (T=23°C) to obtain the internal humidity ratio's time constant ($\tau_{h,int}$). 138

Figure 5.5. Negative and positive step change in temperature and measured RH with CRHS at constant humidity ratio to obtain the internal temperature time's constant ($\tau_{t,int}$).. 139

Figure 5.6. Comparison of experiment and humidity sensor model for negative and positive step change in humidity ratio at a constant RH. 140

Figure 5.7. Flowchart for the FBR model. 141

Figure 5.8. Schematic of the small-scale test facility. 143

Figure 5.9. Sorption isotherm of silica gel at 25°C. 145

Figure 5.10. Comparison of outlet humidity ratio profile for (a) exchanger and (b) duct sensor between experiment and numerical models (FBR model and FBR+ Sensor model). 147

Figure 5.11. (a) Comparison of outlet temperature and (b) humidity ratio profiles between experiment, numerical model (FBR model), and combined FBR and sensor model for the duct sensors. 149

Figure 5.12. (a) Comparison of outlet temperature and (b) humidity ratio profiles between experiment, numerical model (FBR model), and combined FBR and sensor model for the exchanger sensors. 150

Figure 5.13. Comparison of latent effectiveness from the numerical model (FBR) and BSM (and sensible effectiveness from the combined FBR and sensor model) at several non-isothermal conditions ((velocity:1-2 m/s, NTU_o:1.8–3)). 152

Figure 5.14. Quasi-steady-state humidity ratio profile (FBR model) that the exchanger sensor is exposed to and its response (FBR+ Sensor model) for time constants of $\tau_{t,int}$=25s, $\tau_{h,int}$=5s and τ_s=3s at (a) cold and dry period and (b) hot and humid period (NTU_o=3, Cr^*=3, λ=0.08, Cr_m^*=0.3, η=0.1 and at the AHRI summer test conditions (H^*=1.6)). 155

Figure 5.15. Quasi-steady-state humidity ratio profile (FBR model) that the duct sensor is exposed and its response (FBR+ Sensor model) for time constants of $\tau_{t,int}$=25s, $\tau_{h,int}$=5s and τ_s=3s at (a) cold and dry period and (b) hot and humid period (NTU_o=3, Cr^*=3, λ=0.08, Cr_m^*=0.3, η=0.1 and at the AHRI summer test conditions (H^*=1.6)). 156

Figure 5.16. (a) Quasi-steady-state humidity ratio profile (FBR model) for FBR with sawtooth profile and its response (FBR+ Sensor model) for time constants of $\tau_{t,int}$=25s, $\tau_{h,int}$=5s and τ_s=3s at (a) cold and dry period and (b) hot and humid period (NTU_o=3, Cr^*=3, λ=0.08, Cr_m^*=0.3, and η=0.1 at the AHRI summer test conditions (H^*=1.6)). 158

Figure 5.17. Effect of operating condition parameter (H*) on the latent effectiveness error at NTU_o=3, Cr^*=3, Cr_m^*=0.3, and λ=0.08 and measurement sensors with time constants of $\tau_{t,int}$=25s, $\tau_{h,int}$=5s and τ_s=3s. 159

Figure 5.18. Average of the hot (and humid) and cold (and dry side) latent effectiveness errors for sensors exposed to sawtooth, and semi sawtooth (exchanger and duct sensors) profiles and the average of latent effectiveness errors for duct and exchanger sensors. 160

Figure 5.19. Comparison of the average effectiveness error for different sensor configurations with the original time constants ($\tau_{t,int}$=25s, $\tau_{h,int}$=5s and τ_s=3s) and when the original time constants are doubled ($\tau_{t,int}$=50s, $\tau_{h,int}$=10s and τ_s=6s)..... 161

LIST OF TABLES

Table 2.1. Geometrical details and thermophysical properties of the exchanger. 24

Table 2.2. Operating conditions and sensor time constant for the validation of results. 39

Table 3.1. Different configurations of FBRs and their corresponding winter (W) and summer (S) outlet temperature profiles at the supply side (SA) and exhaust side (EA). 62

Table 3.2. Dimensionless variables and parameters for heat transfer in FBRs. 66

Table 3.3. Geometrical details, thermophysical properties of the exchanger, dimensionless parameters, and sensor time constant 71

Table 4.1. Thermal regenerators' optimization studies. 87

Table 4.2. Definition of dimensionless parameters for the effectiveness of FBRs in Eqn. (4.1). 89

Table 4.3. Economic and design parameters for optimizing FBRs. 97

Table 4.4. Decision variables and their ranges for optimizing FBRs. 100

Table 4.5. Base exchanger design parameters and its performance. 100

Table 4.6. NSGA-II main parameters in MATLAB. 101

Table 4.7. Ideal objective values over the range of decision variables in Table 4.4. 102

Table 4.8. Different scenarios (SCs) for the importance of objectives for FBRs design. 103

Table 4.9. The sensitivity of objective functions with an increase in the decision variables over their ranges of variation. 106

Table 4.10. Decision variables and objective values corresponding with the selected FBRs for different objective weightage scenarios for the optimization problem in Eqn. (4.22) (WO/TS: without TS and W/TS: with TS). 110

Table 4.11. Decision variables and objective values corresponding with the selected FBRs for different objective weightage scenarios for the optimization problem in Eqn. (4.23) (WO/TS: without TS and W/TS: with TS). 113

Table 4.12. Decision variables and objective values corresponding with the selected FBRs for different objective weightage scenarios for the optimization problem in Eqn. (4.24) (WO/TS: without TS and W/TS: with TS). 115

Table 4.13. Decision variables and objective values corresponding with the selected FBRs for different objective weightage scenarios for the optimization problem in Eqn. (4.25) (WO/TS: without TS and WTS: with TS). 117

Table 5.1. Different configurations of FBRs and their corresponding outlet air property profiles (temperature and humidity profiles). 127

Table 5.2. Comparison of the procedure for RH measurement between the actual procedure and proposed procedure in this chapter. 136

Table 5.3. Geometrical details, thermophysical properties of the exchanger, dimensionless parameters, and sensor time constant. 144

Table 5.4. Inlet conditions for the isothermal experiment ($\Delta T_{inlets}=0$, $\Delta W_{inlets}\neq 0$). 147

Table 5.5. Comparison of latent effectiveness from the experiment, FBR model, and the combined FBR and sensor model for the isothermal test conditions ($\Delta T_{inlet}=0$, $\Delta W_{inlet}\neq 0$). .. 147

Table 5.6. Inlet conditions for the non-isothermal experiment ($\Delta T_{inlet}\neq 0$, $\Delta W_{inlet}\neq 0$). 148

Table 5.7. Comparison of latent and sensible effectivenesses from experiment, FBR model and combined FBR and sensor model. 150

Table 5.8. AHRI summer test conditions ($H^{*}=1.6$) 154

Table B.1. Effectiveness error $\Delta\varepsilon$ (%) for $\lambda=0.0$. 188

Table B.2. Effectiveness error $\Delta\varepsilon$ (%) for $\lambda=0.02$. 189

Table B.3. Effectiveness error $\Delta\varepsilon$ (%) for $\lambda=0.04$. 190

Table B.4. Effectiveness error $\Delta\varepsilon$ (%) for $\lambda=0.06$. 191

Table B.5. Effectiveness error $\Delta\varepsilon$ (%) for $\lambda=0.08$. 192

Table B.6. Effectiveness error $\Delta\varepsilon$ (%) for $\lambda=0.12$. 193

Table B.7. Effectiveness error $\Delta\varepsilon$ (%) for $\lambda=0.16$ 194

Table B.8. Effectiveness error $\Delta\varepsilon$ (%) for λ=0.20 195

Table C.1. Thermodynamics and properties equations for the FBR model..... 196

NOMENCLATURE

ACRONYMS

AAEE	air-to-air energy exchanger
AHRI	Air Conditioning, Heating and Refrigeration Institute
BC	boundary condition
EA	exhaust air
EX	exchanger
FBR	fixed-bed regenerator
HVAC	heating, ventilation, and air conditioning
PWF	present worth factor
SA	supply air
SDGs	sustainable development goals
TS	temperature swing
UN	United Nations
WO/TS	without temperature swing
W/TS	with temperature swing

SYMBOLS

a_1 to a_4	temperature swing correlation constants
A_d	surface area of desiccant, m^2
A_g	cross-sectional area of the airflow duct, m^2
A_m	matrix cross-sectional area, m^2
$A_{h,rec}$/ $A_{c,rec}$	area corresponding to annual heating/cooling energy recovered with FBR, h·K
A_s	heat transfer surface area of exchanger channel, m^2
A_{ts}	heat transfer surface area of sensor, m^2
C^*	heat capacity rate ratio
Cp	specific heat capacity, J/kg·K
Cr^*	matrix heat capacity ratio

Crm_o^*	overall matrix moisture capacity ratio
C_λ	conduction parameter correction
CC_{FBR}	capital cost of FBR, $
d	inflation rate, %
D_h	hydraulic diameter, m
ER_{ann}	annual energy recovered saving with FBR, $
ES_{ann}	yearly energy saving with FBR, $
ES_{tot}	adjusted total energy saving with FBR over its lifecycle period, $
e_c	cooling unit energy price, $/kWh
e_h	heating unit energy price, $/kWh
e_p	unit energy price for pumping airflow, $/kWh
f_{app}	apparent fanning friction factor
f_k	objective function
g_j	inequalities constraint
H	enthalpy per mass of dry air, kJ/kg
h	convective heat transfer coefficient, $W/m^2 \cdot K$
H^*	operating condition factor
$\overline{H}$	average enthalpy over a period, kJ/kg
$(hA_s)^*$	convective conductance ratio
h_c	channel height, m
h_m	convective mass transfer coefficient, $kg/m^2 \cdot s$
h_{ad}	heat of adsorption, kJ/kg
h_{fg}	heat of vaporization, kJ/kg
i	interest rate, %
k	thermal conductivity, W/m·K
L	length of the heat exchanger, m
LC	lifecycle of FBR, year
$\dot{m}'$	rate of phase change per unit of length, kg/s·m
$\dot{m}$	flow rate, kg/s
m_T	slope of the temperature profile
n	number of middle channels in exchanger

N_s	number of spatial nodes
NTU_o	overall number of transfer units
NTU_{mt}	number of moisture transfer units
NTU_{ht}	number of heat transfer units
Nu	Nusselt number
Nu_{FD}	fully developed Nusselt number
P	cycle time, s
P_c	cold period, s
P_h	hot period, s
Pr	Prandtl number
PBP	payback period, year
PP	pumping power, W
Re	Reynolds number
RH	relative humidity, %
RH_s	relative humidity measured by relative humidity sensor, %
T	temperature, °C
T_{des}	design temperature, °C
$T_{initial}$	initial temperature, °C
T_s	temperature measured by temperature sensor, °C
$\overline{T}$	average temperature over a period, °C
T^*	dimensionless temperature
t	time, s
t_p	matrix plate thickness, m
t^*	dimensionless time
u	mass fraction of water in the desiccant, kg/kg
V	mean airflow velocity, m/s
V_{NS}	airflow velocity corresponding to non-instantaneous movement of exchanger, m/s
V_{ts}	volume of temperature sensor, m^3
$\dot{V}$	volumetric flow rate, m^3/s
v_g	decision variables

$v_g^{(U)}/v_g^{(L)}$	upper/lower bound for decision variables
W	width of exchanger, m
W_m	desiccant maximum moisture capacity, kg/kg
W_s	measured humidity ratio by sensor, kg/kg
WO	weightage of importance of objectives
x	axial coordinate, m
x^*	dimensionless axial distance ($x/D_h \cdot Re \cdot Pr$)
x^+	$x/D_h Re$, dimensionless axial distance for fluid flow

GREEK SYMBOLS

α	thermal diffusivity, m^2/s
α^*	rectangular aspect ratio
β	symbolic function
ΔH_l	latent energy difference between hot/humid and dry/cold inlet conditions, kJ/kg
ΔH_s	sensible energy difference between hot/humid and dry/cold inlet condition, kJ/kg
Δp	pressure drop, Pa
ΔT_{actual}	actual temperature swing, °C
ΔT_{sensor}	sensor measurement temperature swing, °C
$\Delta\varepsilon$	effectiveness error due to transient characteristic of temperature sensor, %
ε	effectiveness, %
η	distribution of phase change energy between the desiccant and the airflow
η_p	fan efficiency, %
λ	conduction parameter
$\rho_{d,dry}$	dry desiccant vapor density, kg/m^3
ρ_g	air density, kg/m^3
ρ_m	matrix density, kg/m^3
ρ_{ts}	temperature sensor density, kg/m^3
ρ_v	water vapor density, kg/m^3

τ_s	sensor time constant, s
τ_s^*	dimensionless time constant
$\tau_{h,int}$	internal humidity time constant of humidity sensor, s
$\tau_{h,int}$	internal temperature time constant of humidity sensor, s
φ	symbolic function

SUBSCRIPTS

ave	average
c	cold and dry period
d	desiccant
dry	dry properties
g	air mixture (dry air and water vapor)
h	hot and humid period
ht	dimensionless heat transfer group for regenerators
i	inlet condition
int	internal
lc	latent effectiveness for the cold and dry period
lh	latent effectiveness for the hot and humid period
m	matrix
max	maximum
min	minimum
mt	dimensionless mass transfer group for regenerators
o	outlet condition
sh	sensible effectiveness for the hot and humid period
sc	sensible effectiveness for the cold and dry period
th	total effectiveness for the hot and humid period
tc	total effectiveness for the cold and dry period
v	water vapor
w	water

CHAPTER 1

INTRODUCTION

1.1 MOTIVATION

Ensuring access to affordable, reliable, and sustainable energy for all (goal 7) is one of the United Nations (UN) sustainable development goals (SDGs) [1]. Buildings play a crucial role in achieving this goal since they account for about one-third of the global final energy consumption, half of the worldwide electricity consumption, and one-third of the worldwide carbon emissions [2]. About 60% of the energy consumed by buildings in Canada goes to space heating, cooling, and ventilation [3]. Furthermore, according to the Intergovernmental Panel on Climate Change (IPCC) report [4], the global energy demands in 2050 are expected to increase by 179% and 183%, for residential and commercial buildings, respectively, compared to the 2010 levels. Radical changes in the current trends of energy consumption and energy-related CO_2 emission in buildings mandate all countries to immediately implement cost-effective best practices and technologies to reduce energy consumption in buildings, especially in heating, ventilation, and air conditioning (HVAC) systems [4,5].

HVAC systems maintain the required indoor conditions to preserve thermal comfort and replace the stale indoor air with fresh outdoor air (which is called ventilation) to maintain indoor air quality (IAQ). The ventilation process is highly energy-intensive, especially during extreme climate conditions. Hence, HVAC engineers and researchers are developing new technologies to reduce energy consumption for ventilation while providing acceptable IAQ prescribed by standards [6]. Air-to-Air Energy Exchangers (AAEEs) is a well-recognized solution to increase the energy efficiency of the ventilation process by recovering energy/heat from the exhaust

airstream and preconditioning the outdoor supply airstream. Different types of AAEEs are available in the market, including fixed-plate exchangers, heat pipes, energy/heat wheels, fixed-bed regenerators (FBRs), and run-around membrane exchangers (RAMEEs).

AAEEs can be categorized into two main types: recuperative and regenerator types, based on the method of heat and moisture exchange between the supply and exhaust airstreams. In recuperators, the energy is directly exchanged (through separating walls) between the airstreams that continuously flow through the exchanger in their own airflow channels. However, in the regenerator type, the two airstreams periodically flow through the same exchanger channels. The energy from the hot (and humid) airstream is stored in the exchanger during one period (which is called the hot (and humid) period), and this energy is released to the cold (and dry) airstream during the subsequent period of operation (which is called cold (and dry) period). Regenerators can attain high effectiveness and are less susceptible to frosting than recuperators.

There are two types of regenerators, rotary (energy/heat wheel) and stationary (fixed bed) regenerators. Regenerators capable of transferring only heat are referred to as "sensible" regenerators, while the regenerators capable of exchanging heat and moisture (by coating desiccant to the surface of exchangers) are referred to as "desiccant-coated" regenerators in this thesis. Rotary regenerators have one rotating exchanger (a wheel), and fixed-bed regenerators (FBRs) have one or two fixed exchangers with reversible fans or dampers to redirect airstreams through the exchangers. FBRs have been used for heat recovery in high-temperature applications such as glass furnaces, coke ovens, and open-hearth steel furnaces for decades [7–10]. In recent times, FBRs have been attracting increasing attention for energy recovery in HVAC applications [11–16] due to their high effectiveness and low maintenance [17].

Due to the transient nature in the operation of FBRs (due to storing and releasing energy in the consequent periods of operation in the exchanger), the temperature and humidity profiles of airstreams at the outlet of FBRs vary with time. This variation causes challenges for sensors to measure the temperature and humidity accurately and, thereby, affect the effectiveness evaluation of FBRs. Effectiveness is the vital parameter to quantify the performance of FBRs and represents their energy recovery potential. Thus, validated models are required to comprehend the transient nature of FBRs and sensors and their impacts on the measurement of air properties. Although models were available for FBRs in high-temperature applications since 1950 [18,19], the transient region was not considered since it was negligible for those applications because of the extended hot and cold periods. Typical hot and cold periods of FBRs are about 20 minutes for glass furnace application [9,10], whereas, in the HVAC field, the periods are shorter in the order of 15-120 seconds [15,17,20]. The shorter period of operations impacts the measurement of airstream properties at the outlet of FBRs in HVAC applications because of the slow response of sensors.

This research aims to develop numerical models to capture the transient behavior of FBRs and sensors. The developed numerical models should be capable of capturing the transient nature of FBRs and sensors and will be helpful to provide practical recommendations for accurate measurement (during experiment or operation in the field) of the outlet air temperature and humidity. ASHRAE standard 84 and CSA C439-18 standard [21,22] have recently included guidelines to test the performance of FBRs (temperature and humidity measurements requirements). However, these requirements have not been investigated in the literature. Hence, the present study will verify these requirements and provide recommendations for the future version of such standards. Furthermore, the application of FBRs in HVAC is recent, and the optimization of FBRS has not been reported in the literature. More specifically, optimization of

FBRs considering their transient nature of the operation is missing in the current literature. Therefore, this research also will optimize FBRs considering their transient nature of operation. Hence, this PhD research will be useful to analyze and optimize energy efficient FBRs for HVAC applications.

1.2 BACKGROUND

1.2.1 HVAC systems with energy recovery exchangers

HVAC systems are essential to provide acceptable indoor air quality and thermal comfort for occupants irrespective of the ambient conditions. Figure 1.1 shows a schematic of an HVAC system with an AAEE for energy recovery. The supply airstream (outdoor air) is provided to the building through the supply fan whereas the exhaust fan removes the stale indoor air from the building. Auxiliary heating and cooling equipment are required to condition the supply airstream before introducing it to the building. The AAEE recovers energy from the exhaust airstream to precondition the supply airstream. The energy that would otherwise be wasted is instead recovered and used to precondition the supply airstream.

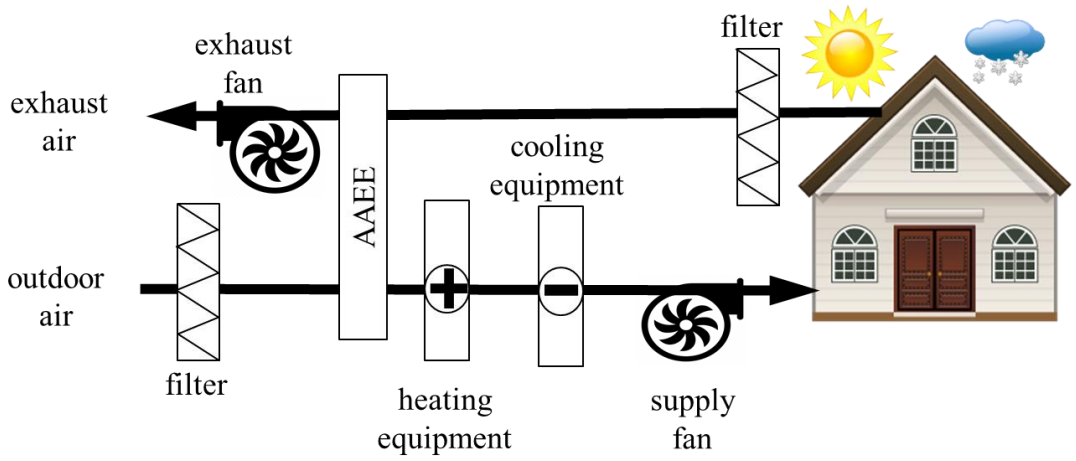

Figure 1.1. A schematic of an HVAC system with an air-to-air energy exchanger (AAEE).

1.2.2 **Fixed-bed regenerators**

Figure 1.2 shows a schematic diagram of an FBR with two stationary exchangers (EX1 and EX2), two fans, and dampers. The exchangers (possibly coated with desiccant) in Fig. 1.2 undergo two periods of operation to transfer energy between the exhaust and supply airstreams. In the first period, the dampers are positioned as shown in Fig.1.2 (a), and as a result, the exhaust airstream flows through EX1, and the supply airstream flows through EX2. The indoor airstream (in winter condition) is warmer and contains more moisture than the outdoor airstream; thus, the exhaust airstream heats and humidifies EX1, while EX2 (with the energy stored in the previous period of operation) heats and humidifies the supply airstream. In the second period, all the dampers turn 90 degrees, and hence, the flow through the exchangers is reversed (Fig.1.2 (b)). The exhaust airstream flows through EX2, and the supply air flows through EX1. Thus, the exhaust air heats and humidifies EX2, while EX1 heats and humidifies the supply airstream.

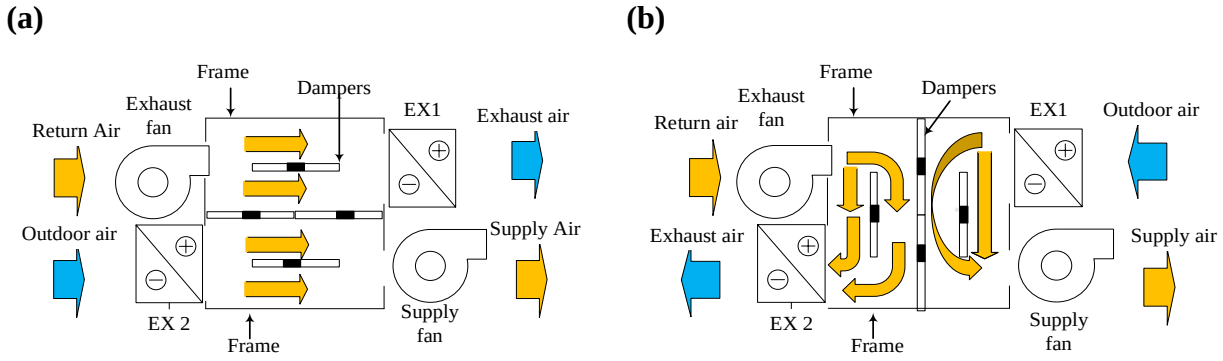

Figure 1.2. A schematic showing the operation of an FBR for energy recovery in buildings. Schematics (a) and (b) represent the two periods of operations.

The energy from the exhaust airstream is intermittently stored in the exchanger before it is transferred to the supply airstream as explained earlier. Therefore, the operation of FBR (in winter condition) includes a hot (and humid) flow period (warm and humid indoor air flows through exchanger) and a cold (and dry) flow period (cold and dry outdoor airstream flows through

exchanger). For sensible FBRs, the operation includes a hot period as well as a cold period. Although the operation of FBRs is explained for cold and dry winter conditions, their operation in any other climate conditions is similar; however, the direction of heat and moisture transfer is different. The duration of each period varies between 15-120 seconds for HVAC applications [17]. The design of FBRs in Fig. 1.2 requires two exchangers to provide a continuous supply of air and is called a double-core FBR. FBRs could also be designed with a single exchanger (single-core FBR) with a reversible fan that reverses airflow through the EX.

Due to the intermittent storage and release of energy in FBRs, the outlet temperature and humidity of both airstreams never attain a steady-state condition. The outlet properties, instead, rise and fall cyclically with the reversal of airflow. Thus, FBR reaches a quasi-steady-state condition in which the outlet profiles of airstreams repeat themselves from period to period. Unlike FBRs, the airflow properties at the outlet of rotary regenerators reach constant conditions, which means the sensor transient response would not impact the temperature and humidity measurement (and hence effectiveness). The energy wheel is a rotary type regenerator and has been extensively studied for energy recovery in HVAC applications [23–28]. The rotary regenerators typical rotational speed is 0.5-3 rpm for power plants and 0.5-20 rpm for HVAC applications [29].

ASHRAE standard 84 [21] and CSA C439-18 standard [22] have recently been modified to include guidelines for testing the performance of FBRs. Both standards require at least 30 temperature and humidity samples per period (the period is assumed to be 60 seconds) with instruments that have response time shorter than the sampling rate (maximum response time is 2 seconds). However, the measurement requirements mentioned in these standards have not been studied and verified in the literature. Temperature and humidity measurement requirements for testing FBRs at the quasi-steady-state condition will be presented in detail in this study.

1.3 LITERATURE REVIEW

A literature review was conducted in the engineering scientific database of Engineering Village (www.engineeringvillage.com) and the ASME databases to provide insights on the previous research studies on regenerators. The literature search is divided into two parts: literature on rotary regenerators and fixed-bed regenerators (FBRs), and literature on optimization of regenerators. Literature statistics on rotary regenerators (wheels) and FBRs are discussed and compared in the following subsection, followed by the optimization statistics. A detailed literature review on each objective of the thesis is also presented in the introduction section of each chapter.

1.3.1 Energy recovery regenerators

Through a detailed literature review, 582 papers have been collected on FBRs and wheels over the period of 1950-2020. The papers are classified based on their focus (either wheels or FBRs) and applications in Figs. 1.3 and 1.4, respectively. As shown in Fig. 1.3, most studies have focused on wheels (81%), and many studies on FBRs have been done from 2011 to 2020 (36 out of 109 papers).

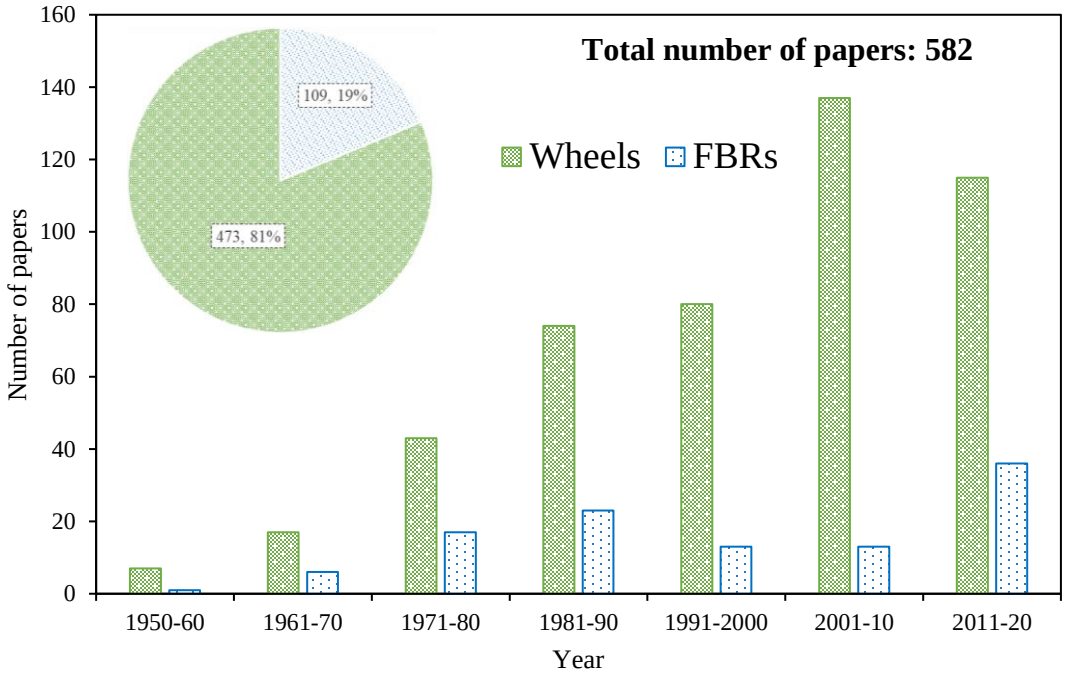

Figure 1.3. Papers published on FBRs and wheels between 1950 and 2020.

According to Figure 1.4, 70% and 62% of studies on wheels and FBRs respectively were theoretical (numerical and analytical), and the rest were experimental. Despite the abundance of numerical studies, no numerical research focused on the transient nature of FBRs. A breakdown of the previous studies' topics and objectives on regenerators is also presented in Fig. 1.4 (b). Heat and energy recovery for HVAC applications was the focus in 147 papers on wheels, while for FBRs, it is only 30 papers. Despite the number of studies on FBRs for heat/energy recovery, the study focuses on FBRs for HVAC applications is minimal. In the recent studies of FBRs for HVAC applications, mathematical models have been used to predict the effectiveness, but the transient nature of FBRs and its impact on measured effectiveness have not been explored. Overall, the model and analysis of this transient behaviour of FBRs coupled with temperature and humidity sensors are not in the current literature, which is the research gap this thesis addresses. Hence,

further studies are required to analyze heat and mass transfer in FBRs and the transient nature of FBRs for HVAC applications.

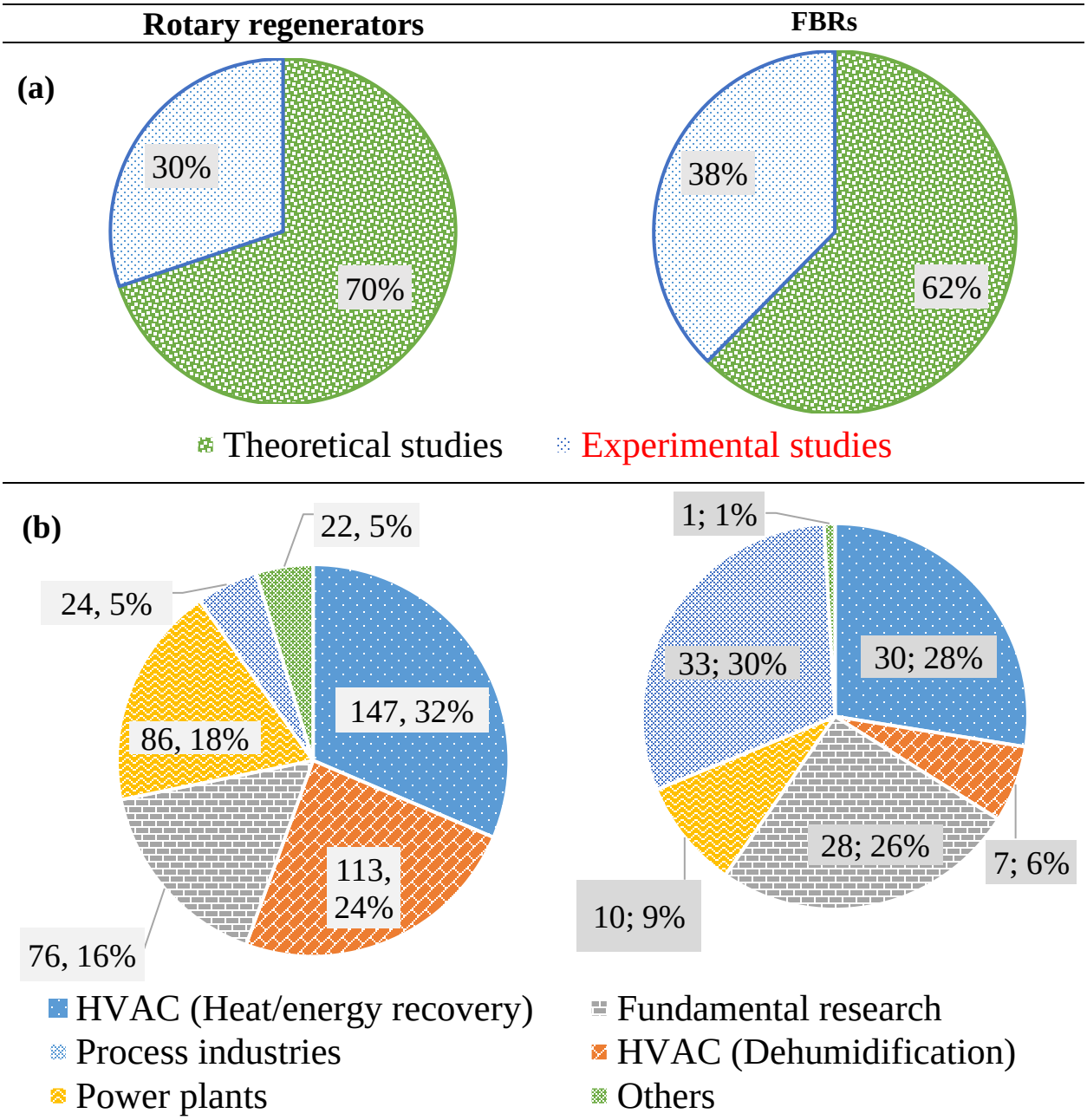

Figure 1.4. Classification of studies on FBRs and wheels.

1.3.2 **Optimization of regenerators**

This section provides a brief statistical overview of research published on the optimization of regenerators between 1950 and 2020. Figure 1.5 presents the distribution of publications.

According to Fig. 1.5, the optimization of regenerators has received increasing attention over the last two decades. A classification of optimization studies on regenerators is provided in Fig. 1.6. The papers are divided into three main categories, namely fundamental research (13%), HVAC applications (38%), and other industrial applications (49%, including power plants and process industries). Out of 32 papers on HVAC applications, only 9 papers analyze and optimize FBRs, which means that FBRs have received small attention compared to wheels. Hence, research on the modeling and optimization of FBRs to minimize their operating and capital costs are limited. Furthermore, there is no study on the literature considering the transient nature while optimizing FBRs. Thus, this study aims to fill this research gap in the literature.

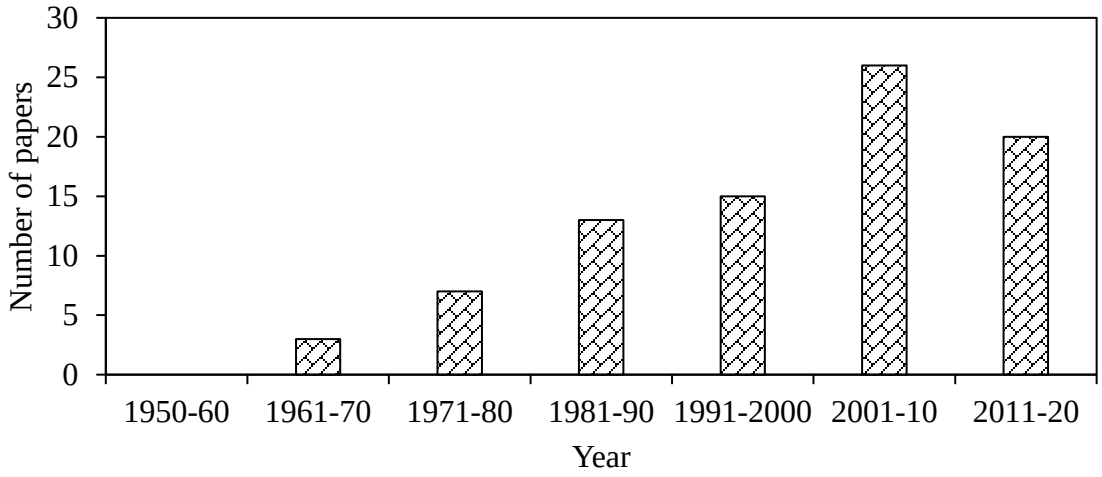

Figure 1.5. Published papers (85) on optimization of regenerators between 1950 and 2020 from Engineering Village and ASME database.

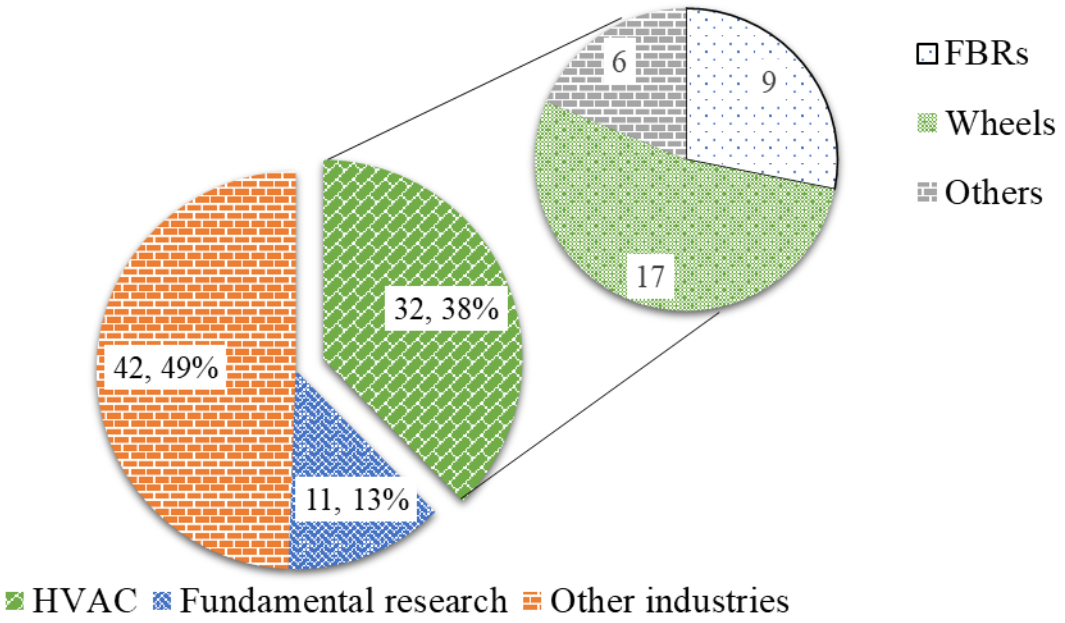

Figure 1.6. Classification of studies on optimization of regenerators between 1950 and 2020.

In addition to the gaps identified in the literature, part of the current research objectives is associated with an NSERC-CRD project between the University of Saskatchewan and Tempeff, an HVAC manufacturing company in Winnipeg. Tempeff sells sensible FBRs and would like to optimize the current heat exchangers and develop desiccant-coated FBRs. This Ph.D. research aims to analyze and optimize the performance of FBRs through numerical modeling. In addition, another Ph.D. student, Mr. Eswaran N. Krishnan, conducted experiments on FBRs as part of this NSERC-CRD project. The numerical results of this study are validated using results from these experiments.

1.4 RESEARCH OBJECTIVES

This PhD study aims to develop a transient numerical model to accurately evaluate and optimize the performance of FBRs in HVAC applications. To address the gaps identified in the literature review and the requirements of Tempeff, the objectives of this Ph.D. research are:

1. To develop and validate a transient numerical model for sensible FBRs

2. To quantify sensor errors over a wide range of design and operating conditions of sensible FBRs and make recommendations for testing standards
3. To optimize sensible FBRs considering transient characteristics
4. To develop and validate a transient numerical model for desiccant-coated FBRs and quantify sensor errors.

1.5 PUBLICATIONS

The research conducted during this PhD study has been documented in four peer-reviewed journal articles, five conference papers, and two poster presentations. Additionally, I contributed to Easwaran Krishnan publications (four journal papers, two conference papers, and one poster presentation) that are not included in this thesis.

1.5.1 Peer-reviewed journal papers

1. **H. Ramin**, E. N. Krishnan, A. Gurubalan, W. O. Alabi, and C. J. Simonson, 2021, "A transient numerical model for sensible fixed-bed regenerator in HVAC applications," *International Journal of Heat and Mass Transfer*, vol. 177, pp. 1-17.
2. **H. Ramin**, E. N. Krishnan, A. Gurubalan, W. O. Alabi, and C. J. Simonson, 2020, "Transient sensor errors and their impact on fixed-bed regenerator (FBR) testing standards," *Science and Technology for the Built Environment*, vol. 27, pp. 656-678.
3. **H. Ramin**, E. N. Krishnan, A. Gurubalan, and C. J. Simonson, 2021, "The effect of transient characteristics on the optimization of fixed-bed

regenerators (FBRs)," *ASME Journal of Thermal Science and Engineering Applications,* vol. 14 (5), pp. 1-16.

4. **H. Ramin,** E. N. Krishnan, A. Gurubalan, and C. J. Simonson, "A transient numerical model for desiccant-coated FBRs," under review for publication to *Science and Technology for the Built Environment*.

1.5.2 Conference papers and poster presentations

1. **H. Ramin,** E. N. Krishnan, and C. J. Simonson, "Effectiveness of fixed-bed regenerators for energy recovery in buildings applications," *Proceedings of the 12th Symposium on Building Physics*, 6-9 September 2020, Tallinn, Estonia. (Virtual presentation)
2. **H. Ramin,** E. N. Krishnan, A. Gurubalan and C. J. Simonson, "Transient performance of fixed-bed regenerators for energy recovery in building applications," *Proceedings of the ASME 2020 Heat Transfer Summer Conference*, July 12-15, 2020, Orlando, Florida, USA. (Virtual presentation)
3. **H. Ramin,** E. N. Krishnan, W. O. Alabi, and C. J. Simonson, "Temperature measurement correction for the determination of the effectiveness of fixed-bed regenerators (FBRs) for HVAC applications," *2020 ASHRAE Summer Virtual Conference*, June 29 – July 2, 2020. (Virtual presentation)
4. **H. Ramin,** E. N. Krishnan, and C. J. Simonson, "High-efficiency energy recovery ventilator for energy consumption reduction in buildings," *2020 Graduate Research Conference (GSA)*, Saskatoon, Saskatchewan, Canada, 13-14th February 2020. (In-person presentation)

5. **H. Ramin,** E. N. Krishnan, and C. J. Simonson, "High-efficiency energy recovery ventilator for reducing energy consumption in buildings," *The second People Around the World (PAW) conference*, Saskatoon, Saskatchewan, Canada, 6-7th February 2020 (Poster presentation)/ (In-person presentation)
6. **H. Ramin,** E. N. Krishnan, and C. J. Simonson, "Energy recovery exchanger for energy conservation in buildings," *The 1st Engineering Graduate Research conference,* Saskatoon, SK, Canada, 12th September 2019 (Poster presentation)/ (In-person presentation)
7. **H. Ramin,** E. N. Krishnan, and C. J. Simonson, "Fixed-bed regenerators for HVAC applications," *The 27th Canadian Congress of Applied Mechanics (CANCAM),* Sherbrooke, QC, Canada, 27-30th May 2019. (In-person presentation)

1.6 THESIS OVERVIEW

The thesis is structured in a manuscript-based style and consists of six chapters and two appendices. The thesis structure, objectives, and the chapter documenting each thesis objective are presented in Fig. 1.7.

Chapter 1 includes an introduction, background of the research, a list of publications, and the thesis structure. The manuscripts addressing four objectives of the thesis are presented in Chapters 2 to 5. Finally, Chapter 6 presents the conclusions of the research and proposed future works.

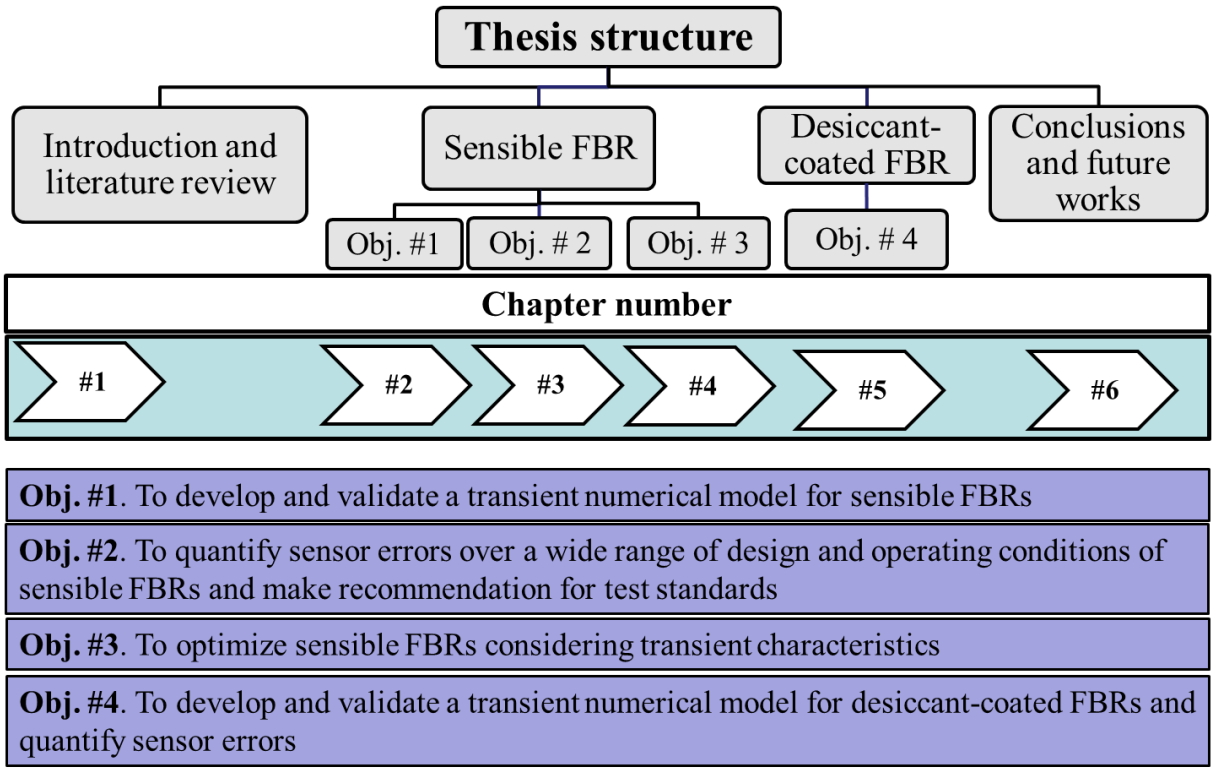

Figure 1.7. Overview of this PhD thesis structure representing thesis objectives and chapters.

The first objective of the thesis is addressed in Chapter 2. This chapter introduces the transient numerical model for sensible FBRs. The numerical model consists of an FBR model and a sensor model and is validated with the experimental results from the small-scale test facility (measured by PhD student Easwaran N. Krishnan) and the literature correlations. The numerical model can capture the transient behavior of sensible FBRs and temperature sensors and accurately predict the measurement errors that can occur due to the transient characteristics of FBRs and sensors at different operating conditions in HVAC applications.

The validated transient numerical model is then used to quantify errors in temperature and effectiveness resulting from the FBR's and sensors' transient characteristics over a wide range of design and operating conditions. The results are presented in Chapter 3, which addresses the second objective of this research. Practical recommendations for temperature measurement are

provided for different types of FBRs developed for HVAC applications. As part of this objective, the temperature measurement requirements from ASHRAE standard 84 and CSA C439-18 standard are examined.

Temperature swing (TS) occurs in the supply air due to the transient nature of FBRs and creates a variable load on the heating/cooling equipment. It can also contribute to the occupant's thermal discomfort. A correlation for TS is developed as a function of design parameters of sensible FBR and presented in Chapter 4. The optimization of FBRs is performed considering TS as an additional objective to the traditional parameters, namely exchanger effectiveness, pressure drop, payback period, and exchanger mass. A decision-making procedure is also integrated into the optimization process to select the optimized FBRs from Pareto fronts. The results are presented in Chapter 4, which addresses the third objective of this PhD research.

This thesis final objective, which is a transient numerical model for desiccant-coated FBRs, is addressed in Chapter 5. Similar to the transient numerical model for sensible FBRs, the developed transient numerical model for desiccant-coated FBRs consists of an FBR model and sensor models (both temperature and humidity). The numerical model is validated using experimental results measured by Easwaran N. Krishnan. The numerical model predicts the complex transient heat and mass transfer process in desiccant-coated FBRs and the transient characteristics of humidity and temperature sensors. The model can predict the measurement errors because of the transient characteristics of the desiccant-coated FBRs and the humidity and temperature sensors at different design and operating conditions. The requirements for simultaneous humidity and temperature measurements in the ASHRAE standard 84 and CSA C439-18 standards are examined, and practical recommendations are also provided.

The thesis conclusions, contributions, and future works are presented in Chapter 6. The copyright permissions for the published papers used in this thesis are shown in Appendix A.

To avoid repetition and have a logical thesis flow, the final version of the submitted/published papers are slightly modified wherever needed. An overview is also added to the beginning of each chapter which includes contributions of authors for each paper. The modifications to the papers are discussed in the overview of each chapter, if applicable.

CHAPTER 2

TRANSIENT NUMERICAL MODEL FOR SENSIBLE FBRs

2.1 OVERVIEW

This chapter describes the transient numerical model for sensible FBRs, which is the first objective of this PhD thesis. The model description, solution procedure, and validation are explained in detail. A description of the small scale-test facility used to validate the numerical results is also described. The developed model can capture the transient behavior of FBRs and temperature sensors and thereby accurately predict the measurement errors due to slow response of sensors at different operating conditions in HVAC applications.

This chapter was published as a research paper in the *International Journal of Heat and Mass Transfer* in June 2021 (Click here). The author of this thesis (Hadi Ramin) developed the numerical model and prepared the original draft of the paper. Mr. Krishnan (PhD student) conducted the experiments for validation and wrote the experimental section of the paper, Dr. Annadurai (Postdoctoral Fellow), Dr. Alabi (Postdoctoral Fellow), and Prof. Simonson (Supervisor) contributed to this paper by critically reviewing the paper.

A Transient Numerical Model for Sensible Fixed-Bed Regenerator in HVAC Applications

(Published in International Journal of Heat and Mass Transfer, June 2021)

Hadi Ramin, Easwaran N Krishnan, A. Gurubalan, Wahab O. Alabi, and Carey J. Simonson

2.2 ABSTRACT

Fixed-bed regenerators (FBRs) are energy recovery exchangers that can significantly reduce the energy required to condition outdoor ventilation air in HVAC systems. FBRs have high sensible effectiveness but produce an outlet air temperature that varies with time. In this chapter, a numerical model is developed to evaluate the performance of FBRs, and more specifically, the transient nature of their operation. This transient nature poses difficulties for experimental testing; thus, the developed model consists of an exchanger (FBR) model and a sensor model to differentiate the actual exchanger performance from the performance that would be measured in an experiment. The developed numerical model is validated with experimental data and correlations from the literature. The numerical model is capable of capturing the transient behaviour of FBRs and temperature sensors to accurately predict the measurement errors (and thus effectiveness errors) that can occur due to the transient response characteristics of FBRs and sensors at different operating conditions in HVAC applications. A maximum effectiveness error of 16% was obtained for the condition under study in this chapter.

2.3 **INTRODUCTION**

In recent decades, air infiltration and energy losses through the envelope of buildings have decreased significantly through increased thermal resistance and building airtightness. As such, modern buildings are more isolated from the outside, which leads to a greater need for fresh outdoor air and high energy demand for ventilation to maintain the required indoor air quality [16]. Furthermore, as other energy losses from buildings are reduced, the fraction of energy needed for ventilation air increases. A common way to reduce the energy requirement for conditioning ventilation air is to incorporate air-to-air energy exchangers (AAEEs) into building heating, ventilating, and air conditioning (HVAC) systems to recover energy from the exhaust air as shown in Fig. 2.1 [24]. In terms of energy exchange, AAEEs are broadly classified into recuperative and regenerative exchangers. In recuperative exchangers, the hot and cold airstreams flow through separate channels within the exchanger. However, in regenerators (shown in Fig. 2.2 (a) &(b)), the hot and cold airstreams flow through the same channels intermittently. The heat from the hot fluid is stored in the exchanger matrix (hot period), which is then released to the cold fluid during subsequent exposure of the exchanger to the cold fluid (cold period) (as shown Fig. 2.2 (a) &(b)) [30].

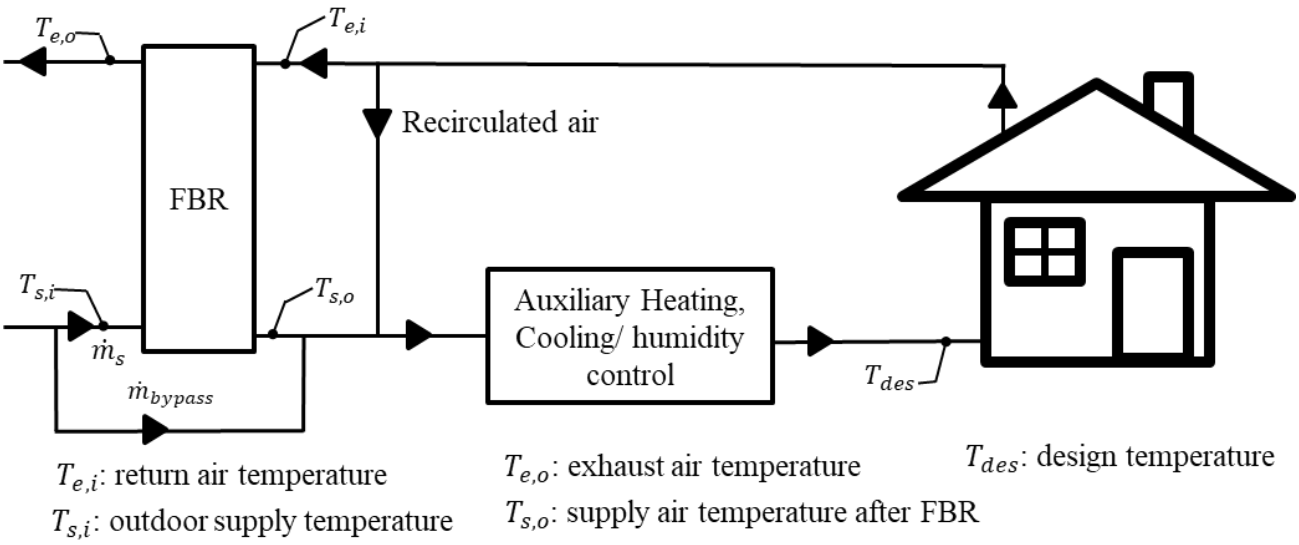

Figure 2.1. A schematic of an HVAC system with FBRs for heat recovery.

Rotary regenerators (energy wheels) and fixed-bed regenerators (FBRs) are two types of regenerators. Energy wheels rotate cyclically between hot and cold airstreams for continuous operation, while dampers alternate the airflow through stationary matrixes in FBRs. The rotary regenerators' typical rotational speed is 0.5-3 rpm for power plants and 0.5-20 rpm for HVAC applications [29]. Energy wheels have been extensively studied for energy recovery in HVAC applications [23–28], and FBRs have been used for heat recovery in high-temperature applications such as glass furnaces, coke ovens, and open-hearth steel furnaces [7–10]. In recent times, FBRs have been attracting increasing attentions for energy recovery in HVAC applications due to their high effectiveness [11–16]. Typical hot and cold periods of FBRs are about 20 minutes for glass furnace applications [9,10], whereas, in the HVAC industry, a shorter period duration of 15-120 seconds is required [15,17,20].

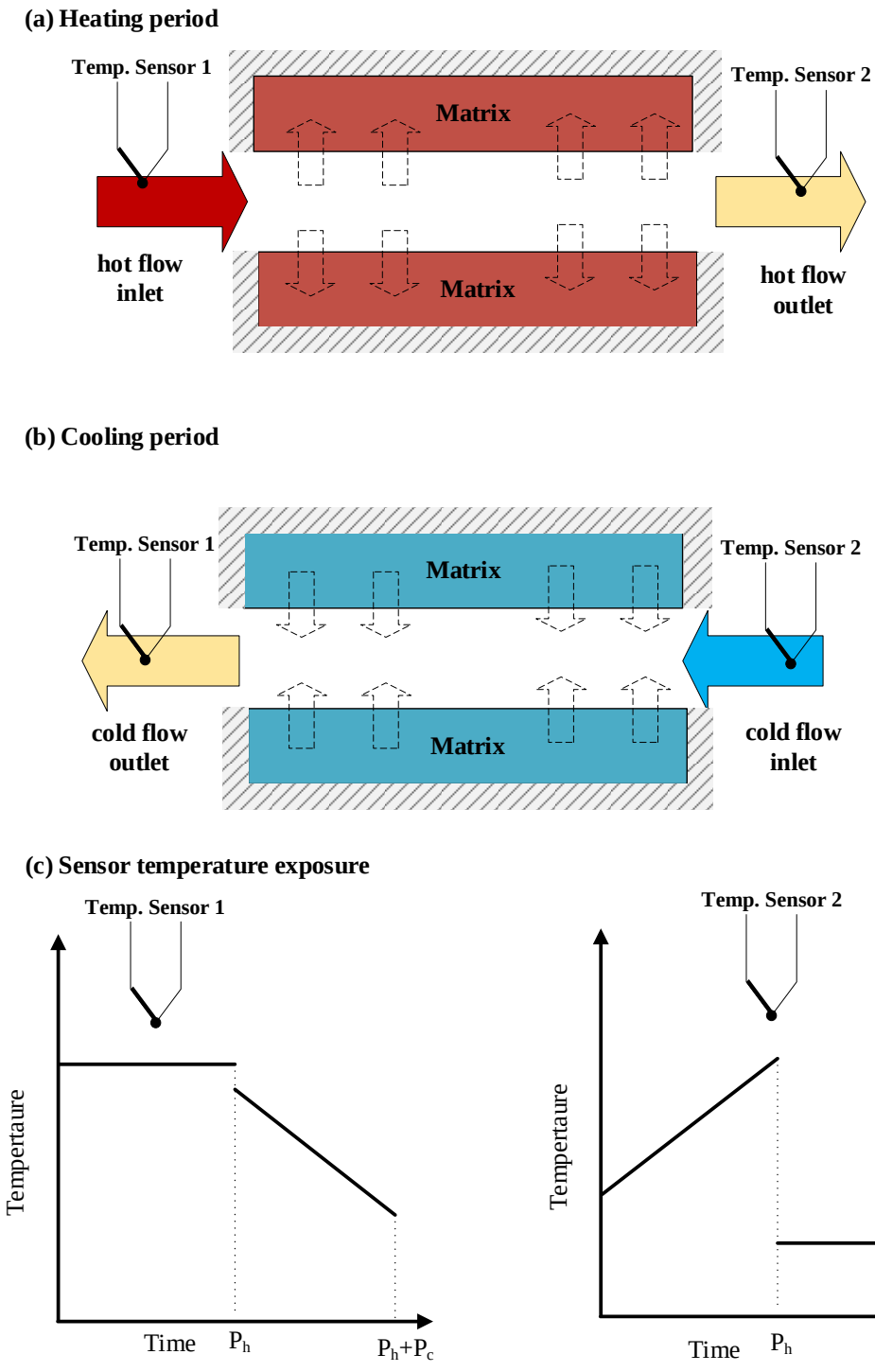

Figure 2.2. A schematic of alternate heating and cooling periods of FBRs and the corresponding temperature profile for temperature measurement sensors.

The same governing equations govern the heat transfer process of FBRs as that of energy wheels [19,31]. But in contrast to energy wheels and recuperative exchangers, FBRs never attain a steady-state condition; instead, FBRs reach a periodic steady-state where the outlet air temperature changes during each period but is repeated from period to period. Furthermore, due to switching between the hot and cold flows, the temperature measured at the outlet (of FBR) at the beginning of each period is affected by the temperature that the sensor was exposed to during the previous period (as shown in Fig. 2.2 (c)) because of the thermal mass of the sensor [20,32,33]. Although models were available for FBRs in high-temperature applications since 1950 [18,19], the transient region was negligible for those applications because of the extended hot/cold period (20 minutes). Krishnan et al. [20] reported significant deviations in the experimental determination of the effectiveness of FBRs due to sensor transient, especially at the shorter operating cycles (15 seconds). In recent studies of FBRs for HVAC applications [13,15,16], mathematical models have been used to predict the effectiveness, but the initial transient region has not been explored. Overall, the model and analysis of this transient behavior of FBRs coupled with temperature measurement sensors are not in the current literature, which is the research gap this chapter addresses.

A detailed numerical model to evaluate the sensible effectiveness and analyze the transient nature of the outlet air temperature of FBRs is developed. The developed numerical model consists of an exchanger (FBR) model and a temperature sensor model. The exchanger model captures the transient behavior of the outlet temperature profile of FBRs, while the sensor model predicts the temperature recorded by the temperature sensors. This chapter elucidates the significance of transient temperature measurements in FBRs, and the effect of transient temperature measurement

for operating conditions of balanced/unbalanced flow rate, as well as equal/unequal hot/cold periods.

2.4 NUMERICAL MODEL FOR THE FBR AND TEMPERATURE SENSOR

2.4.1 Exchanger (FBR) model

Exchangers consist of many small channels that air flows through the channels intermittently. Numerical models are usually performed on a representative channel since all the channels have similar flow and thermal conditions.

2.4.1.1 Physical exchanger

Figure 2.3 (a) shows a picture of a small-scale FBR, consisting of 26 aluminum plates (Al-3003) in a parallel configuration. A summary of the geometrical details and thermophysical properties of the exchanger is provided in Table 2.1.

Table 2.1. Geometrical details and thermophysical properties of the exchanger.

Air Channel	Length (L), (mm)	Width (W) (mm)	Hydraulic diameter (D_h) (mm)	Channel height (h_c) (mm)	Aspect ratio (α^*)
	200	80	4.08	2.1	0.03
Aluminium Plate	Thermal conductivity (k_m)(W/m·k)	Density (ρ_m) (kg/m^3)	Specific heat (Cp_m) (J/kg·K)	Thickness (t_p) (mm)	number of plates
	220	2730	904	0.7	26
Air properties	Thermal conductivity (k_g) (W/m·k)	Density (ρ_g) (kg/m^3)	Specific heat (Cp_g)(J/kg·K)	-	-
	0.024	1.23	1005	-	-

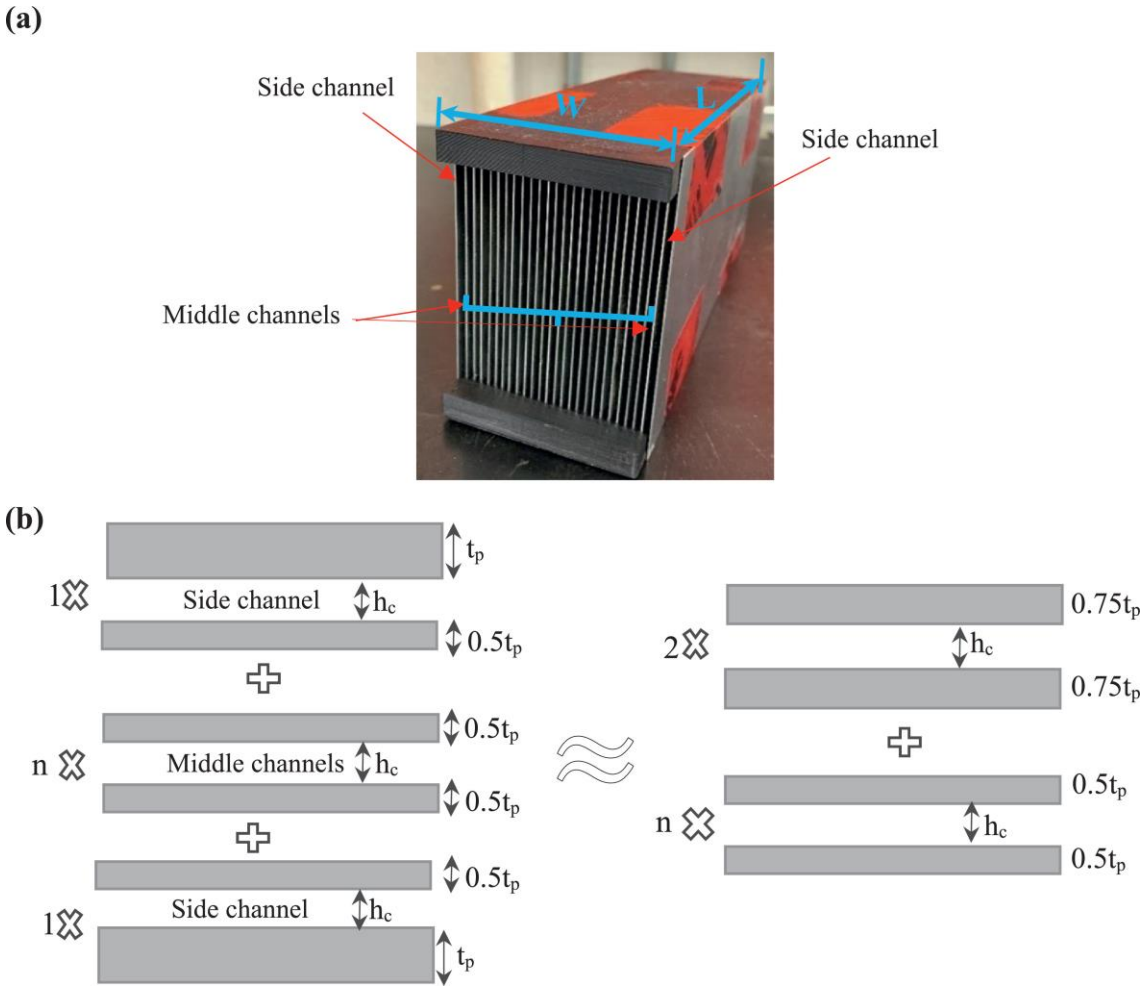

Figure 2.3. (a) A picture of the small-scale FBR, and (b) the proposed geometrical configuration for numerical modeling.

A representative parallel plate channel can be selected to perform numerical modeling. However, the side channels' boundary conditions (channels at both sides) are different from those in the middle. As shown in Fig. 2.3(a), the middle channels share their thickness (t_p) with the neighboring channels, while the side channels share only one plate thickness (t_p) with the neighboring channels. Therefore, the middle and side channels should be treated differently. Figure 2.3(b) illustrates the proposed channel configuration of the exchanger for numerical modeling purposes. As shown in Fig. 2.3(b), it is assumed that the exchanger comprises 'n' middle channels with a thickness of $0.5t_p$ and two channels with a thickness of $0.75t_p$. The weighted average outlet

temperature of the middle and side channels is considered to be the outlet temperature of airstreams at the outlet of FBR.

2.4.1.2 Assumptions

The assumptions used in the model of the FBR are listed below:

i. The heat transfer process is modeled using the bulk air temperature; hence the numerical modeling of FBR is simplified to one-dimensional for the airflow.
ii. The temperature gradient across the thickness and the width of the matrix are considered to be negligible [34] ($Bi<0.1$), and the matrix temperature is assumed to vary only in the longitudinal direction.
iii. The velocity and temperature profiles of airstreams develop simultaneously inside the channel [34] ($Pr=0.7$).
iv. The thermophysical properties of the air and matrix are constant.
v. Frosting and condensation do not happen in the exchanger.
vi. The switching between hot and cold airflows happens instantaneously.
vii. The impacts of flow maldistribution inside the channels are neglected and representative channel is used for the modeling.

Condensation and frosting are practical problems that might limit the application of FBRs in HVAC applications. Often energy exchangers are selected and operated to avoid any uncontrolled condensation or frosting within FBRs and thus this model does not consider frosting and condensation. Nizovtsev et al. [15] studied the impact of condensation on regenerative heat exchangers.

2.4.1.3 Governing equations

A schematic diagram of the representative channel and the heat transfer process between the hot and cold airstreams and the matrix are presented in Fig.2.4. The flow configuration is counterflow, and the one-dimensional governing energy equations for the airstream (subscript 'g') and matrix (subscript 'm'), considering the above-mentioned simplifying assumptions, are presented in Eqns. (2.1) and (2.2) [35,36]:

$$\rho_g Cp_g A_g \frac{\partial T_g}{\partial t} + V\rho_g Cp_g A_g \frac{\partial T_g}{\partial x} + h\frac{A_s}{L}(T_g - T_m) = \frac{\partial}{\partial x}\left(k_g A_g \frac{\partial T_g}{\partial x}\right) \quad (2.1)$$

$$\rho_m C_{P_m} A_m \frac{\partial T_m}{\partial t} - h\frac{A_s}{L}(T_g - T_m) - \frac{\partial}{\partial x}\left(k_m A_m \frac{\partial T_m}{\partial x}\right) = 0 \quad (2.2)$$

where T, x, ρ, C_p, k, V, h, L, and t are temperature, axial coordinate, density, specific heat capacity, thermal conductivity, mean airflow velocity, convective heat transfer coefficient, length of channel and time respectively. Other symbols, as used in the above equations (2.1 &2.2), are the cross-sectional area of the channel (A_g), matrix (A_m), and heat transfer surface area (A_s).

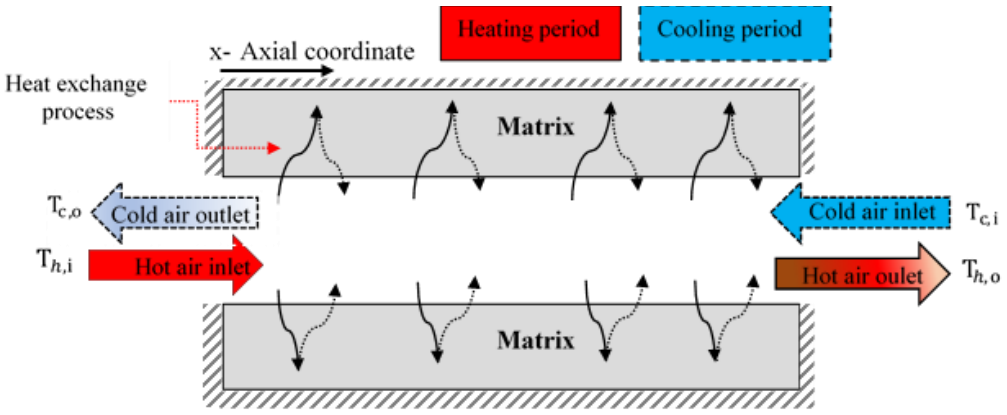

Figure 2.4. A schematic showing the heat transfer process in the representative channel of FBR.

2.4.1.4 Boundary conditions

The inlet conditions of hot and cold airstreams are presented in Eqns. (2.3) and (2.4).

$$T_g(x = 0, mP \le t \le mP + P_h) = T_{h,i} \qquad m = 0,1,2, \ldots \tag{2.3}$$

$$T_g(x = L, mP + P_h \le t \le (m+1)P) = T_{c,i} \quad m = 0,1,2, \ldots \tag{2.4}$$

where $T_{h,i}$ and $T_{c,i}$ are the inlet temperature of the hot and cold airstreams, respectively. P is the total cycle time, P_h is the hot period, P_c is the cold period and m is an integer to count the cycles of operations.

The ends of the matrix are assumed to be adiabatic [35,36]:

$$\left.\frac{\partial T_m}{\partial x}\right|_{x=0} = \left.\frac{\partial T_m}{\partial x}\right|_{x=L} = 0 \tag{2.5}$$

2.4.1.5 Convective heat transfer coefficient

For laminar flow inside a channel with Reynolds number between 100-1000, the hydrodynamic and thermal entry region is about 5-30% of the total length of the channel [37]. The airflow in the FBR is laminar and within this range of Reynolds number; thus, the convective heat transfer coefficient for the simultaneous (thermal and hydrodynamic) developing flow is used for the modeling [38].

2.4.1.6 Performance criteria

The performance of an FBR is quantified using the sensible effectiveness, which is defined as the ratio of the actual heat transfer rate to the maximum possible heat transfer rate [21,22], and is mathematically represented as follows:

$$\varepsilon = \frac{(\dot{m}C_p)_h \left(\overline{T}_{h,o} - T_{h,i}\right) or (\dot{m}C_p)_c \left(\overline{T}_{c,o} - T_{c,i}\right)}{\min\left((\dot{m}C_p)_h, (\dot{m}C_p)_c\right) \left(T_{h,i} - T_{c,i}\right)} \quad (2.6)$$

where $T_{h,i}, T_{c,i}$ are the inlet temperature of the hot and cold airflows respectively, while $(\dot{m}C_p)_h$ and $(\dot{m}C_p)_c$ are the hot and cold stream heat capacity rates, respectively. As noted previously, the temperature of the air leaving an FBR varies with time, and $\overline{T}_{h,o}$, $\overline{T}_{c,o}$ are the time-averaged outlet temperatures of hot and cold airstreams, respectively, and are mathematically represented by Eqns. (2.7) and (2.8).

$$\overline{T}_{h,o} = \frac{1}{P_h}\int_0^{P_h} T_{h,o}\,dt \quad (2.7)$$

$$\overline{T}_{c,o} = \frac{1}{P_c}\int_0^{P_c} T_{c,o}\,dt \quad (2.8)$$

2.4.2 **Temperature sensor model**

2.4.2.1 Physical model and assumptions

The temperature sensors at the outlet of FBRs are immersed in the airstreams, whose temperature varies with time within each period. It is assumed that the resistance to the heat conduction of the temperature sensor is much smaller than the resistance to convection across the airstream. This is a reasonable assumption as the temperature sensors are usually made small. Thus, the temperature of the sensor is uniform at any time, and the lumped capacitance method is applicable and valid [34]. Another assumption is that sensors thermal properties are constant, and the heat transfer through radiation with the surrounding environment is insignificant.

2.4.2.2 Governing equation

With the assumption of the validity of the lumped capacitance method [34], the energy equation for temperature sensors is given in Eqn. (2.9).

$$\left(T_g - T_s\right) = \frac{\rho_{ts} V_{ts} Cp_{ts}}{hA_{ts}} \frac{dT_s}{dt} = \tau_s \frac{dT_s}{dt} \tag{2.9}$$

where ρ_{ts}, V_{ts}, Cp_{ts}, A_{ts} are the density, volume, specific heat capacity, and surface area of the temperature sensor, respectively. h is the convective heat transfer coefficient, and T_s is the temperature of the sensor (sensor measurement), while T_g is the air temperature. Also, τ_s ($= \frac{\rho_{ts} V_{ts} Cp_{ts}}{hA_{ts}}$) is the time constant of the sensor, which is defined as the time it takes to reach 63.2% of the total difference between the initial and final temperature [34].

2.4.2.3 Sensor initial condition

Before exposure to the airflow at the outlet of the exchanger (FBR), the initial sensor temperature is presented in Eqn. (2.10).

$$T_{s,0} = T_{initial} \tag{2.10}$$

2.4.3 Combined FBR and sensor model

The FBR model predicts the actual temperature of the air at the outlet of FBR. With the temperature (T_g) from the FBR model, the sensor temperature measurement is obtained using the sensor model in Eqn. (2.9). The combined FBR and sensor model take the actual temperature from the FBR model and use this to obtain the sensor measurements from Eqn. (2.9). The time constants for the sensors can be obtained experimentally or from the manufacturer's datasheet.

2.4.4 **Numerical solution for the FBR model**

The transient transport equations for the conservation of energy in the airflow and matrix (Eqns. (2.1) and (2.2)) are discretized using the finite volume method [39]. The upwind differencing and the central differencing schemes are used to approximate the convection term for the airflow and the diffusion term in the matrix. The resulting algebraic equations for the airflow are solved using the Gauss-Seidel iteration technique, while the Tridiagonal Matrix Algorithm is used to solve the energy equation in the matrix.

The numerical solution starts with initial values for the air and matrix temperatures. Although the quasi-steady-state condition is used for the performance calculation of FBR, the current numerical solution is time accurate, and time is incremented whenever the following convergence criterion (Eqn. (2.11)) is satisfied for the dependent variables; i.e., the air and matrix temperatures:

$$\frac{\sum_{i=1}^{N_s}(T(i)^{j+1} - T(i)^{j})}{N_s \times \left(T_{h,i} - T_{c,i}\right)} \leq 10^{-5} \tag{2.11}$$

where T is the temperature (air and matrix), N_s is the numbers of spatial nodes, a0nd i, j are integers. The convergence criterion is selected to be 10^{-5} as decreasing this value to 10^{-6} has a negligible effect (less than 0.05%) on the predicted effectiveness.

The outlet temperature of airstreams in FBRs varies with time, but exchanger reaches a quasi-steady-state condition. At this condition, the outlet temperature of FBR varies with time but repeats itself in a cyclic version [11]. The onset operating condition of a quasi-steady state is identified using Eqns. (2.12) and (2.13) [40].

$$\left|\frac{\dot{m}_h\left(T_{h,i} - T_{h,o}\right) - \dot{m}_c\left(T_{c,o} - T_{c,i}\right)}{\min(\dot{m}_h, \dot{m}_c)\,(T_{h,i} - T_{c,i})}\right| \leq 10^{-2} \tag{2.12}$$

$$\left|\frac{\partial \epsilon}{\partial t}\right| \approx \left|\frac{\epsilon^{k} - \epsilon^{k-1}}{P}\right| \leq 10^{-4} \tag{2.13}$$

where ϵ is the effectiveness of FBR, and $\dot{m}_h$, $\dot{m}_c$ are the hot and cold mass flowrates respectively. ϵ^k and ϵ^{k-1} are the effectiveness at the current and previous cycles, respectively. Decreasing the quasi-steady-state conditions criteria (10^{-2} and 10^{-4}) in Eqns. (2.13) and (2.13) by a factor of 10 has an insignificant effect (less than 0.1%) on the predicted quasi-steady-state effectiveness, whereas increasing the solution time by approximately a factor of two. A Matlab code has been developed to solve the algebraic equations. A flowchart presented in Fig. 2.5 shows the numerical procedure to solve the FBR and sensor model's governing equations.

The numerical solution is carried out within a uniform spatial grid with a constant time step. The grid independence test is performed to determine the grid size and time step for the numerical solution. It is observed that decreasing the spatial grid size to less than 0.0007 m and time step less than 0.01 s have a negligible effect (<0.1%) on the predicted effectiveness. Therefore, a time step of 0.01 s and a spatial grid size of 0.0007 m are selected for the numerical study.

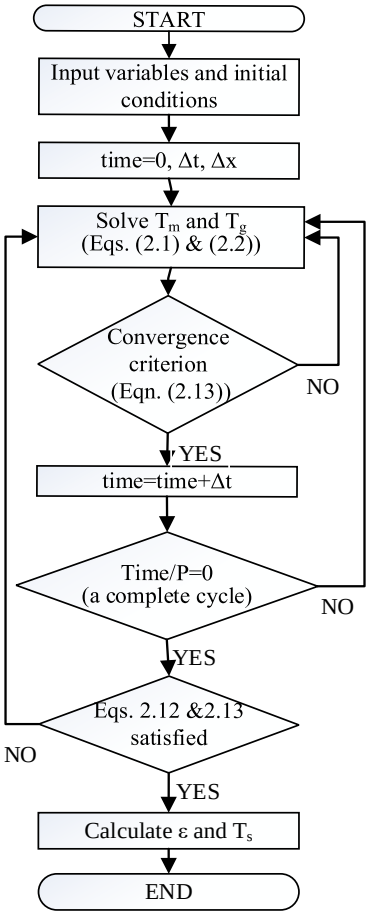

Figure 2.5. Numerical flowchart.

2.4.5 **FBR model validation**

The effectiveness-Number of Transfer Units (ε-NTU) method is a commonly used approach for the design of heat exchangers. Effectiveness can be presented as a function of dimensionless groups and flow arrangements [19]. The dimensionless groups are extracted from the governing equations, and for sensible regenerators, effectiveness can be obtained from Eqn. (2.14) and its functional terms are listed in Eqns. (2.15)- (2.18).

$$\epsilon = \phi(\mathrm{NTU_o}, C^*, C_r^*, (hA_s)^*) \tag{2.14}$$

where:

$$\mathrm{NTU}_o = \frac{1}{\left(\dot{m}\mathrm{C_p}\right)_{\mathrm{g,min}}}\left[\frac{1}{(\mathrm{hA_h})_{\mathrm{h}}} + \frac{1}{(\mathrm{hA_c})_{\mathrm{c}}}\right]^{-1} \tag{2.15}$$

$$\mathrm{Cr}^* = \frac{\left(\mathrm{MC_p}\right)_{\mathrm{m}}}{\left(\dot{m}\mathrm{C_p}\right)_{\mathrm{g,min}}(\mathrm{P_c} + \mathrm{P_h})} \tag{2.16}$$

$$\mathrm{C}^* = \frac{\left(\dot{m}\mathrm{C_p}\right)_{\mathrm{g,min}}}{\left(\dot{m}\mathrm{C_p}\right)_{\mathrm{g,max}}} \tag{2.17}$$

$$(\mathrm{hA_s})^* = \frac{(\mathrm{hA_s})_{\mathrm{h}}}{(\mathrm{hA_s})_{\mathrm{c}}} \tag{2.18}$$

where $\mathrm{NTU_o}$, Cr^*, C^*, and $(\mathrm{hA_s})^*$ are the overall number of transfer units, overall matrix heat capacity ratio, the ratio of minimum to maximum heat capacity rate of the airstreams, and convective conductance ratio, respectively. For the range of $0.25 \leq (hA_s)^* \leq 4$, the effect of convective conductance ratio, $(hA_s)^*$on effectiveness is negligible [19].

Axial heat conduction in the matrix is significant in FBRs compared to rotary exchangers because of the higher thickness of plates, and it also decreases the effectiveness of regenerators [41,42]. Bahnke and Howard [41] proposed a dimensionless group (λ) (Eqn. (2.19)) to quantify the effect of axial conduction within the matrix:

$$\lambda = \frac{k_m A_{m,t}}{L\, C_{min}} \tag{2.19}$$

where k_m is the thermal conductivity and L is the length of the exchanger, $A_{m,t}$ $(= A_{m,h} + A_{m,c})$ is the total area for longitudinal conduction and C_{min} is the minimum heat capacity rate of the airflows. $A_{m,h}$ and $A_{m,c}$ are the matrix hot and cold side cross-sectional area, respectively.

Empirical correlations have been proposed for regenerators' sensible effectiveness as a function of dimensionless parameters [19,43]. Such correlations for different flow conditions are listed in sections 2.4.5.1 and 2.4.5.2.

2.4.5.1 Balanced flow condition

For the balanced flow regenerators ($C^* = 1$), effectiveness is obtained from Eqn. (2.20) [19]:

$$\epsilon = \frac{NTU_o}{1 + NTU_o}\left[1 - \frac{1}{9(Cr_o^*)^{1.93}}\right]\left[1 - \frac{C_\lambda}{2 - C^*}\right] \tag{2.20}$$

where:

$$C_\lambda = \frac{1}{1 + \frac{NTU_o(1 + \lambda\Phi)}{1 + \lambda NTU_o}} - \frac{1}{1 + NTU_o} \tag{2.21}$$

$$\Phi = \left(\frac{\lambda NTU_o}{1 + \lambda NTU_o}\right)\tanh\left(\frac{NTU_o}{(\lambda NTU_o/1 + \lambda NTU_o)^{0.5}}\right) \tag{2.22}$$

Eqn. (2.20) is accurate within 1% for the range of $1 \leq NTU_o \leq 20$, $2 \leq Cr_o^* \leq \infty$, $0.5 \leq (\mathrm{hA})^* \leq 1$ and $0 \leq \lambda \leq 0.08$.

2.4.5.2 Unbalanced flow condition

It is essential to evaluate the effect of unbalanced flow conditions on the predicted effectiveness since it frequently occurs in HVAC applications [40]. Therefore, the present study also entails the validation of the FBR model under unbalanced flow conditions. The effectiveness of such flow conditions can be obtained from Eqn. (2.23) as listed in the literature [19].

$$\epsilon = \frac{1 - \exp\left\{\epsilon_{r,\lambda\neq0}\left(C^{*2} - 1\right)/\left[2C^*\left(1 - \epsilon_{r,\lambda\neq0}\right)\right]\right\}}{1 - C^*\exp\left\{\epsilon_{r,\lambda\neq0}\left(C^{*2} - 1\right)/\left[2C^*\left(1 - \epsilon_{r,\lambda\neq0}\right)\right]\right\}} \tag{2.23}$$

where:

$$\epsilon_{r,\lambda=0} = \frac{NTU_{o,m}}{1 + NTU_{o,m}}\left[1 - \frac{1}{9\left(Cr_{o,m}^*\right)^{1.93}}\right] \tag{2.24}$$

$$\epsilon_{r,\lambda\neq 0} = C_{\lambda}\epsilon_{r,\lambda=0} \tag{2.25}$$

$$NTU_{o,m} = \frac{2NTU_0.C^*}{1+C^*} \tag{2.26}$$

$$Cr_m^* = \frac{2Cr^*.C^*}{1+C^*} \tag{2.27}$$

In Eqn. (2.25), C_λ is obtained from Eqn. (2.21) using the values of $NTU_{o,m}$ and Cr_m^* computed from equations (2.26) & (2.27), respectively. The accuracy of Eqn. (2.23) is the same as Eqn. (2.20) presented in the previous subsection for the balance flow condition.

2.4.5.3 Validation of FBR model

Eqns. (2.20) and (2.23) are valid when $0 \leq \lambda \leq 0.08$, therefore the results of this present numerical (FBR model) model for FBRs are validated with the numerical results of Bahnke and Howard [41] whenever the operating condition is outside this range. Bahnke and Howard [41] results are valid for the range of dimensionless parameters: $1 \leq NTU_o \leq 100, 0.9 \leq C^* \leq 1, 1 \leq C_r^* \leq \infty,\ 0.01 \leq \lambda \leq 0.32,\ and\ 0.25 \leq (hA)^* \leq 1$.

The maximum effectiveness difference between the current FBR model results and results obtained from Eqns. (2.20) and (2.23) over the range of $1 \leq NTU_o \leq 20,\ 2 \leq Cr^* \leq 10,$ $0.5 \leq (hA)^* \leq 1$ and $0 \leq \lambda \leq 0.08$ are found to be less than 1%. Furthermore, for higher values of conduction parameters ($0.08 \leq \lambda \leq 0.32$), the predicted effectiveness from the FBR model is in agreement with the numerical results of Bahnke and Howard [41] with a maximum difference of 0.5%. Figure 2.6 presents an example of comparisons between the current FBR model and the relevant literature [19,41] results for balanced/unbalanced flow FBRs.

2.4.6 **Validation of the combined FRB and sensor model**

The combined FBR and sensor model results are validated with the results from a small-scale test facility, as the experimental data includes both FBR and the sensor effects. The combined model validation includes validation of (1) transient temperature profile before reaching the quasi-steady state, (2) transient during the quasi-steady state, and (3) sensible effectiveness with experimental results from the small-scale test facility.

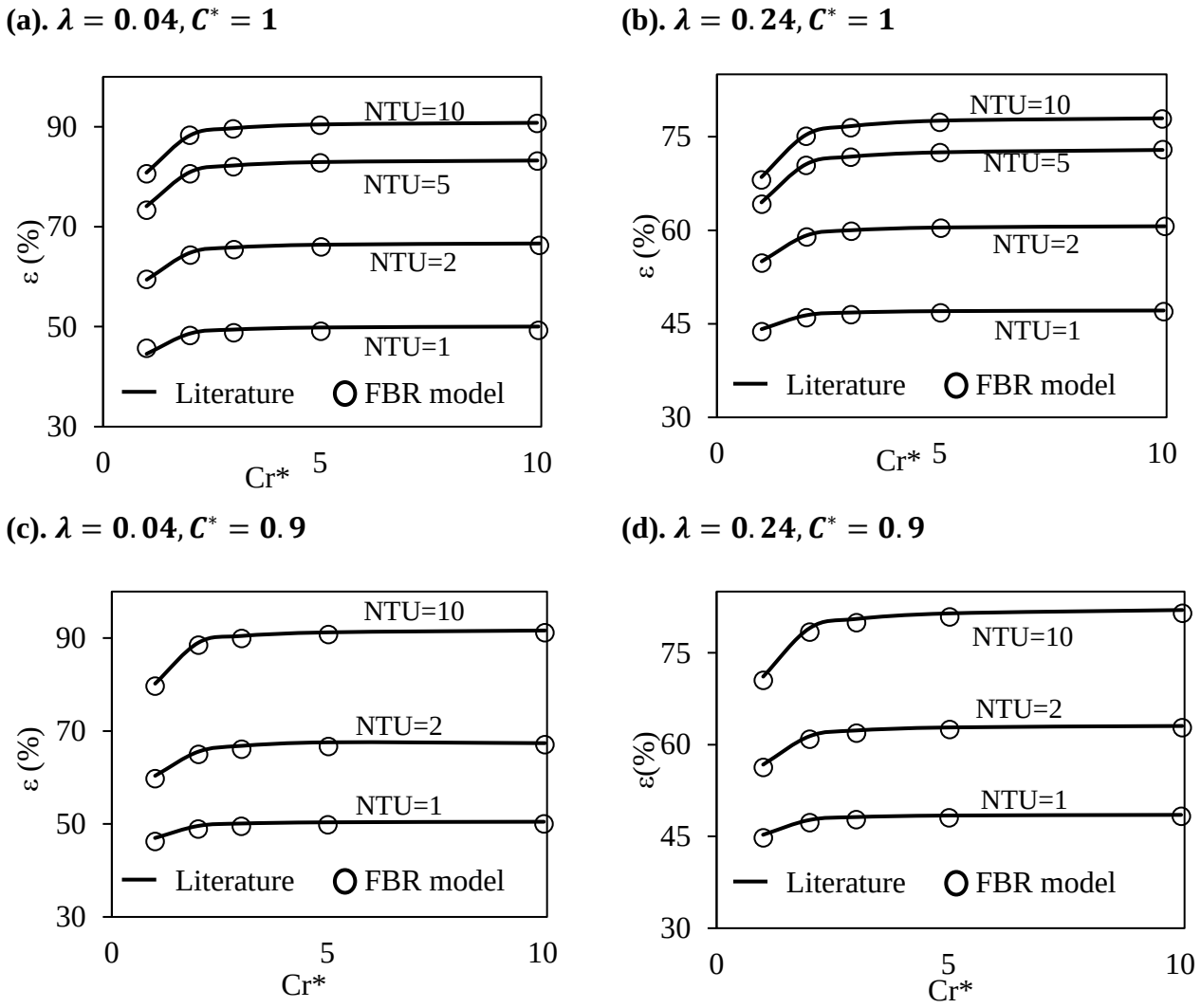

Figure 2.6. Comparison of results of the FBR model and the literature [19,41] for balanced and unbalanced flow conditions λ=0.04 and 0.24.

2.4.6.1 Small-scale experimental facility

A small-scale test facility is developed to determine the effectiveness of FBRs. The test facility consists of supply airlines (hot and cold airstreams) and a test section. The supply airlines provide continuous conditioned air to the test section. A schematic of the test section is shown in Fig. 2.7. The thick insulation inside the test section substantially reduces the heat transfer between the exchanger and its surroundings. A pneumatic-powered linear actuator unit is used to slide the exchanger cyclically between the hot and cold airstreams within the test section. The exchanger in the test section is alternatively exposed to the hot and cold airstreams to simulate the alternate heating and cooling processes of FBRs. The exchanger movement time between airflow is small, and it takes 0.3 s to slide the exchanger between the airstreams. Temperature is measured using T-type (0.08 mm wire diameter) thermocouples. The uncertainty in temperature measurements is ±0.2°C, and constant temperature at the exchanger inlet is maintained with a maximum temperature deviation of ±0.3°C. A detailed description of the facility development, measurement procedures, and uncertainty analysis can be found in the previous work of the authors of this chapter [20].

Airflow mixers are located upstream of measurement sensors to mix the outlet flow. To measure the air temperature at the outlet of the exchanger, a set of temperature sensors (thermocouples) are attached to the exchangers (called exchanger sensors), and another set is fixed to the airflow ducts (called duct sensors), as shown in Fig. 2.7. The duct sensors do not move with the exchanger, while the exchanger sensors are moved between airstreams along with the exchanger. The initial temperatures of the duct and exchanger sensors are different because of their exposure to different airstreams during the previous period. For the hot and cold periods, the initial temperatures of the duct and exchanger sensors are as follows.

For the duct sensors:

$$T_{initial} = T_{h,i} \quad \text{for hot period} \tag{2.28}$$

$$T_{initial} = T_{c,i} \quad \text{for cold period} \tag{2.29}$$

For the exchanger sensors:

$$T_{initial} = T_{c,i} \quad \text{for hot period} \tag{2.30}$$

$$T_{initial} = T_{h,i} \quad \text{for cold period} \tag{2.31}$$

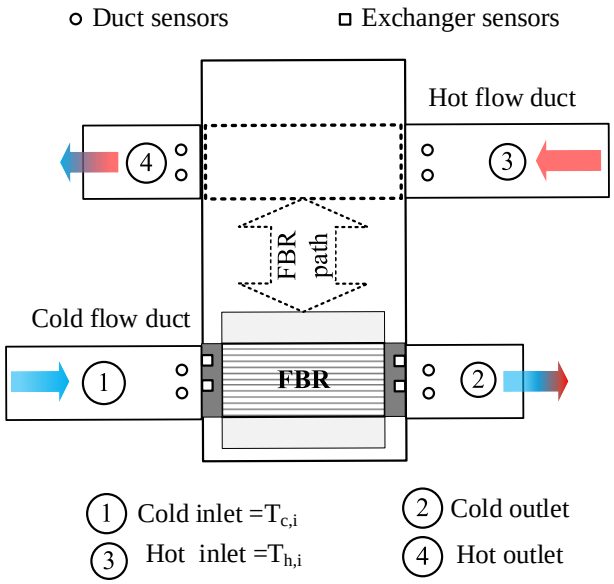

Figure 2.7. A schematic of the test section and thermocouples to measure the air temperature.

Table 2.2 provides the operating conditions of the experiments used for the validation of the combined FRB and sensor model. The time constant of the thermocouples used in the test facility is obtained experimentally.

Table 2.2. Operating conditions and sensor time constant for the validation of results.

Flow rate		Inlet temperature (°C)		Face velocity	Cycle time	Re	NTU_o	Cr*	Sensor time
(L/s)	(kg/s)	Hot side	Cold side	(m/s)	(s)				constant (s)
7.6	0.00926	40.0	24.0	2.0	20-240	520	2.4	0.8-10	1.5

2.4.6.2 Transient temperature before quasi-steady-state condition

The FBR outlet temperature measurements from the exchanger sensors, and the combined FBR and sensor model, are presented in Fig. 2.8. Before the start of the experiment, the exchanger matrix is at the cold flow temperature ($T_{c,i}$). At time zero, the exchanger is moved to the hot flow duct, and hot air flows through the exchanger and heats the exchanger matrix (for 60 s). The exchanger is then moved to the cold flow duct and the stored heat is transferred to the cold flow (for 60 s). This alternate movement of the exchanger between the airflows is continued until the exchanger's outlet temperature reaches the quasi-steady-state condition. Figure 2.8 shows that the combined FBR and sensor model prediction for temperatures are in good agreement with the experimental measurements during the entire transient process before reaching the quasi-steady state condition. It is important to note that the exchanger sensor's initial conditions at the beginning of hot and cold periods are the cold inlet flow and hot inlet flow temperatures, respectively, as presented in Eqns. (2.30) and (2.31). Also, the combined FBR and sensor model and the experimental results agree well at the beginning of hot and cold periods, where the sensor effect appears to be significant.

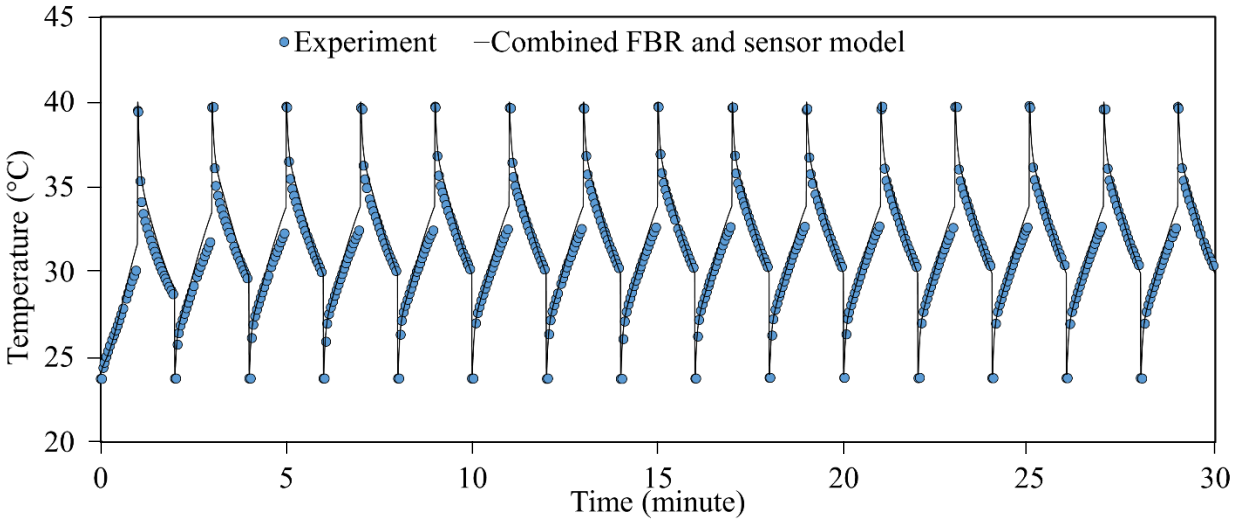

Figure 2.8. Transient outlet temperature profile of FBR, a comparison between combined FBR and sensor model and experimental results from exchanger sensors (NTU_o=2.4, face velocity=2.0 m/s, sensor time constant=1.5 s).

2.4.6.3 Quasi-steady-state temperature validation

A comparison between the experimental and numerical results (both the FBR model and the combined FBR and sensor model) for temperature profile at the quasi-steady-state condition is presented in this section. Figure 2.9 shows the temperature profiles from experiment with the duct sensors, FBR model, and combined FBR and sensor model, along with the inlet temperatures. A schematic of the FBR test facility is included in this figure to enhance the demonstration and understanding of the temperature profiles. The experimental and the FBR model temperatures are in good agreement, except at the beginning of the hot and cold periods, as shown in Fig. 2.9. The observed difference can be attributed to the transient response of the temperature sensors. The initial temperatures of the duct sensors in the hot/cold period are equal to the inlet hot/cold temperatures (Eqns. (2.28) and (2.29)). It takes some time for the duct sensors to respond to the change in temperature during hot and cold periods. The combined FBR and sensor model captures this initial transient behavior, and the combined model results are in good agreement with the experimental measurement for the entire hot and cold periods.

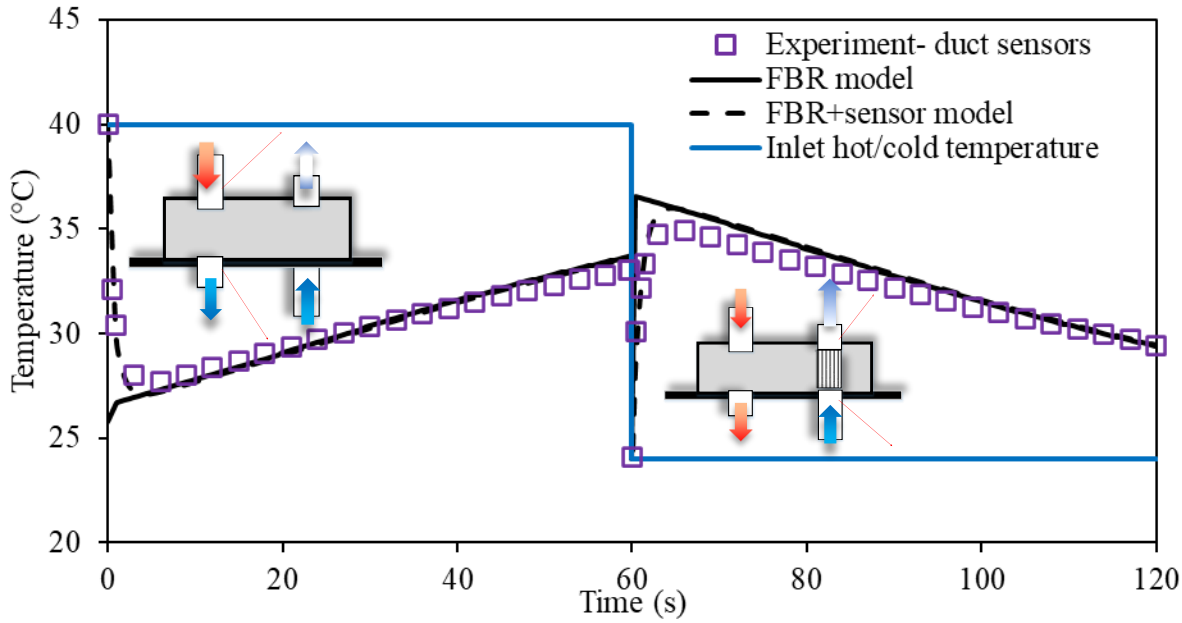

Figure 2.9. Quasi-steady-state temperature profile from the experiment with duct sensors, FBR model, and combined FBR and sensor model as well as the inlet temperatures (NTU=2.4, face velocity=2.0 m/s, sensor time constant=1.5 s).

Figure 2.10 presents the same temperature profiles as in Fig. 2.9; however, the experimental measurements are shown for the exchanger sensors. Again, the temperature profile from the experiment and the numerical model of the FBR model are in good agreement except at the beginning of the hot and cold periods due to the transient response of temperature sensors. For the hot period, the exchanger sensors' initial temperature is equal to the cold inlet temperature (Eqn. (2.30)). Similarly, the exchanger sensors are initially at the hot inlet temperature during the cold period (Eqn. (2.31)). With the combined FBR and sensor model, this initial transient behavior of sensors is included in the model, and the comparison between this combined model and experimental temperature profiles exhibits a good agreement, as seen in Fig. 2.10.

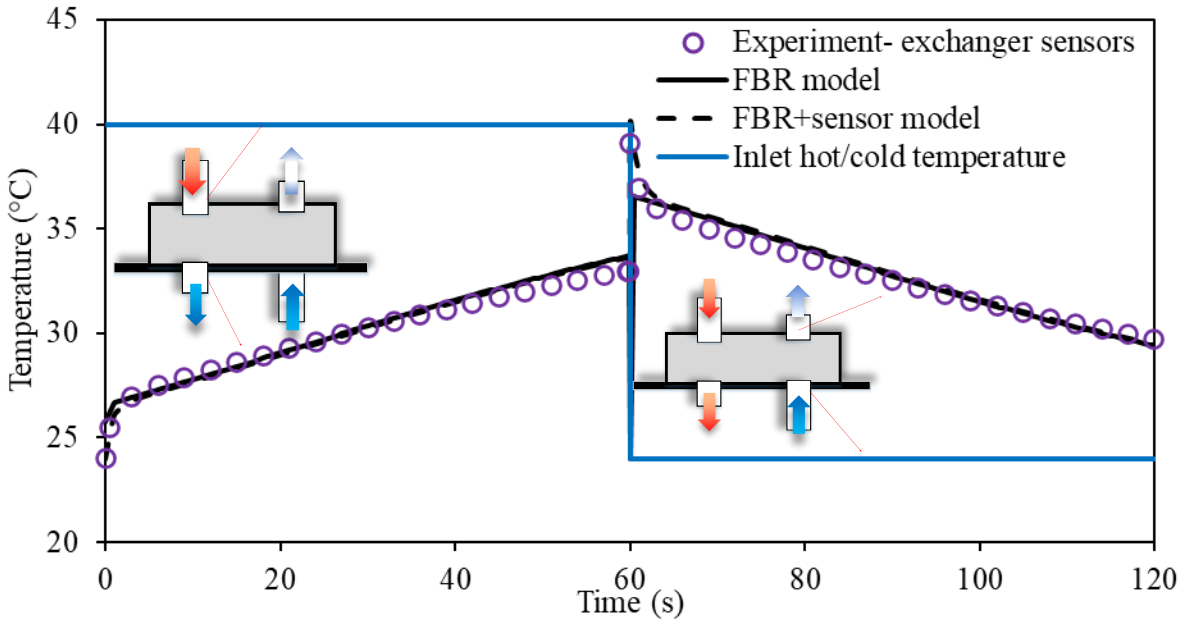

s

Figure 2.10. Quasi-steady-state temperature profile from the experiment with exchanger sensors, FBR model, and combined FBR and sensor model as well as the inlet temperatures (NTU=2.4, face velocity=2.0 m/s, sensor time constant=1.5 s).

Figure 2.11 shows the comparison of the quasi-steady-state temperature profile (from the FBR model), and the experimental results (from both the duct and exchanger sensors). The measurements from the duct and exchanger sensors are different at the beginning of hot/cold periods, but after about six seconds in each period, both duct and exchanger sensor temperature measurements become almost equal, as seen in Fig. 2.11. The sensor measurements after the initial transient region are also in good agreement with the FBR model. The good agreement between the FBR model and experimental measurements after this initial transient is further evidence of the significance of the sensor transient response to the temperature change in FBRs.

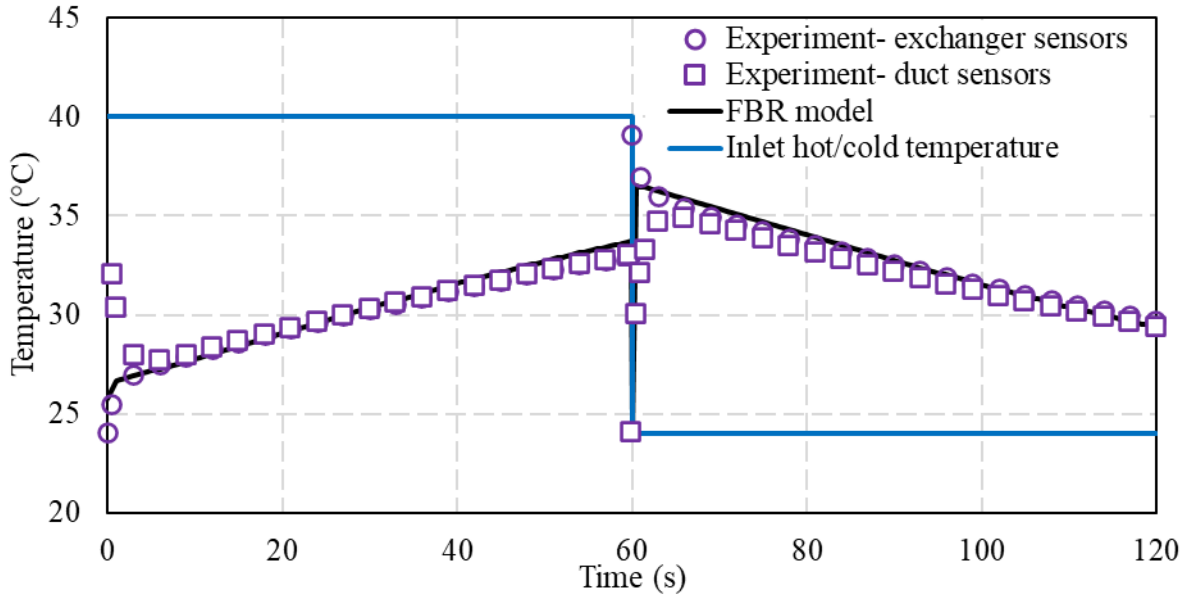

Figure 2.11. Quasi-steady-state temperature profile from the experiment with duct and exchanger sensors, FBR model, as well as the inlet temperatures (NTU_o=2.4, face velocity=2.0 m/s, sensor time constant=1.5 s).

Except at the beginning of each period, the air temperature varies linearly through the rest of the periods. Krishnan et al. [20,44] utilized this linear behavior to modify the temperature profile at the beginning of periods. The modification involves using a linear "backfit" method to modify the temperature profile to consider the initial trainset region resulting from temperature sensors' transient response.

2.5 SENSIBLE EFFECTIVENESS

The experimental results obtained in this study are modified according to the linear backfit method presented by Krishnan et al. [20], and the adjusted experimental effectiveness values are compared with the current FBR model results, and graphical representation is provided in Fig. 2.12. The numerical results agree with the modified experimental data within the range of experimental uncertainty.

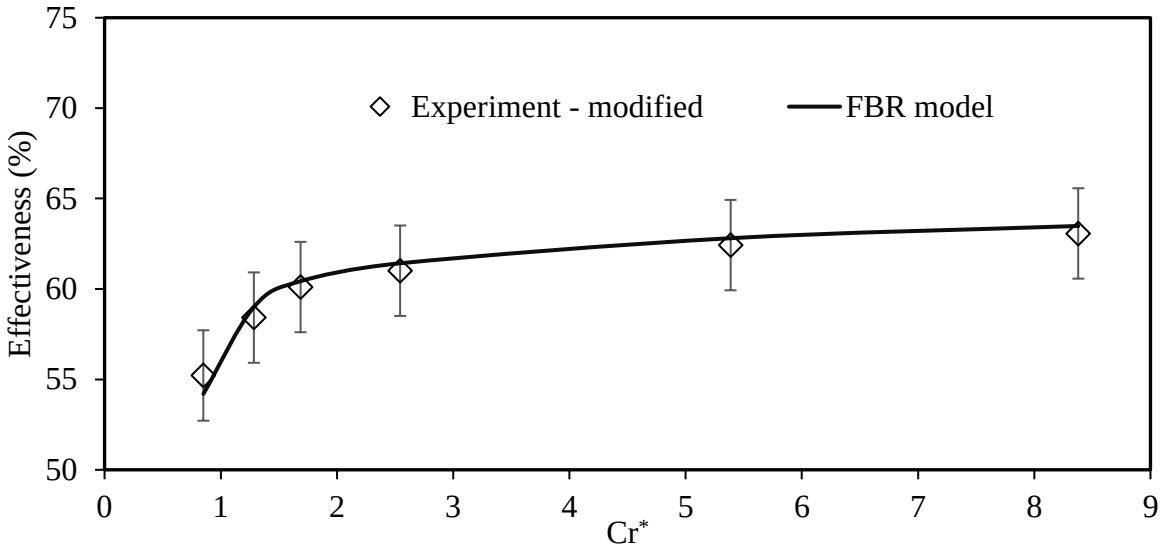

Figure 2.12. FBR effectiveness from the experiment and the FBR model (NTU_o=2.4, face velocity=2.0 m/s, sensor time constant=1.5 s).

2.5.1 **Effect of non-instantaneous movement of exchanger between ducts on the predicted effectiveness**

The FBR model development assumes that the exchanger movement between the two airflow ducts happens instantaneously. It takes time (around 0.3 s) for the exchanger to move between the airflows in an actual situation. To estimate the error due to this non-instantaneous movement of the exchanger between airflow ducts, the inlet velocity is assumed to change gradually (exponentially) during the exchanger movement. This velocity profile (corresponding to the non-instantaneous movement of the exchanger (V_{NS})), along with the assumed constant velocity profile (V) (corresponding to the rapid movement of exchanger between airflow ducts in the numerical modeling), are presented in Fig. 2.13.

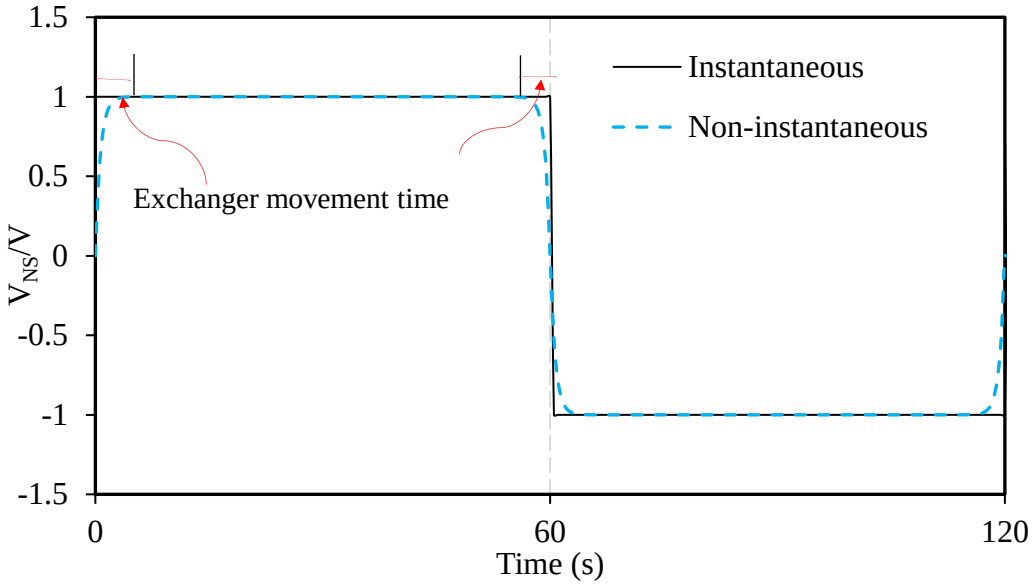

Figure 2.13. Velocity profiles corresponding to the instantaneous and non-instantaneous movement of exchanger between the airflow ducts.

Figure 2.14 shows the changes in effectiveness that occur when the switching between airstreams is not instantaneous for the range of Cr^* between 0.8 and 9 (P_h=P_c=10-90 s). The results (Fig. 2.14) show that including the exchanger movement with a switching time of 1 second in the model increases the effectiveness by less than 0.4%, and with 0.3 seconds switching time, the maximum effectiveness change is less than 0.3%. Thus, the assumption of instantaneous movement of exchanger between the ducts is valid and does not have any significant effects on the predicted results from the FBR model.

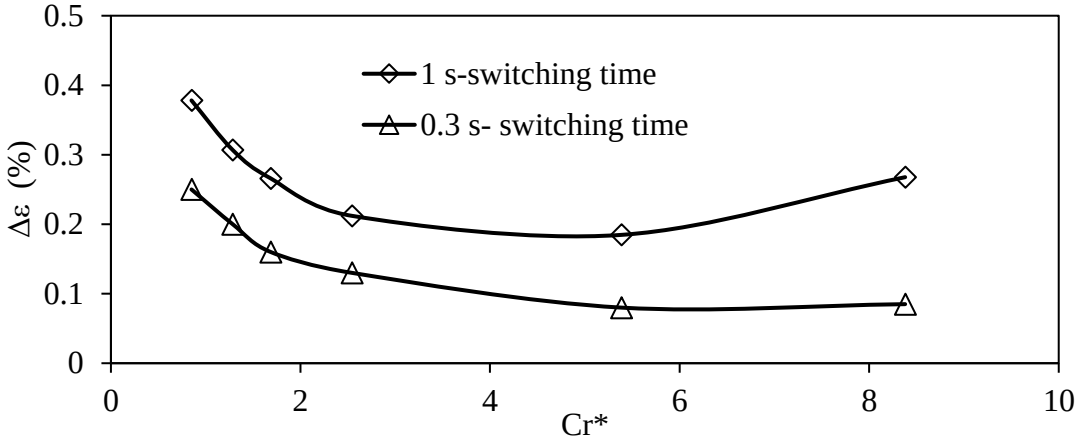

Figure 2.14. Changes in effectiveness when exchanger movement time is included in the model ($\Delta\varepsilon=\varepsilon_{movement}-\varepsilon_{instantaneous\ movement}$).

2.6 APPLICATIONS OF THE COMBINED FBR AND SENSOR MODEL

The developed model (combined FBR and sensor) is applied to evaluate the temperature profile and effectiveness of FBRs under the operating conditions suitable for HVAC applications. The performance under the operating conditions of balanced/unbalanced flow rate and equal/unequal hot and cold period are compared. The FBR model's temperature is the actual air temperature; thus, the difference between the FBR model's effectiveness and the combined FBR and sensor models is called "effectiveness error", and mathematically represented by Eqn. (2.32).

$$\Delta\epsilon = \epsilon_{(FBR\ model)} - \epsilon_{(combined\ FBR\ and\ sensor\ model)} \quad (2.32)$$

Effectiveness error is the error due to the transient response of sensors. These errors are obtained for both the duct and exchanger sensors over the range of cycle time of 20-240 seconds and at the operating conditions presented in Table 2.2.

2.6.1 Quasi-steady-state temperature and effectiveness of a balanced FBR

Figure 2.15 represents the temperature profiles from the FBR model and the combined FBR and sensor models (with duct sensors) at two different cycle times (15 and 120 seconds) under a balanced flow rate condition for an FBR. The effect of the sensor response to the transient

temperature of FBR for the shorter cycle duration is noticeably significant than the extended cycle time. As shown in Fig. 2.15 with dotted circles, the sensor temperature measurements at deviated from the actual temperature profile for almost 70% of the hot/cold period for the FBR with cycle time of 15 seconds, while this deviation is only 10% for the FBR operating with 120 s cycle time.

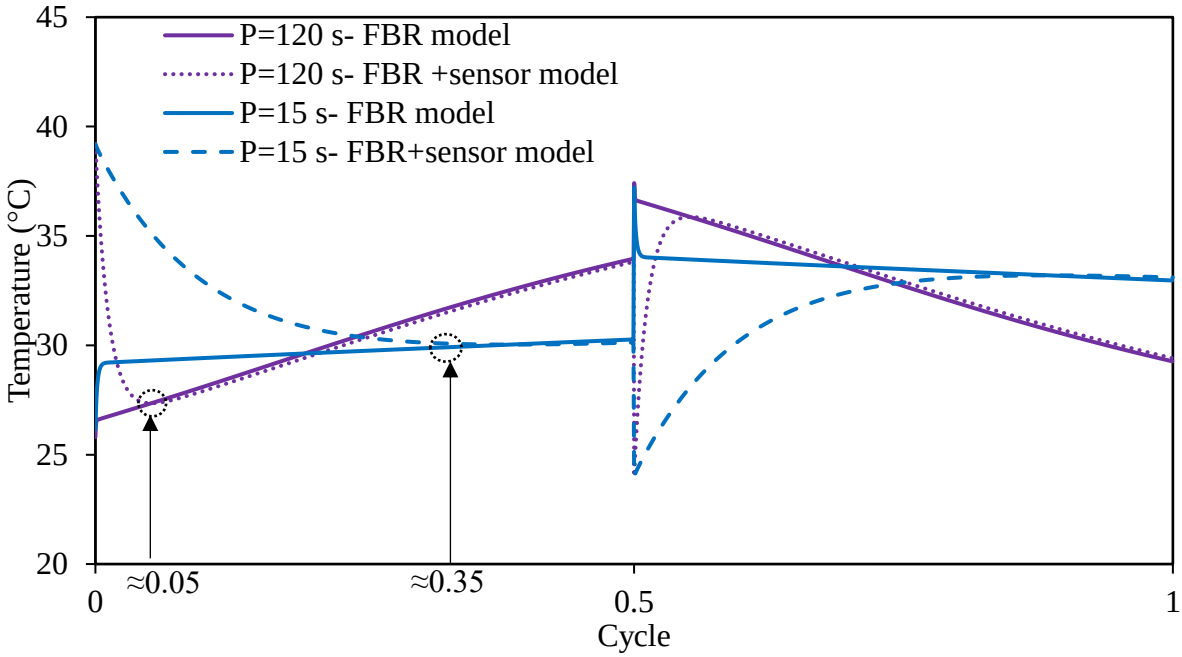

Figure 2.15. Comparison of temperature profiles from the FBR and combined FBR and sensor model (time constant=1.5 s) at P=120 and15 s (NTU=2.4, face velocity=2.0 m/s, time constant=1.5. s).

Figure 2.16 presents the effectiveness error due to sensors' response with a time constant of 1.5 s for both duct and exchanger sensors at different cycle times using Eqn. (2.32). The effectiveness error decreases for both sensors' locations (duct and exchanger) when cycle time increases. While sensors located at the duct underestimate the effectiveness, exchanger sensors overestimate the measured effectiveness values. Although the effectiveness error is small (less than 1%) at 240 seconds, these errors are significant for 15 seconds cycle. The effectiveness errors (Fig. 2.16) are approximately 12% and 8% for the duct and exchanger sensors at cycle time 15 s, respectively.

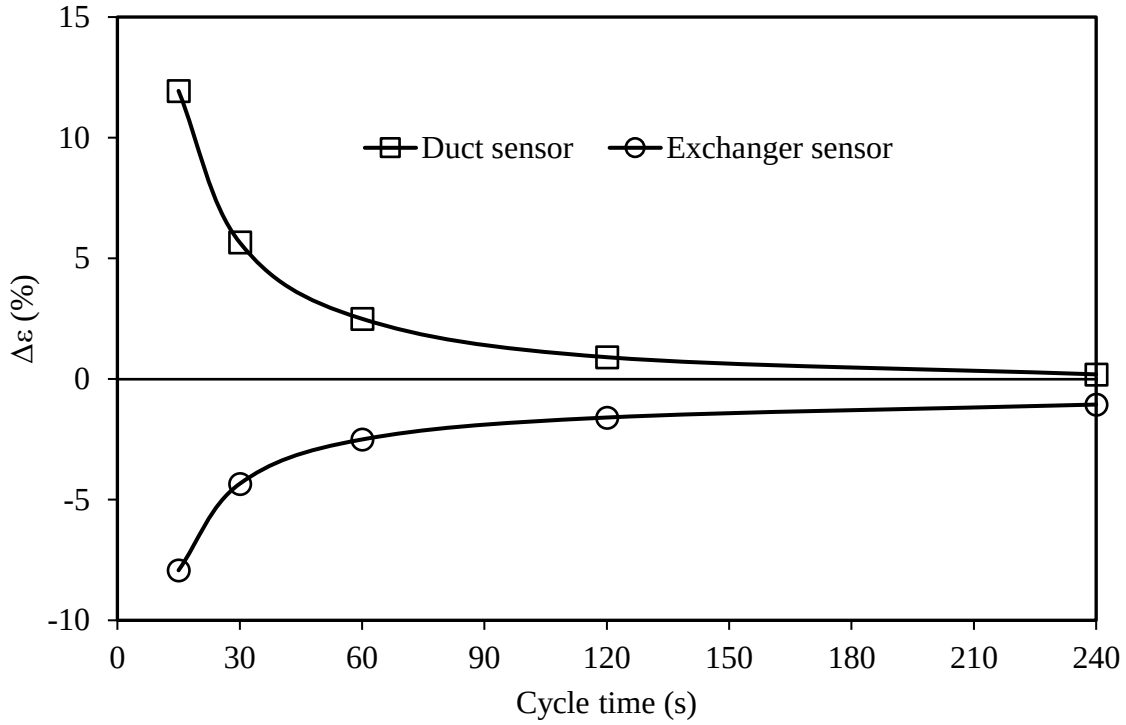

Figure 2.16. Effectiveness error (Δε) for the duct and exchanger sensors for a balanced flow rate (NTU=2.4, face velocity=2.0 m/s) at different cycle times (time constant=1.5 s).

2.6.2 **Unbalanced flow rate**

Figure 2.17 represents the temperature profile for an unbalanced flow ($C^* = C_{cold}/C_{hot} = 0.9$), and the temperature profile from the combined FBR and sensor model for the duct sensor with a time constant of 1.5 s. The balanced flow rate profile is also included for ease of comparison. The average temperatures of the unbalanced exchanger are higher in the hot and cold periods compared to those of the balanced FBR.

Figure 2.18 shows the comparison of the effectiveness error for balanced and unbalanced FBRs at different cycle durations. Compared to the balanced FBR, the effect of sensor response is slightly larger in the unbalanced FBR. In the unbalanced flow condition, the exchanger sensor is more sensitive when compared to the duct sensors.

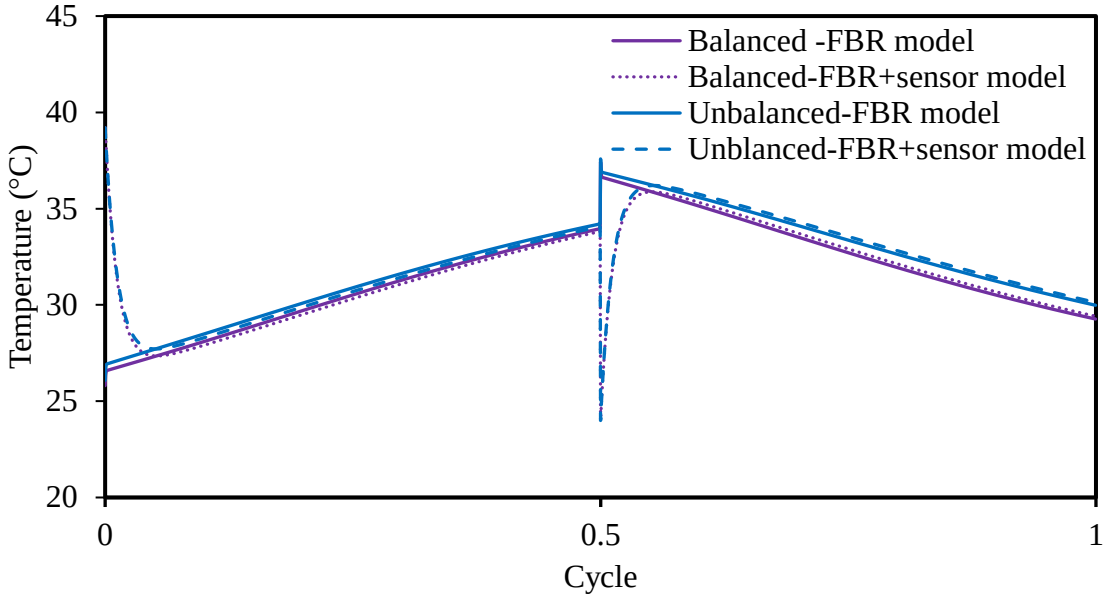

Figure 2.17. Comparison of temperature profiles from the FBR and combined FBR and sensor model for balanced and unbalanced flow exchanger at 120 s cycle duration (face velocity=2.0 m/s, time constant=1.5 s).

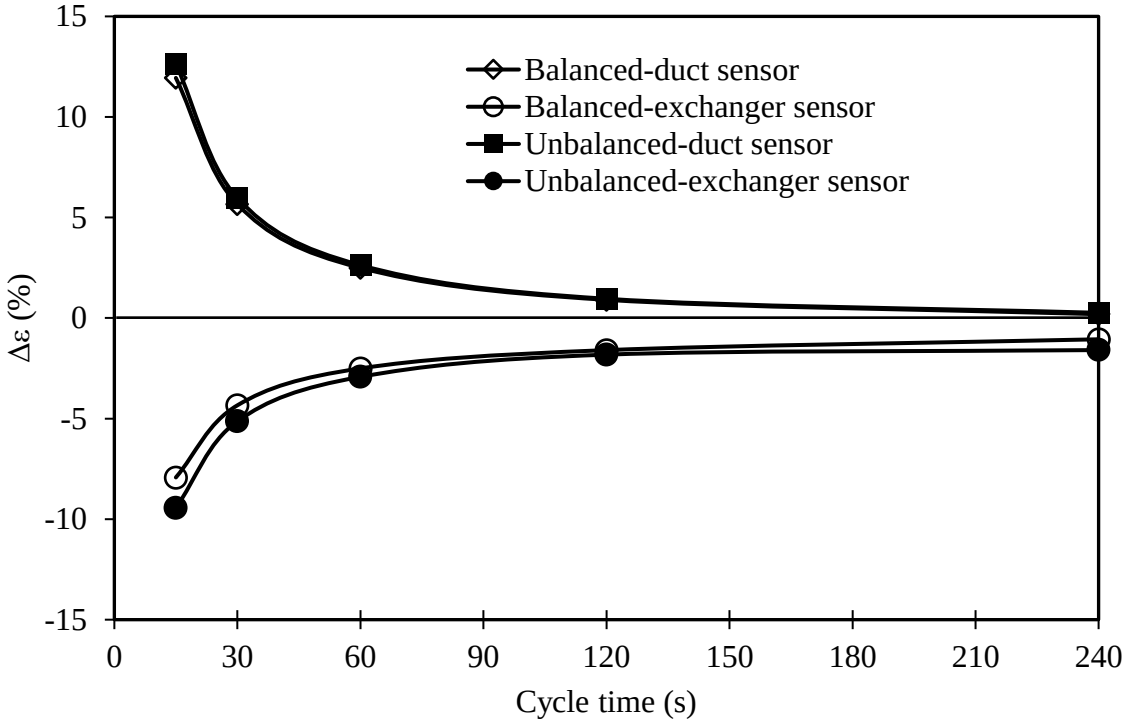

Figure 2.18. Effectiveness error (Δε) of balanced and unbalanced FBR from the duct and exchanger sensors at different cycle times (face velocity=2.0 m/s, time constant=1.5 s).

2.6.3 **Hot and cold periods (with balanced flow rate)**

The duration of hot and cold periods (P_h and P_c) could be unequal in the HVAC applications [16]. The temperature profile from the FBR model and the combined FBR and sensor model (for a duct sensor with a time constant of 1.5 seconds) are presented in Fig. 2.19, for equal ($P_h = P_c = 0.5\,P$) and unequal ($P_h = 0.25\,P\,, P_c = 0.75\,P$) hot/cold periods. The flow rate is maintained balanced in this section. The cycle time is 120 seconds, and all other parameters are kept constant. The average period temperature for the unequal periods is lower than that of the equal periods.

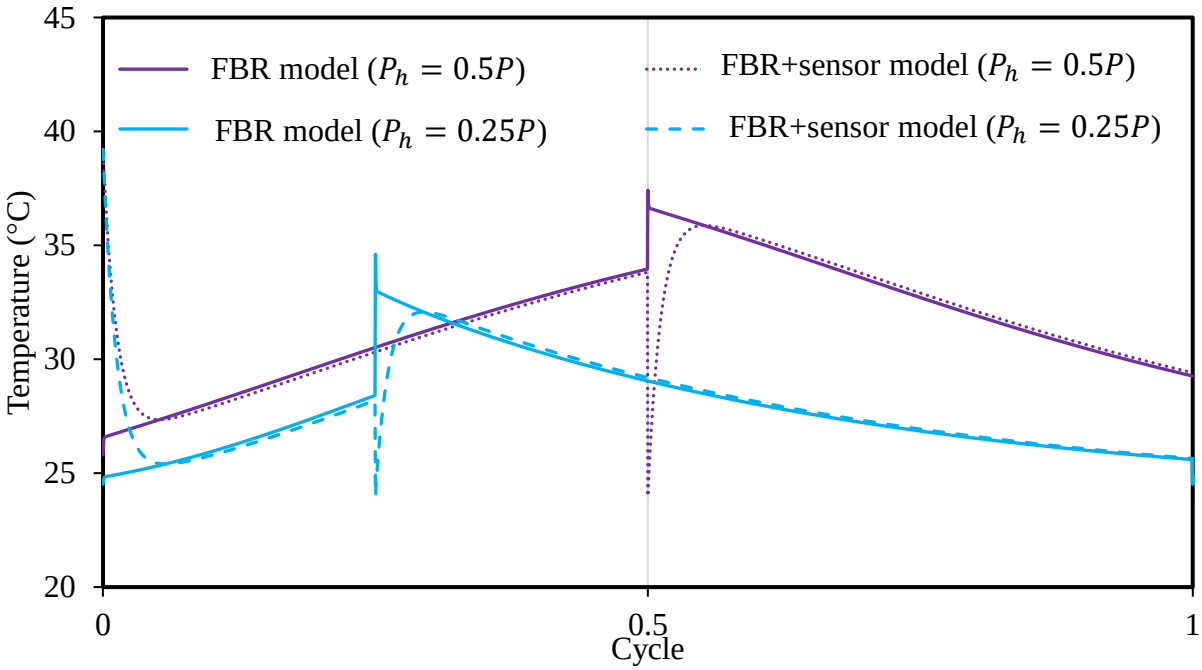

Figure 2.19. Air temperature profile from the FBR model and the combined FBR and sensor model for the equal and unequal hot and cold period duration at 120s cycle duration (NTU=2.4, face velocity=2.0 m/s, and time constant =1.5 s).

Figure 2.20 shows the comparison of the effectiveness errors for equal and unequal periods at different cycle durations. Compared to the equal period, the magnitude of effectiveness error (due to the transient response of sensors to temperature change) increases for the exchanger sensor, while it decreases for the duct sensor during an unequal period. At the operating conditions considered in this study, the exchanger sensors overestimate the effectiveness for the equal and

unequal period by a maximum of about 8% and 16% (at a cycle time of 15 seconds), respectively. On the other hand, the duct sensor's corresponding maximum effectiveness errors are 12% and 10.5% for equal and unequal periods, respectively.

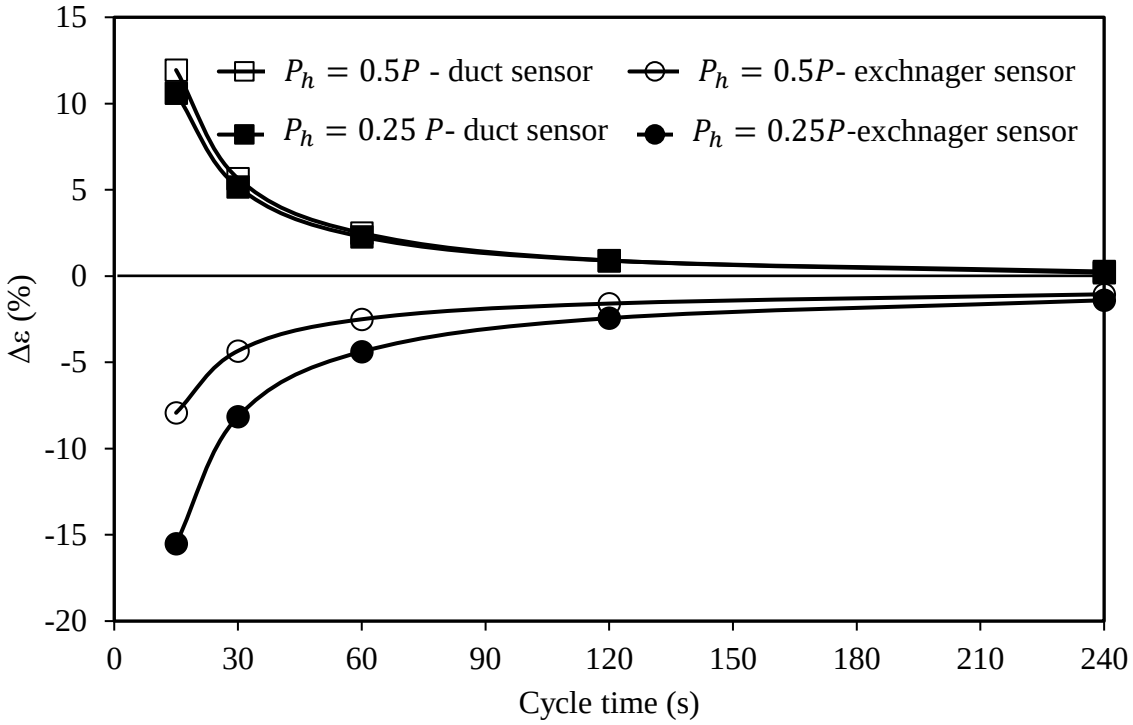

Figure 2.20. Comparison of effectiveness error (Δε) of equal and unequal hot and cold period for the duct and exchanger sensors at the different cycle times ((NTU=2.4, face velocity=2.0 m/s, and time constant=1.5 s).

2.7 SUMMARY AND CONCLUSIONS

This chapter addressed the first objective of this PhD thesis, which is to develop and validate a transient numerical model for sensible FBRs. A 1-D numerical model to evaluate the performance of FBRs and to capture the transient response characteristics of FBRs and sensors at different operating conditions in HVAC application was presented and validated. The model consists of an exchanger (FBR) model and a sensor model. The exchanger (FBR) model was validated against available correlations and data in literature over a wide range of design parameters (NTU_o and Cr^* and longitudinal conduction parameter (λ)). In addition, since experimental measurements include sensor transient response, the experimental data from a small-scale test facility were used to validate the combined FBR and sensor model for both the initial transient and the quasi-steady-state operation of FBRs. The numerical model can predict the effectiveness error due to the slow response of the sensor. It was found that the location of temperature sensors (i.e., stationary (duct sensors) or attached to the moving exchanger (exchanger sensors)) influences the temperature profile and can cause error in the predicted effectiveness.

The temperature profile and effectiveness errors were obtained for several operating conditions of FBRs for HVAC applications as an application of the presented model. The operating conditions include a balanced/unbalanced flowrate and equal/unequal hot and cold periods. For the balanced flow conditions, the maximum effectiveness error is around 10% for sensors with a time constant of 1.5 s and a cycle time of 15 s. The effectiveness error increases (maximum 15%) for unbalanced flow compared to balanced flow FBRs. For the unequal hot and cold periods (balanced flow rate), the effectiveness errors from the duct sensor are close to the equal periods (maximum of 11%). In contrast, the exchanger sensors (with a time constant 1.5 s) overestimate

the effectiveness by a maximum of 16% for unbalance period compared to 8% (at a cycle time of 15 s) for an equal hot/cold period.

In the next chapter, the model (developed in this chapter) will be used to quantify effectiveness errors over a wide range of design conditions and for different FBR configurations. Furthermore, temperature measurement requirements in testing standards will be studied and recommendation will be provided for accurate performance evaluation.

CHAPTER 3

TRANSIENT SENSOR ERRORS AND THEIR IMPACT ON TESTING STANDARDS FOR SENSIBLE FIXED-BED REGENERATOR (FBR)

3.1 OVERVIEW

This chapter uses the validated transient numerical model for sensible FBRs in the previous chapter to quantify the effectiveness errors that result due to the transient response characteristics of sensors over a wide range of design parameters and for different FBR configurations. In this chapter the second objective of the current PhD thesis, "To quantify sensor errors over a wide range of design and operating conditions of sensible FBRs and make recommendations for testing standards", is addressed and documented. Practical recommendations for the selection of sensors for the measurement of the temperature of the outlet airstreams are provided for different configurations of FBRs (single-core and double-core FBRs) in HVAC applications. Furthermore, the current chapter examines the temperature measurement requirements in the current North American testing standards (ASHRAE 84 and CSA C439-18 standards) for AAEEs.

This chapter was published as a research paper in *Science and Technology for the Built Environment* in November 2020 (Click here). To avoid repetition, the governing equations section of the paper was removed, and proper reference is provided to the previous chapter. The author of this thesis (Hadi Ramin) developed the numerical model, performed the simulations, and prepared the original draft of the paper. Mr. Krishnan (PhD student) conducted the experiments for validation and wrote the experimental section; Dr. Annadurai (Postdoctoral fellow), Dr. Alabi (Postdoctoral fellow) and Prof. Simonson (supervisor) contributed to this paper by critically reviewing the paper.

Transient sensor errors and their impact on fixed-bed regenerator (FBR) testing standards[***]

(Published in Science and Technology for the Built Environment, November 2020)

Hadi Ramin, Easwaran N Krishnan, A. Gurubalan, Wahab O. Alabi and Carey J Simonson

3.2 ABSTRACT

Fixed-bed regenerators (FBRs) are a favourable option for energy recovery in building HVAC systems due to their high sensible effectiveness. Unlike other types of energy recovery exchangers, the air temperature at the outlet of FBRs varies with time, which creates challenges when measuring the outlet temperature and effectiveness of FBRs since the actual outlet air temperature will include the transient response of the FBR and the temperature sensor. In this chapter, a validated numerical model of FBRs that takes into account the sensor response is used to quantify the temperature and effectiveness errors that result due to sensors response characteristics over a wide range of design parameters. The main contribution of this chapter is the practical recommendations for the temperature measurement for different configurations of FBRs developed for HVAC applications. The recommendations presented in this chapter could be implemented in future versions of the current standards (ASHRAE 84 and CSA C439-18 standards) for performance testing of air-to-air energy exchangers. The recommendations depend on the shape of the air temperature profile at the outlet of FBRs which is either sawtooth or semi-sawtooth profiles. It was found that effectiveness can be obtained accurately for FBRs with sawtooth profile regardless of the sensor time constant, while to obtain effectiveness with 5%

accuracy for FBR with semi-sawtooth profile, the sensor dimensionless time constant (sensor time constant over recovery period) should not exceed 0.07.

3.3 INTRODUCTION

The building sector is responsible for about 40% of the total global energy consumption and more than 30% of global CO_2 emissions [45]. Heating, ventilating, and air conditioning (HVAC) systems consume a substantial part of the energy used in buildings. For instance, space cooling (70%) dominates the building energy consumption in the Middle East region [46,47], and space heating is the major contributor (60%) of Canada's building energy consumption [48].

The energy required for ventilation air is critical due to increasing air-tightness and improving building envelopes [49]. Considering the energy consumption of HVAC systems and the importance of ventilation on the health and productivity of buildings' occupants [6], recovering energy from the exhaust air becomes essential for energy efficiency in buildings. Thus, various types of air-to-air energy recovery exchangers have been incorporated into the HVAC systems to help with this recovery [24].

Fixed-bed regenerators (FBRs) have recently been the subject of several studies for energy recovery in HVAC applications [11,20,32,50] because of their advantages of high ratio of heat transfer area to volume and high heat transfer effectiveness. In literature, FBRs are referred to as single-core regenerators, double-core regenerators [22], room-based ventilators [16,51], reversing-flow regenerators [22], and exchanger with a periodic change in the flow direction [12,52,53].

FBR is an energy exchanger with one or two stationary matrixes that store/reject heat as hot/cold air flows through the matrixes alternately, as shown in Fig. 3.1. This alternate heating and cooling processes in FBRs cause the outlet air temperature of FBRs to vary linearly with time [20,33]. Figure 3.1 presents the FBR's inlet and outlet air temperatures during the hot (P_h) and cold (P_c) periods. After many cycles, the outlet temperature of an FBR reaches a quasi-steady-state condition where the outlet temperature profile will be the same for every cycle [11]. The variation

of the outlet air temperature (even at the quasi-steady-state condition) poses challenges for measuring the air temperature and, consequently, the effectiveness. This is due to the transient characteristics of the sensor, which causes the measured temperature to lag the actual temperature [20,21,50].

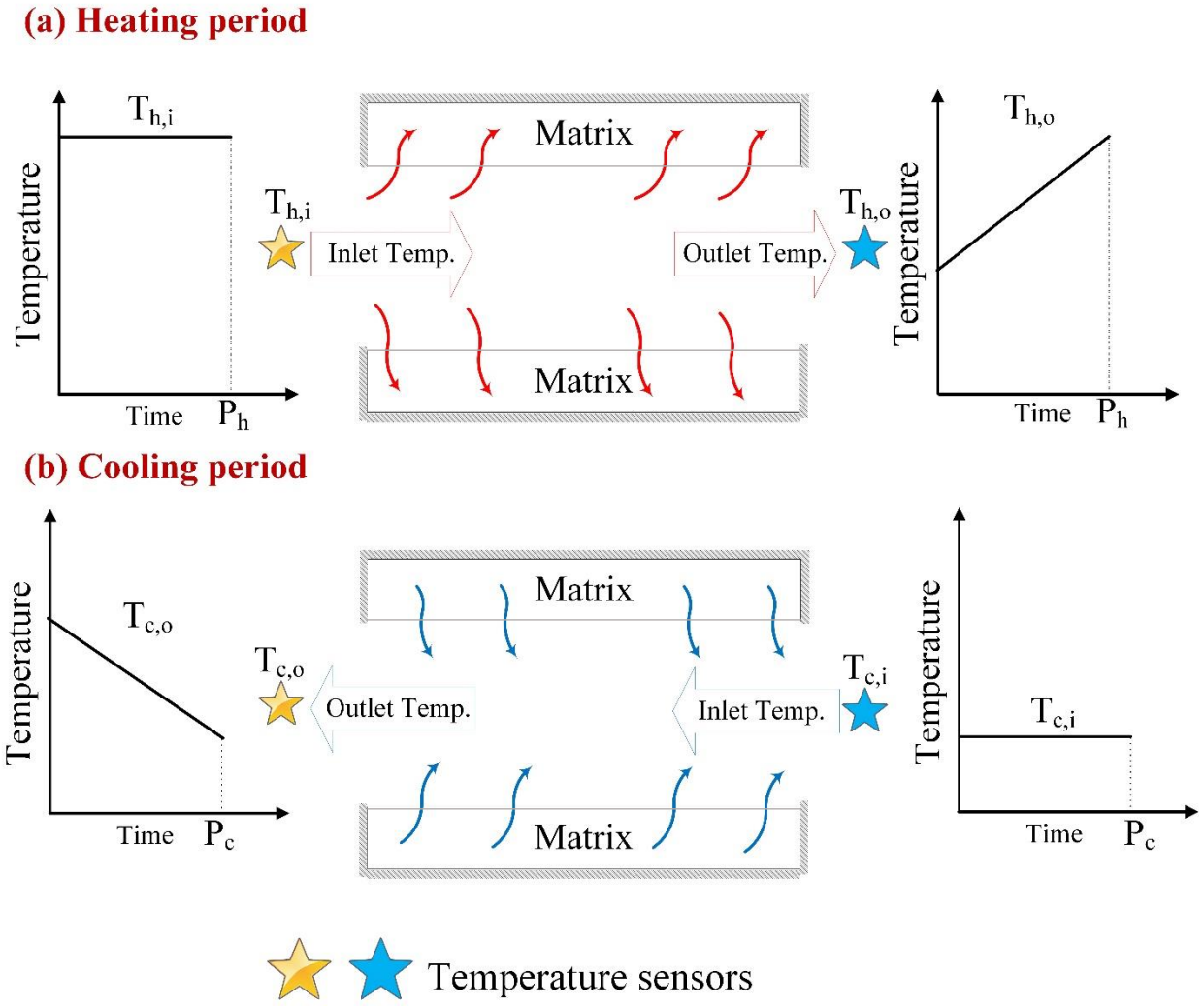

Figure 3.1. A schemotic of inlet and outlet temperatures during alternate hot and cold periods of FBRs.

In addition to the temperature variation during a period, the exposure of the temperature sensors to different temperature conditions in the previous period affects their temperature measurement in the subsequent period. For example, Fig. 3.1 shows that the sensor measures the

outlet temperature during the cold period ($T_{c,o}$) was previously exposed to the hot inlet air ($T_{h,i}$) during the previous hot period. Therefore, both the initial condition of the sensor and the slope of the temperature profiles are critical in obtaining the effect of sensor transient characteristics in the temperature measurement [33,54–56]. With a small-scale test facility, Krishnan et al. [20] and Ramin et al. [50] studied the effects of the location of temperature sensors on the performance evaluation of FBRs for HVAC applications. For a thermocouple with a time constant of 1.5 seconds and a short recovery period (7.5 seconds), their results showed that a maximum of 15% error in effectiveness estimation occurs, which is due to the transient response of temperature sensors. However, further studies are required to provide more values to inform experiments and test standards. Ramin et al. [33] presented an analytical solution for the response of a sensor exposed to a semi-sawtooth profile. Though, this solution is complicated and requires the knowledge of slope and intercept of the outlet air temperature of FBR (from numerical solution); also, this solution needs to be expanded to cover different configurations of FBRs.

ASHRAE standard 84 [21] and CSA C439-18 standard [22] have been recently updated to include FBR performance testing. Both standards require a sampling rate that leads to collecting at least 30 temperature samples per recovery period (the recovery period is assumed to be 60 seconds). The temperature must be measured using instruments that have a response time shorter than the sampling rate. However, the temperature sensors' requirements mentioned in these standards have not been studied and validated. It is also recommended in the ASHRAE standard 84 and CSA C439-18 standard to continue the testing of FBRs for one hour before reaching the quasi-steady state condition. This recommendation has been previously studied and verified for a wide range of operation conditions [32]. Thus, the focus of this chapter is on the impacts of

temperature sensor transients' characteristics on the quasi-steady-state temperature profile and effectiveness.

Hence, the main objective of this chapter is to quantify the effect of sensor's transient characteristics on temperature measurements over a wide range of sensors time constants and FBR's design parameters (overall number of transfer units (Too), matrix heat capacity rate ratio (Cr^*), and longitudinal conduction parameter (λ)) suitable for practical applications in HVAC systems. This chapter will also examine the temperature sensor requirements in ASHRAE standard 84 [21] and CSA C439-18 standard [22].

3.4 FBR CONFIGURATIONS AND THEIR OUTLET TEMPERATURE PROFILES

FBRs can be broadly classified as single and double-core exchangers, and their outlet temperature profiles depend on the configuration, as summarized in Table 3.1. This table summarizes the different designs of FBRs reported in the literature [16,17], along with test standards [21,22]. The summer and winter temperature profiles at the outlet of exchangers are also presented on the supply and exhaust sides in Table 1. The temperature profiles are provided for two consecutive periods of exposure of the sensor to illustrate the initial temperature condition before each hot/cold period. For the single-core exchanger or room-based heat recovery exchanger (ventilator) [13], as shown in the first row of Table 3.1, the sensors at the outlet of the supply and exhaust side of the exchanger are exposed to a periodic positive/negative (depending on the season) semi-sawtooth temperature profile.

Table 3.1. Different configurations of FBRs and their corresponding winter (W) and summer (S) outlet temperature profiles at the supply side (SA) and exhaust side (EA).

#	Ref.	FBR configuration	Outlet temperature profile on the SA and EA sides	
1	Nizovtsev et al.[16]	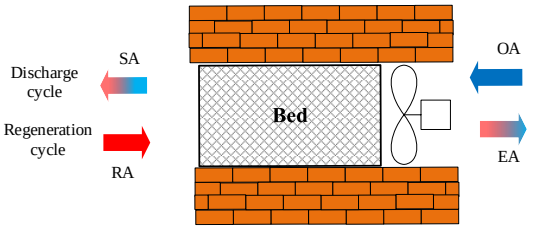	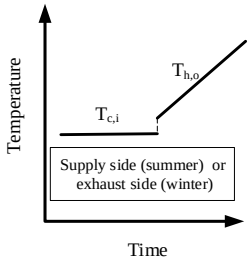	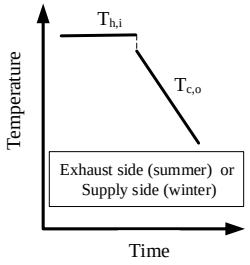
2	CSA C439-18 standard [22]	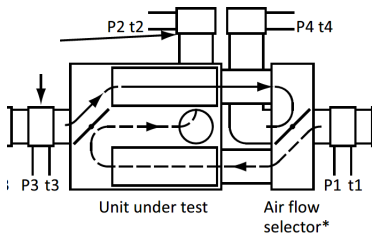	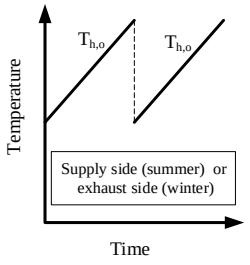	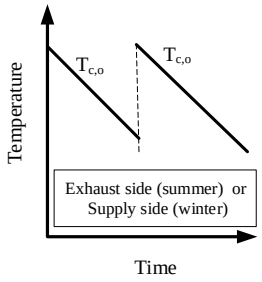
3	ASHRAE standard 84 [21]	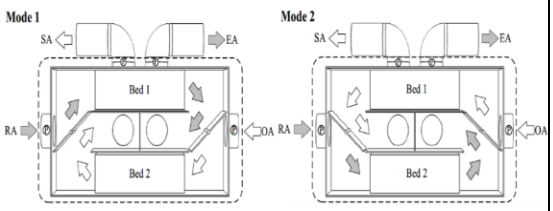	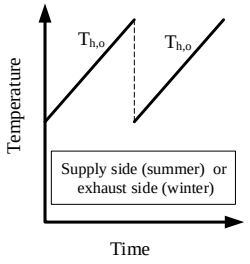	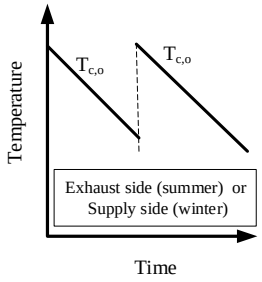
4	Tempeff [17]	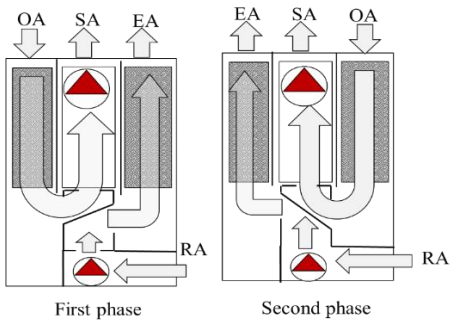	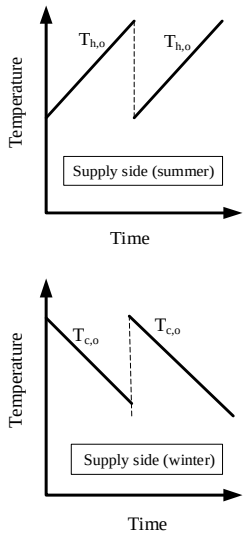	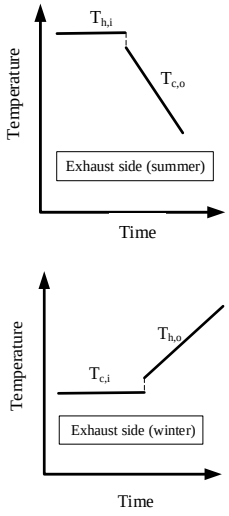

For the double-core exchangers, as presented in the CSA C439-18 standard [22] and ASHRAE standard 84 [21], sensors at the outlet of supply or exhaust airstreams are exposed to periodic positive/negative sawtooth temperature profiles, depending on the season. On the other hand, the double-core exchanger developed by Tipoff [17] experiences a periodic sawtooth and semi-sawtooth temperature profiles on the supply and exhaust side of the exchanger, respectively. Compare to the sawtooth profile, the semi-sawtooth profile has a flat part before a positive/negative ramp.

Based on the shape of the temperature profile at the outlet of the exchanger, FBRs can be classified into three main types as follows.

1. Single-core FBRs with a semi-sawtooth profile shape (configuration 1 in Table 3.1): The temperature sensors are exposed to positive/negative (depending on the season) semi-sawtooth temperature.

2. Double-core FBRs with a sawtooth profile (configurations 2 and 3 in Table 3.1): The temperature sensors are periodically exposed to a positive/negative (depending on the season) sawtooth temperature profile.

3. Double-core FBRs with combined sawtooth and semi-sawtooth temperature profiles (configuration 4 in Table 3.1): This is a combination of type 1 and 2 FBRs with respect to the temperature profile.

Thus, it can be concluded that the temperature sensors are exposed to either a positive/negative sawtooth or semi-sawtooth profile depending on the configuration of FBRs and season.

3.5 NUMERICAL MODEL AND EXPERIMENTAL TEST FACILITY

Although there are correlations in the literature to calculate the effectiveness of thermal regenerators [19,25,43], there is no straightforward method to obtain the instantaneous temperature profile within the recovery and regeneration periods of FBRs at different design conditions. This instantaneous temperature profile during each period is essential to quantify the error due to the transient response of temperature sensors. In this chapter, a validated numerical model by Ramin et al. [50] is used to obtain that temperature profile and determine the sensor impact on temperature measurement. The airstreams will be referred to as hot and cold airstreams hereafter for ease of understanding and to avoid over mentioning the season.

3.5.1 Performance parameter

The performance of an FBR is quantified using effectiveness, which is defined as the ratio of the actual to the maximum possible heat transfer rate [21,22], and mathematically represented by Eqns. (3.1) and (3.2) for the hot side and cold period, respectively:

$$\varepsilon_{\mathrm{h}} = \frac{\dot{\mathrm{m}}_{\mathrm{h}} C_p \left(\overline{\mathrm{T}}_{\mathrm{h,o}} - \mathrm{T}_{\mathrm{h,i}}\right)}{\min(\mathrm{C}_{\mathrm{h}}, C_c)\left(\mathrm{T}_{\mathrm{h,i}} - \mathrm{T}_{\mathrm{c,i}}\right)} \tag{3.1}$$

$$\varepsilon_{\mathrm{c}} = \frac{\dot{\mathrm{m}}_{\mathrm{c}} C_p \left(\overline{\mathrm{T}}_{\mathrm{c,o}} - \mathrm{T}_{\mathrm{c,i}}\right)}{\min(\mathrm{C}_{\mathrm{h}}, C_c)\left(\mathrm{T}_{\mathrm{h,i}} - \mathrm{T}_{\mathrm{c,i}}\right)} \tag{3.2}$$

where $\dot{\mathrm{m}}_{\mathrm{h}}$ and $\dot{\mathrm{m}}_{\mathrm{c}}$ are the mass flow rate of the hot and cold airstreams, respectively. The temperature of the air leaving FBR varies with time, hence $\overline{\mathrm{T}}_{\mathrm{c,o}}$ and $\overline{\mathrm{T}}_{\mathrm{h,o}}$ are the time-averaged cold and hot temperatures, respectively. These temperatures are obtained using Eqns. (3.3) and (3.4).

$$\overline{\mathrm{T}}_{\mathrm{c,o}} = \frac{1}{\mathrm{P}_{\mathrm{c}}} \int_0^{\mathrm{P}_{\mathrm{c}}} \mathrm{T}_{\mathrm{c,o}} \mathrm{dt}, \tag{3.3}$$

$$\overline{\mathrm{T}}_{\mathrm{h,o}} = \frac{1}{\mathrm{P}_{\mathrm{h}}} \int_0^{\mathrm{P}_{\mathrm{h}}} \mathrm{T}_{\mathrm{h,o}} \mathrm{dt} \tag{3.4}$$

3.5.2 **Governing equations**

The governing equations, boundary conditions and numerical solution were presented in section 2.4.1. In this section, dimensionless equations are presented.

The importance of using the dimensionless equations is that the dimensionless temperature will be independent of the selection of the hot and cold flow temperatures. Thus, errors due to the transient response of sensors will be quantified, regardless of the choice of the hot or cold temperatures, hence independent of the climate conditions. Utilizing the dimensionless variables from Table 3.2, the matrix and air energy equations for the hot flow and cold flow periods (Eqns. (2.1) and (2.2)) transform to Eqns. (3.5 and 3.6) and (3.7 & 3.8), respectively [19], subject to boundary conditions (BCs) and inlet conditions highlighted in Eqns. (3.9)-(3.11).

$$\frac{\partial T_m^*}{\partial t^*} = \frac{ntu_h}{C_{r,h}^*}(T_h^* - T_m^*) + \frac{\lambda_h}{C_{r,h}^*}\frac{\partial^2 T_m^*}{\partial {X^*}^2} \tag{3.5}$$

$$\frac{\partial T_h^*}{\partial X^*} = ntu_h(T_w^* - T_h^*) \tag{3.6}$$

$$\frac{\partial T_m^*}{\partial t^*} = \frac{ntu_c}{C_{r,c}^*}(T_m^* - T_c^*) + \frac{\lambda_c}{C_{r,c}^*}\frac{\partial^2 T_m^*}{\partial {X^*}^2} \tag{3.7}$$

$$\frac{\partial T_c^*}{\partial X^*} = ntu_c(T_c^* - T_w^*) \tag{3.8}$$

BCs and inlet conditions are:

$$\left.\frac{\partial T_m^*}{\partial X^*}\right|_{X^*=0} = \left.\frac{\partial T_m^*}{\partial X^*}\right|_{X^*=L} = 0 \tag{3.9}$$

$$T_h^*(X^* = 0, 2m \le t^* \le 2m + 1) = 1 \tag{3.10}$$

$$T_c^*(X^* = 1, 2m + 1 \le t^* \le 2m + 2) = 1 \tag{3.11}$$

From the above equations, the dimensionless temperature will be a function of several dimensionless variables, as presented in Eqn. (3.12):

Table 3.2. Dimensionless variables and parameters for heat transfer in FBRs.

Dimensionless Variables	Length	time	
	$X^* = \frac{x}{L}$	$t^* = \frac{t}{P_h}$	
	Hot side temperature	Cold side temperature	Matrix temperature
	$T_h^* = \frac{T_h - T_{c,i}}{T_{h,i} - T_{c,i}}$	$T_c^* = \frac{T_c - T_{c,i}}{T_{h,i} - T_{c,i}}$	$T_m^* = \frac{T_m - T_{c,i}}{T_{h,i} - T_{c,i}}$
Dimensionless parameters	Hot side	$ntu_h = (hA)_h / C_h$	$\lambda_h = \frac{k_m A_{m,h}}{LC_h}$
		$C_{r,h}^* = \frac{(mC_p)_m P_h}{C_h}$	$C_h = (\dot{m}C_p)_{g,h}$
	Cold side	$ntu_c = (hA)_c / C_c$	$\lambda_c = \frac{k_m A_{m,c}}{LC_c}$
		$C_{r,c}^* = \frac{(mC_p)_m P_c}{C_c}$	$C_c = (\dot{m}C_p)_{g,c}$
Overall Dimensionless parameters	$C_r^* = \frac{C_r}{\min(C_h, C_c)}$	$C^* = \frac{\min(C_h, C_c)}{\max(C_h, C_c)}$	$NTU_o = \frac{1}{\min(C_h, C_c)} \left[\frac{1}{(hA)_h} + \frac{1}{(hA)_c} \right]^{-1}$
	$\lambda = \frac{\lambda_c C_c + \lambda_h C_h}{\min(C_c, C_h)}$	$(hA)^* = \frac{(hA) on\ the \min(C_h, C_c)\ side}{(hA) on\ the \max(C_h, C_c)\ side}$	

$$T_h^* \text{ or } T_c^* = \phi(X^*, t^*, ntu_h, ntu_c, C_{r,h}^*, C_{r,c}^*, \lambda_c, \lambda_h) \quad (3.12)$$

The dimensionless parameters for the hot and cold airflows can be combined into the overall dimensionless parameters presented in Table 3.2 [19]. Twherefore, the dimensionless temperatures (Eqn. (3.12)) become a function of seven independent dimensionless variables, as presented in Eqn. (3.13):

$$T_h^* \text{ or } T_c^* = \beta(X^*, t^*, NTU_o, C^*, C_r^*, (hA)^*, \lambda) \quad (3.13)$$

In most HVAC practical applications, $(hA)^* = 1$; thus, the dimensionless temperatures for the effectiveness calculation (at the outlet of FBRs $X^* = 0\ and\ 1$) becomes a function of four parameters $(NTU_o, C^*, C_r^*\ and, \lambda)$.

From the definition of the dimensionless variables, the effectiveness of FBR in Eqns. (3.3) & (3.4) simplifies to Eqn. (3.14) and (3.15) for $C_{min} = C_c$:

$$\varepsilon_c = \bar{T}^*_{c,o} \tag{3.14}$$

$$\epsilon_h = \frac{1 - \bar{T}^*_{h,o}}{C^*} \tag{3.15}$$

In many practical applications and the test standards (CSA C439-18 standard [22] and ASHRAE standard 84 [21]), the flow in regenerators are considered to be balanced ($C^* = \frac{C_c}{C_h} = 1$), and hence the results are presented for such a balanced flow condition.

Temperature sensors usually have a small mass, which makes the lumped capacitance method applicable [34] for the corresponding transient energy balance. The energy balance for the sensors is presented in Eqn. (3.16);

$$\frac{dT_s}{dt} = \frac{1}{\tau_s}\left(T_g - T_s\right) \tag{3.16}$$

where τ_s is the time constant of the temperature sensor, and T_s is the temperature that the sensor records. Equation (3.16) can be rewritten using the dimensionless variables as Eqn. (3.17);

$$\frac{dT^*_s}{dt^*} = \frac{P_h}{\tau_s}\left(T^*_g - T^*_s\right) = \frac{1}{\tau^*_s}\left(T^*_g - T^*_s\right) \tag{3.17}$$

where τ^*_s is the time constant to recovery period ratio (dimensionless time constant of temperature sensor), and is mathematically depicted by Eqn. (3.18):

$$\tau^*_s = \frac{\tau_s}{P_h} \tag{3.18}$$

Therefore, the temperature obtained from Eqn. (3.13) gives the actual outlet air temperature of the exchanger, and the one obtained from Eqn. (3.17) is what temperature sensors record. Figure 3.2 (a-d) shows different possible outlet air temperature profiles from the numerical model (see Table 3.1) of FBRs along with their corresponding sensor measurements (for $\tau^*_s = 0.2$), obtained from Eqn. (3.17) for Ndu_{om}=1, Cr^*=1, and λ=0.

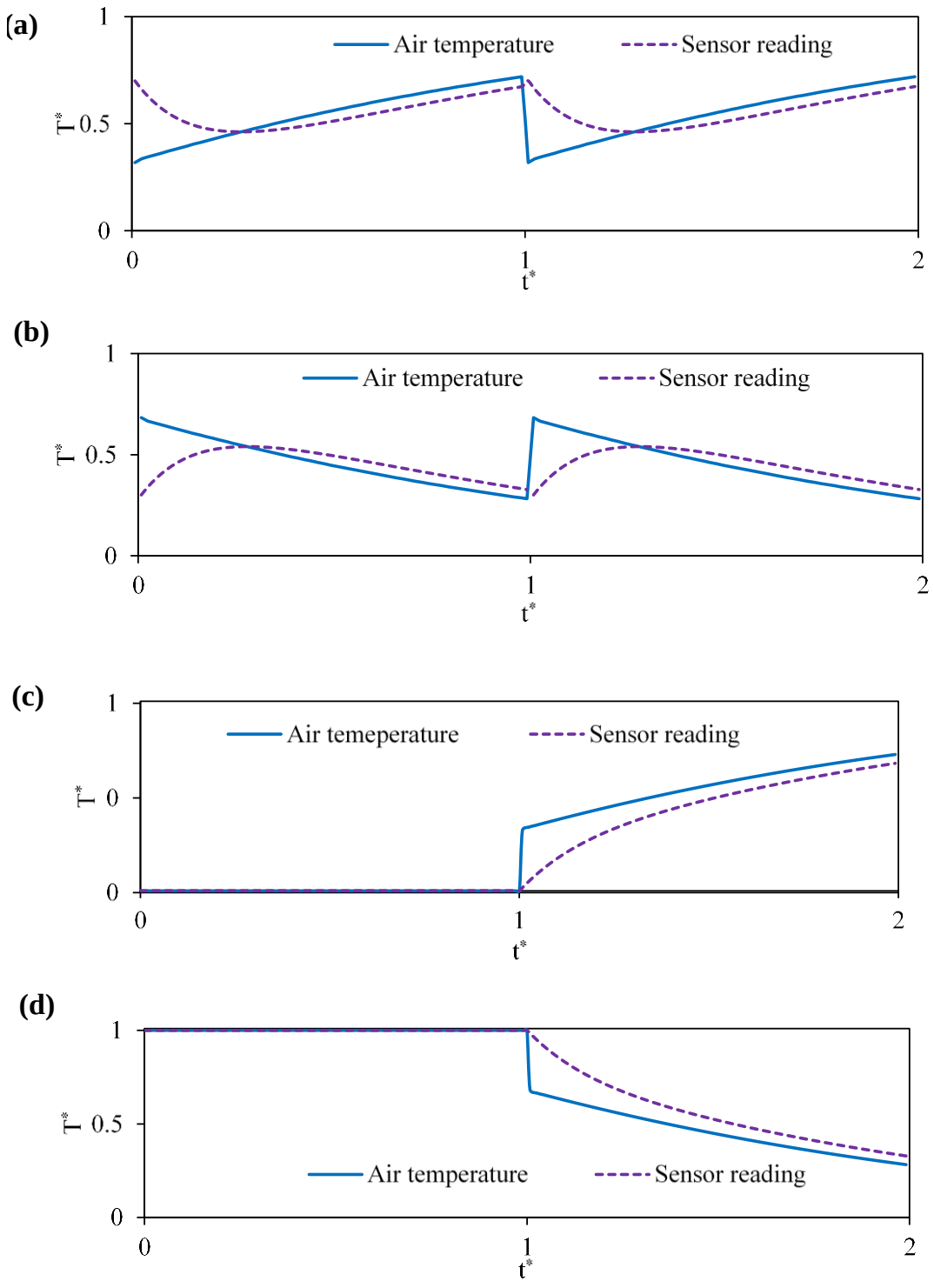

Figure 3.2. Outlet air temperatures of positive/negative sawtooth ((a) & (b)) and the semi-sawtooth ((c) & (d)) profile and their corresponding sensor measurements with τ_s^*=0.2 (Too=1.0, Cr^*=1.0, and λ=0).

The deviation between the average actual air temperature and the sensor recording for both positive/negative sawtooth profiles is equal. This means that effectiveness errors (a function of average outlet temperature) due to the sensor measurements are identical for the positive and negative sawtooth profiles. This conclusion is also applicable to the positive/negative semi-sawtooth profile. Therefore, in terms of error due to temperature measurement, there is no difference between positive and negative temperature profiles (either sawtooth or semi-sawtooth). Hence, in the rest of the chapter, further analyses are carried out only for the positive sawtooth (hot period) (Fig. 3.2 (a)) and the positive semi-sawtooth temperature profiles (hot period) (Fig. 3.2(c)).

3.5.3 **FBR small-scale test facility**

A small-scale test facility was used to validate the numerical model [50]. The schematic diagram of the facility is shown in Fig. 3.3. The principle of operation, instrumentation and data analysis procedures of the experiments are reported in the author's previous [20,44].

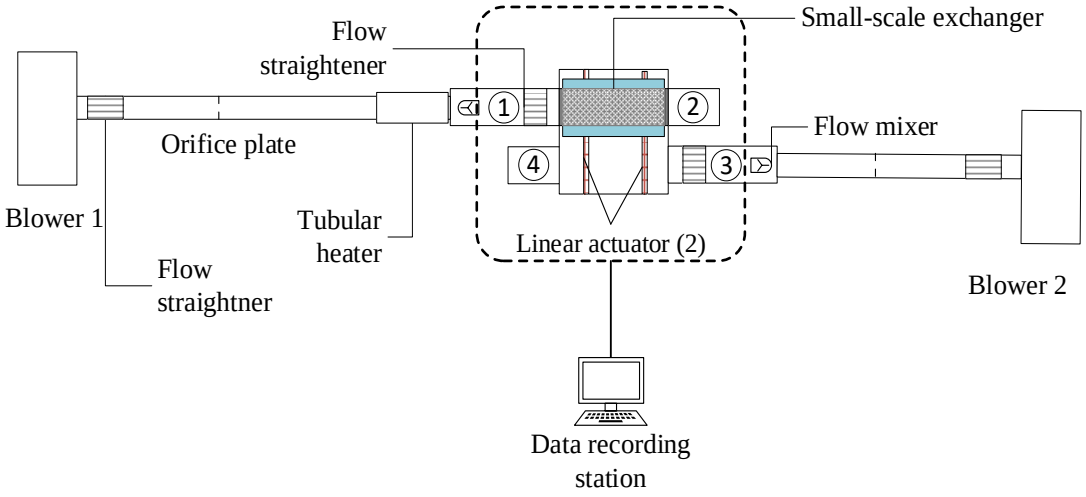

Figure 3.3. A sschematic of the small-scale test facility.

The schematic of the exchanger (made of aluminum plates) and its thermo-physical properties are shown in Fig. 3.4 and Table 3.3, respectively. A linear actuator unit (LAU) is used to slide the exchanger between the hot and cold airstreams to mimic the alternate heating and cooling process of FBRs. The temperature of the hot and cold airstreams is measured using calibrated T-type thermocouples (with a time constant (i_s) of 1.5 seconds) with an uncertainty of ±0.2 °C. The uncertainty in flow rate measurements is ±2%. Uncertainty analysis has been performed by following the rule of error propagation [57], and the uncertainties in sensible effectiveness and normalized temperatures are 3% and 1.5%, respectively. Generalized uncertainty analysis of small-scale testing has been presented, and the contribution of errors from temperature and flow rate measurements on sensible effectiveness is reported in the author's previous publication [20]. Energy balance was performed, and results showed that for a wide range of test conditions, the test facility conserves energy (with a deviation of less than 5%). The experiment is continued until the exchanger attains the quasi-steady-state condition.

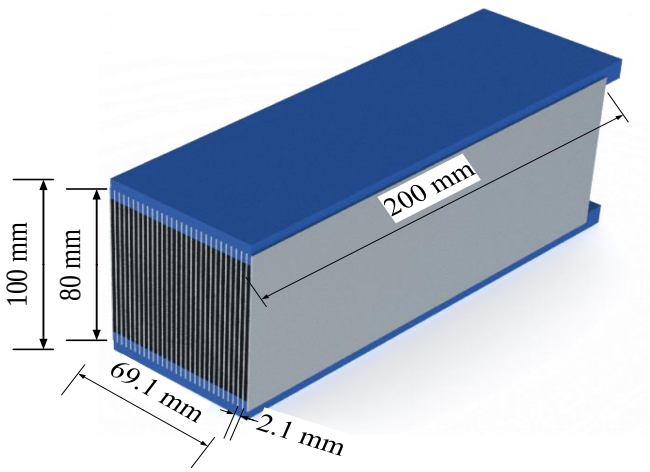

Figure 3.4. A schematic of the small-scale exchanger.

Table 3.3. Geometrical details, thermophysical properties of the exchanger, dimensionless parameters, and sensor time constant

Exchanger channel	Length(mm)	200
	Width (mm)	80
	Height (mm)	2.1
	Hydraulic diameter (mm)	3.5
Aluminum plates	Thickness (mm)	0.62
	Thermal conductivity (W/m·K)	220
	Density (kg/m^3)	2730
	Specific heat capacity (J/kg·K)	904
Dimensionless parameters	Too	2.4
	Cr^*	1.2-8
	C^*	1.0
	λ	0.3
Temperature Sensor	Time constant (s)	1.5

3.5.4 **Validation of the results**

The effectiveness calculated from the literature correlations [19,41] and from the small-scale test facility is used to validate the numerical model and presented in the author's previous paper [50]. In the present study, the temperature profile from the numerical model (including the sensor response) is compared with the temperature profile from the small-scale test facility.

Figure 3.5 (a) shows the comparison of the quasi-steady-state dimensionless temperature profiles at the outlet of FBR from the small-scale experiment and the numerical model (including the sensor response) for both hot and cold periods (60 s). From Fig. 3.5 (a), it can be observed that the temperature from the numerical model (including the sensor response from Eqn. (3.17)) and the experiment are in good agreement. Therefore, the numerical model is accurate in predicting the transient behavior of the outlet temperature of FBR and sensor response. The measured temperature profiles from the experiment (including sensor response) at different recovery periods are modified following the method presented in [20], and the resulted effectiveness values are

compared with the prediction from the numerical model; this effectiveness comparison is presented in Fig. 3.5(b). This figure demonstrates that the numerical model results agree with the experimental effectiveness within the uncertainty bounds. Hence, the developed numerical model can be confidently used to evaluate the performance of FBR for different operating conditions.

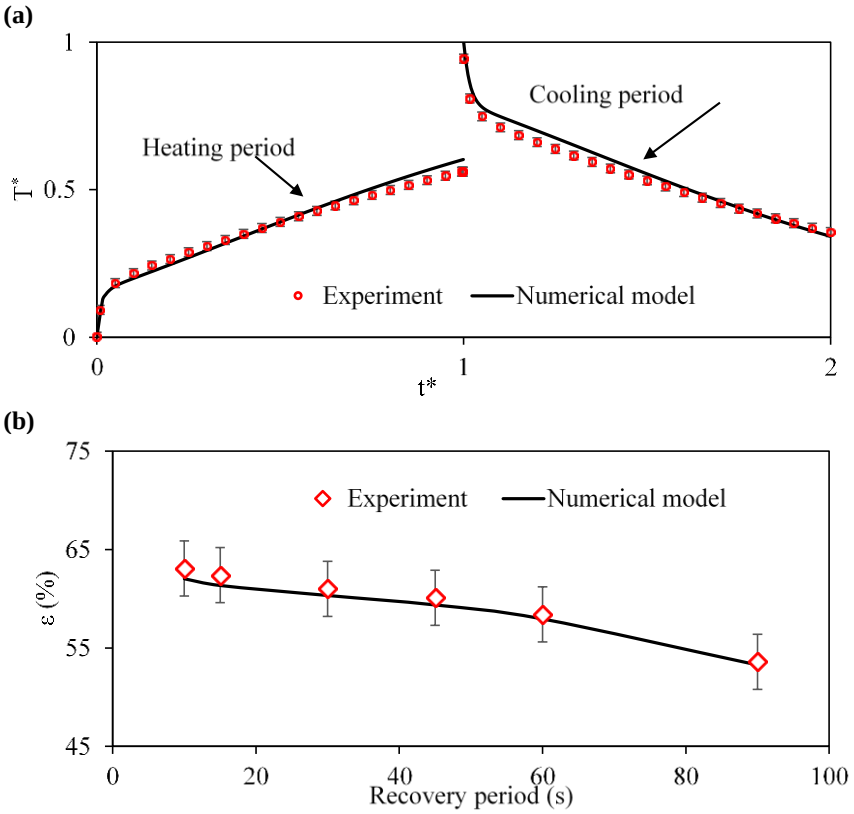

Figure 3.5. (a) Numerical and experimental temperature comparison from the beginning of the experiment (Too=2.4, Cr^*=1.2-8, λ=0.3) and (b) comparison of sensible effectiveness from experiment and numerical model.

3.6 RESULTS AND DISCUSSION

The effects of sensor time constant on the temperature measurements at the quasi-steady-state condition are discussed in detail in this section. The actual air temperature is obtained from Eqn. (3.13) over a wide range of Ndu_{om}, Cr^*, and λ. The sensor temperature measurements are obtained from Eqn. (3.17) for different dimensionless time constant (τ_s^*). The difference between

effectiveness obtained from Eqns. (3.13) and (3.17), is reported as the effectiveness error ($\Delta\epsilon$) due to the transient response of sensors (Eqn. (3.19)):

$$\Delta\epsilon = |\epsilon_{\text{actual}} - \epsilon_{sensor}| \tag{3.19}$$

3.6.1 FBRs with a sawtooth profile

Figure 3.6 (a) presents the sawtooth temperature profile at the outlet of FBRs during the quasi-steady-state condition. The temperature measurement from sensors (Eqn. (3.17)) with two different dimensionless time constants ($\tau_s^* = 0.2$ and 0.5) is also presented in Fig. 3.6 (a). For the sawtooth profile (despite different temperature profiles from sensors with different time constants), the predicted effectiveness from both sensors is calculated to be the same, and the effectiveness from sensors is equal to the actual effectiveness. Thus, the effectiveness of FBRs with the sawtooth outlet temperature is not sensitive to the time constant of the sensor. In other words, $\Delta\epsilon$ is equal to zero at different dimensionless time constants (τ_s^*). However, the shape of the temperature profile is not precisely captured with sensors, and the temperature swing cannot be obtained accurately (ΔT_{sensor} and ΔT_{actual} in Fig. 3.6 (a) are presented for $\tau_s^* = 0.2$ only). Additionally, the ratio of $\Delta T_{sensor}/\Delta T_{actual}$ decreases when the time constant increases, as depicted in Fig.3.6 (b). In this figure, the sensor measured temperature difference over the period (temperature swing) is about 6% of the actual FBR temperature difference for $\tau_s^* = 2$. In other words, with increasing sensor time constant (to two times as recovery period), the variation of measured temperature within the period decreases significantly; however, the average measured temperature is equal to the actual average air temperature (equal effectiveness).

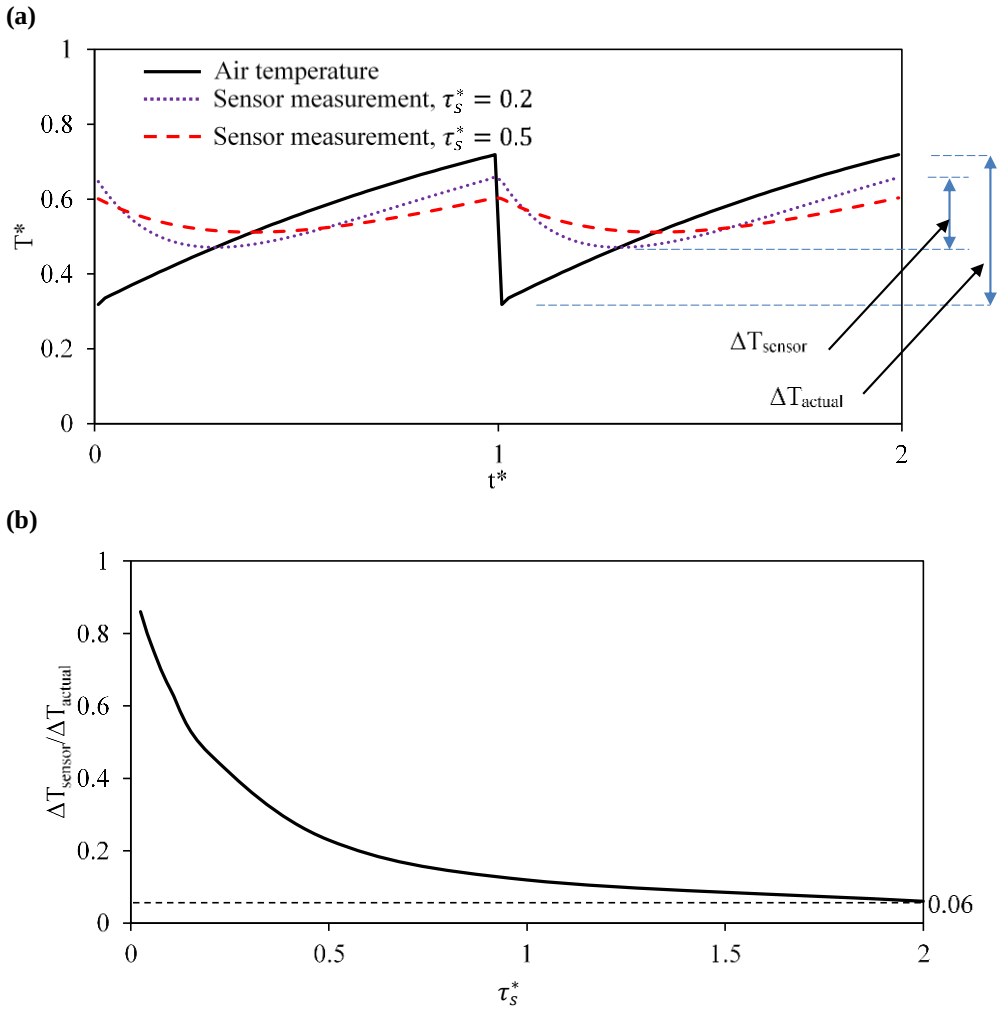

Figure 3.6. (a) Quasi-steady-state temperature profile and sensor measurements with two dimensionless time constant of u_s^*=0.2 and 0.5, and (b) $\Delta T_{sensor}/\Delta T_{actual}$ for FBR with sawtooth temperature (NTU_o=1, Cr^*=1, and λ=0).

Experiments can be designed to select the appropriate temperature sensors that capture the temperature shape (temperature swing) within a required precision. For example, Fig. 3.7 (a-d) shows the required τ_s^* (maximum values) to capture 90 % or 80 % of the temperature swing for FBRs with a sawtooth temperature profile over a wide range of design parameters. For example, to capture 90% of temperature swing for an FBR ($NTU_o = 5\,, Cr^* and\ \lambda = 0.0$), the maximum dimensionless time constant of about 0.06 must be selected (Figure 3.7 (b)). Increasing conduction parameter (λ) has a small effect on the required dimensionless time constant (τ_s^*).

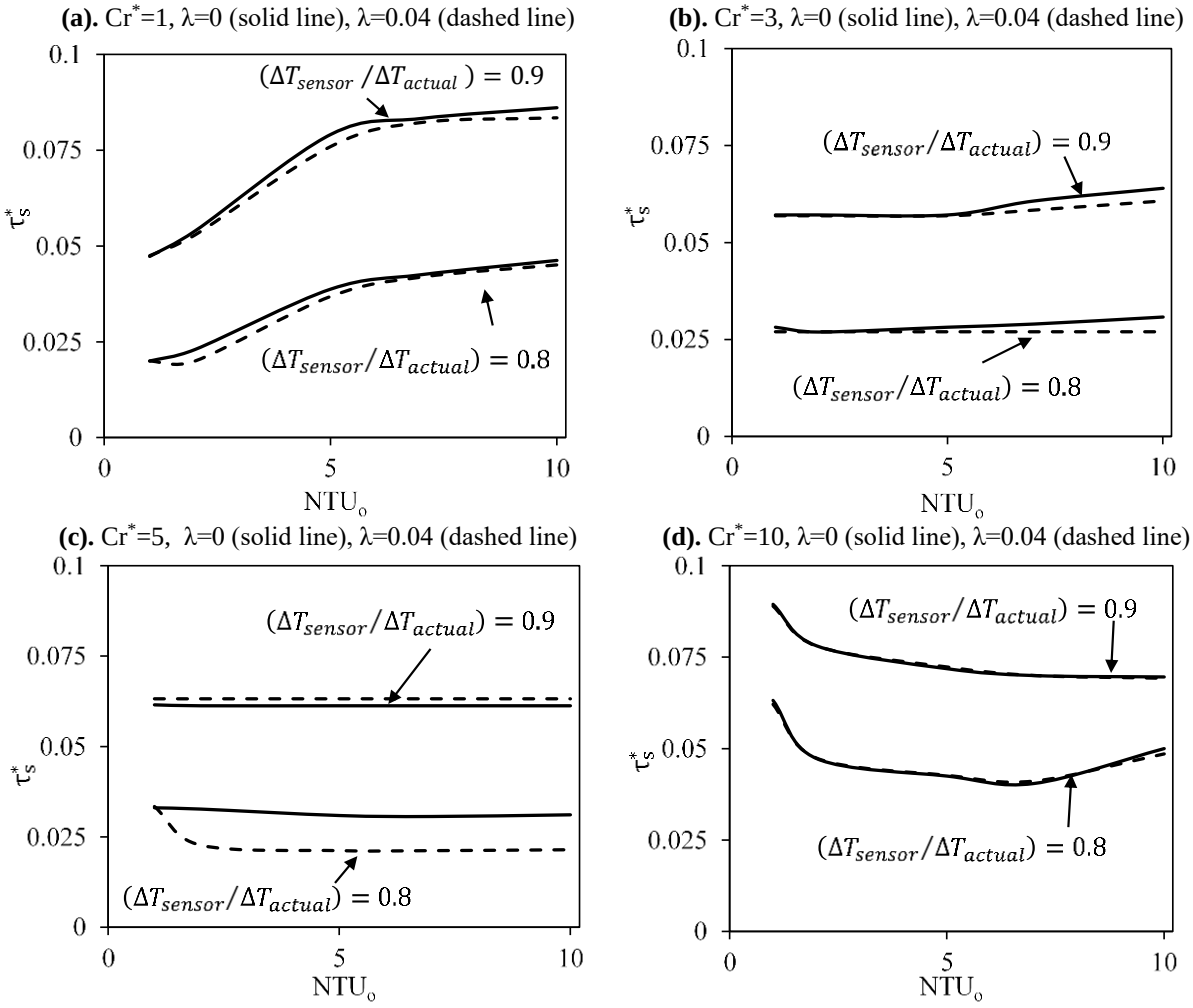

Figure 3.7. The required dimensionless sensor time constant (τ_s^*) to capture 80% and 90% of the actual temperature swing ($\Delta T_{sensor}/\Delta T_{actual}$ =80% and $\Delta T_{sensor}/\Delta T_{actual}$=90% for λ=0 (solid), 0.04 (dashed), NTU_o=1-10 and Cr^*=1,3,5 and10.

3.6.2 **FBRs with a semi-sawtooth profile**

Figure 3.8 (a) presents the semi-sawtooth temperature profile at the outlet of FBRs during a quasi-steady-state condition. The temperature measurements from sensors with two different dimensionless time constants of $\tau_s^* = 0.2\ and\ 0.5$ are also presented along in Fig. 3.8 (a). Both sensors' measurements follow the actual air temperature profile. However, the shape of the temperature profile and the effectiveness cannot be measured accurately. Unlike FBRs with a sawtooth profile, the sensor temperature measurement does not cross the actual air temperature

profile of FBRs with semi-sawtooth profiles. Therefore, the calculation of the temperature swings (ΔT_{sensor} and ΔT_{actual}) does not provide any significant insight into the relationship between the sensor and the actual temperature swing. Therefore, temperature swing is not discussed for FBRs with a semi-sawtooth temperature profile. Figure 3.8 (b) shows that the effectiveness measurements from sensors depend on the sensor time constant, and the effectiveness error increases significantly with an increase in the sensor time constant.

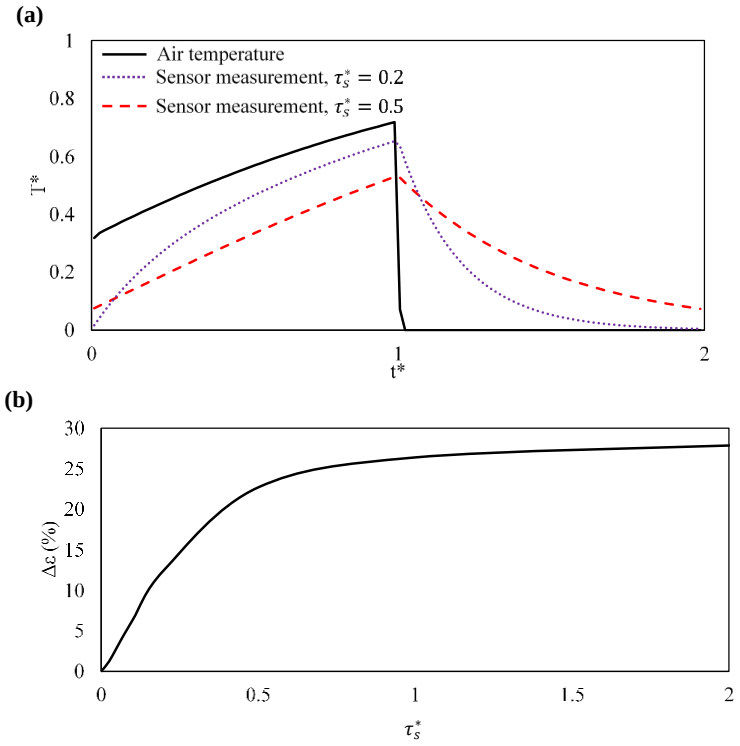

Figure 3.8. Quasi-steady-state temperature profile and sensor measurements with two dimensionless time constant of τ_s^*=0.2 and 0.5, and (b) effectiveness error (Δε) for FBR with semi-sawtooth temperature (NTU_o=1, Cr1, and λ=0).

At the quasi-steady-state condition, the sensors exposed to a semi-sawtooth temperature profile would not measure the temperature and effectiveness correctly. Comprehensive results of effectiveness errors (Δϵ in Eqn. 3.19) for FBRs with semi-sawtooth profile at different dimensionless time constant (τ_s^*), and longitudinal heat conduction parameter (λ) values (over a wide range of the design parameters of NTU_o and Cr^*) are presented in Appendix B. Tables B.1 to

B.9 summarize the effectiveness error due to the temperature sensor response at different ranges of dimensionless design parameters and time constants. Using the values reported in those tables, one can estimate the magnitude of errors for sensors with different time constants at specific dimensionless parameters.

Figure 3.9 presents the effectiveness error as a function of dimensionless time constant (τ_s^*) for different design conditions (NTU_o=1-10 and Cr^*=1-10). According to Fig. 3.9, the effectiveness error increases with an increase in τ_s^*. At smaller NTU_o (<2) and Cr^*(<2), the effectiveness errors are significant, which becomes smaller at higher NTU_o(=10) and Cr^*(=10). The effectiveness error also increases with an increase in the longitudinal conduction parameter (λ), and at higher NTU_o(>5) and Cr^*(>5) values, the effect of axial conduction in the matrix becomes more significant in the effectiveness error.

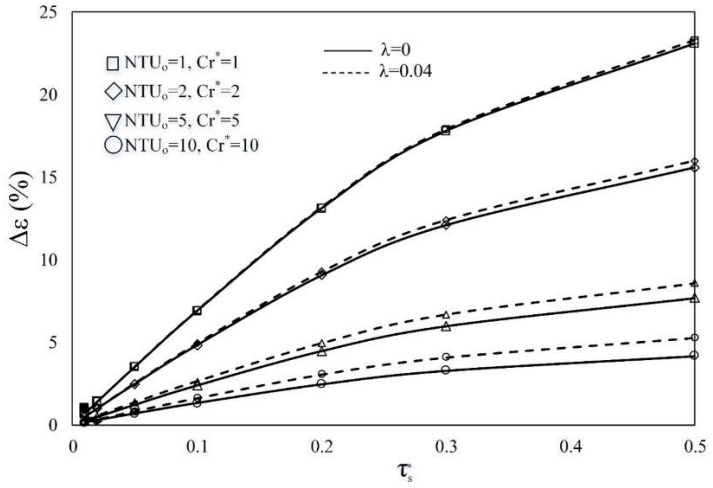

Figure 3.9. Effectiveness error as a function of τ_s^* at different design parameters of NTU_o and Cr^* (λ=0, and 0.04).

Using the results presented in Appendix B, experiments can be designed to select sensors to maintain the effectiveness error within specific ranges. For example, Fig. 3.10 shows the dimensionless time constants that result in effectiveness error (Δε) less than 1%, 2%, and 3% at different NTU_o and Cr^* values for λ=0 and 0.04. At small values of Cr^*, the dimensionless time

constant (τ_s^*) needs to be smaller for a certain value of effectiveness error. And at higher values of NTU_o (keeping the same Cr^*), a sensor with higher values of dimensionless time constant could be used to have a certain effectiveness error. The results in Fig. 3.10 also show that more accurate (smaller sensor time constant) should be used when the conduction parameter increases.

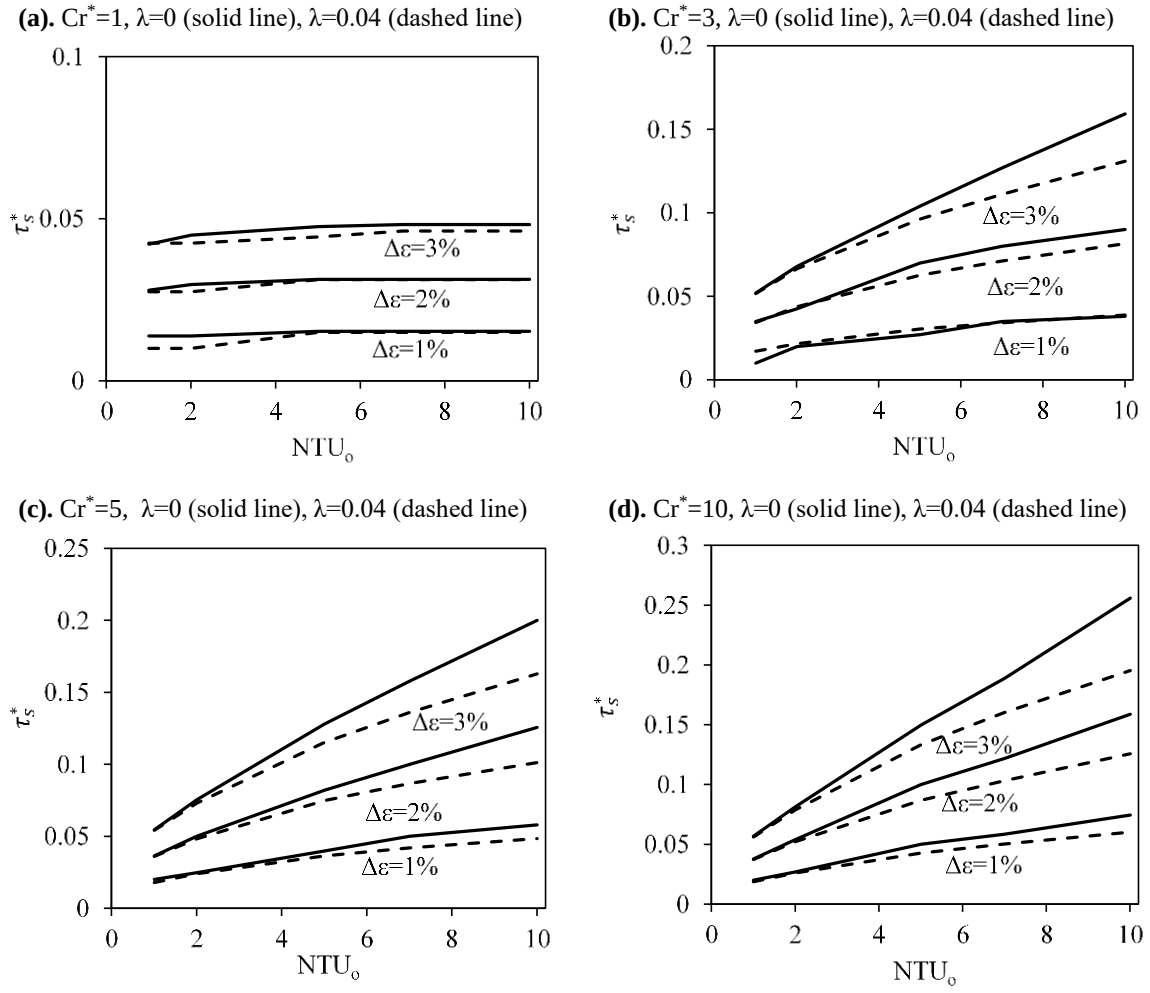

Figure 3.10. Required dimensionless sensor time constant (τ_s^*) that results in effectiveness error less than 1%, 2% and 3% for NTUo=1-10 and Cr*=1, 3, 5, and 10 for FBR with semi-sawtooth outlet profile.

Furthermore, Fig. 3.11 shows max effectiveness error (Max Δε) versus τ_s^* at different λ over the range of $1<NTU_o<10$ and $1<Cr^*<10$. Again, the impacts of conduction parameters are small and the maximum effectiveness error is less than 2% for $\tau_s^*<0.02$. Also, the value of

τ_s^*≈0.015 gives a maximum error of 1%, which can be translated to a time constant of 1 second for FBR with a recovery period of one minute. To obtain effectiveness with 5% accuracy, the sensor dimensionless sensor time constant should not exceed 0.07 (Fig. 3.11(b)).

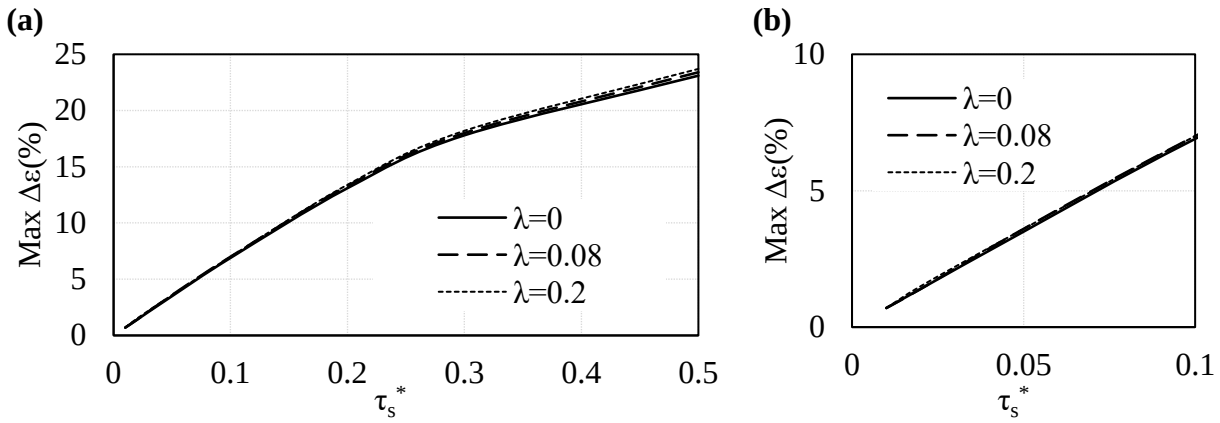

Figure 3.11. (a) Maximum effectiveness error versus dimensionless time constant over the range of 1<NTU_o<10 and 1<Cr^*<10 for FBR with semi-sawtooth profile (b) closer look at the smaller values of τ_s^*.

3.6.3 **Testing standards**

ASHRAE standard 84 [21] and CSA C439-18 standard [22] do not differentiate between the FBRs with saw-tooth and semi saw-tooth outlet temperature profiles because the scope of these standards is limited to FBRs with sawtooth profile. The results obtained in this study show that the temperature sensor requirements in standards are stringent and could be relaxed for FBRs with a saw-tooth outlet temperature profile in terms of effectiveness. Also, the results in Appendix B could be used to determine the requirements for temperature sensors of FBRs with a semi saw-tooth temperature profile. The standards require a sensor response time of 2 seconds for a recovery period of 60 seconds (which means that $\tau_s^* = 0.034$) regardless of the design conditions. Our results in Figure 3.10 shows that over a wide range of design conditions, this dimensionless time constant (i.e. $\tau_s^* = 0.034$) results in effectiveness error of about 1% (except for small Cr^* in Figure

3.10 (a)). Thus, it can be concluded that the standard requirements are also conservative for FBR with a semi-sawtooth profile. It should be noted that the standards use "response time" rather than the time constant for sensor transient characteristics. Response time has different definitions, it has been referred to as the time required to reach 90% or 95% of the change compared to 63.2% for the time constant. Thus, the response time is larger than the time constant; though in the discussions above it was assumed that time constant and response time are equal. The requirements for reaching the quasi-steady-state condition in standards are also verified in the previous study of the same authors [32].

3.7 SUMMARY AND CONCLUSIONS

The airstream temperature at the outlet of FBRs varies with time both during the initial transient period and subsequently during quasi-steady-state conditions. Hence, it is difficult for the sensors to accurately measure the temperature due to (i) steep slope of temperature variation and (ii) its exposure to a different temperature condition during the previous period. In this chapter, two distinct outlet temperature profiles for FBRs of positive/negative sawtooth and semi-sawtooth profiles were identified (depending on FBR configurations). The double-core FBR generally has a positive/negative sawtooth profile while the single-core FBR has a semi-sawtooth profile. Both profiles were analyzed for temperature measurement requirements over a wide range of design conditions using the developed numerical model. This chapter addressed the second objective of this PhD research which is "to quantify sensor errors over a wide range of design and operating conditions of sensible FBRs and make recommendations for testing standards".

It was found that regardless of FBR configurations, the ASHRAE standard 84 and CSA C439-18 standards provide very conservative requirements for the temperature sensors, and thus

both standards provide methods that accurately determine the effectiveness of FBRs. The analysis in this chapter revealed that the single-core (which usually produces a semi-sawtooth profile at the outlet) and double-core (which usually produces a sawtooth profile at the outlet) FBRs require different considerations for temperature measurement and effectiveness determination.

For FBRs with a sawtooth outlet temperature profile (double-core FBRs as per the ASHRAE standard 84 and CSA C439-18 standard), the effectiveness can be accurately measured regardless of the sensor time constant. However, the shape of the temperature profile (temperature swing) cannot be captured correctly. The results in this chapter provide the minimum sensor time constant to capture 80% and 90% of the temperature swing over a wide range of design conditions.

For FBRs with a semi-sawtooth temperature profile (single-core FBRs and some double-core FBRs), the effect of sensor response significantly influences the effectiveness estimation. The effectiveness error due to sensor transient response over a wide range of NTU_o, Cr^*, and λ and at different dimensionless time constants (τ_s^*) are evaluated and presented as graphs (in the manuscript) and tables (in the Appendix B).

At smaller NTU_o and Cr^*, the effectiveness error due to sensor transient response increases for FBRs with a semi-sawtooth temperature profile, and this error is around 25% for NTU_o=1 and Cr^*=1 at $\tau_s^* = 0.5$. An increase in the axial conduction in the matrix increases the effectiveness error, and the effect is more significant at higher NTU_o and Cr^*. The test configurations in the ASHRAE standard 84 and CSA C439-18 standard produce a sawtooth temperature profile (double-core FBRs), which allows for accurate effectiveness measurement. Many double-core FBRs produce a sawtooth temperature profile on the supply air side, but a semi-sawtooth profile on the exhaust side. Thus, sensor time constant and selection needs careful consideration when taking the field measurements on the exhaust airside. The results of the current study will be

helpful in developing standard recommendations in the future ASHRAE standard 84 and CSA C439-18 standards for testing the FBR.

The next chapter contains optimization of sensible FBRs considering its transient characteristics (variation of temperature at its outlet, i.e., temperature swing). In addition, a correlation will be developed to predict the temperature swing as a function of design conditions.

CHAPTER 4

OPTIMIZATION OF SENSIBLE FIXED-BED REGENERATORS (FBRs) CONSIDERING THEIR TRANSIENT CHARACTERISTICS

4.1 OVERVIEW

This chapter presents optimization of sensible FBRs considering their transient characteristics, i.e., Temperature Swing (TS). The temperature of the airstreams at the outlet of FBRs varies with time during each period of operation. A correlation was developed to predict TS as a function of design parameters. Then, the FBR is optimized considering TS as an additional objective to the commonly used objectives of effectiveness, pressure drop, payback period and exchanger mass. In this chapter, the third objective of the current PhD thesis, which is "to optimize sensible FBR considering its transient characteristics", is addressed and documented.

This chapter was published as a research paper in *ASME Journal of Thermal science and Engineering Applications* in June 2021 (Click here). The author of this thesis, Hadi Ramin, developed the correlation, performed optimization, and prepared the original draft of the paper. Mr. Krishnan (PhD student) conducted the experiments for validation and critically reviewed the paper; Dr. Annadurai (Postdoctoral fellow), and Prof. Simonson (supervisor) contributed to this paper by critically reviewing the paper.

The effect of transient characteristics on optimization of fixed-bed regenerators

(Published in the ASME Journal of Thermal science and Engineering Applications, June 2021)

Hadi Ramin, Easwaran N Krishnan, A. Gurubalan and Carey J Simonson

4.2 ABSTRACT

Fixed-bed regenerators (FBRs) have high sensible effectiveness, making them an energy-efficient Air-to-Air Energy Recovery Exchanger (AAEE) to reduce energy consumption for ventilation in buildings. FBRs operate by alternately storing and releasing heat in fixed exchangers, which results in an outlet temperature that varies with time during both hot and cold periods. This variation in FBR's outlet temperature adds a new optimization variable that needs to be considered when designing FBRs. For example, in HVAC systems, careful design is required to prevent large variations in FBR outlet temperatures (Temperature Swing (TS)), which might deteriorate occupant thermal comfort and introduce a variable load on the HVAC system. In this chapter, a correlation for TS is developed as a function of FBR design parameters. FBR optimization is performed considering TS as an additional objective to the traditional parameters of exchanger effectiveness, pressure drop, payback period, and mass. A selection procedure (decision-making procedure) is also integrated into the optimization process to select the optimized FBRs from Pareto fronts. The results show that when TS is included as an additional objective to the optimization and selection process, the selected optimized FBRs have higher mass and effectiveness. The results also show that including TS in optimizing FBRs does not reduce TS

significantly (less than 1°C), while penalties for exchanger mass and pressure drop are considerable (between 30-60%).

4.3 INTRODUCTION

Ventilation is crucial for maintaining indoor air quality and thermal comfort in buildings. Ventilation measures are critical for infection control related to the recent COVID-19 outbreak. According to the REHVA (Federation of European Heating, Ventilation and Air Conditioning Associations) COVID-19 guidance, while physical distancing is proven to be an effective measure to reduce the spread of illness in close contact with an infected person, adequate ventilation and proper air distribution could significantly reduce the risk of aerosol concentration and cross-infection in the built environments [58]. ASHRAE TC 5.5 recommends supplying outdoor air ventilation rates to maintain occupants' health and combating infectious bioaerosols [59]. However, outdoor air needs to be conditioned before introducing it to the buildings. This process could be energy-intensive, especially for very hot or cold climate conditions. For example, in Saskatchewan (Canada), the indoor and outdoor temperature difference could be high (about 60 ^{o}C) in winter.

Different air-to-air energy recovery exchangers (AAEEs) have been developed to recover energy from the building exhaust airflow to precondition the fresh outdoor air supply to buildings. Therefore, AAEEs reduce energy consumption for ventilation purposes [24]. With a high heat transfer area to volume ratio, few moving components compared to energy/heat wheels, and less susceptible to corrosion and fouling [20], FBRs are considered as an effective AAEE for energy recovery in building applications.

Due to the transient nature of the storing/releasing process, the air temperature at the outlet of FBRs never attains a steady-state (i.e., a constant air temperature); instead, it undergoes a quasi-

steady-state condition. FBR's outlet temperature profile varies with time at this condition but remains unchanged from period to period [19]. Because of this transient behaviour, temperature swing (TS) happens in the supply air, putting a variable load on the heating/cooling equipment. Temperature swings might also contribute to the occupant's thermal discomfort.

Fixed-bed regenerators are widely used for heat recovery in high-temperature applications such as glass furnaces, coke ovens, and open-hearth steel furnaces [7,9]. The applications of FBRs for energy recovery purposes in buildings have received considerable attention over the last years [13,15,20,28,32,52,60–62]. The authors have previously investigated the transient behaviour of sensible FBRs (Chapter 2) [50] and their impacts on temperature measurement to examine experimental temperature measurement requirements in testing standards for FBRs (Chapter 3) [28].

In this chapter, sensible FBR is optimized considering its transient behaviour, i.e., the temperature swing (TS). Several optimization studies have been conducted in the literature to optimize thermal regenerators (wheels and FBRs) for different applications (such as power plants, steel industry, HVAC, gas furnace, etc.). Such studies are summarized in Table 4.1. Single and multi-objective optimizations have been performed to find the geometrical (length, thickness, porosity, diameter, etc.) and operational (mass flow rate, rotational speed, etc.) variables at which effectiveness, entropy generation, total exchanger cost, and volume of regenerators are optimized. Table 4.1 shows that most studies have been performed to optimize the performance of wheels. No study on the literature focuses on optimizing FBRs for HVAC applications to the authors' best knowledge. Even for other applications, optimizing FBRs considering their transient behaviour has not been reported in the literature.

Table 4.1. Thermal regenerators' optimization studies.

#	paper	Regenerators type/application	Decision variable/s	Objective/s
1	(2020) Güllüce and Özdemir [63]	wheels/power plant	pitch of the undulated plate, the inner height of the undulated plate, outer diameter, length, and angular velocity	effectiveness, entropy generation, total exchanger cost, and volume
2	(2019) Wang et al. [64]	wheels/steel industry	height, rotor diameter, and hot/cold fluid sector angle	effectiveness, pressure drop, and exchanger mass
3	(2017) Lee et al. [65]	wheels/power plant	plate angle of undulated plate and pitch of the undulated plate	effectiveness and pressure drop
4	(2016) Raja et al. [66]	wheels/power plant	frontal area, rod diameter, thickness, rotational speed, and porosity of the matrix	effectiveness and pressure drop
5	(2013) Mioralli and Ganzarolli[67]	wheels/power plant and HVAC systems	porosity of matrix	effectiveness at a constant pressure drop
6	(2013) Tusek et al. [68]	packed-bed regenerators/ active magnetic regenerators	diameter, length, plate thickness, and porosity	effectiveness and pressure drop
7	(2011) Rao and Patel [69]	wheels/power plant	regenerator frontal area, matrix rotational speed, matrix rod diameter, matrix thickness, porosity, and split	effectiveness and pressure drop
8	(2010) Dallaire et al.[70]	wheels/power plant	length and porosity	heat transfer rate per unit frontal surface area
9	(2009) Sanaye and Hajabdollahi [71]	wheels/gas furnace preheater	frontal area, the ratio of hot/cold frontal area, matrix thickness, matrix rotational speed, matrix rod diameter, and porosity	pressure drop and effectiveness
10	(2009) Natarajan and Pitchandi [72]	FBRs/gas furnace preheater	reduced length and reduced period	pressure drop, effectiveness, and Entropy generation
11	(2009) Chung et al.[73]	wheels/HVAC	the wheel speed and the area ratio of regeneration to dehumidification	moisture removal capacity
12	(2008) Sanaye et al. [74]	wheels/HVAC	volumetric flow rates of cold and hot airstreams, matrix rotational speed, and the frontal exchanger area	effectiveness
13	(2006) Gao et al. [75]	FBRs/ glass-melting furnace	gas mass flux, reversal time, regenerator height, and sphere diameter	effectiveness
14	(2003) Jassim [76]	wheels/HVAC	characteristic dimensionless groups	cost, exergy, and effectiveness
15	(1993) Shen and Worek [77]	regenerators	characteristic dimensionless groups	pressure drop, effectiveness, and entropy generation

4.4 THERMAL AND OPERATIONAL MODELING FOR OPTIMIZATION OF FBRS

In this section, the geometrical description, thermal and hydrodynamic models connected to FBR optimization are presented. A schematic of an exchanger consisting of parallel plates (and a representative channel) under consideration for optimization is illustrated in Fig. 4.1.

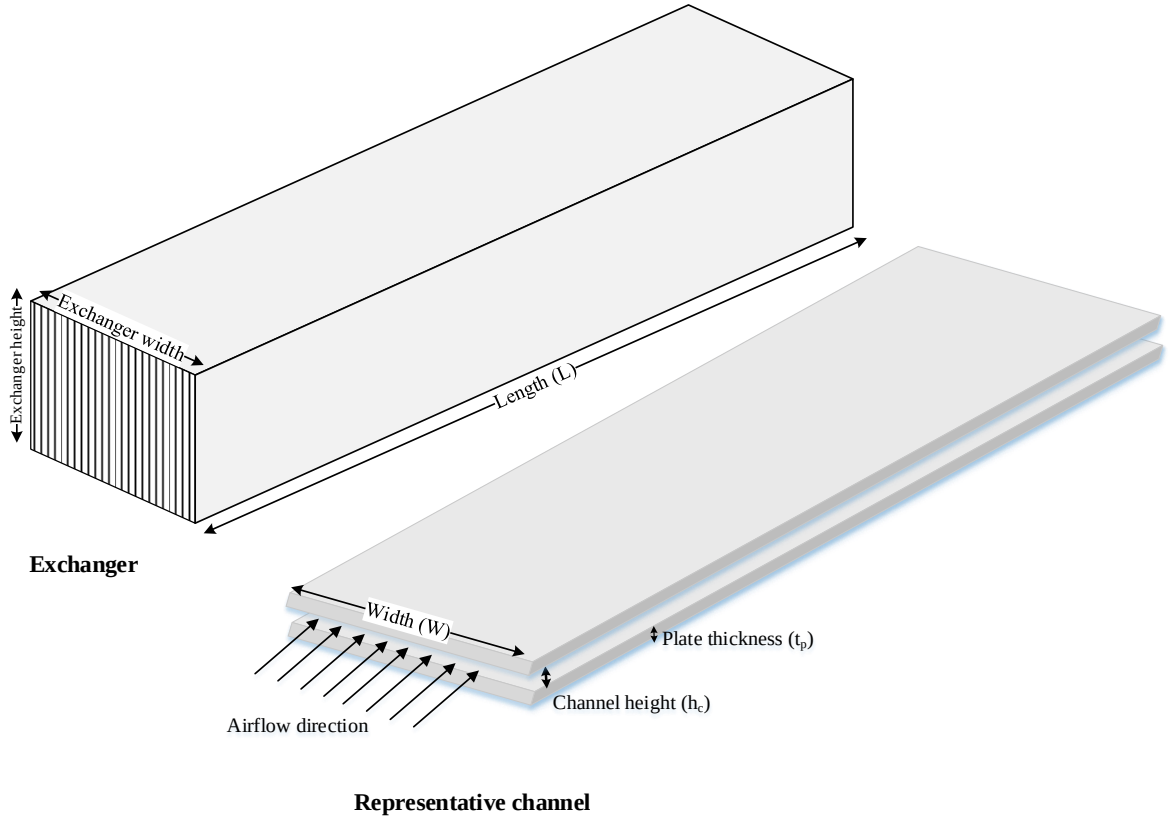

Figure 4.1. A schematic of FBR and the representative parallel plates channel for optimization.

4.4.1 Effectiveness

The effectiveness-number of transfer units (ε-NTU) method is a commonly used approach for the design of heat exchangers [35]. Effectiveness, which is defined as the ratio of the actual heat transfer rate to the maximum possible heat transfer rate, can be presented as a function of dimensionless groups and flow arrangements [19]. The dimensionless groups are extracted from

the governing equations, and for sensible regenerators, effectiveness is obtained from Eqn. (4.1) [19].

$$\epsilon_s = \frac{NTU_o}{1+NTU_o}\left[1-\frac{1}{9(Cr_o^*)^{1.93}}\right]\left[1-\frac{C_\lambda}{2-C^*}\right] \quad (4.1)$$

Parameters in Eqn. (4.1) are defined in Table 4.2. Mean Nusselt number for simultaneous developing flow are extracted from [38] for rectangular channels with several aspect ratios (α^*=0, 0.25,0.333, 0.5, and 1) as a function of x^*=(L/(Re.Pr.Dh)), the dimensionless axial distance for heat transfer. For other aspect ratios in the optimization process, the mean Nusselt number is obtained by linear interpolation between available aspect ratios.

Eqn. (4.1) is accurate within 1% for the range of $1 \le NTU_o \le 20$, $2 \le Cr^* \le \infty$, and $0 \le \lambda \le 0.08$, and this equation is used to obtain the effectiveness of FBR in this study.

Table 4.2. Definition of dimensionless parameters for the effectiveness of FBRs in Eqn. (4.1).

Parameter	Description	Eqn. #
$\mathrm{NTU_0} = \frac{1}{(\dot{m}C_p)_{g,min}}\left[\frac{1}{(hA_h)_h}+\frac{1}{(hA_c)_c}\right]^{-1}$	overall number of transfer units	(4.2)
$\mathrm{Cr^*} = (MC_p)_m/\left((\dot{m}C_p)_{g,min}(P_c+P_h)\right)$	overall matrix heat capacity ratio	(4.3)
$C^* = (\dot{m}C_p)_{g,min}/(\dot{m}C_p)_{g,max}$	the ratio of minimum to maximum heat capacity rate of the airstreams	(4.4)
$\lambda = \frac{k_m A_{m,t}}{L\, C_{min}}$	longitudinal wall conduction parameter based on the total conduction area	(4.5)
$C_\lambda = 1/(1+NTU_0(1+\lambda\Phi)/(1+\lambda NTU_0)) - 1/1+NTU_0$	conduction parameter correction	(4.6)
$\Phi = \left(\frac{\lambda NTU_0}{1+\lambda NTU_0}\right)\tanh\left(\frac{NTU_0}{(\lambda NTU_0/1+\lambda NTU_0)^{0.5}}\right.$	intermediate function for C_λ	(4.7)

4.4.2 **Temperature swing (TS)**

Previous studies and experimental measurements have shown that FBR's outlet temperature varies linearly with time within each operation period [11,19,20,50]. From the dimensionless governing equations for a FBR [28], it can be inferred that the outlet temperature of FBR during the hot and cold periods are as follows:

$$T^*_{h,o} \; or \; T^*_{c,o} = \beta_1(\, t^*, NTU_o, C^*, Cr^*, \lambda) \tag{4.8}$$

Where $T^*_{h,o} \; and \; T^*_{c,o}$ are the dimensionless temperatures $\left(i.e. \frac{T_{h,o}-T_{c,i}}{T_{h,i}-T_{c,i}} \; and \; \frac{T_{c,o}-T_{c,i}}{T_{h,i}-T_{c,i}}\right)$ and β_1 is a symbolic function. For equal hot and cold period (P_h=P_c) and balanced FBR ($C^* = 1$), the dimensionless temperature profile is simplified in Eqn. (4.9).

$$T^*_{h,o} \; or \; T^*_{c,o} = \beta_2(\, t^*, NTU_o, Cr^*, \lambda) \tag{4.9}$$

Thus, the outlet temperature is a function of dimensionless design parameters of $NTU_o, C^*_r \; and \; \lambda$.

FBR outlet temperature profiles are presented in Fig. 4.2 for the hot and cold periods. Temperature swing (TS) is obtained using the slope of the temperature profile (Fig. 4.2) from Eqn. (4.10).

$$TS = m_T \times (T_{h,i} - T_{c,i}) \tag{4.10}$$

Where m_T is the slope of the dimensionless temperature profile. At a specific design condition (NTU_o, Cr* and λ), the slopes of the temperature profiles in the hot and cold periods ($m_{T\,(\text{hot period})} = -m_{T_{(\text{cold period})}}$) and their intercepts ($b_{(\text{hot period})} + b_{(\text{cold period})} = 1$) are associated. The associations are also shown in Fig. 4.2.

The FBR outlet temperature profile (and its slope) is a function of NTU_o, C^*_r, λ, as mentioned previously. From a validated numerical model [50], 230 simulations over a wide range of design parameters ($NTU_o = 1-10, C^* = 1, Cr^* = 1-10, \lambda = 0-0.24$) were performed to

obtain slopes of the outlet temperature profiles. Using this data, two approaches are adopted to predict the slope of the temperature profile at any given design conditions. A neural network is trained using the Neural Network Fitting App in MATLAB 2019b [78] to predict the slope in the first approach. A correlation is also fitted to the 230 available data points from the simulation results in the second approach.

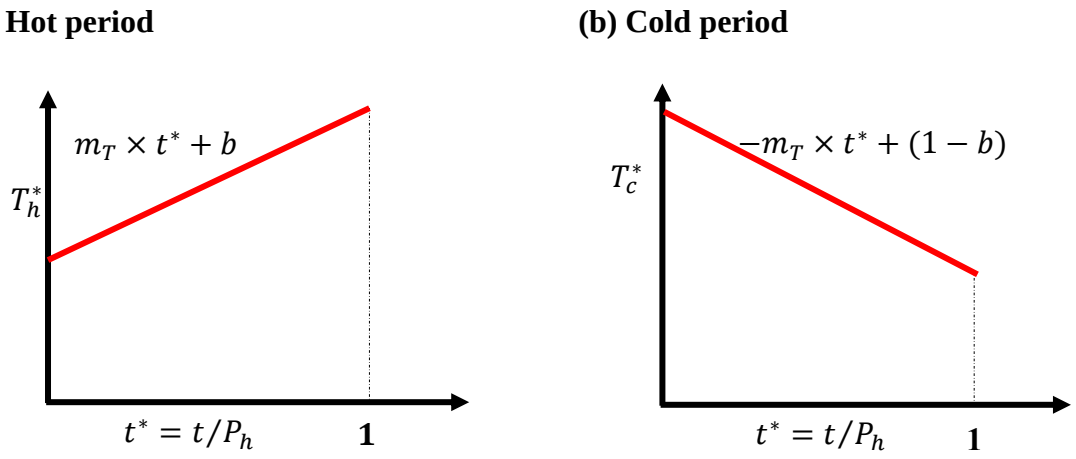

Figure 4.2. Dimensionless temperature profile at the outlet of FBR in (a) hot and (b) cold periods.

Neural network approach: Neural Network Fitting App [78] uses a two-layer-feed-forward network with hidden sigmoid neurons and linear output neurons to fit multi-dimension data points. The network is trained with the Levenberg-Marquardt backpropagation algorithm [78], and the data set is randomly divided into training (70%), validation (15%), and testing (15%) samples. The performance of the Neural Network were examined for different training and testing ratios and it was found that the performance of the network was the best for the training/test ratio of 70/30. The Levenberg–Marquardt algorithm inherits the speed advantage of the Gauss-Newton algorithm and the stability of the steepest descent method [79]. The trained network has the MSE (mean squared errors) smaller than (2×10^{-5}) and regression R-value of 0.999, which means that

the trained network has excellent performance to predict the slope of the temperature profile at the outlet of FBR.

Correlation approach: the following correlation has been fitted with the data set:

$$m_T = a_1 + a_2\left(\frac{NTU_o}{1+NTU_o}\right)\left(\frac{1}{Cr^*}\right)^{a_3}(1-C_\lambda)^{a_4} \quad (4.11)$$

Where: a_1=0.03593, a_2=0.7563, a_3=1.045 and a_4=0.1.

The reason to choose the form of correlation in Eqn. (4.11) is its similarity to effectiveness correlation (Eqn. (4.1)), which is also a function of the same dimensionless parameters.

Figure 4.3 (a) and (b) show comparisons between the slope of temperature profile from the correlation (Eqn. (4.11)) and the neural network with the actual values from simulation (230 data points). The correlation predictions agree with the simulation results within ±10%, while the neural network results are within ±5% of the actual values from the data points. The neural network approach seems more accurate in predicting the slop of temperature profiles than the curve fitting approach; this conclusion is also reported in previous studies [80,81]. For this optimization study, the neural network will be used because of its accuracy. The correlation is a simple and straightforward approach to estimate the temperature swing for practical applications.

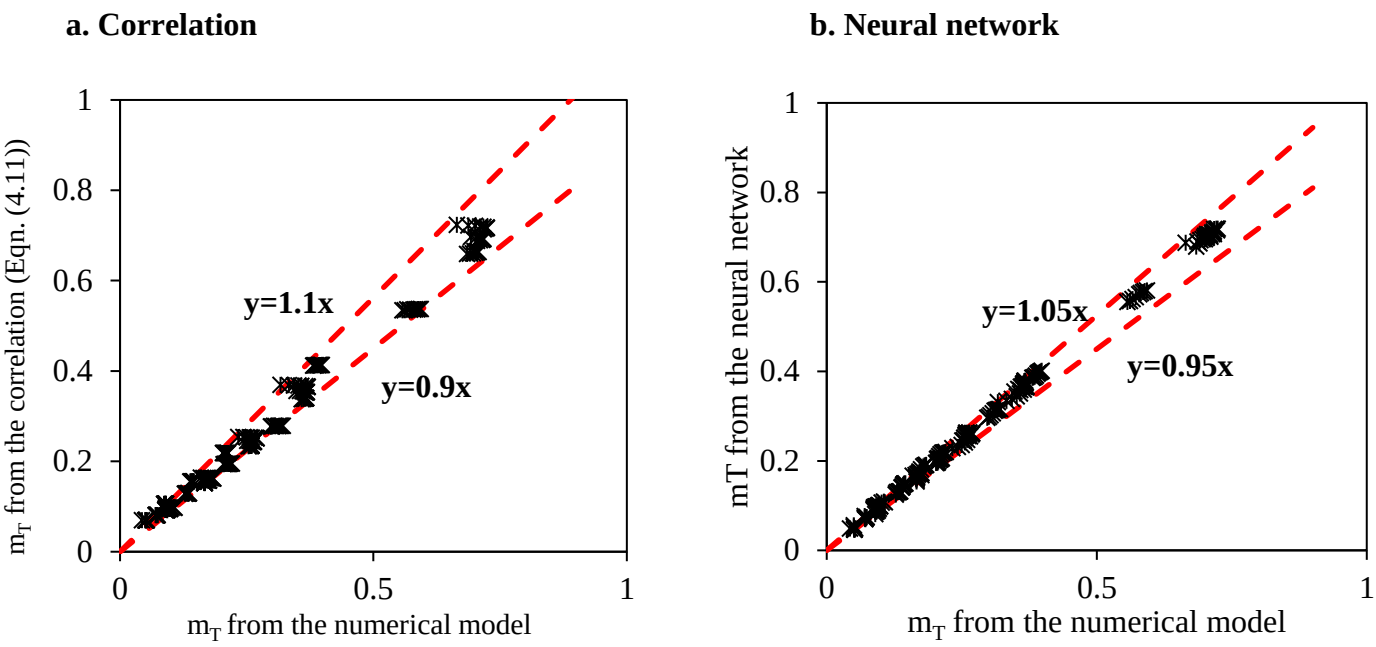

Figure 4.3. Comparison of prediction of the temperature profile slopes (m_T) from (a) the correlation in Eqn. (4.11) and (b) the neural network with the simulation results.

It can be seen from Eqn. (4.11) that the slope of temperature profile (hence TS) increases with an increase in NTU_o (Fig. 4.4 (a)) while it decreases when Cr^* (Fig. 4.4 (b)) and C_λ increase. From Fig. 4.4 (a), at $Cr^* \geq 2$ the slope of temperature profile is plateaued out for $NTU_o > 3$. The impact of longitudinal conduction is more significant at smaller Cr^*(Fig. 4.4 (a) and (b)).

4.4.3 **Pressure drop and fan energy consumption**

Pressure drop is obtained from the following equation, which includes both the effect of wall friction and change of the momentum for developing flow [19]:

$$\Delta p = \rho_g f_{app} \frac{LV^2}{D_h} \tag{4.12}$$

Where f_{app} is apparent Fanning friction factor, and the values are adopted from graphs provided in [19] for different α^*as a function of dimensionless axial distance for fluid flow ($x^+ = x/D_h Re$).

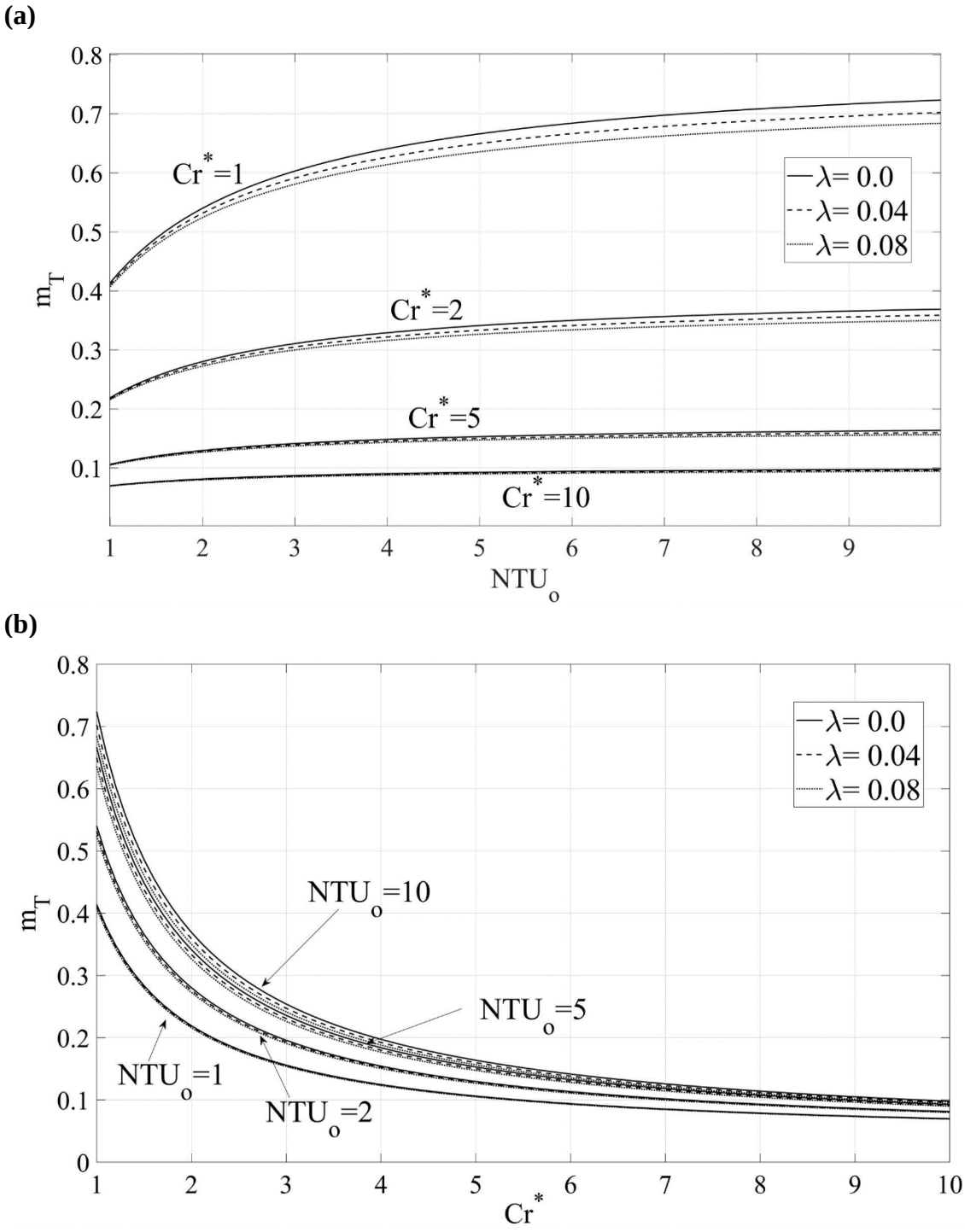

Figure 4.4. Variation of m_T versus (a) NTU_o and (b) Cr^* at different conduction parameters of λ=0, 0.04 and 0.08.

Like the heat transfer coefficient, the apparent fanning friction factor for other aspect ratios is obtained through linear interpolation.

Fluid pumping power is proportional to pressure drop within the exchanger, as presented in Eqn. (4.13) [19].

$$PP = \frac{\dot{V}\Delta p}{\eta_p} \tag{4.13}$$

In the Eqn. (4.13), PP is pumping power, $\dot{V}$ is the volumetric flow rate, Δp is the pressure drop and η_p is the fan efficiency.

4.4.4 **Payback period**

The payback period of FBR is a function of an initial investment, operation costs, and the amount of energy recovered when FBR is integrated within the building HVAC systems. The amount of recovered energy with FBR depends on FBR effectiveness, airflow rate, and outdoor weather conditions. The most severe weather conditions and yearly weather data could be used to estimate the energy recovered by FBRs; the latter approach considers the hourly weather data and is used in this chapter [82].

A schematic of an HVAC system with an FBR is presented in Fig. 4.5 (a). The outdoor supply temperature ($T_{s,i}$) is heated/cooled (winter/summer) to $T_{s,o}$ when it exchanges heat with the return air ($T_{e,i}$) from the conditioned space in FBR. When FBR is unable to meet the required design condition, auxiliary heating/cooling equipment and/or recirculated air are used to adjust the supply air temperature to the design temperature (T_{des}) before introducing it to the conditioned space. It is assumed that if FBR is not needed to meet the design condition, the supply air is bypassed. The hourly outdoor temperature is plotted as a monotonically increasing function with the actual temperature data as the ordinate and time (number of hours) as the abscissa (Fig. 4.5

(b)). This figure shows the areas representing the recovered annual heating/cooling energy and the auxiliary energy requirements. The yearly temperature data are extracted using Climate Consultant 6.0 software [83], which uses the annual 8760 hours EPW format climate data.

The sensible effectiveness (Eqn. (4.1)) could be rewritten using the temperatures in Fig. 4.5 (a)**:**

$$\epsilon_s = \left(T_{s,i} - T_{s,o}\right)/\left(T_{s,i} - T_{e,i}\right) \tag{4.14}$$

The annual energy (heating and cooling) saving is assumed to be equal (uniform) over the equipment's lifecycle. The annual energy saving with FBR is equal to the annual heating and cooling energy recovered (ER_{ann}) subtracted by additional pumping power (PP) cost in the HVAC system with FBR in place.

$$ES_{ann} = ER_{ann} - e_p PP \tag{4.15}$$

e_p ($\$/kWh$) is the unit energy price for pumping airflow and ER_{ann} is the annual energy recovered saving with FBR. ER_{ann} is obtained using the representing areas for recovered heating and cooling from Fig. 4.6 (b) and mathematically presented in Eqn. (4.16):

$$ER_{ann} = e_h q_{h,rec} + e_c q_{c,rec} \tag{4.16}$$

Where e_h ($\$/kWh$) and e_c($\$/kWh$) are the heating and cooling unit energy price. $q_{h,rec}$ and $q_{c,rec}$ are the total heating and cooling energy recovered with FBRs and represented by:

$$q_{h,rec} = \dot{m}_{air} Cp_g A_{h,rec} \tag{4.17}$$

$$q_{c,rec} = \dot{m}_{air} Cp_g A_{c,rec} \tag{4.18}$$

$A_{h,rec}$ and $A_{c,rec}$ are the area corresponding to the annual heating and cooling energy recovered with FBR, respectively in Fig. 4.5 (b).

The payback period (PBP) of FBRs is calculated using Eqn. (4.19).

$$PBP = \left(\frac{CC_{FBR}}{ES_{ann} \times PWF}\right) \times LC = \left(\frac{CC_{FBR}}{ES_{tot}}\right) \times LC \tag{4.19}$$

CC_{FBR} and ES_{tot} are the FBR capital cost and the adjusted (calculated at the year of investment) total energy saving with FBR over its lifecycle (LC). The file cycle is considered ten years in this study and ES_{ann} is the annual energy saving with FBR. Eqn. (4.19) is applicable for retrofit applications; for new designs, the capital cost should be adjusted to consider the capital cost saving corresponding to the smaller auxiliary heating/cooling equipment [82]. In this chapter, this improvement is neglected for simplicity.

The capital cost of investment is obtained from a local company for a standard design. The present worth factor (PWF) is used to convert the annual energy saving over the equipment lifecycle to ES_{tot}. The PWF is a function of LC, interest rate (i), and inflation rate (d) as in Eqn. (4.20) [84].

$$PWF = \begin{cases} \frac{1+i}{d-i}\left[1-\left(\frac{1+i}{1+d}\right)^{LC}\right] & i \neq d \\ \frac{LC}{1+i} & i = d \end{cases} \tag{4.20}$$

Table 4.3 summarizes the economic and design condition input parameters used in this study.

Table 4.3. Economic and design parameters for optimizing FBRs.

Variable	**Symbol**	**value**
Lifecycle (year)	LC	10
Interest rate (%)	I	5
Inflation rate (%)	d	5
Unit energy price for electricity ($\$/kWh$)	e_p	0.14
Unit energy price for heating ($\$/kWh$)	e_h	0.03
Unit energy price for cooling ($\$/kWh$)	e_c	0.14
Heating temperature design condition (°C)	T_c	-16.7
Indoor design condition (°C)	T_h	22

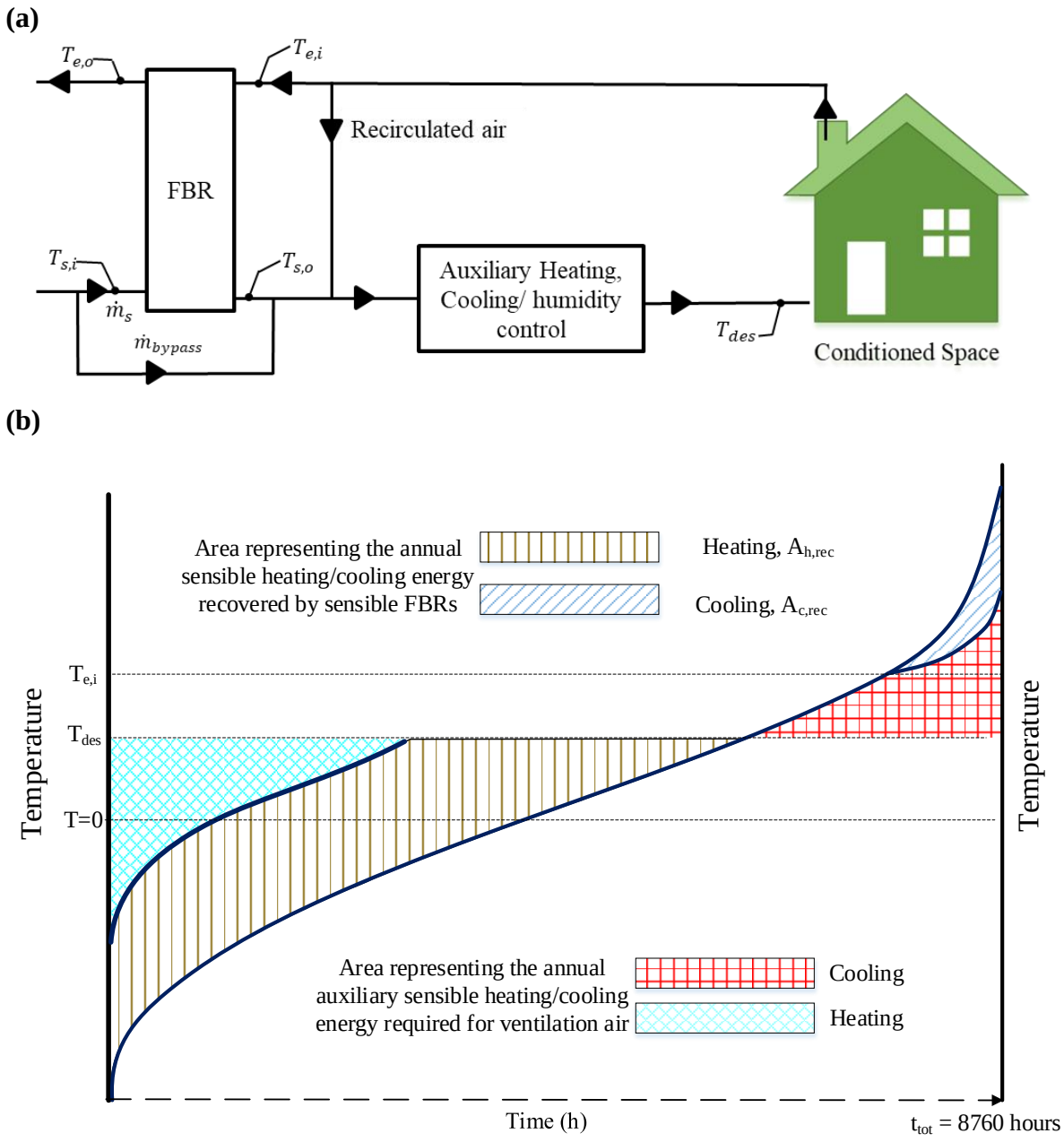

Figure 4.5. (a) A schematic of an HVAC system with FBRs for sensible energy recovery (b) distribution of outdoor air temperature, the temperature at the outlet of FBR and energy recovered with FBR, and additional energy required to condition the ventilation air.

4.5 MULTI-OBJECTIVE OPTIMIZATION AND MULTI-CRITERIA DECISION-AID PROCEDURE

4.5.1 Multi-objective optimization

Most engineering problems have several objectives to optimize simultaneously. A general multi-objective problem is given by Eqn. (4.21)[85]:

$$\begin{aligned} &\text{Minimize} \quad f_k(v) && k = 1, \dots, K; \\ &Subject\ to \quad g_j(v) \geq 0 && j = 1,2, \dots, J; \\ &v_g^{(L)} \leq v_g \leq v_g^{(U)} && g = 1,2, \dots, G; \end{aligned} \tag{4.21}$$

Where $f_k(v)$ are the objective to be optimized, $g_j(v)$ are the inequalities constraints, and v_g is a vector of decision variables ($v_g = [v_1, v_2, \dots, v_G]^T$). $v_g^{(L)}$ and $v_g^{(U)}$ are the upper and lower bounds for the decision variables. FBR effectiveness, pressure drop, exchanger mass, payback period, and temperature swing are considered as objectives in this chapter. There are a set of trade-off solutions known as Pareto-optimal solutions (Pareto fronts) when a multi-objective optimization problem is solved. The solutions (alternative designs) on the Pareto front are non-dominated solutions meaning that an objective cannot be improved without degrading other objectives.

Exchanger length, plate thickness, channel height, and recovery period are considered as the decision variables for optimizing FBR in this study. Table 4.4 presents the range of the decision variables for FBR optimizations based on practical FBR design recommendations. In addition, the exchanger flow rate is considered constant, but the impacts of variable flow rate on the optimized results are investigated by changing the flow rate. A base FBR design is considered for comparison

with the optimized solutions. The base FBR design parameters and its performance are presented in Table 4.5.

Table 4.4. Decision variables and their ranges for optimizing FBRs.

Decision variable	Symbol	range
Exchanger length (m)	L	0.5-1.5
Plate thickness (mm)	t_p	0.5-3
Channel height (mm)	h_c	2-6
Recovery period (s)	$P_h \; or \; P_c$	30-120

Table 4.5. Base exchanger design parameters and its performance.

Parameter	Value	Parameter	Value
Exchanger length- L (m)	1.0	Location	Toronto
Exchanger width- W (m)	0.75	NTU_o	1.7
Exchanger height-H (m)	0.3	Cr^*	3.4
Plate thickness-t_p (mm)	0.7	λ	0.04
Number of channels	50	Effectiveness-ε (%)	61.0
Channel height, h_c (mm)	4.5	Pressure drop- Δp (Pa)	3.4
Exchanger mass- M_{FBR} (kg)	69.7	Payback period-PBP (year)	3.8
Face velocity – V (m/s)	1.3	Temperature swing- TS (°C)	6.9
Recovery period-P_h or P_c (s)	60	Exchanger volume (m^3)	0.26

4.5.1.1 Optimization procedure (NSGA-II)

Evolutionary algorithms are common approaches to find the Pareto-optimal solutions for multi-objective problems. NSGA-II (non-dominated sorting genetic algorithm II) is proposed by Deb et al. [86] and became a commonly used evolutionary algorithm to solve the multi-objective optimization problems; hence, in this chapter, NSGA-II is used to find the Pareto fronts [78]. The NSGA-II main parameters to solve the problem in MATLAB are presented in Table 4.6.

Table 4.6. NSGA-II main parameters in MATLAB.

Parameter	Value
Population size	500
Creation function	Constraint dependent
Selection function/tournament size	Tournament/2
Reproduction	Crossover function/ 0.8
Mutation function	Constraint dependent
Crossover function	Intermediate
Migration direction/fraction	Forward/0.2
Function tolerance	1e-7
Constraint tolerance	1e-4

4.5.1.2 MCDA procedure

MCDA (multiple-criteria decision aid) is a valuable tool to help the designers and decision-makers with selecting the best design out of available alternatives [87]. The Pareto fronts obtained from multi-objective optimization problems provides the designer's alternatives. Yet, they need to look for a good compromise by examining trading-off between the conflicting criteria (financial, performance, environmental, etc.) to select the best design out of many alternatives. MCDA has been applied in different scientific areas, and numerous MCDA methodologies (such as TOPSIS, LINMAP, VIKOR, AHP, and Goal Programming) exist in the literature [88]. Linear Programming Technique for Multidimensional Analysis of Preference (LINMAP) is one of the classical MCDA methods used in different scientific fields [33] and is used in this chapter to rank the alternatives. LINMAP ranks alternatives by comparing their closeness to the ideal objective values. Ideal objective values are obtained by optimizing each objective individually over the range of decision variables. The ideal objective values are presented in Table 4.7.

Table 4.7. Ideal objective values over the range of decision variables in Table 4.4.

Objective	Value
Effectiveness-ε (%)	90.9
Pressure drop- Δp (Pa)	1.1
Payback period-PBP (year)	0.2
Temperature swing- TS (°C)	1.3
Exchanger mass- M_{FBR} (kg)	20.3

4.5.2 **Integration of optimization and MCDA**

Figure 4.6 shows a flowchart representing the procedure to optimize FBR and ranking alternatives from Pareto fronts using LINMAP. The Pareto fronts are obtained once the convergence criteria for the NSGA-II algorithm are reached; then, various alternatives on the Pareto fronts will be ranked using LINMAP. The appropriate weightage (WO), which reflects each objective's importance compared with other objectives, needs to be selected depending on the design requirements and preferences for the ranking procedure in LINMAP.

Six scenarios (SCs) for the objective's relative importance (weight of objective (WO)) are considered in this study and are presented in Table 4.8. The weights add up to 1 at each row. For example, in scenario one (SC_1), all objectives are considered to be equally important. Therefore, in an optimization problem that includes all objectives, the weight of each objective will be 0.20 (5× WO_1=1). For the same problem, when temperature swing is not included in optimization, the weight of each objective would be 0.25 (4× WO_1=1 and WO_1=1/4). The proposed scenarios in Table 8 are selected to demonstrate the impact of TS in several optimization scenarios. Effectiveness is considered the most important objective and is given higher weight in most scenarios (2-5), while Scenario 6 prioritizes TS (twice as important as other objectives) over other objectives. Several standard approaches (e.g., AHP: analytic hierarchy process) systematically determine the weight of an objective in an optimization problem [89]. However, this is not the

focus of this study and scenarios are selected for simplicity and inclusion of different possible scenarios for design.

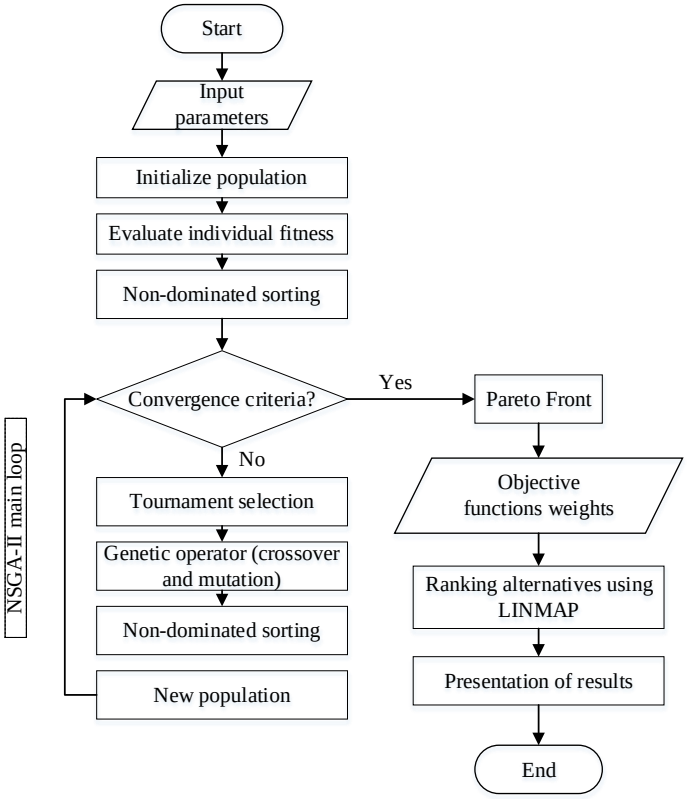

Figure 4.6. Multi-objective optimization and ranking process flowchart.

Table 4.8. Different scenarios (SCs) for the importance of objectives for FBRs design.

Importance Weight	**Effectiveness**	**Pressure drop**	**Payback Period**	**Exchanger mass**	**Temperature Swing**	**Value of WOs**	
						Without TS	**With TS**
Scenario 1 (SC_1)	WO_1	WO_1	WO_1	WO_1	WO_1	1/4	1/5
Scenario 2 (SC_2)	2 WO_2	WO_2	WO_2	WO_2	WO_2	1/5	1/6
Scenario 3 (SC_3)	$3WO_3$	$2WO_3$	$2WO_3$	$2WO_3$	$2WO_3$	1/9	1/11
Scenario 4 (SC_4)	$3WO_4$	WO_4	WO_4	WO_4	$2WO_4$	1/6	1/8
Scenario 5 (SC_5)	2 WO_5	$2WO_4$	WO_5	WO_5	$2WO_5$	1/6	1/8
Scenario 6 (SC_6)	WO_6	WO_6	WO_6	WO_6	$2WO_6$	1/4	1/6

Four optimization problems that combine different objectives are considered in this chapter. These problems are selected based on the optimization problems in the literature (presented in Table 4.1) and the manufacturer recommendations. The optimization is first

performed for each problem without considering TS as an objective in the optimization problem. Then TS is added to the same problem to understand how TS changes the Pareto fronts and selected optimized designs.

4.6 RESULTS AND DISCUSSIONS

In this section, the sensitivity of the objective functions to the decision variables is presented (section 4.6.1). Then the four optimization problems are solved with/without considering TS as an objective (section 4.6.2). LINMAP ranking procedure is used to obtain the optimized FBR design for different scenarios of the importance of objectives (weight of objective: WO) from the Pareto fronts.

4.6.1 Sensitivity of objective functions to the decision variables

Figure 4.7 (a-d) show the variation of objective functions to the decision variables. Reference decision variables are chosen from Table 4.5. Each decision variable is allowed to change within its range of variation in Table 4.4, while other decision variables are kept constant at the base exchanger design values.

Table 4.9 summarizes the trend (increase or decrease) of different objective functions with an increase in the decision variables over their range of variations and justification for the changes in objective values. Higher effectiveness, lesser pressure drop, exchanger mass, temperature swing, and payback period are favourable for the design of FBRs. It should be noted that the exchanger cross-sectional area is kept constant for this optimization study. Also, the exchanger volume is changed when the exchanger length is altered.

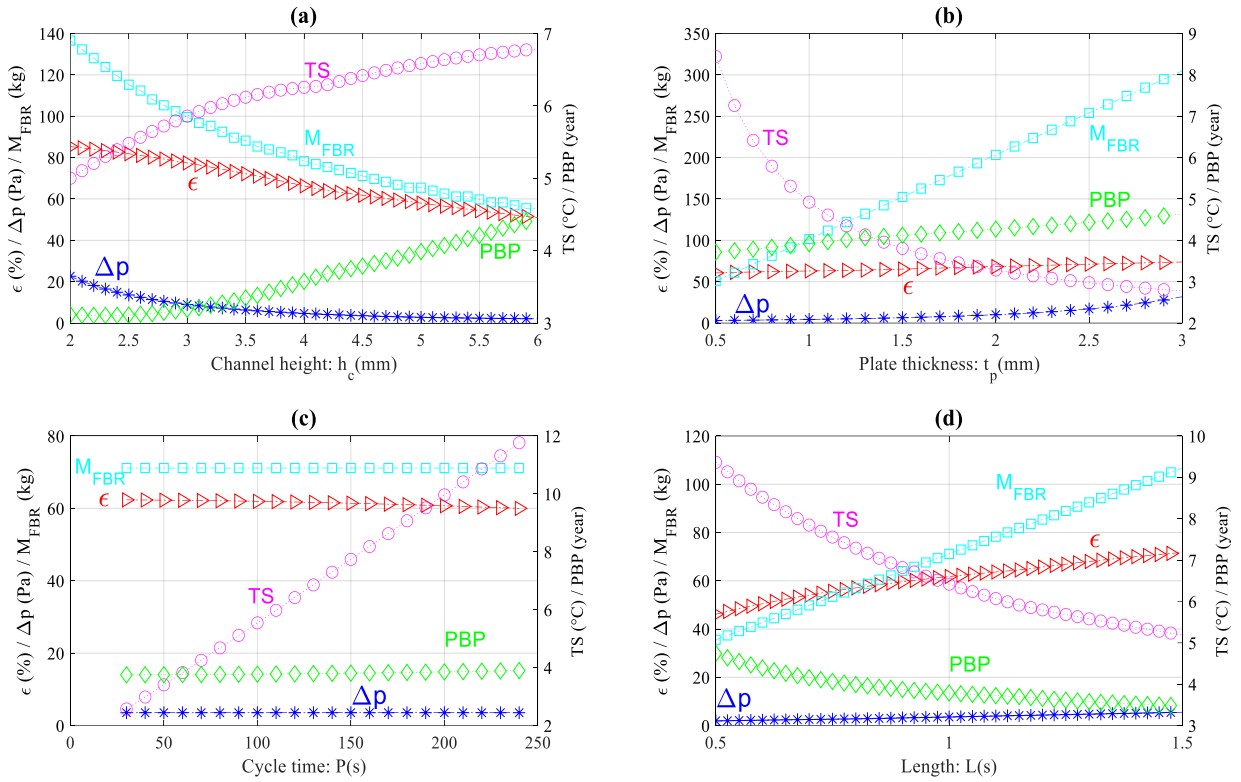

Figure 4.7. Variation of ε, Δp, M_{FBR} (left Y-axis) and PBP and TS (right Y-axis) with (a) h_c (b) t_p, (c) P, and (d) L.

4.6.2 **Optimization of FBRs with/without temperature swing (TS)**

In this section, four optimization problems are considered to span the related objectives (ε, Δp, M_{FBR}, and PBP) with and without TS, as shown in Eqns. (4.22) to (4.25). At first, optimization is performed without including TS as an objective to the problem; then, TS is added as an additional objective to the same problem to understand its impact on the Pareto fronts and selected optimized FBRs for scenarios in Table 4.8.

Table 4.9. The sensitivity of objective functions with an increase in the decision variables over their ranges of variation.

Obj.	decision variable	Objective function variation with an increase in decision variable and the reasons for this trend
ε	h_c	**decrease:** lower heat transfer coefficient (h) and thermal mass decrease NTU_o and Cr^* respectively; also, fewer plates decrease axial conduction (λ).
	t_p	**increase:** higher thermal mass increases Cr^*; also, λ increases.
	P_h	**decrease:** longer recovery period decreases Cr^*.
	L	**increase:** higher heat transfer surface area and thermal mass, increases NTU_o and Cr^*.
Δp	h_c	**decrease:** smaller channel velocity and surface area
	t_p	**increase:** higher channel velocity
	P_h	**no impact**
	L	**increase:** longer channel length
M_{FBR}	h_c	**decrease:** smaller number of channels
	t_p	**increase:** longer plate length
	P_h	**no impact**
	L	**increase:** higher length
TS	h_c	**increase:** smaller NTU_o, Cr^* and λ; combined impacts is an increased TS
	t_p	**decrease:** higher NTU_o, Cr^* and λ; combined impacts reduce TS
	P_h	**increase:** constant NTU_o and λ while decreasing Cr^* increase TS
	L	**decrease:** higher NTU_o, Cr^* and smaller λ; combined impacts reduce TS
PBP	h_c	**increase:** smaller Δp, M_{FBR} , and ε; combined impacts increase PBP
	t_p	**increase:** higher Δp, M_{FBR}, and ε; combined impacts increase PBP
	P_h	**increase:** constant Δp and M_{FBR} with smaller ε; combined impacts increase PBP
	L	**decrease:** higher Δp, M_{FBR} and ε; combined impacts reduce PBP

(1) First problem: effectiveness and pressure drop

$$Minimize\ f_k(x) = \min\left\{\frac{1}{\epsilon}, \Delta\text{p}\right\} \quad (4.22)\text{-a}$$

$$Minimize\ f_k(x) = \min\left\{\frac{1}{\epsilon}, \Delta\text{p}, \text{TS}\right\} \quad (4.22)\text{-b}$$

(2) Second problem: effectiveness and payback period

$$Minimize\ f_k(x) = \min\left\{\frac{1}{\epsilon}, \text{PBP}\right\} \quad (4.23)\text{-a}$$

$$Minimize\ f_k(x) = \min\left\{\frac{1}{\epsilon}, \text{PBP}, \text{TS}\right\} \quad (4.23)\text{-b}$$

(3) Third problem: effectiveness, payback period and pressure drop

$$Minimize\ f_k(x) = \min\left\{\frac{1}{\epsilon}, \text{PBP}, \Delta p\right\} \quad (4.24)\text{-a}$$

$$Minimize\ f_k(x) = \min\left\{\frac{1}{\epsilon}, \text{PBP}, \Delta p, \text{TS}\right\} \quad (24)\text{-b}$$

(4) Fourth problem: effectiveness, payback period, pressure drop and exchanger mass

$$Minimize\ f_k(x) = \min\left\{\frac{1}{\epsilon}, \text{PBP}, \Delta p, M_{FBR}\right\} \quad (4.25)\text{-a}$$

$$Minimize\ f_k(x) = \min\left\{\frac{1}{\epsilon}, \text{PBP}, \Delta p, M_{FBR}, \text{TS}\right\} \quad (4.25)\text{-b}$$

Eqns. (4.22-4.25) are solved under the constraints in Eqn. (4.26) and for the decision variables listed in Eqn. (4.27).

$$NTU_o and\ Cr^* \geq 1 \quad (4.26)$$

$$v_g = \{L, t_p, h_c, P_h (= P_c)\} \quad (4.27)$$

4.6.2.1 Maximum effectiveness, minimum pressure drop, and temperature swing

The first optimization problem in Eqn. (4.22) optimizes FBR considering effectiveness and pressure drop as objectives. Figure 4.8 (a)-(c) compare the Pareto fronts for optimization problems with and without TS as an additional objective. Figure 4.8 (d) represents the variation of exchanger

mass versus effectiveness for the alternative designs on the Pareto fronts. The results show that TS has no significant impact on the Pareto fronts solutions, except for several non-dominated points, which appear at low effectiveness and medium pressure drop region. These points are part of the Pareto fronts because of their small temperature swing values (and hence becoming non-dominated solutions). These points correspond to thicker plates (2.1mm).

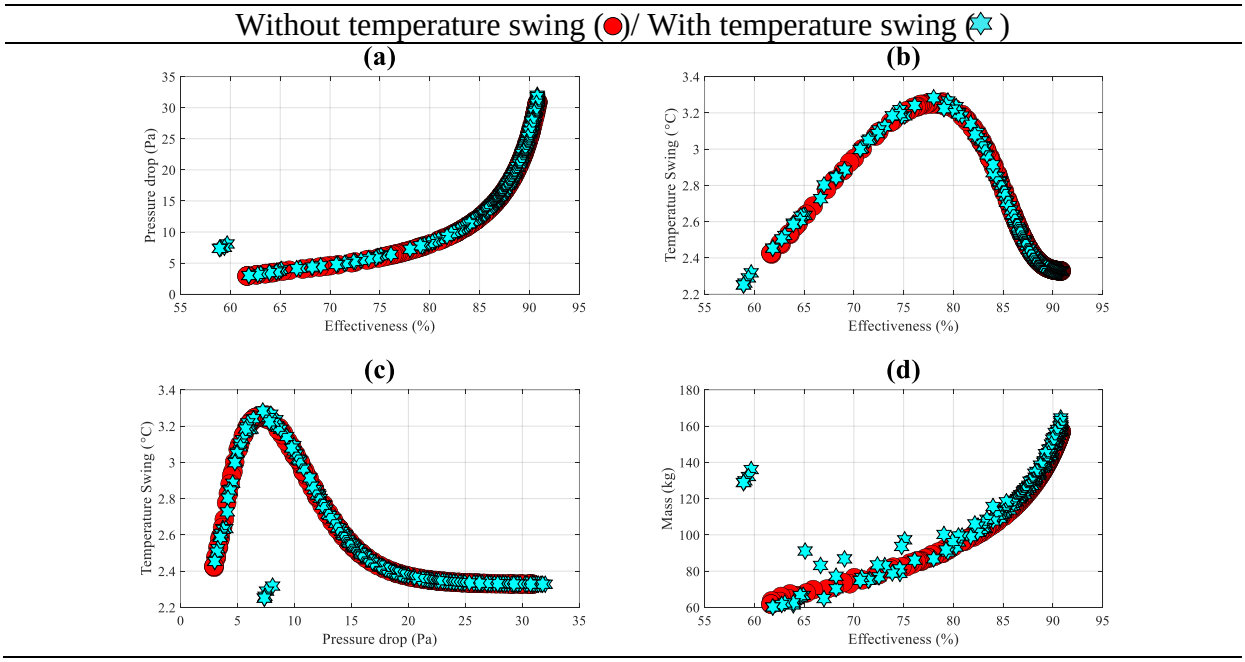

Figure 4.8. (a)-(c) Pareto fronts for the optimization problem in Eqn. (4.22) and (d) variation of exchangers mass on the Pareto fronts versus effectiveness.

Figure 4.9 (a-c) shows the variation of the decision variables with respect to effectiveness on the Pareto fronts in Fig. 4.8. At the lower effectiveness region for optimization with TS, the exchangers are shorter (around 0.6 m compared to the ones on the Pareto front without TS of L >1.3 m), channel height is about 3 mm (smaller channel height with TS), and the plate thickness is 2.1 mm (other exchangers on the Pareto fronts have thicknesses of about 0.5 mm). The recovery period is 30 seconds in all cases as it maximizes effectiveness over its range and has no impact on pressure drop.

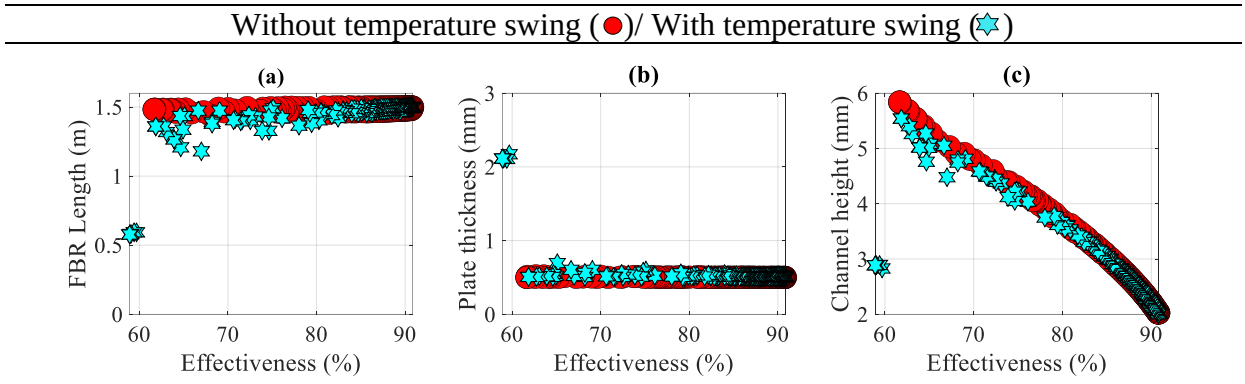

Figure 4.9. (a-c) Variation of the decision variables with effectiveness on the Pareto front for the optimization problem in Eqn. (4.22).

Table 4.10 presents selected exchangers for the different weight of objective (WO) scenarios presented in Table 4.8. The selected exchangers for all six scenarios have higher effectiveness, pressure drop, and smaller temperature swing values when compared to the base exchanger design. In all cases (except SC_6), the selected exchangers are 1.5 m long, with a 0.5 mm thick plate and a recovery period of P_h=30s; but the channel heights are different. In the first five scenarios, when TS is added to the optimization problem, the selected exchangers have a smaller channel height to accommodate more plates in the FBR (higher Cr^* and NTU_o), while all other design parameters remain unchanged. The selected FBRs have a higher effectiveness ($\varepsilon\approx88\%$) and pressure drop values with a smaller temperature swing (TS<2.5 °C) when TS is included. For the last weight of objective scenario (SC_6) where TS is twice as important as effectiveness and pressure drop, the selected FBR has a length of 0.58 m with a plate thickness of 2.1 mm. The exchanger mass increases from 102 kg to 129 kg to have 0.7 °C temperature swing reduction. This point belongs to the set of new points in the low effectiveness region in Fig. 4.8 (a) for the optimization problem with TS. For SC_6, the selected optimized exchanger has a smaller pressure drop (7.4 Pa) and effectiveness (58.9%).

Table 4.10. Decision variables and objective values corresponding with the selected FBRs for different objective weightage scenarios for the optimization problem in Eqn. (4.22) (WO/TS: without TS and W/TS: with TS).

Parameter	EX_{base}	SC_1		SC_2		SC_3		SC_4		SC_5		SC_6	
		WO/TS	**W/TS**	**WO/TS**	**WTS**	**WO/TS**	**W/TS**	**WO/TS**	**W/TS**	**WO/TS**	**W/TS**	**WO/TS**	**W/TS**
L (m)	1	1.50	1.50	1.50	1.50	1.50	1.50	1.50	1.50	1.50	1.50	1.50	0.58
t_p(mm)	0.7	0.50	0.50	0.50	0.51	0.50	0.50	0.50	0.50	0.50	0.50	0.50	2.1
P_h(s)	120	30	30	30	30	30	30	30	30	30	30	30	30
h_c(mm)	4.0	3.4	2.6	3.0	2.5	3.1	2.6	2.7	2.4	3.4	2.6	3.4	2.9
M_{FBR} (kg)	69.7	102	130	114	134	109	130	122	139	102	130	102	129
ε_s (%)	61.0	82.8	88.2	85.7	88.4	84.7	88.2	87.1	89.3	82.8	88.2	82.8	58.9
Δp (Pa)	3.4	10.0	18.5	13.3	19.2	11.9	18.5	15.7	22.1	10.0	18.5	10.0	7.4
PBP (year)	3.8	3.0	3.0	3.0	3.0	3.0	3.0	3.0	3.0	3.0	3.0	3.0	4.4
TS(°C)	6.9	3.0	2.4	2.7	2.4	2.8	2.4	2.5	2.3	3.0	2.4	3.0	2.3

It can be concluded from the selected values in Table 4.10 that the improvement of TS values for all scenarios is less than 1°C when TS is included in the optimization problem. Simultaneously, there are considerable penalties for the exchanger mass (≈17-30 kg heavier) and pressure drop (≈ 2-10 Pa more pressure drops except for SC_6).

FBR flow rate exchanger was considered to be constant in the optimization problems (constant face velocity). The optimization problem was solved at 80% and 120% of the original face velocity to investigate the impact of flow rate on the optimization problem. The Pareto fronts (effectiveness versus pressure drop) at different face velocities are presented in Fig. 4.10. The shape of Pareto fronts for the problems with and without TS at different face velocities are similar. The MCDA procedure for different weight of objective (WO) scenarios presented in Table 4.8 are repeated, and it was found that the improvements in temperature swing (when TS is added the optimization problems) are negligible. At the same time, penalties for pressure drop and exchanger mass are considerable.

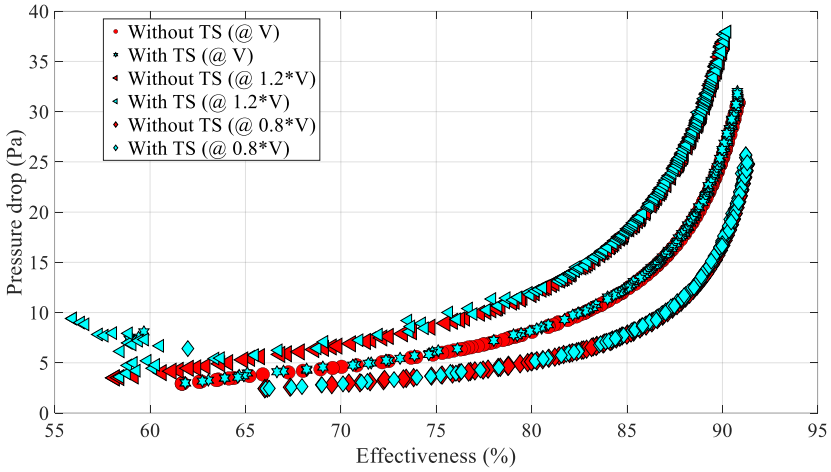

Figure 4.10. Pareto fronts for the optimization problem in Eqn. (4.22) at three different face velocities of V, 0.8V and 1.2V with and without TS.

4.6.2.2 Maximum effectiveness, minimum payback period, and temperature swing

Figure 4.11 (a)-(c) represents Pareto fronts for optimizing FBRs as in Eqn. (4.23) (effectiveness and payback period as objectives) with/without considering TS as an objective for optimization. When TS is considered as an objective in the optimization problem, several non-dominated solutions (at smaller effectiveness) appear on the Pareto fronts which have small temperature swing values (Fig. 4.11 (b)) and higher payback periods (Fig. 4.11 (c)). The smaller TS values are obtained with shorter exchanger length, thicker plate thickness, and increased channel heights. The small TS values make these points non-dominated by other points and appear on the Pareto fronts.

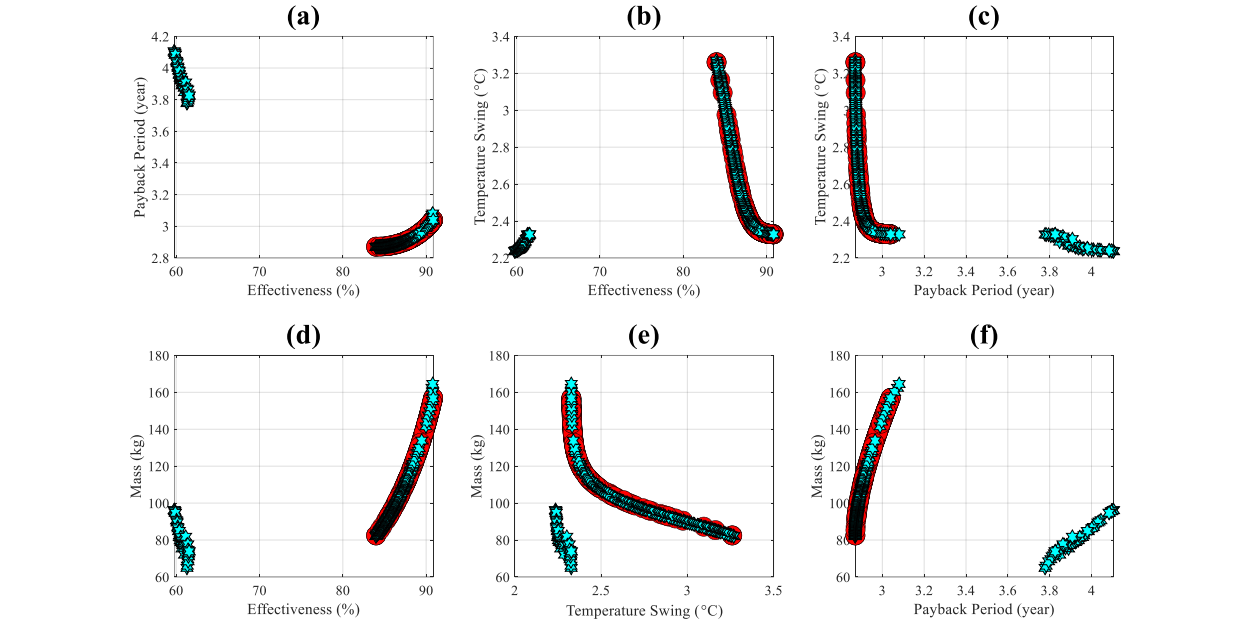

Figure 4.11. (a)-(c) Pareto fronts for the optimization problem in Eqn. (4.23) and (d)-(f) exchanger mass versus effectiveness, temperature swing, and payback period for the Pareto fronts.

The exchanger properties correspond with the six decision-making scenarios (as in Table 4.8) are presented in Table 4.11. All selected exchangers (with and without TS) have a plate thickness of 0.5 mm and a recovery period of 30 seconds. When TS is considered as an objective in optimizing FBR, longer exchangers are to be selected. The selected exchangers are less than 1 m long for optimization without TS and > 1.15 m long with TS. Effectiveness increases for longer exchanger and TS decreases, while the payback period remains almost constant. Heavier exchangers (M_{FBR}) are selected to minimize the temperature swing. The simultaneous increase in effectiveness, pressure drop, and exchanger mass cancels out the payback period changes. Higher pressure drop and exchanger mass are the downsides of the optimized FBRs considering TS as an objective, while higher effectiveness contributes to the fact that payback periods remain unchanged. Unlike the previous optimization problem (in section 4.6.2.1), the additional design points on the Pareto fronts for optimization with TS are not selected for any decision-making

scenarios, even for the SC_6, where temperature swing is prioritized over other objectives. For these points, effectiveness values are small, and the payback periods are long, which both are unfavourable for FBR design.

Table 4.11. Decision variables and objective values corresponding with the selected FBRs for different objective weightage scenarios for the optimization problem in Eqn. (4.23) (WO/TS: without TS and W/TS: with TS).

Parameter	EX_{base}	SC_1		SC_2		SC_3		SC_4		SC_5		SC_6	
		WO/TS	W/TS	WO/TS	WTS	WO/TS	W/TS	WO/TS	W/TS	WO/TS	W/TS	WO/TS	W/TS
L (m)	1	0.82	1.15	0.86	1.17	0.83	1.17	0.92	1.27	0.86	1.27	0.82	1.27
t_p(mm)	0.7	0.50	0.50	0.50	0.50	0.50	0.50	0.50	0.50	0.50	0.50	0.50	0.50
P_h(s)	120	30	30	30	30	30	30	30	30	30	30	30	30
h_c(mm)	4.0	2.02	2.02	2.02	2.02	2.02	2.02	2.02	2.00	2.02	2.00	2.02	2.00
M_{FBR} (kg)	69.7	85	120	90	122	87	122	96	134	90	134	85	134
ε_s(%)	61.0	84.4	88.4	85.2	88.6	84.7	88.6	85.9	89.5	85.2	89.5	84.4	89.5
Δp(Pa)	3.4	16.6	23.6	17.6	24.0	17.0	24.0	18.7	26.7	17.6	26.7	16.6	26.7
PBP (year)	3.8	2.9	2.9	2.9	2.9	2.9	2.9	2.9	3.0	2.9	3.0	2.9	3.0
TS(°C)	6.9	3.2	2.4	3.0	2.4	3.1	2.4	2.8	2.3	3.0	2.3	3.2	2.3

Again, in this problem, optimization of FBR including TS as an additional objective leads to less than 1ºC improvement in TS. While pressure drop values are increased about 35-60%, and exchanger mass values have increased about 30-60%. Also, improvement in effectiveness is less than 5%.

The FBR flow rate was changed to 80% and 120% compared to the original flow rate to study the impact of flow rate on the results, and it was observed that this does not change the main conclusions of insignificance improvement of TS and considerable penalties for mass and pressure drop in the optimization problem considering TS as an objective.

4.6.2.3 Maximum effectiveness, minimum payback period, pressure drop, and temperature swing

Figure 4.12 (a-e) shows the Pareto fronts for the optimization problem in Eqn. (4.24). Adding TS to the optimization problem, the non-dominated solutions at higher effectiveness and

pressure drop (Fig. 4.12 (a-c)) do not change—like the previous problems. However, at medium to low pressure drop and effectiveness ranges (ε<85% and Δp<20 Pa), the non-dominated solutions are appeared on the Pareto fronts by changing the exchanger mass to reduce TS (Fig. 4.13 (a-d)). Unlike the two previous optimization problems, the Pareto fronts for optimization with TS have more different non-dominate solution points because more objectives need to be optimized simultaneously. The region is also broader to include medium values of effectiveness and pressure drop, as shown in Fig. 4.13 (a-d).

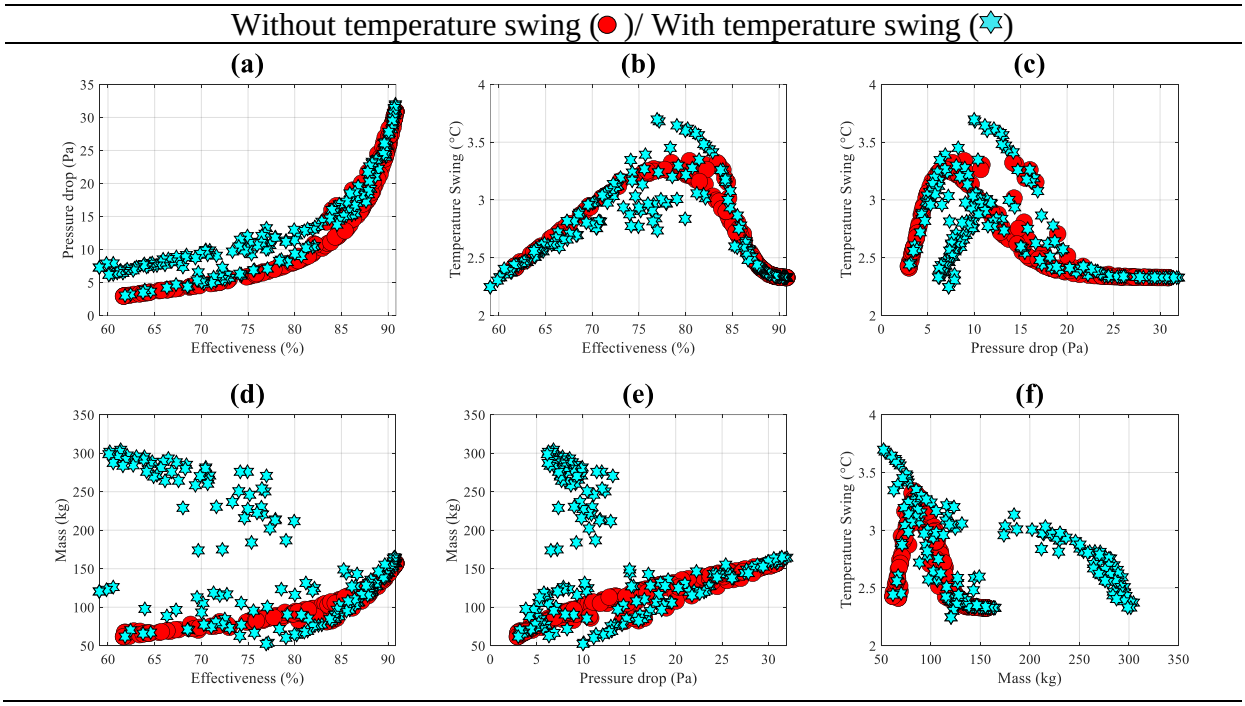

Figure 4.12. Comparison of Pareto fronts for the optimization problem in Eqn. (4.24) with (hexagonal)/without (circles) temperature swing.

Table 4.12 presents the optimized FBRs for different decision-making scenarios considered in Table 4.8. From Eqn. (4.11) (or Fig. 4.4 (b)), the exchangers Cr^*need to be increased to achieve a lower TS. Higher Cr^* is obtained by increasing the exchanger length (higher exchanger mass); this would increase NTU_o and effectiveness, with a penalty of higher pressure drop and exchanger mass. With TS as an objective in the optimization problem, the optimized FBRs will be

heavier (longer) with higher effectiveness, pressure drop, payback period, and smaller TS. The improvement from optimizing TS is insignificant (less than 1ºC), while the penalties are about 35-60% and 10-50% increases in exchanger mass and pressure drop, respectively. Effectiveness enhancement is less than 5%.

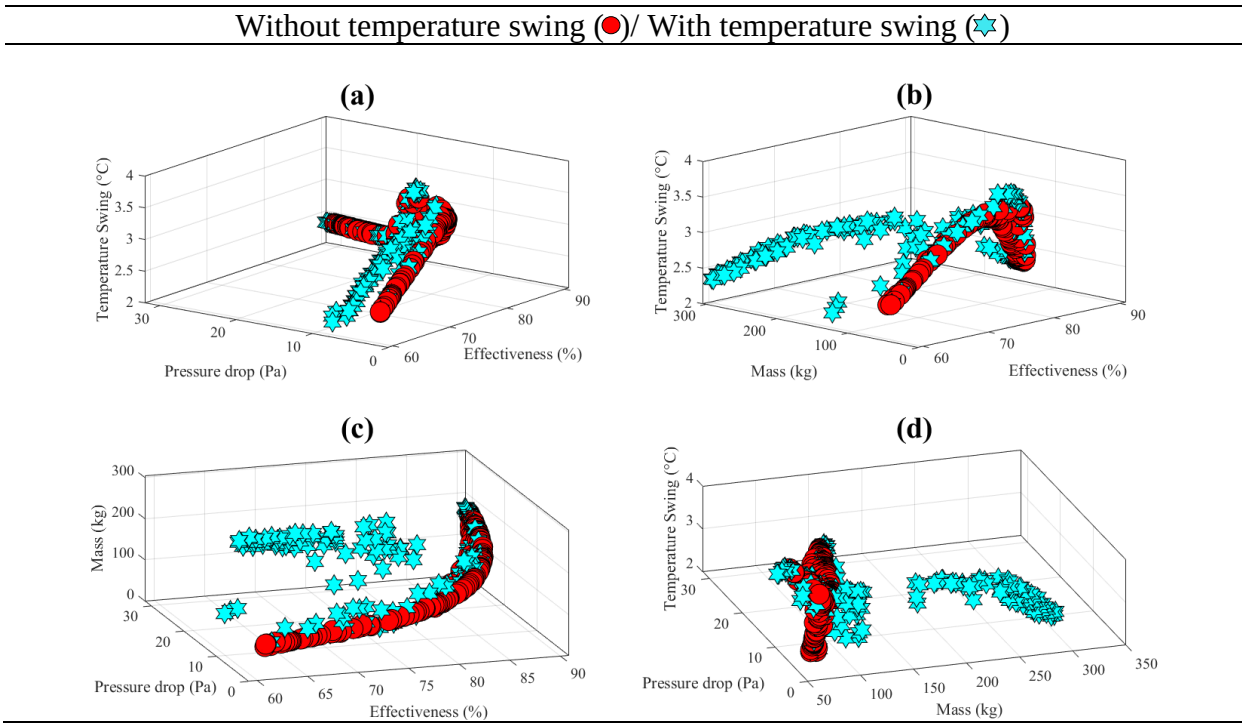

Figure 4.13. Comparison of Pareto fronts for optimization of FBRs in Eqn. (4.24) with (hexagonal)/without (circles) temperature swing.

Table 4.12. Decision variables and objective values corresponding with the selected FBRs for different objective weightage scenarios for the optimization problem in Eqn. (4.24) (WO/TS: without TS and W/TS: with TS).

Parameter	EX $_{base}$	SC_1		SC_2		SC_3		SC_4		SC_5		SC_6	
		WO/TS	**W/TS**	**WO/TS**	**WTS**	**WO/TS**	**W/TS**	**WO/TS**	**W/TS**	**WO/TS**	**W/TS**	**WO/TS**	**W/TS**
L (m)	1	0.79	1.48	0.79	1.48	0.79	1.48	0.96	1.38	1.00	1.48	0.79	1.38
t_p(mm)	0.7	0.50	0.51	0.50	0.51	0.50	0.51	0.50	0.51	0.51	0.51	0.50	0.51
P_h(s)	120	30	30	30	30	30	30	30	30	30	30	30	30
h_c (mm)	4.0	2.02	2.62	2.02	2.62	2.02	2.62	2.15	2.32	2.59	2.62	2.02	2.32
M_{FBR} (kg)	69.7	83	128	83	128	83	128	96	130	87	128	83	130
ε_s (%)	61.0	84.0	87.6	84.0	87.6	84.0	87.6	85.6	88.6	82.8	87.6	84.0	88.6
Δp (Pa)	3.4	16.0	17.3	16.0	17.3	16.0	17.3	17.1	21.0	11.8	17.3	16.0	21.0
PBP (year)	3.8	2.9	3.0	2.9	3.0	2.9	3.0	2.9	3.0	2.9	3.0	2.9	3.0
TS(°C)	6.9	3.3	2.4	3.3	2.4	3.3	2.4	2.8	2.4	3.3	2.4	3.3	2.4

Changing FBR flow rate to 80% and 120% of its original values does not change the main conclusions of insignificance improvement of TS and considerable penalties for mass and pressure drop in this optimization problem.

4.6.2.4 Maximum effectiveness, minimum payback period, pressure drop, and temperature swing

In this section, the optimization problem presented in Eqn. (4.25) is considered. The Pareto fronts with and without including TS as an objective to the problem are obtained. The decision variables and objective values corresponding with different decision-making scenarios in Table 8 are also obtained. The conclusions for this problem are like the optimization problem in section 4.6.2.3. Figure 4.14 shows the Pareto fronts for this optimization problem and Table 4.13 presents the selected optimized exchangers for the six decision-making scenarios in Table 4.8. When TS is included in the optimization problem, the selected exchangers will have smaller TS values. The improvement is less than 1^{o}C, like the previous problems. The penalties for exchanger mass and pressure drop increases are between 50-65% and 12-52%, respectively. The payback period values are increased by less than 0.1 year, while effectiveness improvement is less than 6%.

By changing the airflow of FBR to 80% and 120% of the original flow rate, the main conclusions of negligible reduction in TS and considerable penalties for mass and pressure drop were observed for the optimization problem in this section.

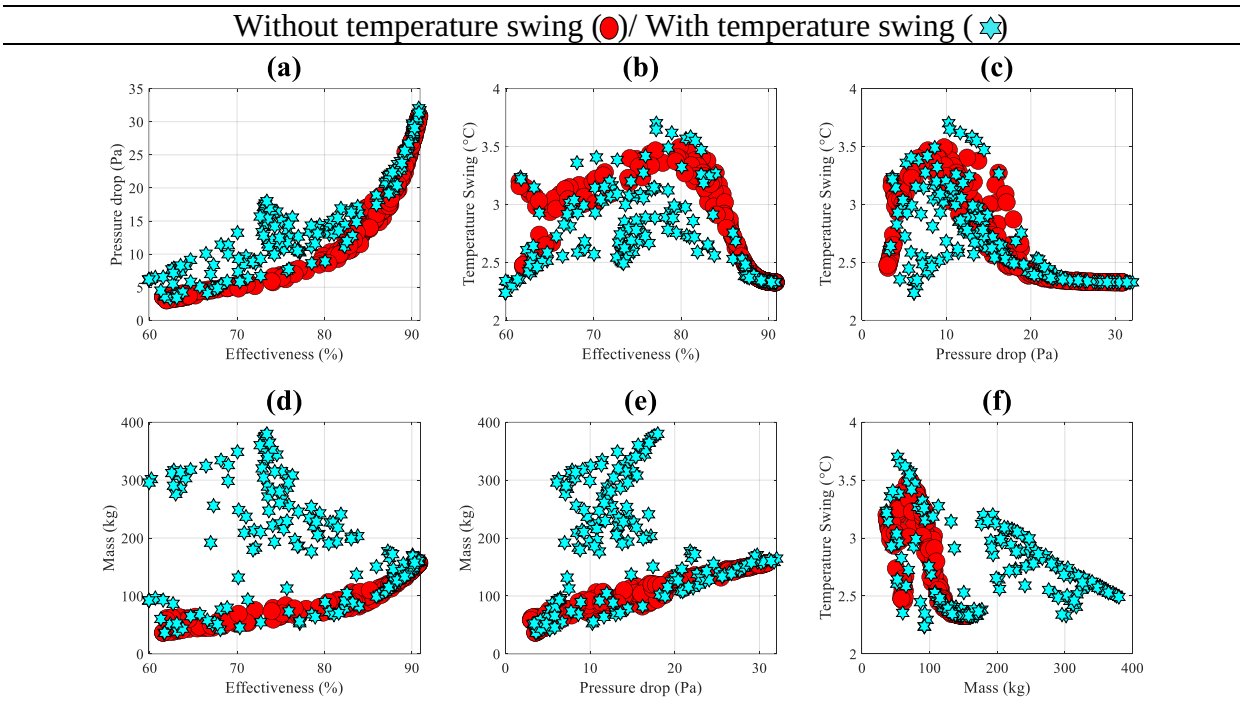

Figure 4.14. Comparison of Pareto fronts for the optimization of FBRs in Eqn. (4.25) with (hexagonal)/without (circles) temperature swing.

Table 4.13. Decision variables and objective values corresponding with the selected FBRs for different objective weightage scenarios for the optimization problem in Eqn. (4.25) (WO/TS: without TS and WTS: with TS).

Parameter	EX $_{base}$	SC_1		SC_2		SC_3		SC_4		SC_5		SC_6	
		WO/TS	**W/TS**	**WO/TS**	**WTS**	**WO/TS**	**W/TS**	**WO/TS**	**W/TS**	**WO/TS**	**W/TS**	**WO/TS**	**W/TS**
L (m)	1	0.76	1.22	0.78	1.22	0.76	1.22	0.80	1.31	0.83	1.48	0.76	1.31
t_p (mm)	0.7	0.50	0.53	0.50	0.53	0.50	0.53	0.50	0.50	0.51	0.56	0.50	0.50
P_h(s)	120	30	30	30	30	30	30	30	30	30	30	30	30
h_c (mm)	4.0	2.07	2.24	2.00	2.24	2.07	2.24	2.00	2.21	2.26	2.81	2.07	2.21
M_{FBR} (kg)	69.7	79	123	82	123	79	123	84	129	81	130	79	129
ε_s (%)	61.0	83.2	87.7	84.0	87.7	83.2	87.7	84.3	88.8	82.9	86.2	83.2	88.8
Δp (Pa)	3.4	14.7	20.3	16.2	20.3	14.7	20.3	16.6	22.3	13.3	14.9	14.7	22.3
PBP (year)	3.8	2.9	3.0	2.9	3.0	2.9	3.0	2.9	3.0	2.9	3.0	2.9	3.0
TS(°C)	6.9	3.4	2.4	3.3	2.4	3.4	2.4	3.2	2.4	3.4	2.6	3.4	2.4

4.7 SUMMARY AND CONCLUSIONS

The temperature of the airstreams at the outlet of FBR varies with time, even at the quasi-steady-state condition. When designing FBR, it is essential that every physical parameter and recovery period is carefully considered to prevent large variations in outlet temperature (temperature swing: TS) of airstreams, which might deteriorate occupant thermal comfort and put a variable load on the HVAC system. A large TS is undesirable and has not been investigated for FBRs and not included in the optimization of FBRs so far. In this chapter, the results of the validated numerical model were used to develop a correlation for TS as a function of design parameters (NTU_o, Cr^* and C_λ). From the developed correlation, it was found that temperature swing decreases with an increase in Cr^* or C_λ and increases when NTU_o is increased.

Optimization of FBRs is performed with and without TS as an objective. A decision-making process, LINMAP, is integrated into the optimization problem to select exchangers from the Pareto fronts. The addition of TS to the optimization problems does not change the Pareto fronts at higher values of effectiveness and pressure drop whereas it changes the Pareto fronts in the low to medium ranges of effectiveness and pressure drop. At these ranges, the exchanger mass is increased to reduce the temperature swing. When TS is included in the decision-making process, a heavier exchanger is chosen to achieve a smaller temperature swing. The reduction of TS is less than 1ºC compared to optimization without considering TS, while the penalties for pressure drop and exchanger mass are between 30-60%. This means that the addition of TS to the optimization problems would not decrease TS significantly while penalties for exchanger mass and pressure drop are considerable. The simulations have been repeated at different flow rates, and the main conclusion of the insignificant reduction of TS at the expense of higher exchanger mass and pressure drop continues to be valid.

The third objective of this thesis, (to optimize sensible FBRs considering transient characteristics), hence, was addressed and documented in this chapter. The HVAC manufacturers and equipment designers could use the TS correlation proposed in this chapter to limit the TS in their design. Although this chapter focus is on HVAC systems, the presented results and correlation for TS could be useful for other industries that use FBR for heat recovery.

In the next chapter, a transient numerical model will be presented to predict the transient characteristics of desiccant-coated FBRs and sensors and to accurately evaluate their performance. Measurement recommendations in the test standards will be analysed and recommendations will be provided for accurate evaluation of performance.

CHAPTER 5

A TRANSIENT NUMERCIAL MODEL FOR DESICCANT COATED FIXED-BED REGENERATORS

5.1 OVERVIEW

This chapter documents the developed transient numerical model for desiccant-coated FBRs, which is the final objective of this PhD thesis. The model consists of an FBR model and sensor models (temperature and humidity). The numerical model, solution procedure, and validation are explained in detail. FBRs with two different outlet air properties profiles are identified and analysed using the developed numerical model. Measurement recommendations are provided for FBRs with both profiles.

This chapter was submitted as a research paper to *Science and Technology for the Built Environment* journal in August 2021 (the paper was accepted in December 7, 2021). To avoid repetition, part of the experimental test facility description of the paper is modified, and proper reference is provided to the previous chapters. The author of this thesis (Hadi Ramin) developed the numerical model and prepared the original draft of the paper. Mr. Krishnan (PhD student) conducted the experiments for validation and wrote the experimental section. Dr. Annadurai (Postdoctoral fellow) and Prof. Simonson (Supervisor) contributed to this paper by critically reviewing the paper.

A transient numerical model for desiccant-coated fixed-bed regenerators

(Submitted to Science and Technology for the Built Environment, August 2021)

Hadi Ramin, Easwaran N Krishnan, A. Gurubalan and Carey J Simonson

5.2 ABSTRACT

Desiccant-coated fixed-bed regenerators (FBRs) can achieve high effectivenesses due to a high ratio of energy transfer area to volume and, therefore, are favourable air-to-air energy exchangers (AAEEs) for HVAC systems. However, unlike other types of AAEEs, the air properties (i.e., temperature and humidity) at the outlet of FBRs vary with time. The variations in outlet airflow properties can cause errors in measurements because the measurements include the transient responses of both the FBR and the sensors. In this chapter, a numerical model is developed to evaluate the performance of desiccant-coated FBRs and their transient operation. The model comprises of a model of the exchanger (FBR model) and models of temperature and humidity sensors (sensor model) to distinguish the actual performance of the FBR alone from the measured performance which includes both the FBR and the sensors response. The model is validated with experimental measurements and available results in the literature. The model can decouple the measured response of the FBR and sensors to predict the FBR performance (and effectiveness errors because of the response of sensors). The effectiveness error can be as high as 70% in some design and operating conditions. This chapter's main contribution is that it provides an insight into the complex heat and mass transfer processes in desiccant-coated FBRs and measurement sensors. The results of this chapter could be used to provide practical recommendations for humidity measurements of different types of desiccant-coated FBRs

developed for HVAC applications. Furthermore, the measurement requirements in the current North American testing standards (ASHRAE 84 and CSA C439-18 standards) for FBRs are examined. Recommendations from this chapter could be implemented in future versions of these standards.

5.3 INTRODUCTION

Air-to-air-energy exchangers (AAEEs) are widely used in HVAC applications because they increase the energy efficiency of HVAC systems by transferring energy/heat between the exhaust airstream (leaving from buildings) and the outdoor fresh supply airstream entering buildings to precondition the supply air. Different types of AAEEs are available in the market, including fixed-plate exchangers, heat pipes, energy/heat wheels, fixed-bed regenerators (FBRs), and run-around membrane exchangers [90–94]. Among these AAEEs, FBRs are gaining more interest nowadays for energy recovery in HVAC applications [11–13,16,32,95], due to their high ratio of energy transfer area to volume which leads to a high effectiveness. In the literature, they are widely referred to as single-core regenerators, double-core regenerators [22], room-based ventilators [16,51], reversing-flow regenerators [22], and exchangers with a periodic change in the flow direction [12,52,53].

Heat and moisture exchange occurs between the supply and exhaust airstreams that alternately flow through the core matrix/s (bed/s) of desiccant-coated FBRs. FBRs are cyclic devices, and each cycle of their operation consists of a hot and humid period and a cold and dry period. Since FBRs operate by storing and releasing heat and moisture, the air properties (i.e., temperature and humidity) at the outlet of FBRs continuously change with time. The air properties never reach a steady-state condition; instead, they change in a quasi-steady-state periodic pattern. That is the outlet properties (temperature and humidity) of airstreams in FBRs vary with time but

cyclically repeat themselves [20,33]. Figure 5.1 shows a single-core FBR and its inlet/outlet air temperature/humidity profile for a complete cycle of operation. The variations in the outlet air properties pose challenges for accurate measurement and, consequently, the prediction of latent and sensible effectiveness of desiccant-coated FBRs. These challenges are due to both the transient nature of the air properties at the outlet of the FBR and the transient characteristics of sensors. Thus, the measured air properties from sensors during experiments would be different from the actual air properties [20,21,50].

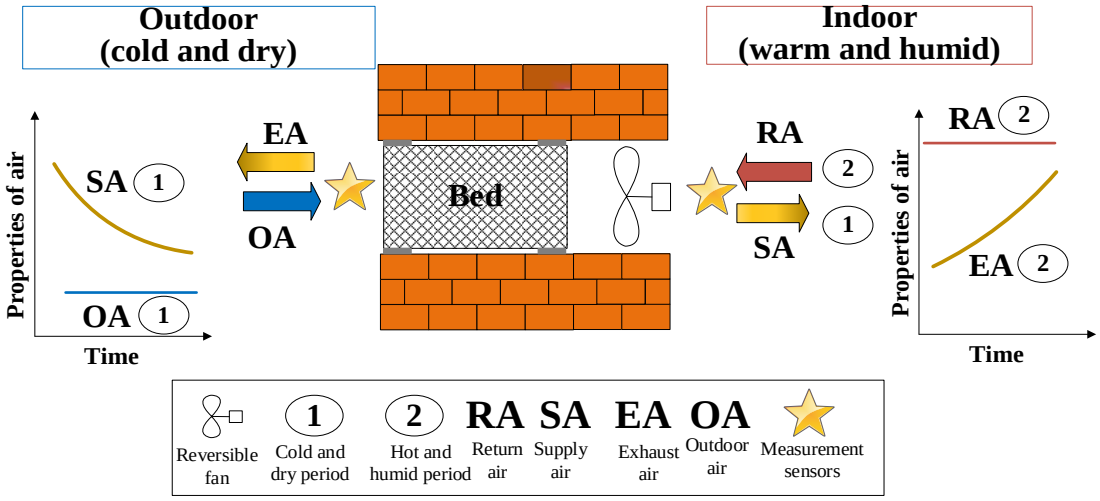

Figure 5.1. A schematic of single-core FBR and the variation of air properties during discharge and regeneration periods for winter climatic conditions.

Besides the variation of properties during each period, the sensors' conditions in the previous period (which is the initial conditions for the subsequent period) affect the sensor's measurements in the subsequent period. For example, Fig. 5.1 shows that the sensor located indoor measuring the outlet air properties during the cold and dry period was previously exposed to the hot and humid indoor air conditions (initial conditions of sensor). Therefore, both the sensor's initial condition and the variation of airflow properties during each period are critical in obtaining

the effect of sensor transient characteristics in the measurement of air properties at the outlet of FBRs [33,54–56].

The transient characteristics of FBRs and sensors and their impacts on effectiveness measurements of sensible FBRs are documented in the literature. A transient numerical model [50] was developed to evaluate the impacts of transient characteristics of sensible FBRs and sensors on the performance evaluation (Chapter 2). The model was validated with experimental measurements from a small-scale test facility [20]. In addition, the temperature sensor requirements for accurate evaluation of effectiveness are recommended (Chapter 3) [28,33]. However, the effects of transient characteristics of desiccant-coated FBRs and sensors on the measurement requirements is not yet studied in the literature. Hence, this study aims to fill this research gap in the literature. This study is essential for the accurate evaluation of desiccant-coated FBR's performance. The coupled heat and mass transfer process of desiccant-coated FBRs and temperature-dependent humidity measurement techniques would make their transient characteristics much more complicated compared to sensible FBRs and temperature sensors. Therefore, this chapter provides insights into the coupled response of desiccant-coated FBRs and humidity sensors.

The measurement requirements for testing FBRs have been recently included in ASHRAE standard 84 [21] and an affirmative appendix in CSA C439-18 standard [22]. These standards require at least 30 measurements per recovery period (for recovery period of 60 seconds) with sensors that have response times shorter than the sampling rate. The standards recommendations for temperature measurement are previously investigated and reported in literature [28,32,33]. According to these studies [28,33], the requirements for accurate sensible effectiveness measurements depend on FBR configurations and design conditions (NTU, Cr^*, and λ).

Furthermore, it was concluded that temperature sensor requirements in these standards are rigorous and could be relaxed depending on the test configurations and operating conditions. Properties measurement requirements, however, for combined heat and moisture transfer for the desiccant-coated FBRs have not been studied in the literature and this chapter examines these measurement requirements.

Overall, in this chapter, a transient numerical model is presented and validated for heat and moisture transfer in desiccant-coated FBRs and sensors. The model is then used to provide insights into the complex process of heat and moisture transfer in FBRs and humidity sensor measurements and provide guidance for the test standards when measuring the transient outlet properties of desiccant-coated FBRs.

5.4 FBR CONFIGURATIONS AND OUTLET PROPERTY PROFILES

The outlet property profiles of airstreams (temperature and humidity) depend on the FBRs configurations and location of sensors. According to the number of exchangers, there are two FBRs types, namely single-core and double-core FBRs. Generally, it can be concluded that the measurement sensors are exposed to either a positive/negative sawtooth or semi-sawtooth profile depending on the configuration of FBRs. The sawtooth profile consists of positive or negative (depends on the direction of energy transfer from the airstream to the exchanger or from the exchanger to the airstream) ramps, while the semi-sawtooth profile has a horizontal part before a positive or negative ramp. This flattened part (horizontal part) of the semi-sawtooth profile represents the initial condition of the sensors before they are exposed to the FBR outlet airstream. In other words, the sensors in FBR with a semi-sawtooth profile are exposed to the inlet conditions followed by the outlet conditions, while FBR with a sawtooth profile are always exposed to the outlet conditions. Table 5.1 presents the various FBR configurations in the literature and test

standards along with their outlet air property profiles (sawtooth or semi-sawtooth profile). According to Table 5.1, the sensors at the outlet of double-core exchangers in the CSA C439-18 standard [22] and ASHRAE standard 84 [21] experience a periodic positive sawtooth profile for the hot and humid period and a periodic negative sawtooth profile for the cold and dry period. Also, for the double-core exchanger developed by Tempeff [17], the supply side sensors are exposed to a sawtooth profile while those on the exhaust side experience a semi-sawtooth profile. For the single-core exchanger or room-based energy recovery exchanger (ventilator) [13], as shown in Table 5.1, the sensors at the FBR supply and exhaust sides are exposed to a semi-sawtooth profile that is labelled exchanger sensor in Table 5.1.

A small-scale test facility was developed by Krishnan et al. [20] at the University of Saskatchewan to evaluate the performance of FBRs; a schematic of the test section in the small-scale test facility is presented in Table 5.1. The exchanger in the test section is moved between two airflow ducts to replicate the alternating nature of FBRs. To measure the air properties at the outlet of the exchanger, a set of measurement sensors are attached to the exchangers (called exchanger sensors that move with the exchanger), and another set is fixed to the airflow ducts (called duct sensors), as shown in the Table. The duct and exchanger sensors are exposed to different airstream profiles as they have different initial conditions, but both are exposed to semi-sawtooth profiles.

From the above discussions and Table 5.1, it can be concluded that three sensors configurations could be considered for desiccant-coated FBRs: (1) sensors exposed to sawtooth profile, (2) exchanger sensors, and (3) duct sensors. The latter two sensors are exposed to semi-sawtooth profiles.

Table 5.1. Different configurations of FBRs and their corresponding outlet air property profiles (temperature and humidity profiles).

<table>
<tr><th colspan="2"></th><th colspan="2">Sawtooth properties profile</th><th colspan="2">Semi-sawtooth properties profile</th></tr>
<tr><td colspan="2"></td><td>Hot & humid outlet</td><td>Cold & dry outlet</td><td>Hot & humid outlet</td><td>Cold & dry outlet</td></tr>
<tr><td rowspan="2">Profile shape</td><td>(a) Exchanger</td><td> 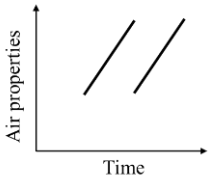
</td><td> 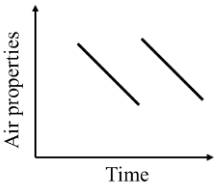
</td><td> 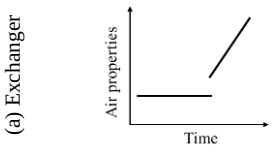
</td><td> 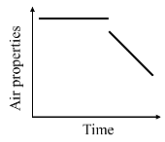
</td></tr>
<tr><td>(b) Duct sensor</td><td></td><td></td><td> 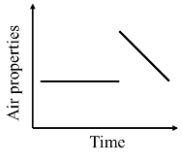
</td><td> 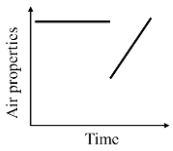
</td></tr>
<tr><td colspan="2"></td><td colspan="2">Examples in literature</td><td colspan="2">Examples in literature</td></tr>
<tr><td colspan="2"></td><td colspan="2"> 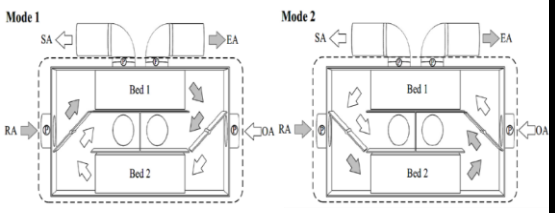

Ref: ASHRAE standard 84 [21]</td><td colspan="2"> 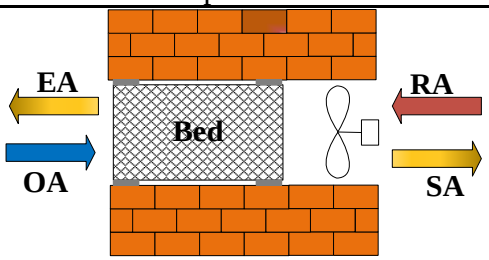

Ref: Room-based ventilation [16]</td></tr>
<tr><td colspan="2"></td><td colspan="2"> 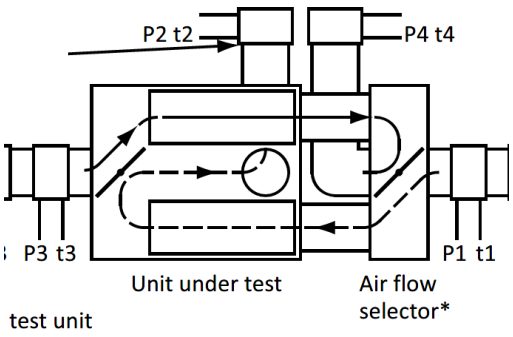

Ref: CSA C439-18 standard [22]</td><td colspan="2"> 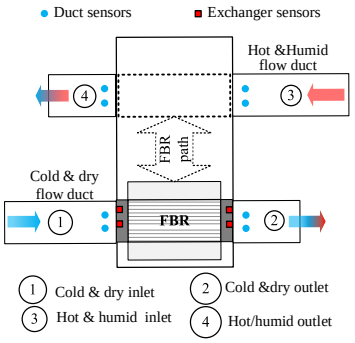

Ref: Small-scale test facility [20]</td></tr>
<tr><td colspan="6"> 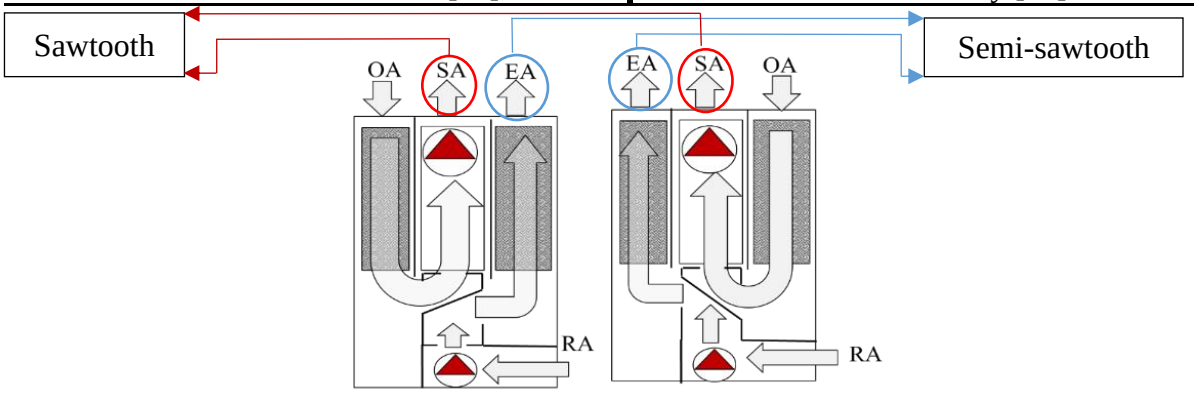

Ref: Double-core FBRs manufactured by Tempeff [17]</td></tr>
</table>

5.5 PERFORMANCE PARAMETERS

The performance of an FBR is quantified using effectiveness [21,22], and the sensible, latent (or moisture), and total (or enthalpy) effectiveness are represented by Eqns. (5.1), (5.2) and (5.3) respectively for both the hot and humid and cold and dry periods.

Sensible effectiveness

$$\varepsilon_{sh} = \frac{\dot{m}_h Cp_g\left(\overline{T}_{h,o} - T_{h,i}\right)}{\min(C_h, C_c)\left(T_{h,i} - T_{c,i}\right)} \qquad (5.1)$$

$$\varepsilon_{sc} = \frac{\dot{m}_c Cp_g\left(\overline{T}_{c,o} - T_{c,i}\right)}{\min(C_h, C_c)\left(T_{h,i} - T_{c,i}\right)}$$

Latent effectiveness

$$\varepsilon_{lh} = \frac{\dot{m}_h\left(W_{h,i} - \overline{W}_{h,o}\right)}{\min(\dot{m}_h, \dot{m}_c)\left(W_{h,i} - W_{c,i}\right)} \qquad (5.2)$$

$$\varepsilon_{lc} = \frac{\dot{m}_h\left(\overline{W}_{c,o} - W_{c,i}\right)}{\min(\dot{m}_h, \dot{m}_c)\left(W_{h,i} - W_{c,i}\right)}$$

Total effectiveness

$$\varepsilon_{th} = \frac{\dot{m}_h\left(H_{h,i} - \overline{H}_{h,o}\right)}{\min(\dot{m}_h, \dot{m}_c)\left(H_{h,i} - H_{c,i}\right)} \qquad (5.3)$$

$$\varepsilon_{tc} = \frac{\dot{m}_h\left(\overline{H}_{c,o} - H_{c,i}\right)}{\min(\dot{m}_h, \dot{m}_c)\left(H_{h,i} - H_{c,i}\right)}$$

The symbols in the above equation are defined in the nomenclature. The temperature, humidity, and enthalpy of the air at the outlet of FBR vary with time; hence the time-averaged values (Temperature: $\overline{T}_{c,o}$ and $\overline{T}_{h,o}$, humidity: $\overline{W}_{c,o}$ and $\overline{W}_{h,o}$, enthalpy: $\overline{H}_{c,o}$ and $\overline{H}_{h,o}$), are used in the effectiveness evaluation in the above equations. The time-averaged outlet air prosperities for any variable (χ : temperature, humidity ratio or enthalpy) in the cold and dry period (Eqn. (5.4)) and the hot and humid period (Eqn. (5.5)) are calculated as follows.

$$\bar{\chi}_{c,o} = \frac{1}{P_c}\int_0^{P_c} \chi_{c,o}\,dt, \qquad (5.4)$$

$$\bar{\chi}_{h,o} = \frac{1}{P_h}\int_0^{P_h} \chi_{h,o}\,dt, \qquad (5.5)$$

P_c and P_h are the duration of the hot (and humid) and cold (and dry) periods, respectively.

The enthalpy of air is calculated in Eqn. (5.6).

$$H = Cp_g T + W(h_{fg} + Cp_w T), \tag{5.6}$$

5.6 NUMERICAL MODEL FOR EXCHANGER (FBR) AND MEASUREMENT SENSORS

Instantaneous temperature and humidity ratio profiles at the outlet of a desiccant-coated FBR during both hot (and humid) and cold (and dry) periods are required to quantify errors due to the transient response of temperature and humidity sensors. In this chapter, a mathematical model developed by Simonson and Besant [36,96] is used to obtain the instantaneous temperature and humidity profiles which is called the FBR model. The FBR model provides the actual outlet condition from the FBR without including the impact of sensors. Then models for the temperature and humidity sensors (sensor model) are implemented to capture what would be measured using sensors. The combined FBR and sensors model results can be compared with experimental measurements as the measurements from an experiment include the sensor responses. The FBR model, temperature sensor model, and humidity sensor model are presented in the following subsections.

5.6.1 FBR model

In FBR, the two separate airstreams (hot (and humid) stream and cold (and dry) stream) alternately flow through the energy exchanger, which consists of numerous channels. Because of the similarity between the flow channels, the governing equations will be presented for a single channel. The schematic of the cross-section of an airflow channel is shown in Figure 5.2. During the hot and humid period, the energy from the hot and humid airstream is absorbed (solid lines in

Fig. 5.2) in the matrix, which is then transferred to the cold and dry air during the subsequent cold and dry period (dashed line in Fig. 5.2).

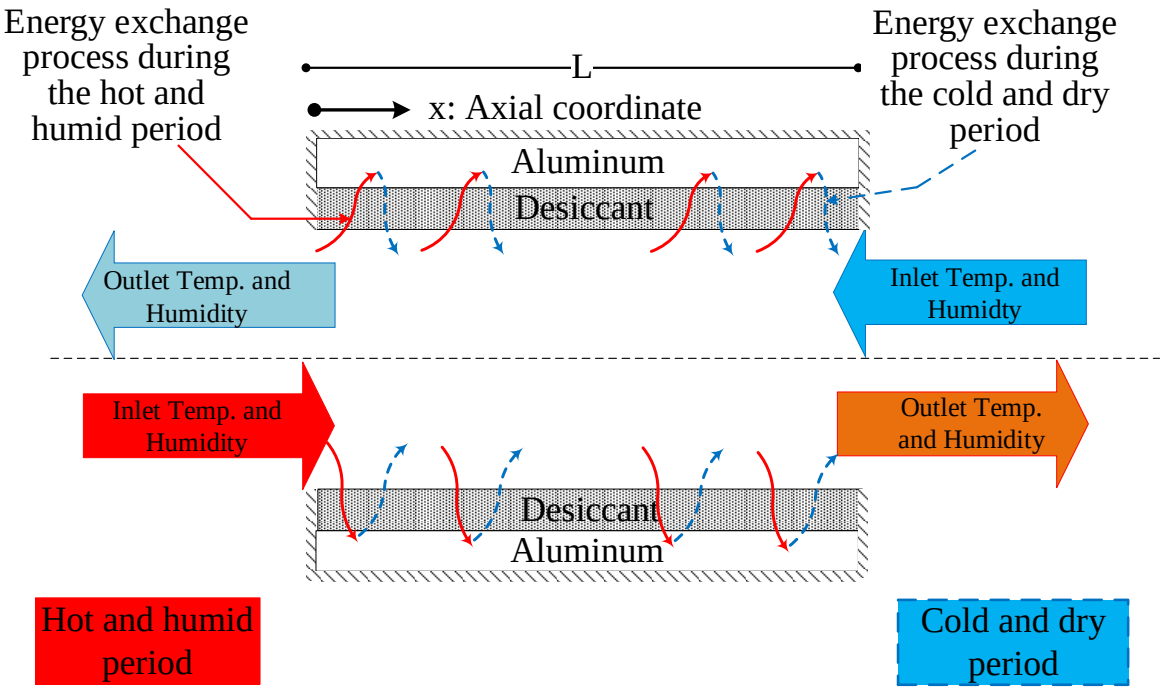

Figure 5.2. A schematic of the numerical domain for heat and mass transfer in a representative channel of desiccant-coated FBR.

The 1-D (bulk mean temperature and moisture concentration) governing equations presented by Simonson and Besant [97,98] for desiccant-coated regenerators are adopted in this chapter. The conservation of mass in the airstream results in two continuity equations, for water vapor and dry air as follows:

$$A_g \frac{\partial \rho_v}{\partial t} + \frac{\partial}{\partial x}\left(\rho_v V A_g\right) + \dot{m}' = 0 \tag{5.7}$$

$$\frac{\partial \rho_a}{\partial t} + \frac{\partial}{\partial x}\left(\rho_a V\right) = 0 \tag{5.8}$$

Where V is the mean airflow velocity, $\dot{m}'$ is the rate of phase change per unit of exchanger length, A_g is the cross-sectional area of the channel and ρ_v is water vapor density and ρ_a is dry air density. The conservation of mass for the desiccant is as follows:

$$\dot{m}' = \rho_{d,dry} A_d \frac{\partial u}{\partial t} \tag{5.9}$$

Where $\rho_{(d,dry)}$ is the density of dry desiccant, and A_d and u are the surface area of the desiccant, and mass fraction of water in the desiccant, respectively. The energy conservation equations for coupled heat and moisture transfer in the airstream (Eqn. (5.10)) and exchanger matrix (Eqn. (5.11)) are as follows:

$$\rho_g C_{P_g} A_g \frac{\partial T_g}{\partial t} + U \rho_g C_{P_g} A_g \frac{\partial T_g}{\partial x} - \dot{m}' h_{ad} \eta + h \frac{A'_s}{L} (T_g - T_m) = 0 \tag{5.10}$$

$$\rho_m C_{P_m} A_m \frac{\partial T_m}{\partial t} - \dot{m}' h_{ad} (1 - \eta) - h \frac{A'_s}{L} (T_g - T_m) = \frac{\partial}{\partial x} \left(k_m A_m \frac{\partial T_m}{\partial x} \right) \tag{5.11}$$

Where t, x, C_p, k, h, L and T are time, axial coordinate, specific heat, thermal conductivity, convective heat transfer coefficient, length of channel and temperature, respectively. Subscripts 'g' and 'm' are used to represent the air and matrix (desiccant + aluminum) variables, respectively. A'_s and A_m represent heat transfer surface area and cross-sectional area of the exchanger plate. The term η in the above equations represents the distribution of phase change energy between the desiccant and the airflow [36]. η is determined form Eqn. (5.12).

$$\eta = \frac{k_g / \sqrt{\alpha_g}}{k_g / \sqrt{\alpha_g} + k_m / \sqrt{\alpha_m}} \tag{5.12}$$

α_g and α_m are thermal diffusivity of the airflow and matrix, respectively and $k_g = hD_h$. The value of η is expected to be between 0 and 0.1 [35]. Several thermodynamics correlations are required to complete the formulation of problem; these equations could be found in [40] and are presented in Appendix C.

Moisture transfer between the airstream and the desiccant during adsorption and desorption is obtained from Eq. (5.13).

$$\dot{m}' = h_m \frac{A_s'}{L}(u_v - u_{v,m}) \tag{5.13}$$

Where h_m and $u_{v,m}$ are the convective mass transfer coefficient and mass fraction of water vapor on the surface of desiccant, respectively. $h_m$is determined using the analogy between heat and mass transfer and $u_{v,m}$is obtained from the sorption isotherms.

The boundary conditions are presented in Eqns. (5.14) -(5.17).

$$T_g(x = 0, mP \le t \le mP + P_h) = T_{h,i}; \qquad m = 0,1,2,\ldots \tag{5.14}$$

$$T_g(x = L, mP + P_h \le t \le (m+1)P) = T_{c,i}; \qquad m = 0,1,2,\ldots \tag{5.15}$$

$$\rho_v(x = 0, mP \le t \le mP + P_h) = \rho_{v_{h,i}}(t); \qquad m = 0,1,2,\ldots \tag{5.16}$$

$$\rho_v(x = 0, mP + P_h \le t \le (m+1)P) = \rho_{v_{c,i}}(t); \quad m = 0,1,2,\ldots \tag{5.17}$$

Furthermore, heat and mass transfer at the ends of the channel are considered to be negligible and the boundary conditions can be written as:

$$\left.\frac{\partial T_m}{\partial x}\right|_{x=0} = \left.\frac{\partial T_m}{\partial x}\right|_{x=L} = 0 \tag{5.18}$$

$$\left.\frac{\partial u}{\partial x}\right|_{x=0} = \left.\frac{\partial u}{\partial x}\right|_{x=L} = 0 \tag{5.19}$$

The fundamental dimensionless groups for heat and mass transfer in desiccant-coated regenerators have been derived from the governing equations presented in Eqns. (5.7,5.8, 5.10, 5.11) [35,98]. Simonson and Besant [35] derived the fundamental dimensionless groups for heat and moisture transfer in the desiccant-coated regenerators; these equations are presented as follows.

$$\frac{\partial \rho_v}{\partial x^*} = NTU_{mt}(\rho_{v,m} - \rho_v) \tag{5.20}$$

$$\frac{\partial \rho_{v,m}}{\partial t^*} = \frac{NTU_{mt}}{Cr^*_{mt}}\left(\rho_v - \rho_{v,m}\right) \tag{5.21}$$

$$\frac{\partial T^*_g}{\partial x^*} = NTU_{ht}\left(T^*_m - T^*_g\right) \tag{5.22}$$

$$\frac{\partial T^*_m}{\partial t^*} = \frac{NTU_{ht}}{Cr^*_{ht}}\left(T^*_g - T^*_m\right) \tag{5.23}$$

Where NTU_{mt} is the number of moisture transfer units, Cr^*_{mt} is the matrix moisture capacity ratio, NTU_{ht} is the number of heat transfer units and Cr^*_{ht} is the matrix heat capacity ratio for a desiccant-coated regenerators. These variables are given in Eqns. (5.24) to (5.27)

$$NTU_{mt} = NTU_o = \left(\frac{1}{\dot{m}Cp_g}\right)_{min}\left[\frac{1}{(hA_s)_h} + \frac{1}{(hA_s)_c}\right]^{-1} \tag{5.24}$$

$$Cr^*_{mt} = Crm^*\frac{\partial u}{\partial RH}\left(\frac{e^{\frac{5294}{T_{ave}}}}{10^6} - 1.61RH_{ave}\right) \tag{5.25}$$

$$NTU_{ht} = \frac{NTU_o}{1 + \eta\frac{\epsilon_l}{\epsilon_s}H^*} \tag{5.26}$$

$$Cr^*_{ht} = \frac{Cr^*}{1 + \eta\frac{\epsilon_l}{\epsilon_s}H^*} \tag{5.27}$$

Where NTU_o and $Cr^* = \frac{MC_{p,m}/P}{\dot{m}c_{P,g}}$ are the overall number of heat transfer units and the matrix heat capacity rate ratio for the sensible regenerators. ϵ_l and ϵ_s are the latent and sensible effectiveness and H^* is the operating condition factor [35]. $H^*$is the ratio of latent to sensible energy differences of airstreams at the inlets of FBR.

$$H^* = \frac{\Delta H_l}{\Delta H_s} \tag{5.28}$$

Figure 5.3 shows H^* on the psychrometric chart for the supply conditions of 23°C and 50% RH. The operation condition factor lies between +6 and -6 for many practical conditions in HVAC

applications [98]. $H^* = \infty$ represents the isothermal condition which both airstreams have the same inlet temperatures but different humidity ratios (i.e., $\Delta T_{inlet}=0$, $\Delta W_{inlet}\neq 0$). On the other hand, at the non-isothermal conditions, the inlet temperature and humidity on the supply and exhaust sides of FBRs are not equal (i.e., $\Delta T_{inlet}\neq 0$, $\Delta W_{inlet}\neq 0$ except for $H^* = 0$ where the humidity ratios of the inlet airflows are equal while the temperatures of airstreams are different (i.e., $\Delta T_{inlet}\neq 0$, $\Delta W_{inlet}=0$)).

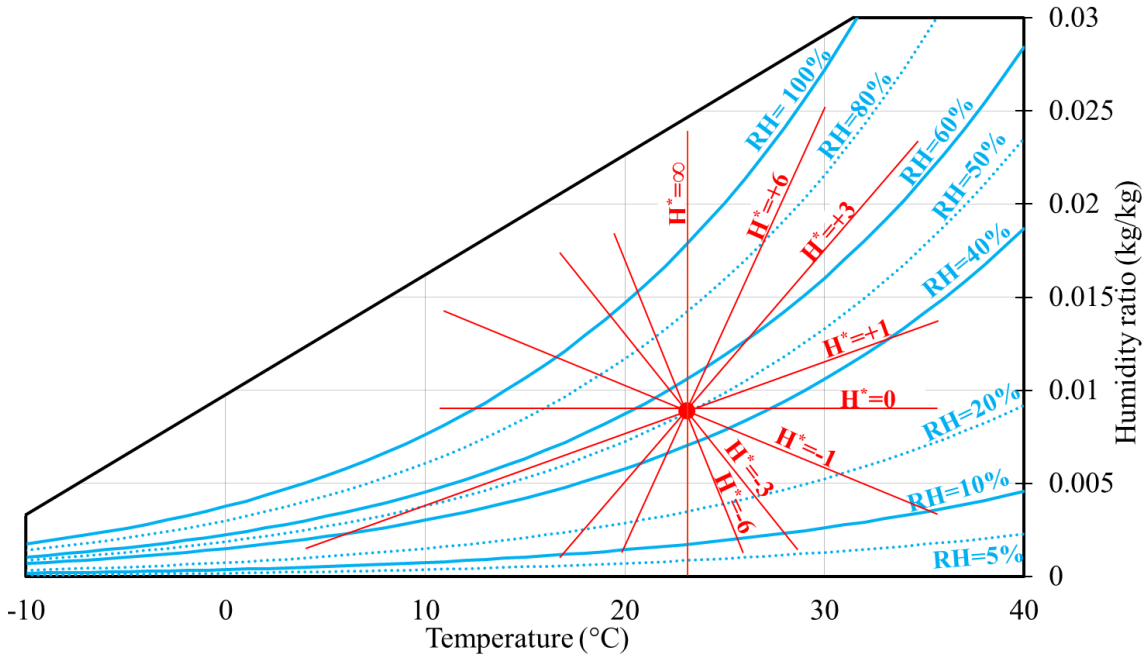

Figure 5.3. Lines of H^* on the psychrometric chart for supply condition of 23°C and 50% RH.

Unlike the dimensionless groups for sensible regenerators [28], the dimensionless groups for heat and moisture transfer (Eqns. (5.24)-(5.27)) are functions of operating conditions (temperature and humidity) [35]. The importance of using the dimensionless equations is that the results can be presented in a generalized way in terms of dimensionless variables.

For many practical applications, the hot and cold periods (P_h and P_c) are equal, and hence, they are considered to be equal in this chapter as well. Also, in many practical applications and the test standards (CSA C439-18 standard [22] and ASHRAE standard 84 [21]), the flow in

regenerators are considered to be balanced ($C^* = \frac{C_c}{C_h} = 1$), and hence the results of the present study are presented for such a balanced flow condition.

5.6.2 Temperature sensor model

The temperature sensor model is based on energy balance for the temperature sensors, assuming the applicability of the lumped capacitance method [28,34], and is presented in Eqn. (5.29).

$$\frac{dT_s}{dt} = \frac{1}{\tau_s}\left(T_g - T_s\right) \tag{5.29}$$

where τ_s is the time constant of the temperature sensor, T_s is the temperature that is measured by the temperature sensor, and T_g is the actual air temperature that the sensor is exposed to.

5.6.3 Humidity sensor model-capacitive relative humidity sensor model

A capacitive relative humidity sensor (CRHS) correlates the electrical capacity of the sensor with RH at a reference temperature and corrects for other temperatures. Thus, the transient response of a CRHS must be carefully analyzed for measurements in the environment, such as the outlet of FBRs where there are simultaneous changes in humidity and temperature. Experimental measurements in the literature show that CRHSs might show anomalous measurements when there are concurrent humidity and temperature changes [99]. Kaplya et al. [99] presented a mathematical model for the CRHS humidity measurement process to explain this anomaly. This model assumes that CRHS is an integrated microprocessor system that performs joint processing of humidity ratio and temperature (using an internal temperature sensor). Therefore, the humidity ratio is assumed to be measured first. The microprocessor element of CRHS converts the humidity ratio to relative humidity using the environment temperature measured by the internal temperature sensor of

CRHS. This process, along with the actual measurement process of CRHS, is presented in Table 5.2. There are two sensor delays corresponding to the humidity ratio measurement and the internal temperature sensor of the CRHS (in step 2 at Table 5.2) and an additional delay (in step 4 at Table 5.2) for the separate temperature sensor to convert the measured RH to humidity ratio for effectiveness calculations. The proposed model is presented in Eqns. (5.30) to (5.33) [99]. Once RH is obtained from this model, humidity ratio is to be calculated for effectiveness evaluations. Thus, using RH from CRHS model and T_s from the temperature sensor model, humidity ratio is obtained (Eqn. (5.33)).

Table 5.2. Comparison of the procedure for RH measurement between the actual procedure and proposed procedure in this chapter.

Actual RH measurement process	**Proposed procedure to model measurement of RH**
1. Change of dielectric constant of hygroscopic dielectric material	1. Humidity ratio and temperature (actual values) are obtained from the numerical model (W_g and T_g)
2. The dielectric material electrical capacity changes (the sensor output is voltage) with RH that is correlated to RH of the environment that the sensor is located.	2. Actual humidity ratio and temperatures will be delayed based on the time constants obtained for the CRHS (W_{int} and T_{int}). 3. Relative humidity (RH_s) is obtained with (W_{int} and T_{int}) from step 2. 4. With RH_s from step 3 and temperature from the temperature sensor model (T_s), the sensor humidity ratio (W_s) is obtained.
	Note: Three delays are involved in this approach. Two delays correspond to the temperature and humidity ratio in step 2. An additional delay for temperature also exists when RH is converted to humidity ratio at step 4.

$$\frac{dW_{int}}{dt} = \frac{1}{\tau_{h,int}}\left(W_g - W_{int}\right) \tag{5.30}$$

$$\frac{dT_{int}}{dt} = \frac{1}{\tau_{t,int}}\left(T_g - T_{int}\right) \tag{5.31}$$

$$RH_s = f_1(W_{int}, T_{int}) \tag{5.32}$$

$$W_s = f_2(RH_s, T_s) \tag{5.33}$$

Subscript "int" represents the internally calculated values. $\tau_{h,int}$ and $\tau_{t,int}$ are the internal humidity time constant and the internal temperature time constant of the humidity sensor, respectively. Also, T_s is obtained from the temperature sensor model (from Eq. 5.29) and W_s is the humidity ratio that is measured by the humidity sensor.

To obtain the internal time constants for humidity and temperature for the current humidity sensor model ($\tau_{h,int}$ and $\tau_{t,int}$), two experiments are designed. (1) the CRHS is exposed to a positive/negative step change in humidity ratio at a constant temperature to obtain the internal humidity ratio's time constant ($\tau_{h,int}$) and (2) the CRHS is exposed to a positive/negative step change in temperature at a constant humidity ratio to estimate the internal temperature sensor's time constant ($\tau_{t,int}$).

Figure 5.4 shows the results for negative and positive step changes in humidity ratio while the temperature is kept constant (Experiment (1)). The sensor in the test section (which is explained in the experimental section 5.7) is used to measure the time constants. In the experiments in Fig. 5.4, the inlet relative humidity was changed by 30%, and the temperature is maintained at 23°C. The experimental data were fitted to an exponential function using the trust region optimization algorithm in MATLAB R2019b. The exponential functions for positive and negative step changes are shown in Eqn. (5.34).

$$f(t) = \begin{cases} 1 - e^{-\frac{t}{\tau}} & positive\ step\ change \\ e^{-\frac{t}{\tau}} & negative\ step\ change \end{cases} \tag{5.34}$$

The time constants for positive and negative step changes in humidity ratio at constant temperature ($\tau_{h,int}$) are calculated to be 6.3 and 6.2 seconds, respectively. The average value of

negative and positive step changes ($\tau_{h,int} = 6.25\ s$) will be used for validation of the results in section 5.8.

Figure 5.5 shows the RH measurement and the fitted model (from Eqn. (5.34)) for the second experiment with a step change in temperature while the humidity ratio is kept constant (T_{cold}=23°C and T_{hot}=38°C). Following the same approach for the humidity ratio step change experiment, the CRHS internal temperature time constants ($\tau_{t,int}$) were calculated to be 28 and 25 seconds for the negative and positive step changes in temperature, respectively. The average value of negative and positive step changes for the experiment ($\tau_{t,int} = 26.5\ s$) will be used for validation of the results in section 5.8.

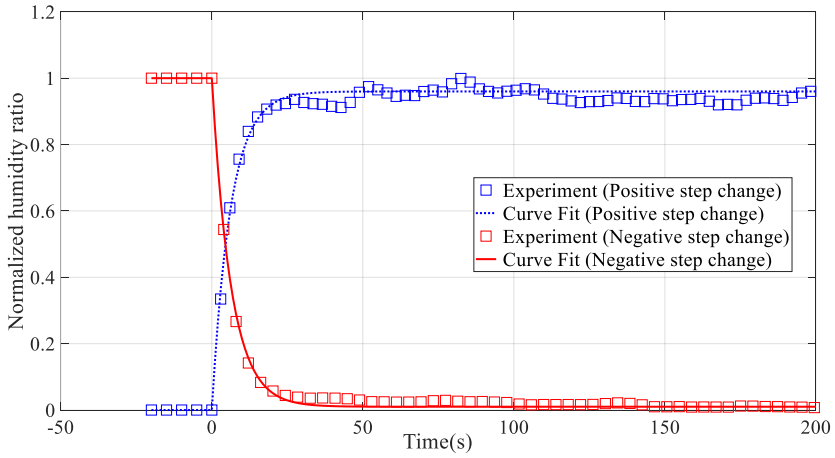

Figure 5.4. Negative and positive step changes in humidity ratio at constant temperature (T=23°C) to obtain the internal humidity ratio's time constant ($\tau_{h,int}$).

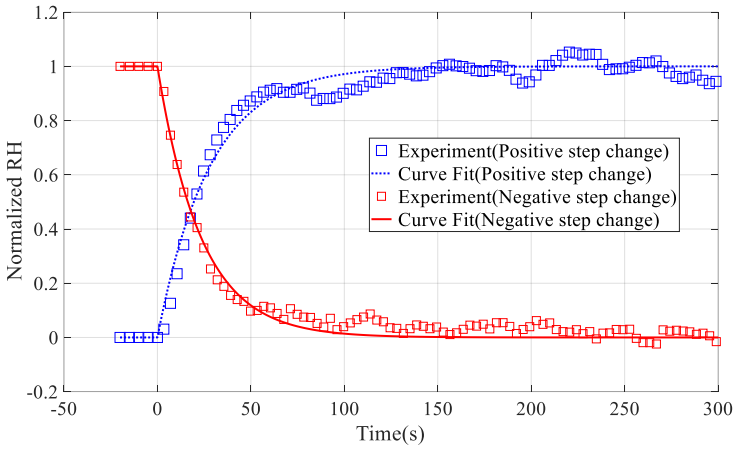

Figure 5.5. Negative and positive step change in temperature and measured RH with CRHS at constant humidity ratio to obtain the internal temperature time's constant ($\tau_{t,int}$).

In order to compare the CRHS model prediction with the actual humidity sensor response, two experiments were conducted where the sensor was exposed to a step change in humidity ratio at a constant RH, and the results are compared with the humidity sensor model prediction in Fig. 5.6 (a) and (b). The average time constants from the positive and negative step change experiments from Figs. 5.4 and 5.5 (i.e., a time constant of 6.25 seconds for $\tau_{h,int}$ and time constant of 26.5 seconds for $\tau_{t,int}$), are used in the model in Fig. 5.6. Also, the temperature sensor time constant of 1.5s ($\tau_s = 1.5s$, as presented in Table 5.3 in section 5.7) is used for the comparison in Fig. 5.6. A good agreement between the results of the experiment and the humidity sensor model is observed in Fig. 5.6. More specifically, an overshoot in the humidity ratio can be seen at the beginning of both negative and positive step changes in Fig. 5.6, and the model accurately predicts this behaviour. This unexpected response at non-isothermal conditions can be attributed to the change in dielectric constant due to the simultaneous changes in humidity and temperature. Similar behaviour for capacitive humidity sensors has been reported previously in the literature [99].

(a). A negative step change in humidity ratio at a constant RH

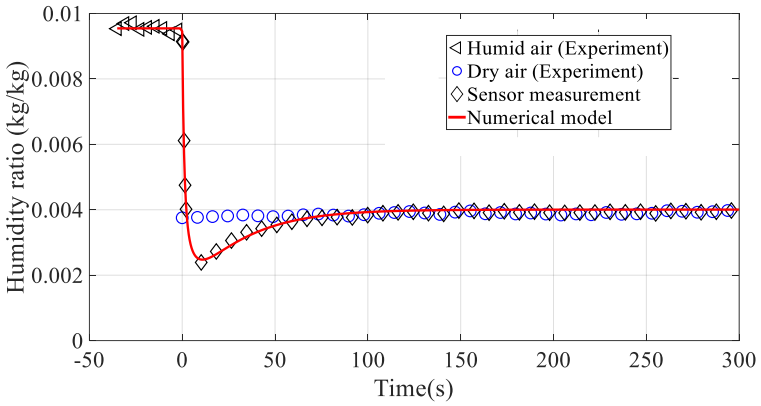

(b). A positive step change in humidity ratio at a constant RH

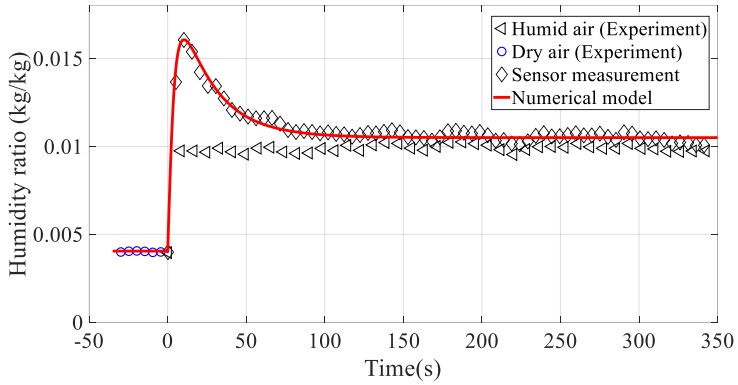

Figure 5.6. Comparison of experiment and humidity sensor model for negative and positive step change in humidity ratio at a constant RH.

5.6.4 **Numerical solution procedure**

The governing conservation energy and mass equations are discretized using a finite volume method [39]. The upwind differencing and central differencing schemes are used to approximate the convection and diffusion terms in the airflow and the matrix (Aluminum + desiccant), respectively. The resulting algebraic equation for the airflow is solved using the Gauss-Seidel iteration technique, and the Tridiagonal Matrix Algorithm (TDMA) is used to solve the energy equation in the matrix. A MATLAB code is developed to solve the set of algebraic equations. The numerical solution flowchart is presented in Fig. 5.7.

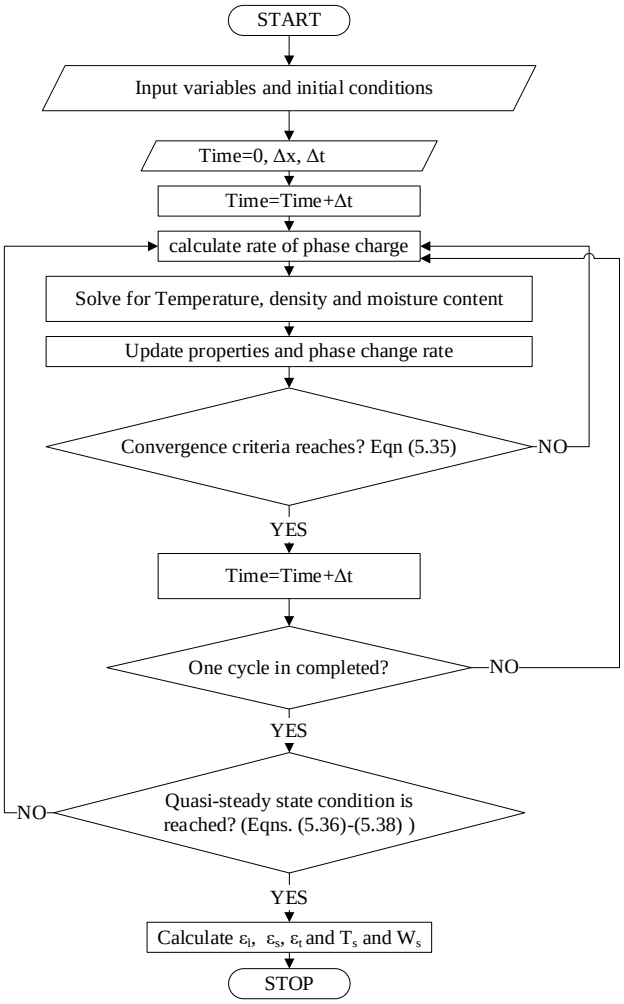

Figure 5.7. Flowchart for the FBR model.

The solution starts with the calculation of phase change rate and time is incremented when the convergence criteria (Eq. (5.35)) for each dependent variables (temperature, and humidity) and the rate of phase change are satisfied.

$$\frac{\sum_{i=1}^{N_s}\left|\chi(i)^{j+1}-\chi(i)^{j}\right|}{n(\chi_{max}-\chi_{min})} \leq 10^{-5} \tag{5.35}$$

When the convergence criterion is reduced to 10^{-6}, there is a negligible (less than 0.05%) impact on the predicted effectiveness. Upon completion of each complete cycle (one hot and humid period + one cold and dry period), the quasi-steady-state conditions in Eqns. (5.36)-(5.38) are

examined. If the solution satisfies the quasi-steady-state conditions, the numerical procedure is finished; otherwise, time is further incremented until the quasi-steady-state conditions are satisfied.

$$\left|\frac{\dot{m}_h\left(H_{h,i}-H_{h,o}\right)-\dot{m}_c\left(H_{c,o}-H_{c,i}\right)}{\min(\dot{m}_h,\dot{m}_c)\left(H_{h,i}-H_{c,i}\right)}\right| \leq 10^{-2} \tag{5.36}$$

$$\left|\frac{\dot{m}_h\left(W_{h,i}-W_{h,o}\right)-\dot{m}_c\left(W_{c,o}-W_{c,i}\right)}{\min(\dot{m}_h,\dot{m}_c)\left(W_{h,i}-W_{c,i}\right)}\right| \leq 10^{-2} \tag{5.37}$$

$$\left|\frac{\partial\epsilon}{\partial t}\right| \approx \left|\frac{\epsilon^k-\epsilon^{k-1}}{P}\right| \leq 10^{-4} \tag{5.38}$$

Eqns. (5.36) and (5.37) ensure that the energy and moisture balance between the energy stored in the first period and energy released in the subsequent next period. Eqn. (5.38) compares the effectiveness values from each completed cycle to the previous cycle before reaching the quasi-steady-state condition. Decreasing the quasi-steady-state conditions in Eqns. (5.36)-(5.38) by a factor of 10 results in a negligible change (less than 0.1%) in the predicted effectiveness.

The numerical solution is performed on a uniform 1-D grid with a constant time step. The grid dependency tests are performed to determine the optimum spatial grid size and time step. Further details on the numerical solution procedure could be found in the literature [36,50,96].

The FBR model gives accurate outlet air properties (without the impacts of sensors), which is used to calculate the correct effectiveness values. The temperature and humidity ratio from the FBR model are used as inputs for the temperature and humidity sensor models. Subsequently, the sensor model predicts the measured T_s and W_s by the sensors in an experiment. Validation of the FBR and FBR+sensor model are presented in section 5.8.

5.7 FBR SMALL-SCALE TEST FACILITY

A schematic of the small-scale test facility is shown in Fig. 5.8. The desiccant-coated exchanger (EX in Fig. 5.8) is moved alternately between two conditioned airstreams. A schematic

of the exchanger is shown in Fig. 3.4. When the exchanger is exposed to hot and humid air, the desiccant adsorbs the moisture, and the matrix (aluminum) stores the heat (hot and humid period). The heat and moisture stored in the exchanger are then transferred to the cold and dry airstream during the subsequent exposure of the exchanger to a cold and dry airstream (cold and dry period). The experiment is continued until the exchanger attains the quasi-steady-state condition.

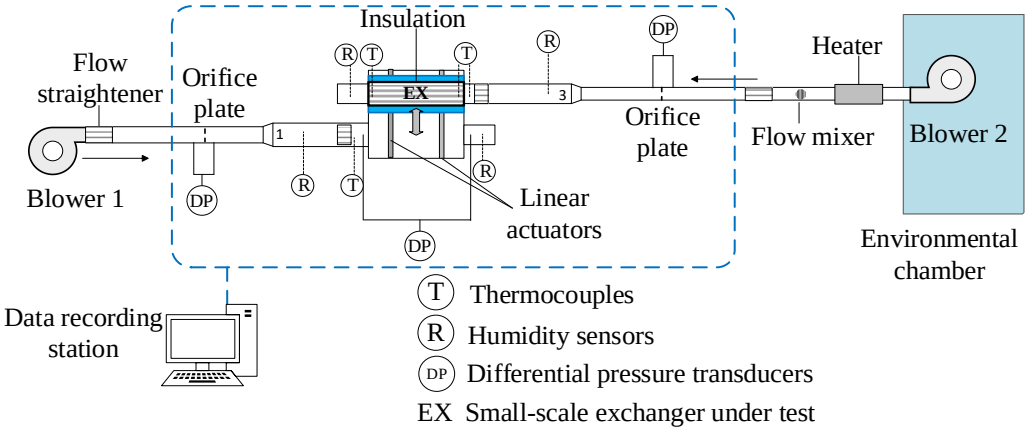

Figure 5.8. Schematic of the small-scale test facility.

The temperatures of the airstreams are measured using calibrated T-type thermocouples with an uncertainty of ±0.2 °C. Capacitive humidity sensors with an uncertainty of ±1.5% are used to measure the humidity of the airstreams. Orifice plates with differential pressure transducers with a total uncertainty of ±8 Pa are also used to measure flow rates. The uncertainty in flow rate measurements is calculated to be ±2%.

The small-scale exchanger consists of 26 equally spaced desiccant-coated aluminum plates. The geometric details, thermo-physical properties of the exchanger, and the time constants of sensors are presented in Table 5.3. A uniform monolayer silica gel desiccant is coated on both sides of the aluminum plates using a sieving method developed at the University of Saskatchewan [100]. The physical properties of desiccants and details of desiccant coating are reported in Table 5.3. Experiments on silica gel were conducted using the Gravimetric Analyzer system (IGA-002,

manufacturer: Hiden Isochema Ltd., United Kingdom) to obtain the silica gel sorption isotherm curve shown in Fig. 5.9. The adsorption curve is used in the validation of the numerical model in section 5.8. More details about sorption isotherm experiments and desiccant-coated exchangers can be found in [100]. Krishnan et al. [20,44] has documented the principle of operation, instrumentation, and data analysis procedures of the experiments.

Uncertainty analysis has been performed by following the rules of error propagation to maintain a 95% confidence interval [57], and the uncertainties in the sensible effectiveness, latent effectiveness are ±3% and ±7%, respectively. Energy balance tests were performed, and results showed that the test facility conserves energy within ±5% for a wide range of test conditions.

Table 5.3. Geometrical details, thermophysical properties of the exchanger, dimensionless parameters, and sensor time constant.

Exchanger channel	Length(mm)	200
	Width (mm)	80
	Height (mm)	2.1
	Hydraulic diameter (mm)	4.1
Aluminum plates	Thickness (mm)	0.69
	Thermal conductivity (W/m·K)	220
	Density (kg/m^3)	2730
	Specific heat capacity (J/kg·K)	904
Silica gel properties	Density (kg/m^3)	350
	Specific heat capacity (J/kg·K)	333
	Mass of coating (g)	45.4
	Desiccant/matrix mass ratio (%)	4.8
Temperature sensor	Time constant (s)	1.5
Humidity sensor	Temperature time constant- $\tau_{t,int}$ (s)	26.5
	Humidity ratio time constant- $\tau_{h,int}$ (s)	6.3

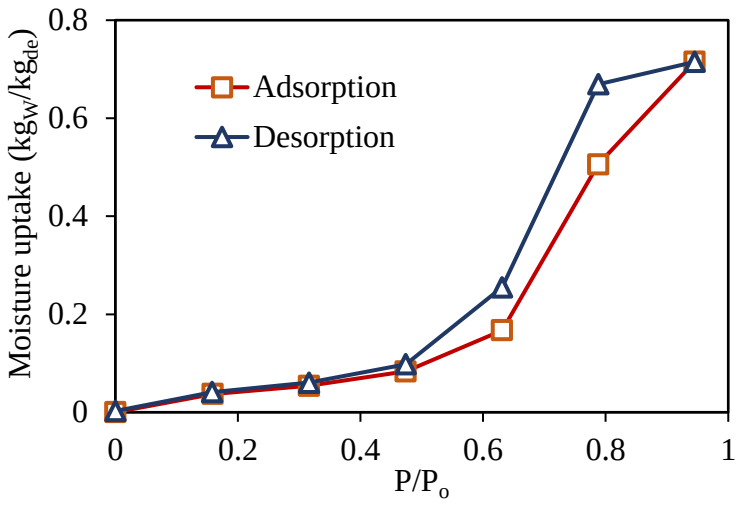

Figure 5.9. Sorption isotherm of silica gel at 25°C.

5.7.1 **Bag sampling method**

Bag sampling method (BSM) is proposed by ASHRAE 84 [21] and CSA C 439-18 [22] standards as an alternative to humidity sensors for accurate measurement of the average humidity ratio (and hence latent effectiveness) at the outlet of FBRs. A sample of FBR outlet air is collected in a bag during the entire period then the bag is allowed to reach equilibrium with the environment (the sampling is repeated several times to compare the samples). The average humidity ratio and hence the latent effectiveness is obtained by measuring the relative humidity and temperature of the air in the bag. The experimental setup, instrumentation, and sampling procedure for the BSM are explained in detail in the literature [21,22]. The BSM uncertainty is ±7% in effectiveness.

5.8 **VALIDATION OF RESULTS**

In this section, the numerical model will be validated against experimental results from the small-scale test facility. The experimental (which includes the sensor responses) temperature and humidity ratio profiles for both isothermal and non-isothermal conditions will be compared against

the combined FBR and sensor models. The effectiveness results from the FBR model will also be compared with experimental results from the bag sampling method (BSM) as this method does not contain the transient response of sensors. Moreover, the current model results have been previously compared and validated with the experimental measurements available in the literature for isothermal conditions [62].

5.8.1 Validation under isothermal conditions ($H^*=\infty$ or $\Delta T_{inlet}=0$, $\Delta W_{inlet}\neq 0$)

Figure 5.10 compares the quasi-steady state humidity ratio profile from the experiment, the FBR model, and the combined FBR and sensor model for the exchanger (Fig. 5.10 (a)) and the duct (Fig. 5.10 (b)) sensors at operating conditions in Table 5.4. The combined FBR and sensor model results agree with the experiment measurement for both the exchanger and duct sensors. The difference between the FBR model, (which neglects the sensor transients) and the experimental results are the greatest at the beginning of each period as expected. The difference is especially prevalent for the duct sensors which are exposed to the largest step change in conditions before periods. By the end of each period, the FBR models and experimental data show a good agreement.

Table 5.5 compares the latent effectiveness values from the FBR model, the combined FBR and sensor model, and the experiment for the isothermal test conditions. The FBR model provides the correct effectiveness value, while the other values are affected by the sensor transients, as mentioned in the model development section. The comparison in this table shows that the combined FBR and sensor model prediction of latent effectiveness agrees with the experimental measurements within ±2% which verifies the combined FBR and sensor model. The exchanger sensors overpredict and the duct sensors underpredict the latent effectiveness for the isothermal condition ($H^*=\infty$).

Table 5.4. Inlet conditions for the isothermal experiment ($\Delta T_{inlets}=0$, $\Delta W_{inlets}\neq 0$).

Hot and humid air		Cold and dry air		Recovery	Face velocity	H^*
T (°C)	RH (%)	T (°C)	RH (%)	period (s)	(m/s)	
28	61	28	37	60	1.5	∞

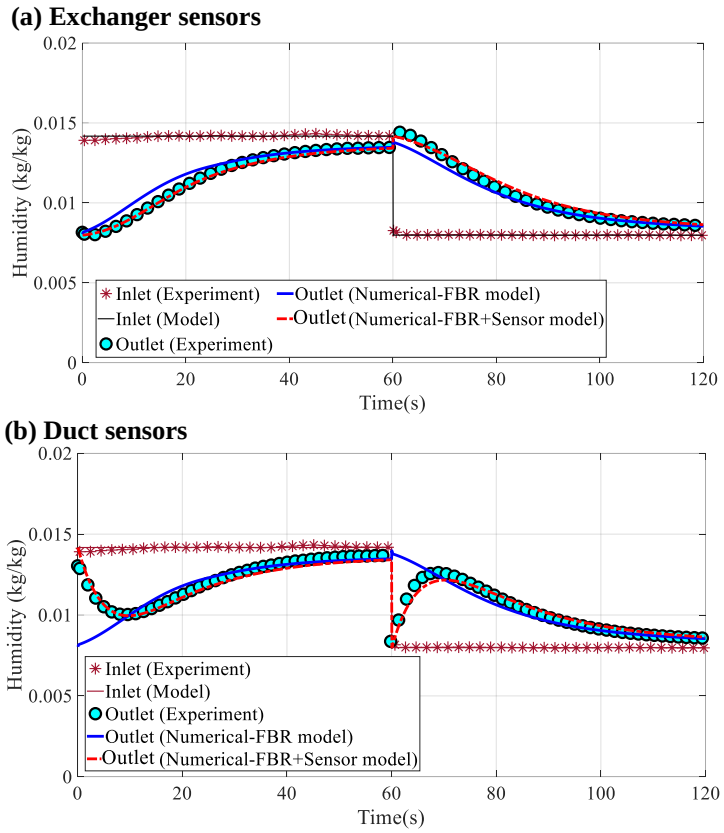

Figure 5.10. Comparison of outlet humidity ratio profile for (a) exchanger and (b) duct sensor between experiment and numerical models (FBR model and FBR+ Sensor model).

Table 5.5. Comparison of latent effectiveness from the experiment, FBR model, and the combined FBR and sensor model for the isothermal test conditions ($\Delta T_{inlet}=0$, $\Delta W_{inlet}\neq 0$).

FBR model	**FBR+ sensor**	**Experiment**	**FBR+ sensor**	**Experiment**
	Exchanger sensor-hot and humid side		Exchanger sensor-cold and dry side	
36%	41%	43±7%	37%	38±7%
	Duct sensor-hot and humid side		Duct sensor-cold and dry side	
36%	31%	33±7%	28%	30±7%

5.8.2 Validation under non-isothermal conditions ($H^*=0.85$ or $\Delta T_{inlet}\neq 0$, $\Delta W_{inlet}\neq 0$)

The experimental and model (FBR and combined FBR and sensor) temperature and humidity profiles at quasi-steady-state conditions are compared for the duct and exchanger sensors in Figs. 5.11 and 5.12, respectively. The inlet conditions for this non-isothermal experiment are presented in Table 5.6. The model predictions for the temperature profile from both the exchanger and duct sensors are in good agreement with the experimental measurements. It should be noted that during the cold period, the duct sensors in the hot duct are exposed to the ambient lab conditions (T=23°C and RH=50%), and hence, the temperature and humidity ratio values do not start from the hot and humid conditions in Table 5.6.

Table 5.6. Inlet conditions for the non-isothermal experiment ($\Delta T_{inlet}\neq 0$, $\Delta W_{inlet}\neq 0$).

Hot and humid air		Cold and dry air		Recovery	Face velocity	H^*
T (°C)	RH (%)	T (°C)	RH (%)	period (s)	(m/s)	
38.3	18.5	14.8	23.2	60	1.5	0.85

An important observation is a peak in the humidity profile for the duct sensors at about 70s during the cold and dry period in Fig. 5.11. The measured outlet humidity ratio peaks during this period and the value becomes higher than the inlet humid air humidity ratio, which is not theoretically possible. These unexpected results are due to the response of the humidity sensor to simultaneous changes in humidity and temperature. These experimental results are difficult to understand without the model. The combined FBR and sensor model can accurately predict this behavior, as shown in Fig. 5.11. Again, the FBR model provides physically realistic or correct results because it is not affected by the sensor transients. Furthermore, the humidity ratio profile for the exchanger sensor in Fig. 5.12 overshoots the inlet conditions at 40-60 seconds; and again the sensor model accurately predicts this phenomenon.

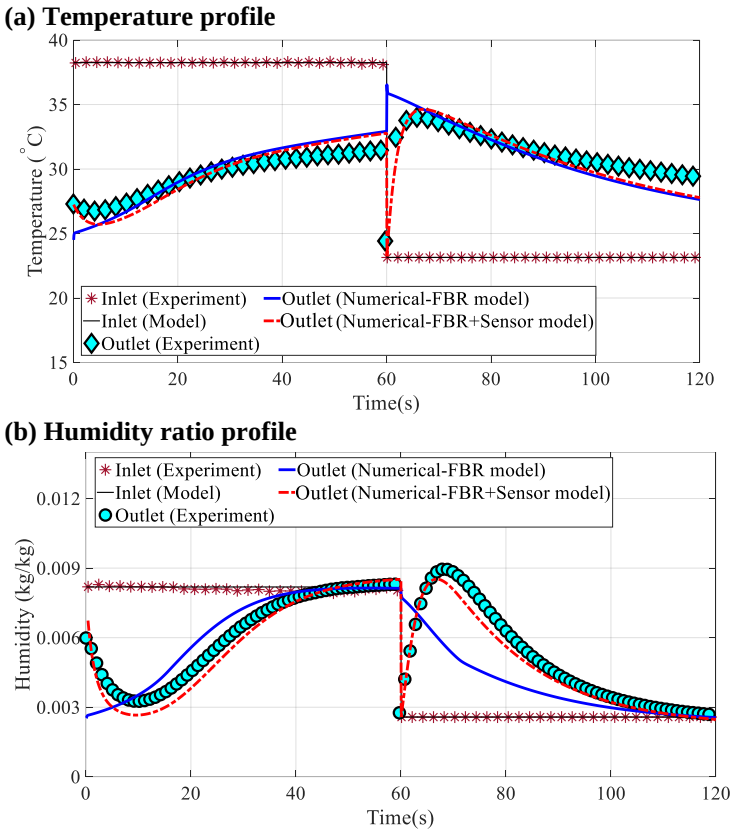

Figure 5.11. (a) Comparison of outlet temperature and (b) humidity ratio profiles between experiment, numerical model (FBR model), and combined FBR and sensor model for the duct sensors.

Table 5.7 compares the latent and sensible effectiveness values from the FBR model, combined FBR and sensor model, and the experiment for the non-isothermal experiment. Comparing the results shows that the combined FBR and sensor model results agree with the experimental measurements within ±2% and ±1% for latent and sensible effectiveness which validate the model. The duct sensor on the dry and cold period predicts latent effectiveness that is about 20% higher than its actual value, mainly because of the peak in humidity caused by the transient response of the humidity sensor.

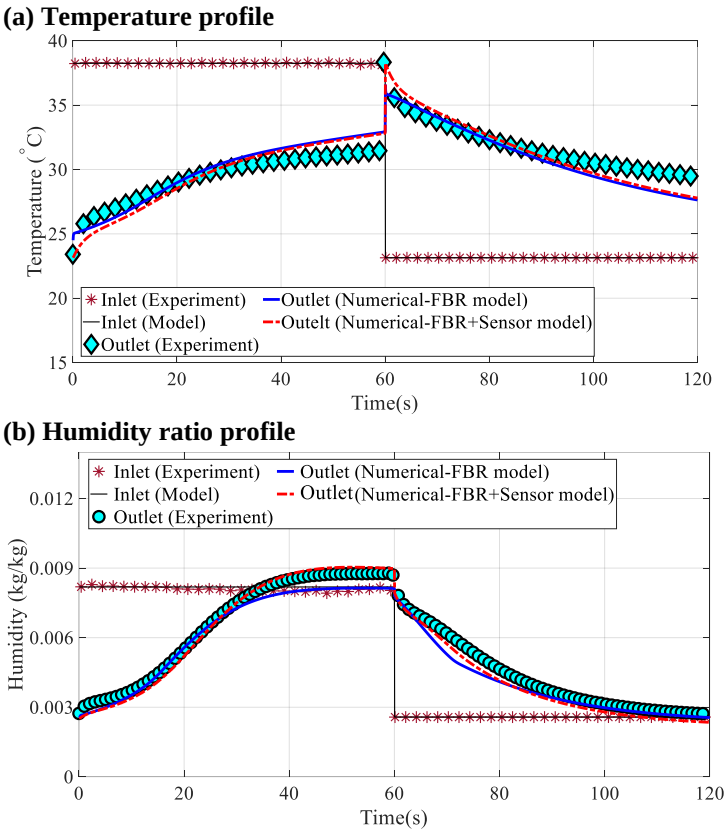

Figure 5.12. (a) Comparison of outlet temperature and (b) humidity ratio profiles between experiment, numerical model (FBR model), and combined FBR and sensor model for the exchanger sensors.

Table 5.7. Comparison of latent and sensible effectivenesses from experiment, FBR model and combined FBR and sensor model.

Latent effectiveness				
FBR model	**FBR+ sensor**	**Experiment**	**FBR+sensor**	**Experiment**
	Exchanger sensor-hot and humid side		Exchanger sensor-cold and dry side	
26%	18.5%	21±7%	27.0%	29±7%
	Duct sensor-hot and humid side		Duct sensor-cold and dry side	
26%	32.5%	31±7%	44.2%	46±7%
Sensible effectiveness				
FBR model	**FBR+ sensor**	**Experiment**	**FBR+ sensor**	**Experiment**
	Exchanger sensor-hot side		Exchanger sensor-cold side	
56%	57.7%	58±3%	56.3	57±3%
	Duct sensor-hot side		Duct sensor-cold side	
56%	58.0%	57±3%	54.6	55±3%

Sensible effectiveness from the combined FBR and sensor model show a good agreement with measurements. These observations show that the model presented for temperature sensors in

Chapter 2 and 3 (for sensible FBRs) can be used for desiccant-coated FBRs and these findings supports the results presented in Chapter 2 and 3.

5.8.3 Effectiveness comparison for the FBR model

Latent effectiveness from the numerical model (FBR model) is compared against the results obtained from the bag sampling method (BSM); the comparison of results is presented in Fig. 5.13 for different test conditions (face velocity:1-2 m/s, NTU_o:1.8 – 3) at both isothermal and non-isothermal conditions. The numerical results agree with the BSM within the experimental uncertainty limits. Furthermore, a recently published experimental paper documented a comprehensive comparison of the numerical model prediction, BSM method, and the experimental results (measured with sensors) for a wide range of operating and design conditions [100]. The findings from this paper indicate a good agreement between the model and experimental measurements from both BSM and sensors. Also, the sensible effectiveness from the model and experiment is shown in the figure, which indicates a good agreement between the model prediction and experimental measurements for sensible effectiveness.

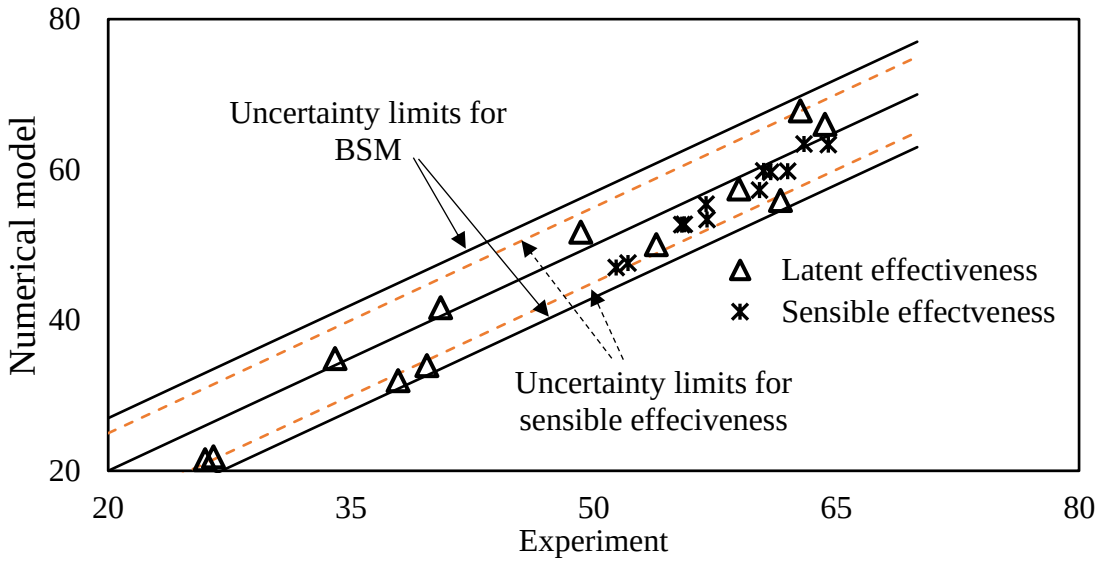

Figure 5.13. Comparison of latent effectiveness from the numerical model (FBR) and BSM (and sensible effectiveness from the combined FBR and sensor model) at several non-isothermal conditions ((velocity:1-2 m/s, NTU_o:1.8–3)).

5.9 APPLICATIONS OF THE COMBINED FBR AND SENSOR MODEL

This section presents applications of the combined FBR and sensor model to evaluate the latent effectiveness of the desiccant-coated FBRs. The sensible effectiveness will be not presented in this section as it could be obtained from the temperature sensor measurements and the model presented in Chapter 2. Also, the impact of the transient nature of FBR and temperature sensor characteristics on the sensible effectiveness measurements are presented in Chapters 2 and 3 and documented in the literature [28,50].

The difference between effectiveness from the FBR model and the combined FBR and sensor model (FBR+ sensor) is reported as the latent effectiveness error ($\Delta\epsilon_L$) that results due to the transient nature of the FBR and temperature and humidity sensors:

$$\Delta\epsilon_L = \epsilon_{L,\mathrm{FBR}} - \epsilon_{L,FBR+sensor} \tag{5.39}$$

Negative $\Delta\epsilon_L$ means that the sensor transients result in overprediction the actual FBR effectiveness while positive error means that the sensor underpredicts the actual effectiveness.

The following sections present the quasi-steady state humidity ratio profiles of FBRs with semi-sawtooth and sawtooth outlet profiles to understand the response of the sensor when exposed to different humidity ratio profiles. Later, the latent effectiveness errors for different operating condition factors and sensor time constants will be presented.

The general sorption curve (Eqn. (5.40)) is used in the simulation presented in this section.

$$\mathrm{u} = \frac{\mathrm{W_m}}{1 - \mathrm{C} + \mathrm{C/RH}} \tag{5.40}$$

In this equation $\mathrm{W_m}$ is the maximum moisture content of desiccant, and C determines the type of desiccant, and u is the mass fraction of water in the desiccant. The general sorption curve can model the sorption characteristics of several desiccants such as molecular sieve, silica gel, and activated carbon [97]. The simulations have been performed for the linear sorption curve with maximum moisture uptake of 0.5 (C=1 and Wm=0.5). Also, the distribution of phase change energy between the desiccant and the airflow is 0.1 ($\eta = 0.1$).

5.9.1 **FBRs with a semi-sawtooth profile**

Figures 5.14 and 5.15 present the quasi-steady state semi-sawtooth humidity ratio profile (FBR model) that the exchanger and duct sensors are exposed to during a cycle time of 120 seconds in FBRs. The first half of the cycle (0-60 seconds) shows the sensor exposure to constant temperature and humidity airflow conditions (the initial condition of the sensors), and the second half of the cycle (60-120 seconds) is the FBR outlet humidity profile. The humidity ratio profiles from the sensor (FBR+ Sensor model) with time constants of ($\tau_{h,int}$=25s, $\tau_{t,int}$=5s and τ_s=3s) are

also presented in these figures. The results in Figs. 5.14 and 5.15 are presented for the AHRI (Air Conditioning, Heating and Refrigeration Institute) summer test conditions (Table 5.8).

For the exchanger sensor in Fig. 5.14, the sensor measurement (FBR+ sensor model) starts from the sensor initial condition and then crosses the FBR profile during the second period (60-120s when the sensors are exposed to outlet of FBR). The sensor measurement gradually distant from the actual values. The measurement peaks during the first period (0-60 second when the sensors are exposed to inlet conditions) and then gradually become closer to the actual value by the end of first period. Due to the simultaneous step changes in temperature and humidity during this period (0-60s), the measured values peaks and then gradually become closer to the actual values.

Table 5.8. AHRI summer test conditions (H^*=1.6)

Air properties	Supply air	Exhaust air
Dry bulb temperature (°C)	35	23.9
Wet bulb temperature (°C)	25.6	17.2

The explanation for the exchanger sensors (Fig. 5.14) applies to the duct sensors in Fig. 5.15. However, for the duct sensors (Fig. 5.15), the sensor (FBR+ Sensor model) measures an additional peak during its exposure to the FBR outlet (about 70s) because of the simultaneous changes in temperature and humidity. But it approaches the actual values by the end of each period.

Latent effectiveness errors ($\Delta\epsilon_L$) are determined from Eqn. (5.39) and are also shown in Figs. 5.14 and 5.15 (cycle time of 120 seconds). The errors are significant and range from 10-20%. The exchanger sensor underestimates the latent effectiveness, while the duct sensor overestimates the latent effectiveness at this operating condition (AHRI summer test condition).

(a) cold and dry period

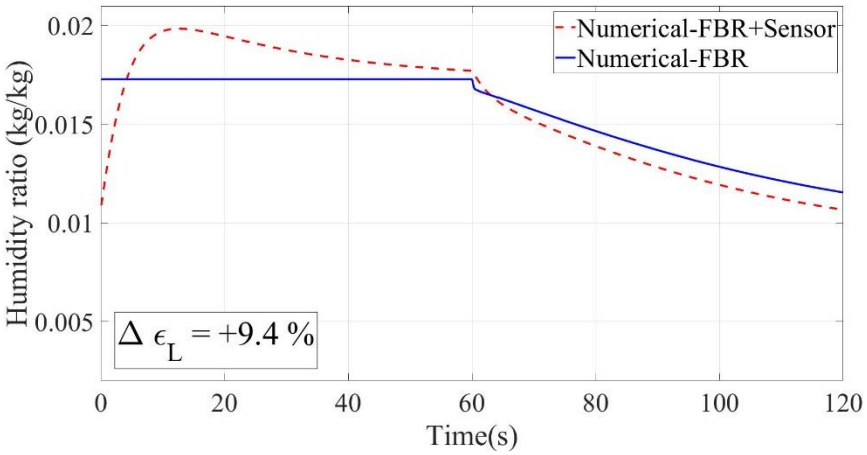

(b) hot and humid period

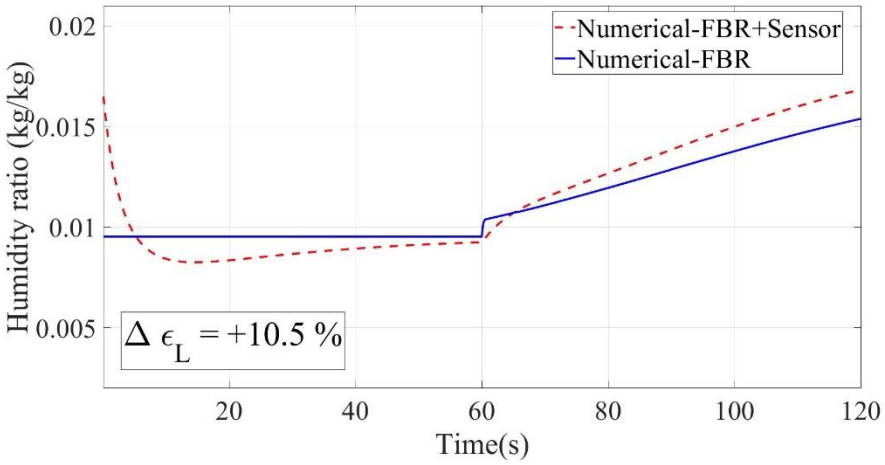

Figure 5.14. Quasi-steady-state humidity ratio profile (FBR model) that the exchanger sensor is exposed to and its response (FBR+ Sensor model) for time constants of $\tau_{t,int}$=25s, $\tau_{h,int}$=5s and τ_s=3s at (a) cold and dry period and (b) hot and humid period (NTU_o=3, Cr^*=3, λ=0.08, Cr_m^*=0.3, η=0.1 and at the AHRI summer test conditions (H^*=1.6)).

The latent effectiveness errors on the hot (and humid) and cold (and dry) sides are not equal; this is an important observation and is different from sensible FBRs as presented in the Chapter 3 [28]. For the sensible FBRs, the sensible effectiveness errors are independent of the period of operation (hot or cold) as presented in Chapter 3 (section 3.5.2) [28], and thus averaging of effectiveness can give the accurate effectiveness of sensible FBRs. On the other hand, the latent effectiveness cannot be averaged on hot (and humid) and cold (and dry) periods to obtain the

average effectiveness, as the sensor errors (FBR+ Sensor model) depend on the period of operation.

(a) cold and dry period

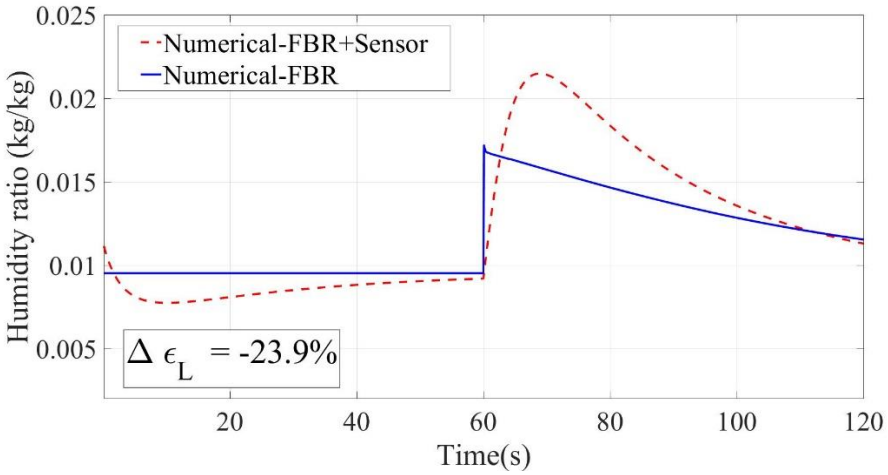

(b) hot and humid period

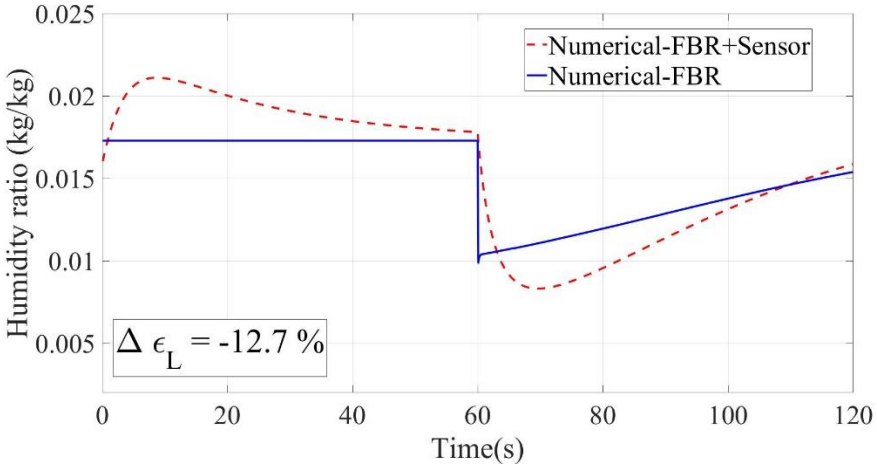

Figure 5.15. Quasi-steady-state humidity ratio profile (FBR model) that the duct sensor is exposed and its response (FBR+ Sensor model) for time constants of $\tau_{t,int}$=25s, $\tau_{h,int}$=5s and τ_s=3s at (a) cold and dry period and (b) hot and humid period (NTU_o=3, Cr^*=3, λ=0.08, Cr_m^*=0.3, η=0.1 and at the AHRI summer test conditions (H^*=1.6)).

5.9.2 FBRs with a sawtooth profile

Figure 5.16 shows the actual quasi-steady-state humidity ratio profile (FBR model) that the sensor with a sawtooth profile is exposed to along with what the sensor (with time constants of $\tau_{t,int}$=25s, $\tau_{t,int}$=5s and τ_s=3s) would measure (FBR+ sensor model) during the humid (and

hot) and dry (and cold) periods. Like the previous section, two consecutive periods are presented in this figure, but both periods are the same for this type of FBR. The sensor measurement (FBR+ sensor model) reaches a maximum value at the dry (and cold) period and then gradually drops. The sensor measurement approaches a minimum value for the humid (and hot) period and gradually rises during the rest of the period. The humidity sensor underestimates the latent effectiveness for the dry (and cold) period while overestimates for the humid (and hot) period at this operating condition. The latent effectiveness error on the hot and humid period is equal to that of the cold and dry period but with an opposite sign. This is an essential practical conclusion as it suggests that for desiccant-coated FBRs exposed to a sawtooth profile, the latent effectiveness can be measured accurately by averaging the effectiveness values on the humid (and hot) and dry (and cold) periods. For sensible FBRs as presented in Chapter 3, the temperature sensors exposed to a sawtooth temperature profile measure the average temperatures (and thereby accurately predict the effectiveness) during each period regardless of the temperature sensor characteristics and the sides where measurements were taken (i.e., hot and cold sides of FBRs). Thus, there is no need to do averaging for sensible FBRs.

(a) cold and dry period

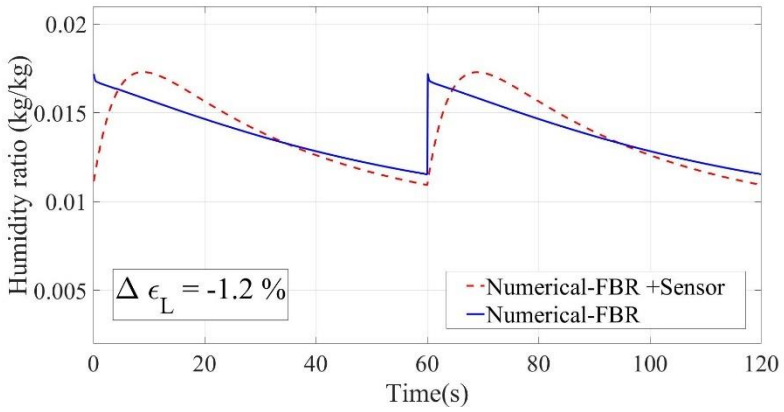

(b) hot and humid period

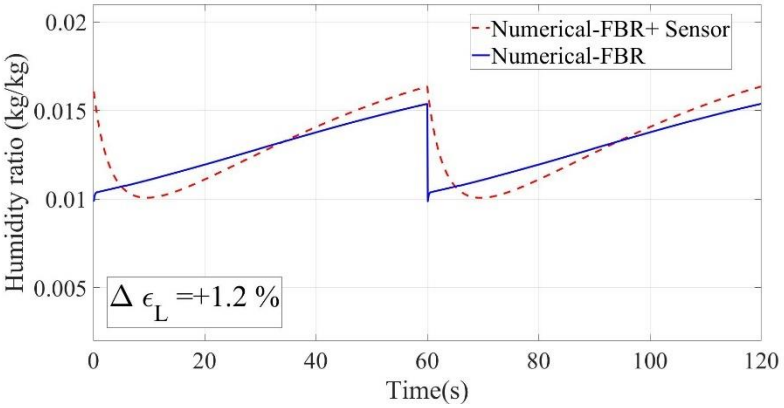

Figure 5.16. (a) Quasi-steady-state humidity ratio profile (FBR model) for FBR with sawtooth profile and its response (FBR+ Sensor model) for time constants of $\tau_{t,int}$=25s, $\tau_{h,int}$=5s and τ_s=3s at (a) cold and dry period and (b) hot and humid period (NTU_o=3, Cr^*=3, λ=0.08, $Cr_m{}^*$=0.3, and η=0.1 at the AHRI summer test conditions (H^*=1.6)).

5.9.3 Impact of operating condition factor (H^*) on latent effectiveness error

The latent effectiveness error depends on the direction of heat and moisture transfer in desiccant-coated FBRs, and this could be quantified by varying H^*(the operating condition factor presented in Fig. 5.3).

Figure 5.17 shows the latent effectiveness error while varying H^* for different sensor arrangements, i.e., duct and exchanger sensors for FBRs exposed to semi-sawtooth profiles and sensors exposed to sawtooth profiles. When H^* approaches zero (when moisture transfer is low,

but the temperature changes are high across the FBR), the latent effectiveness errors increase significantly because of the large internal temperature time constant of the humidity sensor. The latent effectiveness error decreases as H^* increases which is due to small magnitude of temperature changes in these operating conditions across the FBR.

The effectiveness errors for sensors exposed to sawtooth profiles are smaller (less than ±3%) for all H^* values. Furthermore, the effectiveness errors on the dry and humid sides (or supply and exhaust sides) for sensors that experience sawtooth profiles are equal but with an opposite sign, as mentioned in the previous section. Thus, the effectiveness could be average on both sides to obtain the accurate effectiveness for FBR with a sawtooth outlet profile. However, as pointed out in section 5.9.1 and can be seen in Fig. 5.17, the effectiveness error on dry and humid sides of FBRs with semi-sawtooth profile (duct and exchanger sensors) are not equal and both sides need to be treated separately.

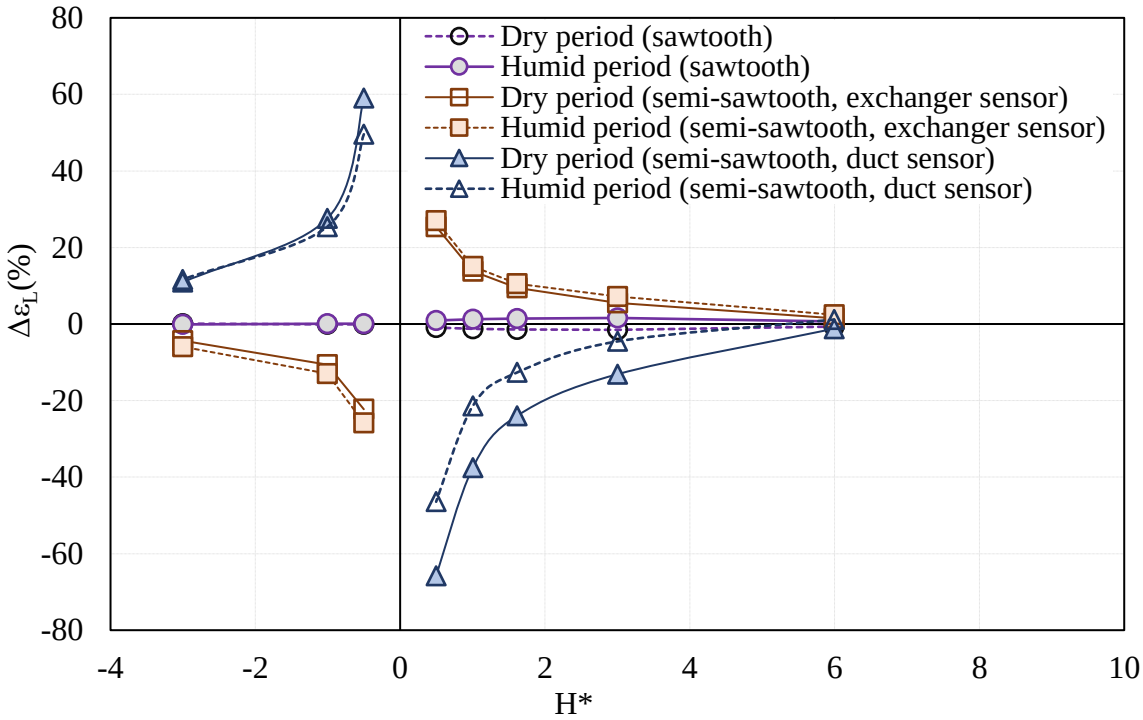

Figure 5.17. Effect of operating condition parameter (H*) on the latent effectiveness error at NTU_o=3, Cr^*=3, Cr_m^*=0.3, and λ=0.08 and measurement sensors with time constants of $\tau_{t,int}$=25s, $\tau_{h,int}$=5s and τ_s=3s.

Figure 5.18 shows the average of the latent effectiveness errors from the hot (and humid) period and cold (and dry) period for different sensor arrangements (duct and exchanger sensors for FBRs with semi-sawtooth profile, and sensors exposed to FBR with sawtooth profile) versus H^*. The sensor with sawtooth profile has average errors that are very close to zero (less than 0.005%) in all values of H^*. The average values of the duct and exchanger sensors ($0.5\times((\Delta\varepsilon_{L,ave})_{exchanger} + (\Delta\varepsilon_{L,ave})_{duct})$) are also presented in this figure. Since the exchanger and duct sensors have opposite effectiveness errors signs, their average could be used to determine the latent effectiveness (with ±5% error) when $H^*>1.6$ and $H^*<-1$, according to Fig. 5.18. Such observation is valuable as test facilities (such as the one developed by Krishnan et al. [20]) could be built to accurately measure latent effectiveness directly from the sensor measurements.

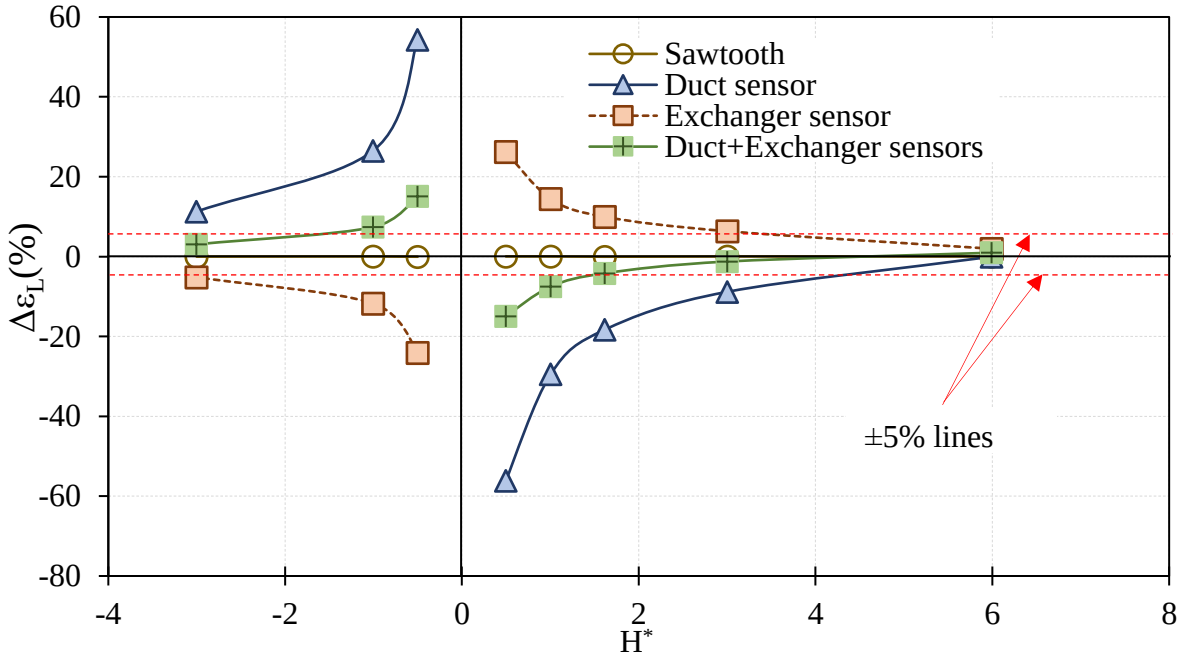

Figure 5.18. Average of the hot (and humid) and cold (and dry side) latent effectiveness errors for sensors exposed to sawtooth, and semi sawtooth (exchanger and duct sensors) profiles and the average of latent effectiveness errors for duct and exchanger sensors.

The effect of doubling all time constants on $\Delta\varepsilon_{L,ave}$ is presented in Fig. 5.19. $\Delta\varepsilon_{L,ave}$ remains very close to zero (less than 0.02%) for the sensors exposed to sawtooth profile over the range of H^*, which suggests that $\Delta\varepsilon_{L,ave}$ are independent of sensors transient characteristics for these types of FBRs. For the duct sensors, the absolute $\Delta\varepsilon_{L,ave}$ increases when sensor time constants doubles. The exchanger sensors absolute $\Delta\varepsilon_{L,ave}$ increase for negative H^* while decreases for positive H^* for doubling the sensors time constants. Further studies are required to understand the impact of sensor transient characteristics on effectiveness errors for the duct and exchanger sensors.

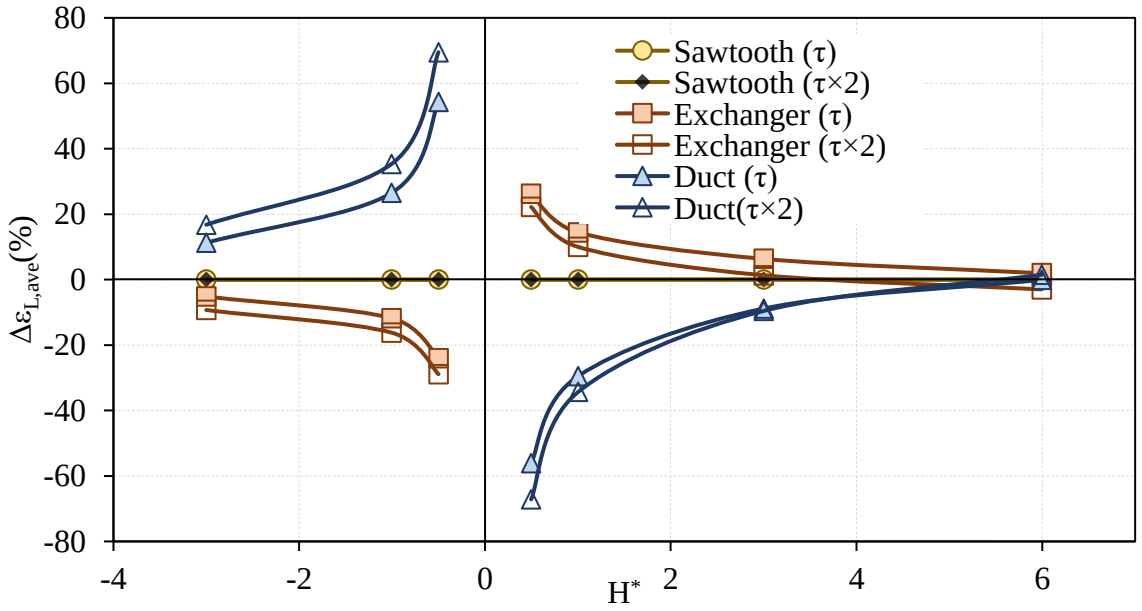

Figure 5.19. Comparison of the average effectiveness error for different sensor configurations with the original time constants ($\tau_{t,int}$=25s, $\tau_{h,int}$=5s and τ_s=3s) and when the original time constants are doubled ($\tau_{t,int}$=50s, $\tau_{h,int}$=10s and τ_s=6s).

5.9.4 **Testing standards**

ASHRAE standard 84 [21] and CSA C439-18 standard [22] do not distinguish between FBRs in terms of their air outlet properties profile, i.e., sawtooth and semi-sawtooth profiles. However, the current study results show that the measurement requirements for desiccant-coated FBRs depend on the shape of their outlet properties profile.

The average latent effectiveness on the dry and humid sides of FBRs with sawtooth profile can be used as an accurate estimate for the latent effectiveness as found in this research regardless of the measurement sensor characteristics. Therefore, it can be concluded that the sensor requirements for FBRs with a sawtooth outlet profile in the standards could be relaxed. However, there is no simple recommendation for FBRs with semi-sawtooth outlet profiles; rather, the latent effectiveness error depends on the location of sensors, sensor transient characteristics, design, and operating conditions. Thus, further studies are required before recommendations can be made on the sensors requirements for FBRs with semi-sawtooth outlet profiles.

The temperature sensor requirements for accurate sensible effectiveness in the testing standards are presented in Chapter 3 and available in the literature [28], indicating that the temperature sensor requirements in standards are stringent and could be relaxed for FBRs with sawtooth outlet temperature profiles. For FBRs with semi-sawtooth profiles, the temperature sensor should be carefully chosen from available tables and graphs (in Chapter 3 and Appendix B) to avoid measurements errors [28]. However, the standard requirement is still conservative for FBR with semi-sawtooth profiles.

The experiment duration to reach the quasi-steady-state condition in the testing standards for sensible FBRs are verified and documented as a conference paper [32]. However, further studies are required to verify the quasi-steady state experiment duration requirements for desiccant-coated FBRs.

5.10 SUMMARY AND CONCLUSIONS

This chapter addresses the fourth objective of this PhD study which is to develop and validate a transient numerical model for desiccant-coated FBR and quantify sensor transient errors. The transient numerical model is essential because both the temperature and humidity of airstreams

at the outlet of the desiccant-coated FBRs vary with time, which poses difficulties for sensors to accurately measure the temperature and humidity changes during the operation of FBRs. The numerical model, consisted of an FBR model and sensor (temperature and humidity sensors) model, has been validated with experimental results from a small-scale test facility. The numerical model can predict the latent effectiveness error due to the transient response of both the humidity and temperature sensors. It was found that the location of the sensors and the configuration of FBR affects the latent effectiveness error. Depending on configurations of FBR, air properties at its outlet follow either sawtooth or semi-sawtooth profiles. There are two different sensor positions for the semi-sawtooth profile, i.e., exchanger sensor and duct sensor. Both the sawtooth, and semi-sawtooth profiles were examined using the validated numerical model.

The latent effectiveness error due to the transient nature of FBRs and sensors depends on the design conditions, operating condition factor (H^*) and the characteristics of the sensors. The error in the measured effectiveness is smaller with a sawtooth profile than with a semi-sawtooth profile. At higher H^* (small temperature difference and considerable moisture content differences between the inlet airstreams of the of FBR, i.e., $|H^*| \gg 1$ or ΔT_{inlet}=small, ΔW_{inlet}=large), the latent effectiveness error is small. However, at smaller H^* ($H^* \approx 0$ or ΔT_{inlet}=large, ΔW_{inlet}=small), the latent effectiveness error may be considerably higher.

For FBRs with a sawtooth profile, the latent effectiveness error on the humid (and hot) and dry (and cold) sides are equal but with the opposite sign. Thus, the effectiveness can be obtained by averaging the effectiveness values from both sides of the FBR. ASHRAE standard 84 and CSA C439-18 standard test configurations produce sawtooth profiles at the outlet of FBRs, and accurate measurement of latent effectiveness is possible by averaging the dry and humid sides of FBR.

For FBRs with semi-sawtooth profiles, the effects of sensor response time and position are significant in the effectiveness evaluation. Also, the dry (and cold) and humid (and hot) sides of the desiccant-coated FBR have different latent effectiveness errors. For these types of desiccant-coated FBR, careful consideration is required to choose the proper measurement instrumentations.

ASHRAE standard 84 and CSA C439-18 standard requirements for sensor characteristics (response time shorter than 2 seconds for FBR with 60s recovery period) at the outlet of the FBR with the sawtooth profile are conservative and could be removed while still maintaining acceptable uncertainty limits. Further studies are required to quantify the impact of different parameters on the latent effectiveness measurements for the desiccant-coated FBRs (with semi-sawtooth profile), which is the topic of future studies. The results of the current study will be helpful to develop the measurement recommendations for the future versions of ASHRAE standard 84 and CSA C439-18 standards for testing the desiccant-coated FBRs.

CHAPTER 6

SUMMARY, CONCLUSIONS, CONTRIBUTIONS AND FUTURE WORK

This PhD study aimed to develop a transient numerical model to accurately evaluate the and optimize the performance of FBRs for HVAC applications. The transient numerical models were developed for sensible and desiccant-coated FBRs, and the models were validated against experimental measurements from the small-scale test facility. The transient model consists of an FBR (exchanger) model and sensor model which can predict the transient characteristics of FBRs and sensors. The results of this study were used to examine the temperature and humidity measurement requirements in the current North American testing standards (ASHRAE Standard 84 and CSA C439-19) for FBRs. The important conclusions related to each objective of this PhD research, the contributions of the thesis, and suggested future potential research topics are summarized in this chapter.

6.1 SUMMARY AND CONCLUSIONS

6.1.1 Objective 1: To develop and validate a transient numerical model for sensible FBR (addressed in Chapter 2)

FBRs are quasi-steady state exchangers and hence, the outlet temperatures of the airstreams vary with time which is different from most of the other types of energy exchangers which have constant temperatures at the outlet during the steady-state condition. This variation poses challenges to accurately measure the temperature at the outlet of FBR, which is needed to determine the sensible effectiveness. A transient numerical model was developed to capture the

transient characteristics of both sensible FBR and temperature sensors. The conclusions from Chapter 2 (objective 1) are:

- It was found that the location of the temperature sensors (whether they are fixed in the outlet duct (duct sensors) or move with the FBR (exchanger sensors)) affects the measured temperature profile and measured effectiveness.
- The duct sensors underestimate the sensible effectiveness, while the exchanger sensors overestimate the sensible effectiveness of FBR.

6.1.2 **Objective 2: To quantify sensor errors over a wide range of design and operating conditions of sensible FBRs and make recommendations for testing standards (addressed in Chapter 3)**

The validated numerical model for sensible FBRs that includes the sensor response was used to quantify the effectiveness errors that result for a range of sensors response characteristics and FBR design parameters. Chapter 3 presents the effectiveness errors at different design conditions and for different FBRs outlet profile shape. The main conclusions from Chapter 3 (objective 2) are:

- It was found that the temperature of the airstreams at the outlet of FBRs follow either sawtooth or semi-sawtooth profiles. The shape of the temperature profile at the outlet affects the temperature measurement requirements.
- For FBRs with sawtooth outlet temperature profiles, the effectiveness can be accurately measured regardless of the sensor time constant. However, the shape of the temperature profile (temperature swing) cannot be captured accurately. In other words, the accurate temperature swing might not be captured while the accurate average temperature is measured for FBR with sawtooth profile.

- For FBRs with semi-sawtooth temperature profile, the effect of sensor response characteristics has a significant effect on the measured effectiveness. The effectiveness errors due to the response of sensors at a wide range of FBR design parameters (NTU_o, Cr^*, and λ) and sensor characteristics (τ_s^*) are assessed and presented in graphs and tables (Appendix B).
- The test configurations in the ASHRAE standard 84 and CSA C439-18 standard produce a sawtooth temperature profile, which results in an accurate effectiveness measurement regardless of the time constant of the temperature sensors. This means that the standards requirement can be relaxed for this type of FBR.
- Temperature measurement requirements in the test standards do not distinguish between FBRs with sawtooth and semi-sawtooth profile. The results obtained in Chapter 3, also, showed that the temperature sensor requirements in standards are stringent and could be relaxed for FBRs with saw-tooth outlet temperature profile for effectiveness evaluations.

6.1.3 **Objective 3: To optimize sensible FBRs considering transient characteristics (addressed in Chapter 4)**

Sensible FBRs operate by alternately storing and releasing heat from exchangers, which results in outlet airstream temperature that varies with time during both hot and cold periods. This variation in the outlet temperature, i.e., temperature swing, could deteriorate occupant thermal comfort and put a variable load on the HVAC systems. Thus, HVAC designers must prevent large temperature swings at the outlet of FBRs. Therefore, the temperature swing must be considered while designing FBRs. Chapter 4 documents the correlation that was developed for temperature swing as a function of design parameters. Chapter 4 also presents multi-objective optimization of FBRs considering temperature swing as an additional objective to the common objectives in the

optimization of exchangers. A multi-criteria decision aid was also used to select the best design from Pareto fronts. The main findings and conclusions from Chapter 4 (objective 3) are:

- It was found that temperature swing (TS) can be predicted as a function of design parameters. A correlation was developed to predict temperature swing (TS) at any design condition. The temperature swing (TS) decreases with an increase in Cr^* or C_λ and increases when NTU_o is increased.
- The addition of TS to the optimization problems does not change the Pareto fronts at higher values of effectiveness and pressure drop but changes the Pareto fronts in the low to medium ranges of effectiveness and pressure drop. At these ranges, the exchanger mass increases to decrease the temperature swing.
- When TS is included in the decision-making process, a heavier exchanger is chosen to produce a smaller TS. The decrease in TS is less than 1ºC when the FBR is optimized considering TS as an objective, while the pressure drop and exchanger mass increase between 30-60%. Thus, including TS when optimizing FBRs would not improve TS significantly, while penalties for exchanger mass and pressure drop are considerable.

6.1.4 Objective 4: To develop and validate a transient numerical model for desiccant-coated FBRs and quantify sensor errors (addressed in Chapter 5)

The air properties (i.e., temperature and humidity) at the outlet of desiccant-coated FBRs vary with time. Measuring air properties at the outlet of the desiccant-coated FBRs is complicated because of the coupled heat and moisture transfer and temperature dependence of humidity sensor (triple time constant involved in the measurement of humidity sensors). A numerical model was developed to evaluate the performance of desiccant-coated FBRs considering their transient nature. The model comprises of an exchanger model (FBR model) and sensor model (temperature

sensor and humidity sensor) to distinguish the actual performance from the measured performance. The developed model is validated with the experimental measurements from a small-scale test facility. The main findings and conclusions from Chapter 5 (objective 4) are:

- Depending on the configuration of FBRs (single-core and double-core) and measurement sensor locations, the outlet properties profile could be generally classified into sawtooth and semi-sawtooth profiles, like sensible FBRs. The measurement requirements depend on the shape of outlet profile, i.e., semi-sawtooth or sawtooth profile. Effectiveness errors for FBRs with a semi-sawtooth profile are larger than for FBRs with a sawtooth outlet profile.
- For FBRs with a sawtooth profile (in the double-core FBRs as per the ASHRAE standard 84 and CSA C439-18 standard), the effectiveness error on the humid (and hot) and dry (and cold) sides are equal but with the opposite sign. Thus, the effectiveness can be obtained by taking average of the effectiveness values from both sides. This is an important distinction from sensible FBRs as the effectiveness error is the same on both the supply and exhaust sides of sensible FBRs. The latent effectiveness error due to the slow response of sensors depends on the design conditions, operating condition factor (H^*) and the characteristics of the measurement sensors.
- For FBRs with a semi-sawtooth profile (such as single-core FBRs), the effects of sensor response time and position on measured effectiveness are significant. The latent effectiveness error due to the transient nature of FBR and sensors depends on the design conditions, operating condition factor (H*) and the characteristics of the measurement sensors. Also, the dry (and cold) and humid (and hot) sides of the desiccant-coated FBR have different effectiveness errors. So, they cannot be simply averaged to determine the effectiveness.

- ASHRAE standard 84 and CSA C439-18 standard recommendations for measurement of air properties at the outlet of FBR are conservative and could be relaxed for FBR with sawtooth profile. Further studies are required to provide specific recommendations for FBR with semi-sawtooth profiles.

6.2 CONTRIBUTIONS

The findings from this research contribute towards understanding and quantifying the transient characteristics of FBRs for energy recovery in HVAC applications. The contributions of this PhD research are summarized in the following:

- A new transient numerical model was developed to capture the transient nature of FBRs (sensible and desiccant-coated FBRs) and temperature and humidity sensors. The model can accurately predict both the outlet airstreams properties profiles and effectiveness.
- Properties measurement requirements in the testing standards for FBRs (ASHRAE standard 84 and CSA C439-18 standard) were examined and recommendations were provided for the future versions of such standards.
- A correlation was developed for temperature swing and FBR is optimized considering its transient characteristics. Furthermore, it was shown that temperature swing does not need to be included with the optimization of FBRs for HVAC applications.

6.3 FUTURE WORK

6.3.1 Optimization of FBRs considering transient characteristics

Sensible FBRs were optimized considering their transient nature of operation in this thesis. Desiccant-coated FBRs have not been optimized for HAVC application and this could be a subject

of future studies. Also, the transient characteristics of the desiccant-coated FBRs could be included in the optimization process. Furthermore, optimization of arrangements of FBRs in HVAC systems could be the subject of future studies. For example, different combinations of sensible and desiccant-coated FBRs in an air handling unit could be proposed and optimized for different climate conditions.

6.3.2 Modeling and optimization of energy transfer enhancement methods

To improve the performance of FBRs and reduce the size and exchanger mass, heat and moisture transfer enhancement techniques such as the corrugation patterns on the surface of the exchanger plate could be studied in detail. Although the current numerical model can predict the effectiveness of FBRs if the average heat transfer coefficient is available, a detailed CFD simulation could shed light on the enhancement techniques to maximize heat and moisture transfer in FBRs. Furthermore flow maldistributions from channel to channel could be the topic of future studies.

6.3.3 Measurement sensor requirements for desiccant-coated FBRs with semi-sawtooth outlet air properties profile

It was concluded that the measurement requirements for desiccant-coated FBR depend on its outlet air profile shape (sawtooth or semi-sawtooth). For desiccant-coated FBRs with sawtooth outlet air properties profile, the standard (ASHRAE standard 84 and CSA C439-18 standard) requirements could be relaxed. However, for desiccant-coated FBRs with semi-sawtooth outlet air properties profiles, the measurement requirements depend on sensor characteristics and position (exchanger or duct sensor), design conditions, operating conditions parameters, and desiccant properties. Further studies are required to quantify the effectiveness errors over a wide range of design and operating parameters.

6.3.4 **Experiment duration before reaching quasi-steady-state conditions**

Measurement requirements in the testing standards for sensible and desiccant-coated FBRs were examined in this research and recommendation were provided to include in the future versions of the standards. To reach the quasi-steady-state conditions, the testing standards recommend a one-hour experiment duration. This requirement for sensible FBRs is studied and the results are published in a conference paper [32]. The results show that sensible FBRs reach a quasi-steady-state condition in less than one hour and the experiment duration recommendation is adequate. However, similar studies are not available for the desiccant-coated FBRs, which could be the subject of future studies.

6.3.5 **Condensation and frosting in FBRs**

Frosting and condensation are practical problems and might limit the application of FBRs in HVAC applications. It is critical to select and operate FBRs in such a way that avoids the uncontrolled formation of condensation and frosting. Future experimental research and numerical studies should be conducted to analyze the formation of condensation and frost within FBRs and their effect on effectiveness and pressure drop.

REFERENCES

[1] United Nations Department of Economic and Social Affairs, 2015, "Transforming Our World: The 2030 Agenda for Sustainable Development" [Online]. Available: https://sdgs.un.org/2030agenda. [Accessed: 02-Jan-2020].

[2] Allouhi, A., El Fouih, Y., Kousksou, T., Jamil, A., Zeraouli, Y., and Mourad, Y., 2015, "Energy Consumption and Efficiency in Buildings: Current Status and Future Trends," Journal of Cleaner Production, **109**, pp. 118–130.

[3] Natural Resources Canada, 2018, "Canada's GHG Emissions by Sector, End-Use, and Subsector," Energy Use Data Handbook Tables [Online]. Available: https://oee.nrcan.gc.ca/corporate/statistics/neud/dpa/showTable.cfm?type=HB&sector=aaa&juris=ca&rn=2&page=1. [Accessed: 20-Aug-2020].

[4] Edenhofer, O., Pichs-Madruga, R., Sokona, Y., C. Minx, J., Farahani, E., Kadner, S., Seyboth, K., Adler, A., Baum, I., Brunner, S., Eickemeier, P., Kriemann, B., Savolainen, J., Schlomer, S., Von Stechow, C., and Zwickesl, T., 2014, *Climate Change 2014: Mitigation of Climate Change. Contribution of Working Group III to the Fifth Assessment Report of the Intergovernmental Panel on Climate Change*, Cambridge University Press, Cambridge.

[5] Berardi, U., 2017, "A Cross-Country Comparison of the Building Energy Consumptions and Their Trends," Resources, Conservation & Recycling, **123**, pp. 230–241.

[6] Mofidi, F., and Akbari, H., 2017, "Personalized Energy Costs and Productivity Optimization in Offices," Energy and Buildings, **143**, pp. 173–190.

[7] Jouhara, H., Khordehgah, N., Almahmoud, S., Delpech, B., Chauhan, A., and Tassou, S. A., 2018, "Waste Heat Recovery Technologies and Applications," Thermal Science and Engineering Progress, **6**, pp. 268–289.

[8] Skiepko, T., and Shah, R. K., 2005, "Modeling and Effect of Leakages on Heat Transfer Performance of Fixed Matrix Regenerators," International Journal of Heat and Mass Transfer, **48**(8), pp. 1608–1632.

[9] Zarrinehkafsh, M. T., and Sadrameli, S. M., 2004, "Simulation of Fixed-Bed Regenerative Heat Exchangers for Flue Gas Heat Recovery," Applied Thermal Engineering, **24**, pp. 373–382.

[10] Reboussin, Y., Fourmigué, J. F., Marty, P., and Citti, O., 2005, "A Numerical Approach for the Study of Glass Furnace Regenerators," Applied Thermal Engineering, **25**, pp. 2299–2320.

[11] Ramin, H., Krishnan, E. N., and Simonson, C. J., 2019, "Fixed Bed Regenerators for HVAC Applications," *27th Canadian Congress of Applied Mechanics*, Sherbrooke, Québec, Canada, pp. 1–6.

[12] Chang, C. C., Liang, J. De, and Chen, S. L., 2018, "Performance Investigation of Regenerative Total Heat Exchanger with Periodic Flow," Applied Thermal Engineering, **130**, pp. 1319–1327.

[13] Borodulin, V. Y., and Nizovtsev, M. I., 2018, "A Criterial Analysis of the Effectiveness of

Air-to-Air Heat Exchangers with Periodic Change of Airflow Direction," Applied Thermal Engineering, **130**, pp. 1246–1255.

[14] Aristov, Y. I., Mezentsev, I. V., and Mukhin, V. A., 2008, "A New Approach to Regenerating Heat and Moisture in Ventilation Systems," Energy and Buildings, **40**(3), pp. 204–208.

[15] Nizovtsev, M. I., Borodulin, V. Y., and Letushko, V. N., 2017, "Influence of Condensation on the Efficiency of Regenerative Heat Exchanger for Ventilation," Applied Thermal Engineering, **111**, pp. 997–1007.

[16] Nizovtsev, M. I., Borodulin, V. Y., Letushko, V. N., and Zakharov, A. A., 2016, "Analysis of the Efficiency of Air-to-Air Heat Exchanger with a Periodic Change in the Flow Direction," Applied Thermal Engineering, **93**, pp. 113–121.

[17] Tempeff, 2020, "Heat Recovery System | Heat Recovery Ventilator | ERV | Energy Recovery" [Online]. Available: https://www.tempeffnorthamerica.com/. [Accessed: 06-Jan-2020].

[18] Hausen, H., 1983, *Heat Transfer in Counterflow, Parallel Flow and Cross Flow*, McGraw-Hill, Inc., New York.

[19] Shah, R. K., and Sekulic, D. P., 2004, *Fundamentals of Heat Exchanger Design*, John Wiley & Sons, Inc., New Jersey.

[20] Krishnan, E. N., Ramin, H., Shakouri, M., Wilson, L. D., and Simonson, C. J., 2020, "Development of a Small-Scale Test Facility for Effectiveness Evaluation of Fixed-Bed Regenerators," Applied Thermal Engineering, **174**, p. 115263.

[21] ASHRAE, 2020, *ANSI/ASHRAE Standard 84-2020, Method of Testing Air-to-Air Heat/Energy Exchangers*, ASHRAE, Atlanta.

[22] CSA Group, 2018, *CSA C439 Laboratory Methods of Test for Rating the Performance of Heat / Energy-Recovery*, CSA Group, Toronto.

[23] Rabah, A. A., Fekete, A., and Kabelac, S., 2009, "Experimental Investigation on a Rotary Regenerator Operating at Low Temperatures," ASME Journal of Thermal Science and Engineering Applications, **1**(4), pp. 1–9.

[24] Justo Alonso, M., Liu, P., Mathisen, H. M., Ge, G., and Simonson, C. J., 2015, "Review of Heat/Energy Recovery Exchangers for Use in ZEBs in Cold Climate Countries," Building and Environment, **84**, pp. 228–237.

[25] Seo, J. W., Lee, D. Y., and Kim, D. S., 2018, "A Simple Effectiveness Model for Heat Wheels," International Journal of Heat and Mass Transfer, **120**, pp. 1358–1364.

[26] Fathieh, F., Besant, R. W., Evitts, R. W., and Simonson, C. J., 2015, "Determination of Air-to-Air Heat Wheel Sensible Effectiveness Using Temperature Step Change Data," International Journal of Heat and Mass Transfer, **87**, pp. 312–326.

[27] Fathieh, F., 2016, "A Novel Transient Testing Method for Heat/Energy Wheel Components," PhD thesis, University of Saskatchewan, https://harvest.usask.ca/handle/10388/7381 .

[28] Ramin, H., Krishnan, E. N., Annadurai, G., Alabi, W. O., and Simonson, C. J., 2021,

"Transient Sensor Errors and Their Impact on Fixed-Bed Regenerator (FBR) Testing Standards," Science and Technology for the Built Environment, **27**(5), pp. 656–678.

[29] Kreith, F., and Michaelides, E. E., 2018, *CRC Handbook of Thermal Engineering*, Taylor & Francis, CRC Press, Boca Raton, Florida.

[30] Klein, H., Klein, S. A., and Mitchell, J. W., 1990, "Analysis of Regenerative Enthalpy Exchangers," International Journal of Heat and Mass Transfer, **33**(4), pp. 735–744.

[31] Nóbrega, C. E. L., and Brum, N. C. L., 2013, *Desiccant-Assisted Cooling: Fundamentals and Applications*, Springer, New York.

[32] Ramin, H., Krishnan, E. N., Annadurai, G., and Simonson, C. J., 2020, "Transient Performance of Fixed-Bed Regenerators for Energy Recovery in Building Applications," *ASME 2020 Heat Transfer Summer Conference*, ASME, Orlando, Florida.

[33] Ramin, H., Krishnan Wahab Alabi, E. N., and Simonson, C. J., 2020, "Temperature Measurement Correction for the Determination of the Effectiveness of Fixed-Bed Regenerators (FBRs) for HVAC Applications," *ASHRAE Transactions*, ASHRAE, Austin, pp. 366–374.

[34] Bergman L., T., Lavine S., A., Incropera, F. P., and DeWitt, D. P., 2011, *Fundamentals of Heat and Mass Transfer*, John Wiley & Sons, Inc., Danvers.

[35] Simonson, C. J., and Besant, R. W., 1999, "Energy Wheel Effectiveness: Part I-Development of Dimensionless Groups," International Journal of Heat and Mass Transfer, **42**(12), pp. 2161–2170.

[36] Simonson, C. J., and Besant, R. W., 1997, "Heat and Moisture Transfer in Desiccant Coated Rotary Energy Exchangers: Part I. Numerical Model," HVAC&R Research, **3**(4), pp. 351–368.

[37] Shang, W., and Besant, R. W., 2008, "Theoretical and Experimental Methods for the Sensible Effectiveness of Air-to-Air Energy Recovery Wheels," HVAC&R Research, **14**(3), pp. 373–396.

[38] Shah, R. K., London, A. L., and White, F. M., 1978, *Laminar Flow Forced Convection in Ducts: A Source Book for Compact Heat Exchanger Analytical Data*, Academic Press, New York.

[39] Versteeg, H. K., and Malalasekera, W., 2007, *An Introduction to Computational Fluid Dynamics*, Pearson Education Limited, Essex.

[40] Simonson, C. J., 1998, "Heat and Moisture Transfer in Energy Wheels," PhD thesis, University of Saskatchewan, https://harvest.usask.ca/handle/10388/etd-04052005-223929?show=full.

[41] Bahnke, G. D., and Howard, C. P., 1964, "The Effect of Longitudinal Heat Conduction on Periodic-Flow Heat Exchanger Performance," ASME Journal of Engineering for Gas Turbines and Power, **86**(2), pp. 105–117.

[42] Shah, R. K., 1975, "Correlation for Longitudinal Heat Conduction Effects in Periodic-Flow Heat Exchangers.," ASME Journal of Engineering for Gas Turbines and Power, (3), pp. 453–454.

[43] Büyükalaca, O., and Yilmaz, T., 2002, "Influence of Rotational Speed on Effectiveness of Rotary-Type Heat Exchanger," Heat and Mass Transfer, **38**, pp. 441–447.

[44] Krishnan, E., Ramin, H., and Simonson, C. J., 2019, "Performance Testing of Fixed-Bed Regenerators for HVAC Applications," *The Second Pacific Rim Thermal Engineering Conference*, Hawaii, pp. 1–5.

[45] Abdel-Salam, M. R. H., Fauchoux, M., Ge, G., Besant, R. W., and Simonson, C. J., 2014, "Expected Energy and Economic Benefits, and Environmental Impacts for Liquid-to-Air Membrane Energy Exchangers (LAMEEs) in HVAC Systems: A Review," Applied Energy, **127**, pp. 202–218.

[46] El-Dessouky, H., Ettouney, H., and Al-Zeefari, A., 2004, "Performance Analysis of Two-Stage Evaporative Coolers," Chemical Engineering Journal, **102**(3), pp. 255–266.

[47] Ramin, H., Hanafizadeh, P., Ehterami, T., and AkhavanBehabadi, M. A., 2019, "Life Cycle-Based Multi-Objective Optimization of Wall Structures in Climate of Tehran," Advances in Building Energy Research, **13**(1), pp. 18–31.

[48] Rezaie, B., Esmailzadeh, E., and Dincer, I., 2011, "Renewable Energy Options for Buildings: Case Studies," Energy and Buildings, **43**(1), pp. 56–65.

[49] Roulet, C. A., Heidt, F. D., Foradini, F., and Pibiri, M. C., 2001, "Real Heat Recovery with Air Handling Units," Energy and Buildings, **33**(5), pp. 495–502.

[50] Ramin, H., Krishnan, E. N., Gurubalan, A., Alabi, W. O., and Simonson, C. J., 2021, "A Transient Numerical Model for Sensible Fixed-Bed Regenerator in HVAC Applications," International Journal of Heat and Mass Transfer, **177**, p. 121550.

[51] Aristov, Y. A., Mezentsev, I. V., and Mukhin, V. A., 2006, "A New Approach to Heat and Moisture Regeneration in the Ventilation System of Rooms. I. Laboratory Prototype of the Regenerator," Journal of Engineering Physics and Thermophysics, **79**(3), pp. 569–576.

[52] Chang, C. C., Lai, C. H., Yang, C. M., Chiang, Y. C., and Chen, S. L., 2013, "Thermal Performance Enhancement of a Periodic Total Heat Exchanger Using Energy-Storage Material," Energy and Buildings, **67**, pp. 579–586.

[53] Chang, C. C., Chen, S. L., Lin, T. Y., and Chiang, Y. C., 2017, "Experimental and Theoretical Investigation of Regenerative Total Heat Exchanger with Periodic Flow for Air-Conditioning Systems," International Journal of Refrigeration, **81**, pp. 123–133.

[54] Hashemian, H., 2011, "Measurement of Dynamic Temperatures and Pressures in Nuclear Power Plants," PhD thesis, The University of Western Ontario, https://ir.lib.uwo.ca/cgi/viewcontent.cgi?referer=&httpsredir=1&article=1290&context=etd.

[55] Wang, S., Tang, J., and Younce, F., 2003, "Temperature Measurement," *Encyclopedia of Agricultural, Food, and Biological Engineering*, Marcel Dekker, Inc, New York, pp. 987–993.

[56] Abe, O. O., Besant, R. W., Simonson, C. J., and Shang, W., 2006, "Relationship between Energy Wheel Speed and Effectiveness and Its Transient Response, Part I: Mathematical Development of the Characteristic Time Constants and Their Relationship with Effectiveness," *ASHRAE Transactions*, pp. 89–102.

[57] Figliola, R. S., and Beasley, D. E., 2010, *Theory and Design for Mechanical Measurements*,

John Wiley & Sons Inc, Hoboken, New Jersey.

[58] COVID-19 Task Force of REHVA's Technology and Research Committee, 2020, *REHVA COVID-19 Guidance Document*.

[59] ASHRAE (TC 5.5), 2020, *Practical Guidance for Epidemic Operation of Energy Recovery Ventilation Systems*, ASHRAE, Atlanta.

[60] Shakouri, M., Krishnan, E. N., Karoyo, A. H., Dehabadi, L., Wilson, L. D., and Simonson, C. J., 2019, "Water Vapor Adsorption-Desorption Behavior of Surfactant-Coated Starch Particles for Commercial Energy Wheels," ACS Omega, **4**, pp. 14378–14389.

[61] Krishnan, E. N., Ramin, H., Gurubalan, A., Alabi, W. O., and Simonson, C. J., 2021, "Methodologies for Predicting the Effectiveness of Full-Scale Fixed-Bed Regenerators from Small-Scale Test Data," ASME Journal of Thermal Science and Engineering Applications, **13**(5), pp. 1–34.

[62] Ramin, H., Krishnan, E. N., and Simonson, C. J., 2020, "Effectiveness of Fixed-Bed Regenerators for Energy Recovery in Buildings Applications," E3S Web Conferences, **172**, pp. 1–8.

[63] Güllüce, H., and Özdemir, K., 2020, "Design and Operational Condition Optimization of a Rotary Regenerative Heat Exchanger," Applied Thermal Engineering, **177**, p. 115341.

[64] Wang, L., Bu, Y., Li, D., Tang, C., and Che, D., 2019, "Single and Multi-Objective Optimizations of Rotary Regenerative Air Preheater for Coal-Fired Power Plant Considering the Ammonium Bisulfate Deposition," International Journal of Thermal Sciences, **136**, pp. 52–59.

[65] Lee, Y. M., Chung, H., Kim, S. H., Bae, H. S., and Cho, H. H., 2017, "Optimization of the Heating Element in a Gas-Gas Heater Using an Integrated Analysis Model," Energies, **10**(12), pp. 1-19.

[66] Raja, B. D., Jhala, R. L., and Patel, V., 2016, "Multi-Objective Optimization of a Rotary Regenerator Using Tutorial Training and Self-Learning Inspired Teaching-Learning Based Optimization Algorithm (TS-TLBO)," Applied Thermal Engineering, **93**, pp. 456–467.

[67] Mioralli, P. C., and Ganzarolli, M. M., 2013, "Thermal Analysis of a Rotary Regenerator with Fixed Pressure Drop or Fixed Pumping Power," Applied Thermal Engineering, **52**(1), pp. 187–197.

[68] Tušek, J., Kitanovski, A., and Poredoš, A., 2013, "Geometrical Optimization of Packed-Bed and Parallel-Plate Active Magnetic Regenerators," International Journal of Refrigeration, **36**(5), pp. 1456–1464.

[69] Rao, R. V., and Patel, V., 2011, "Design Optimization of Rotary Regenerator Using Artificial Bee Colony Algorithm," *Proceedings of the Institution of Mechanical Engineers, Part A: Journal of Power and Energy*, pp. 1088–1098.

[70] Dallaire, J., Gosselin, L., and da Silva, A. K., 2010, "Conceptual Optimization of a Rotary Heat Exchanger with a Porous Core," International Journal of Thermal Sciences, **49**(2), pp. 454–462.

[71] Sanaye, S., and Hajabdollahi, H., 2009, "Multi-Objective Optimization of Rotary Regenerator Using Genetic Algorithm," International Journal of Thermal Sciences, **48**(10),

pp. 1967–1977.

[72] Natarajan, E., and Pitchandi, K., 2009, "Thermodynamic Optimization of Periodic Regenerative Heat Exchanger," World Academy of Science, Engineering and Technology, **56**, pp. 509–517.

[73] Chung, J. D., Lee, D. Y., and Yoon, S. M., 2009, "Optimization of Desiccant Wheel Speed and Area Ratio of Regeneration to Dehumidification as a Function of Regeneration Temperature," Solar Energy, **83**(5), pp. 625–635.

[74] Sanaye, S., Jafari, S., and Ghaebi, H., 2008, "Optimum Operational Conditions of a Rotary Regenerator Using Genetic Algorithm," Energy and Buildings, **40**(9), pp. 1637–1642.

[75] Gao, W., Hodgson, P. D., and Kong, L., 2006, "Numerical Analysis of Heat Transfer and the Optimization of Regenerators," Numerical Heat Transfer, Part A: Applications, **50**(1), pp. 63–78.

[76] Jassim, R. K., 2003, "Evaluation of Combined Heat and Mass Transfer Effect on the Thermoeconomic Optimization of an Air-Conditioning Rotary Regenerator," Journal of Heat Transfer, **125**(4), pp. 724–733.

[77] Shen, C. M., and Worek, W. M., 1993, "Second-Law Optimization of Regenerative Heat Exchangers, Including the Effect of Matrix Heat Conduction," Energy, **18**(4), pp. 355–363.

[78] Mathworks-Inc., 2019, "MATLAB: R2019b."

[79] Lv, C., Xing, Y., Zhang, J., Na, X., Li, Y., Liu, T., Cao, D., and Wang, F. Y., 2018, "Levenberg-Marquardt Backpropagation Training of Multilayer Neural Networks for State Estimation of a Safety-Critical Cyber-Physical System," IEEE Transactions on Industrial Informatics, **14**(8), pp. 3436–3446.

[80] Ghasemi, A., Hassani, M., Goodarzi, M., Afrand, M., and Manafi, S., 2019, "Appraising Influence of COOH-MWCNTs on Thermal Conductivity of Antifreeze Using Curve Fitting and Neural Network," Physica A: Statistical Mechanics and its Applications, **514**, pp. 36–45.

[81] Safaei, M. R., Hajizadeh, A., Afrand, M., Qi, C., Yarmand, H., and Zulkifli, N. W. B. M., 2019, "Evaluating the Effect of Temperature and Concentration on the Thermal Conductivity of ZnO-TiO2/EG Hybrid Nanofluid Using Artificial Neural Network and Curve Fitting on Experimental Data," Physica A: Statistical Mechanics and its Applications, **519**, pp. 209–216.

[82] Asiedu, Y., Besant, R. W., and Simonson, C. J., 2004, "Wheel Selection for Heat and Energy Recovery in Simple HVAC Ventilation Design Problems," 2004 Winter Meeting and Technology Symposium of ASHRAE, pp. 375–392.

[83] University of California, 2014, "Climate Consultant 6.0."

[84] Ramin, H., Hanafizadeh, P., and Akhavan-Behabadi, M. A., 2016, "Determination of Optimum Insulation Thickness in Different Wall Orientations and Locations in Iran," Advances in Building Energy Research, **10**(2), pp. 149–171.

[85] Deb, K., 2001, *Multi-Objective Optimization Using Evolutionary Algorithms*, John Wiley & Sons, Ltd, New York.

[86] Deb, K., Pratap, A., Agarwal, S., and Meyarivan, T., 2002, "A Fast and Elitist Multiobjective Genetic Algorithm: NSGA-II," IEEE Transactions on Evolutionary Computation, **6**(2), pp. 182–197.

[87] Kumar, A., Sah, B., Singh, A. R., Deng, Y., He, X., Kumar, P., and Bansal, R. C., 2017, "A Review of Multi-Criteria Decision Making (MCDM) towards Sustainable Renewable Energy Development," Renewable and Sustainable Energy Reviews, **69**(June 2016), pp. 596–609.

[88] Papathanasiou, J., and Ploskas, N., 2018, *Multiple Criteria Decision-Aid Methods(MCDA)-Methods, Examples and Python Implementations*, Springer, Gewerbestrasse.

[89] Gaddala, U. M., and Devanuri, J. K., 2020, "A Hybrid Decision-Making Method for the Selection of a Phase Change Material for Thermal Energy Storage," ASME Journal of Thermal Science and Engineering Applications, **12**(4), pp. 1–11.

[90] ASHRAE, 2012, *HVAC Systems and Equipment*, ASHRAE, Atlanta.

[91] Diao, Y., Zhang, J., Yu, W., and Zhao, Y., 2014, "Experimental Study on the Heat Recovery Characteristic of a Plate Heat Pipe Heat Exchanger in Room Ventilation," HVAC&R Research, **20**(7), pp. 828–835.

[92] Wemhoener, C., Hässig, W., Wyss, S., and Staubli, J., 2016, "Heat Pump Application in Nearly Zero Energy Buildings," Science and Technology for the Built Environment, **23**(4), pp. 637–650.

[93] Lowenstein, A., 2008, "Review of Liquid Desiccant Technology for HVAC Applications," HVAC&R Research., **14**(6), pp. 819–839.

[94] Fan, H., Simonson, C. J., Besant, R. W., and Shang, W., 2006, "Performance of a Run-around System for HVAC Heat and Moisture Transfer Applications Using Cross-Flow Plate Exchangers Coupled with Aqueous Lithium Bromide," HVAC&R Research, **12**(2), pp. 313–336.

[95] Cerrah, E., McCague, C., and Bahrami, M., 2020, "Sorbent Based Enthalpy Recovery Ventilator," Energy and Buildings, **211**.

[96] Simonson, C. J., and Besant, R. W., 1997, "Heat and Moisture Transfer in Desiccant Coated Rotary Energy Exchangers: Part II. Validation and Sensitivity Studies," HVAC&R Research, **3**(4), pp. 351–368.

[97] Simonson, C. J., and Besant, R. W., 1999, "Energy Wheel Effectiveness: Part II-Correlations," International Journal of Heat and Mass Transfer, **42**(12), pp. 2171–2185.

[98] Simonson, C. J., and Besant, R. W., 1999, "Energy Wheel Effectiveness: Part I-Development of Dimensionless Groups," International Journal of Heat and Mass Transfer, **42**(12), pp. 2161–2170.

[99] Kaplya, V. I., Kaplya, E. V., and Silaev, A. A., 2020, "Identification of the Transient Response of a Capacitive Relative Humidity Sensor," Measurement Techniques, **62**(12), pp. 1099–1105.

[100] Krishnan, E. N., Ramin, H., Gurubalan, A., and Simonson, C. J., "Experimental Methods to Determine the Performance of Desiccant Coated Fixed-Bed Regenerators (FBRs)," International Journal of Heat and Mass Transfer.

APPENDIX A

COPYRIGHT PERMISSIONS

Appendix A contains the copyright permissions for the published and co-authored manuscripts documented in this thesis. For all papers that are included in a thesis, the College of Graduate and Postdoctoral Studies (CGPS) requires a written request from the publisher, *i.e.*, copyright holder (for published manuscripts) and from co-author(s) (for unpublished manuscripts). The permissions for using the published and unpublished manuscripts in this thesis are documented in this appendix.

A.1. PERMISSION FOR MANUSCRIPTS USED IN CHAPTER 2

The manuscript in chapter 2 is published online by Elsevier. Elsevier allows authors to include the accepted/published paper in the thesis without written permission. The statement below has been taken from the Elsevier website.

Source: https://www.elsevier.com/about/policies/copyright/permissions
(accessed: June 25, 2021)

A.2. PERMISSION FOR MANUSCRIPTS USED IN CHAPTER 3

The manuscript in chapter 3 is published online by Taylor & Francis. Taylor & Francis allows authors to include the accepted/published paper in the thesis. The statement below was received from the Taylor & Francis upon the author request.

Dear Hadi Ramin,

Material Requested: 'Hadi Ramin, Easwaran N. Krishnan, Gurubalan Annadurai, Wahab O. Alabi & Carey J. Simonson (2021) Transient sensor errors and their impact on fixed-bed regenerator (FBR) testing standards, Science and Technology for the Built Environment, 27:5, 656-678, DOI: 10.1080/23744731.2020.1846428'.
Thank you for your correspondence requesting permission to reproduce the above content from our Journal in your online thesis and to be posted in the university's repository – University of Saskatchewan.
We will be pleased to grant permission to reproduce your 'Author's Original Manuscript' on the sole condition that you acknowledge the original source of publication.
"This is an Author's Original Manuscript of an article published by Taylor & Francis Group in Science and Technology for the Built Environment available online at https://doi.org/10.1080/23744731.2020.1846428".
You will also need to obtain permission from any co-author's of this article.
Please note we are unable to grant you permission to include the final accepted version within the 12 month embargo period.
Please note: This does not allow the use of the VoR (Version of Record the PDF on the publisher's website) to be posted online, however you may include the VoR as an appendix to the printed version of your thesis.
Using a DOI to link to the VoR on Taylor & Francis Online means that downloads, Altmetric data, and citations can be tracked and collated – data you can use to assess the impact of your work.
This permission does not cover any third party copyrighted work which may appear in the material requested.

Please see below links you may find helpful.

Sharing your work - https://authorservices.taylorandfrancis.com/sharing-your-work/
Accessing your authored works on Taylor & Francis online
- https://authorservices.taylorandfrancis.com/my-authored-works/
Author services - https://authorservices.taylorandfrancis.com/
Please do not hesitate to let me know if I can be of any additional assistance.

With best wishes,

Annabel
Annabel Flude| Permissions Administrator
Journals, Taylor & Francis Group

Permissions e-mail: permissionrequest@tandf.co.uk
Web: www.tandfonline.com

+ 4 Park Square, Milton Park, Abingdon, OX14 4RN
(+44 (0)20 8052 0659

A.3. PERMISSION FOR MANUSCRIPTS USED IN CHAPTER 4

The manuscript in chapter 4 is published online by ASME. ASME allows authors to include the accepted/published paper in the thesis. The statement below was received from the ASME upon the author request.

It is our pleasure to grant you permission to use ***all or any part of the ASME paper*** *"The effect of transient characteristics on optimization of fixed-bed regenerators (FBRs)," by Accepted Manuscript*

Hadi Ramin, Easwaran N Krishnan, Gurubalan Annadurai, Carey J. Simonson, J. Thermal Sci. Eng. Appl., 2021, cited in your letter for inclusion in a thesis entitled TRANSIENT ANALYSIS AND OPTIMIZATION OF FIXED-BED REGENERATORS FOR HVAC APPLICATIONS to be published University of Saskatchewan.

Permission is granted for the specific use as stated herein and does not permit further use of the materials without proper authorization. Proper attribution must be made to the author(s) of the materials. ***Please note****: if any or all of the figures and/or Tables are of another source, permission should be granted from that outside source or include the reference of the original source. ASME does not grant permission for outside source material that may be referenced in the ASME works. As is customary, we request that you ensure full acknowledgment of this material, the author(s), source and ASME as original publisher.*

Many thanks for your interest in ASME publications.

Sincerely,
Beth Darchi
Publishing Administrator
ASME
2 Park Avenue
New York, NY 10016-5990

A.4. PERMISSION FOR MANUSCRIPTS USED IN CHAPTER 5

The manuscript in Chapter 5 is unpublished and thus copyright permissions are obtained from all the co-authors on the manuscripts and are included below.

Copyright Permission Request Form

I am preparing the publication of a paper titled "A transient numerical model for desiccant coated fixed-bed regenerators" to be published as the fifth chapter of my Ph.D. thesis and to be submitted to the Department of Mechanical Engineering at the University of Saskatchewan. The authors contributing to the completion of this manuscript are

Hadi Ramin, Easwaran N. Krishnan, A. Gurubalan, and Carey J. Simonson

I am requesting permission to use the materials described in the manuscript in my Ph.D. thesis and all subsequent editions that may be prepared at the University of Saskatchewan. Please indicate agreement by signing below:

Regards,

Hadi Ramin

June 25, 2021

Permission granted by: Easwaran N. Krishnan

Signature:

Date:

Copyright Permission Request Form

I am preparing the publication of a paper titled “A transient numerical model for desiccant coated fixed-bed regenerators” to be published as the fifth chapter of my Ph.D. thesis and to be submitted to the Department of Mechanical Engineering at the University of Saskatchewan. The authors contributing to the completion of this manuscript are

Hadi Ramin, Easwaran N. Krishnan, A. Gurubalan, and Carey J. Simonson

I am requesting permission to use the materials described in the manuscript in my Ph.D. thesis and all subsequent editions that may be prepared at the University of Saskatchewan. Please indicate agreement by signing below:

Regards,

Hadi Ramin

June 25, 2021

Permission granted by: A. Gurubalan

Signature:

Date:

Copyright Permission Request Form

I am preparing the publication of a paper titled “A transient numerical model for desiccant coated fixed-bed regenerators” to be published as the fifth chapter of my Ph.D. thesis and to be submitted to the Department of Mechanical Engineering at the University of Saskatchewan. The authors contributing to the completion of this manuscript are

Hadi Ramin, Easwaran N. Krishnan, A. Gurubalan, and Carey J. Simonson

I am requesting permission to use the materials described in the manuscript in my Ph.D. thesis and all subsequent editions that may be prepared at the University of Saskatchewan. Please indicate agreement by signing below:

Regards,

Hadi Ramin

June 25, 2021

Permission granted by: Carey J. Simonson

Signature:

Date:

APPENDIX B

EFFECTIVENESS ERROR FROM THE TRANSIENT RESPONSE OF SENSORS AT DIFFERENT OPERATING CONDITIONS

The following tables represent the error in effectiveness for different τ_s^* and λ values over the practical ranges of NTU_o and Cr^*.

Table B.1. Effectiveness error Δε (%) for λ=0.0.

Δε (%) @ λ=0.0								
NTU_o	Cr^*	τ_s^*=0.01	τ_s^*=0.02	τ_s^*=0.05	τ_s^*=0.1	τ_s^*=0.2	τ_s^*=0.3	τ_s^*=0.5
1.0	1.0	0.7	1.4	3.5	6.9	13.1	17.8	23.1
1.0	2.0	0.6	1.2	3.1	6.0	11.6	15.9	21.1
1.0	3.0	0.6	1.2	2.9	5.7	11.1	15.3	20.4
1.0	5.0	0.6	1.1	2.7	5.5	10.7	14.9	20.0
1.0	10.0	0.5	1.1	2.6	5.3	10.4	14.6	19.7
2.0	1.0	0.7	1.3	3.3	6.3	11.6	15.2	19.0
2.0	2.0	0.5	1.0	2.5	4.8	9.1	12.1	15.6
2.0	3.0	0.5	0.9	2.2	4.3	8.2	11.2	14.6
2.0	5.0	0.4	0.8	2.0	4.0	7.6	10.5	13.8
2.0	10.1	0.4	0.7	1.9	3.7	7.2	10.0	13.4
5.0	1.0	0.6	1.3	3.1	5.8	9.9	12.4	14.6
5.0	2.0	0.4	0.8	1.9	3.5	6.2	8.0	9.7
5.0	3.0	0.3	0.6	1.5	2.9	5.2	6.8	8.5
5.0	5.0	0.3	0.5	1.3	2.4	4.5	6.0	7.7
5.0	10.0	0.2	0.4	1.1	2.1	3.9	5.4	7.1
7.0	1.0	0.6	1.3	3.0	5.6	9.3	11.5	13.2
7.0	2.0	0.3	0.7	1.7	3.1	5.4	6.8	8.1
7.0	3.0	0.3	0.5	1.3	2.5	4.4	5.7	7.0
7.0	5.0	0.2	0.4	1.1	2.0	3.7	4.9	6.2
7.0	10.0	0.2	0.3	0.9	1.7	3.2	4.3	5.6
10.0	1.0	0.6	1.2	2.9	5.3	8.7	10.4	11.8
10.0	2.0	0.3	0.6	1.4	2.7	4.5	5.6	6.6
10.0	3.0	0.2	0.5	1.1	2.1	3.6	4.6	5.5
10.0	5.0	0.2	0.4	0.9	1.7	3.0	3.9	4.8
10.0	10.0	0.1	0.3	0.7	1.3	2.5	3.3	4.2

Table B.2. Effectiveness error Δε (%) for λ=0.02.

Δε (%) @ λ=0.02								
NTU_o	Cr^*	τ_s^*=0.01	τ_s^*=0.02	τ_s^*=0.05	τ_s^*=0.1	τ_s^*=0.2	τ_s^*=0.3	τ_s^*=0.5
1.0	1.0	0.7	1.4	3.5	6.9	13.1	17.8	23.1
1.0	2.0	0.6	1.2	3.1	6.0	11.6	16.0	21.2
1.0	3.0	0.6	1.2	2.9	5.7	11.1	15.4	20.5
1.0	5.0	0.6	1.1	2.8	5.5	10.7	14.9	20.1
1.0	10.0	0.5	1.1	2.7	5.3	10.5	14.6	19.8
2.0	1.0	0.7	1.4	3.3	6.4	11.7	15.4	19.2
2.0	2.0	0.5	1.0	2.5	4.9	9.2	12.3	15.8
2.0	3.0	0.5	0.9	2.3	4.4	8.4	11.4	14.8
2.0	5.0	0.4	0.8	2.0	4.0	7.8	10.7	14.1
2.0	10.1	0.4	0.8	1.9	3.7	7.3	10.2	13.6
5.0	1.0	0.7	1.3	3.1	5.8	10.1	12.7	15.1
5.0	2.0	0.4	0.8	1.9	3.6	6.5	8.3	10.2
5.0	3.0	0.3	0.6	1.6	3.0	5.5	7.2	9.0
5.0	5.0	0.3	0.5	1.3	2.5	4.8	6.4	8.2
5.0	10.0	0.2	0.5	1.1	2.2	4.2	5.7	7.6
7.0	1.0	0.6	1.3	3.1	5.7	9.6	11.9	13.8
7.0	2.0	0.4	0.7	1.7	3.2	5.7	7.2	8.7
7.0	3.0	0.3	0.6	1.4	2.6	4.7	6.1	7.5
7.0	5.0	0.2	0.5	1.1	2.2	4.0	5.3	6.7
7.0	10.0	0.2	0.4	0.9	1.8	3.4	4.7	6.1
10.0	1.0	0.6	1.3	3.0	5.5	9.1	11.1	12.6
10.0	2.0	0.3	0.6	1.5	2.9	4.9	6.2	7.3
10.0	3.0	0.3	0.5	1.2	2.3	4.0	5.1	6.2
10.0	5.0	0.2	0.4	1.0	1.8	3.3	4.4	5.4
10.0	10.0	0.2	0.3	0.8	1.5	2.8	3.8	4.8

Table B.3. Effectiveness error Δε (%) for λ=0.04.

Δε (%) @ λ=0.04								
NTU_o	Cr^*	τ_s^*=0.01	τ_s^*=0.02	τ_s^*=0.05	τ_s^*=0.1	τ_s^*=0.2	τ_s^*=0.3	τ_s^*=0.5
1.0	1.0	0.7	1.4	3.6	6.9	13.2	17.9	23.2
1.0	2.0	0.6	1.2	3.1	6.1	11.7	16.0	21.2
1.0	3.0	0.6	1.2	2.9	5.7	11.2	15.4	20.6
1.0	5.0	0.6	1.1	2.8	5.5	10.8	15.0	20.2
1.0	10.0	0.5	1.1	2.7	5.3	10.5	14.7	19.9
2.0	1.0	0.7	1.4	3.3	6.4	11.8	15.5	19.4
2.0	2.0	0.5	1.0	2.5	4.9	9.3	12.4	16.0
2.0	3.0	0.5	0.9	2.3	4.5	8.5	11.5	15.0
2.0	5.0	0.4	0.8	2.1	4.1	7.9	10.8	14.3
2.0	10.1	0.4	0.8	1.9	3.8	7.4	10.3	13.7
5.0	1.0	0.7	1.3	3.2	5.9	10.3	13.0	15.4
5.0	2.0	0.4	0.8	2.0	3.7	6.7	8.6	10.6
5.0	3.0	0.3	0.7	1.6	3.1	5.7	7.5	9.4
5.0	5.0	0.3	0.6	1.4	2.6	5.0	6.7	8.6
5.0	10.0	0.2	0.5	1.2	2.3	4.4	6.0	8.0
7.0	1.0	0.7	1.3	3.1	5.8	9.9	12.2	14.3
7.0	2.0	0.4	0.7	1.8	3.4	5.9	7.6	9.2
7.0	3.0	0.3	0.6	1.4	2.8	5.0	6.5	8.0
7.0	5.0	0.2	0.5	1.2	2.3	4.2	5.6	7.2
7.0	10.0	0.2	0.4	1.0	1.9	3.7	5.0	6.6
10.0	1.0	0.7	1.3	3.1	5.6	9.4	11.5	13.1
10.0	2.0	0.3	0.7	1.6	3.0	5.2	6.7	7.9
10.0	3.0	0.3	0.5	1.3	2.4	4.3	5.5	6.7
10.0	5.0	0.2	0.4	1.0	2.0	3.6	4.7	5.9
10.0	10.0	0.2	0.3	0.8	1.6	3.1	4.1	5.3

Table B.4. Effectiveness error Δε (%) for λ=0.06.

Δε (%) @ λ=0.06								
NTU_o	Cr^*	τ_s^*=0.01	τ_s^*=0.02	τ_s^*=0.05	τ_s^*=0.1	τ_s^*=0.2	τ_s^*=0.3	τ_s^*=0.5
1.0	1.0	0.7	1.4	3.6	7.0	13.2	17.9	23.3
1.0	2.0	0.6	1.2	3.1	6.1	11.7	16.1	21.3
1.0	3.0	0.6	1.2	2.9	5.8	11.2	15.5	20.7
1.0	5.0	0.6	1.1	2.8	5.5	10.8	15.1	20.3
1.0	10.0	0.5	1.1	2.7	5.4	10.6	14.8	20.0
2.0	1.0	0.7	1.4	3.3	6.5	11.9	15.6	19.6
2.0	2.0	0.5	1.0	2.6	5.0	9.4	12.6	16.2
2.0	3.0	0.5	0.9	2.3	4.5	8.6	11.7	15.3
2.0	5.0	0.4	0.8	2.1	4.1	8.0	11.0	14.6
2.0	10.1	0.4	0.8	1.9	3.9	7.6	10.5	14.1
5.0	1.0	0.7	1.3	3.2	6.0	10.5	13.2	15.8
5.0	2.0	0.4	0.8	2.0	3.8	6.9	8.0	10.3
5.0	3.0	0.3	0.7	1.7	3.2	5.9	7.8	9.8
5.0	5.0	0.3	0.6	1.4	2.8	5.2	6.9	9.0
5.0	10.0	0.2	0.5	1.2	2.4	4.6	6.3	8.4
7.0	1.0	0.7	1.3	3.1	5.9	10.1	12.5	14.7
7.0	2.0	0.4	0.8	1.9	3.5	6.2	7.9	9.7
7.0	3.0	0.3	0.6	1.5	2.9	5.2	6.8	8.5
7.0	5.0	0.3	0.5	1.3	2.4	4.5	6.0	7.6
7.0	10.0	0.2	0.4	1.1	2.1	3.9	5.4	7.0
10.0	1.0	0.7	1.3	3.1	5.7	9.7	11.9	13.7
10.0	2.0	0.4	0.7	1.7	3.2	5.5	7.0	8.4
10.0	3.0	0.3	0.6	1.4	2.6	4.6	6.0	7.3
10.0	5.0	0.2	0.5	1.1	2.1	3.9	5.1	6.5
10.0	10.0	0.2	0.4	0.9	1.8	3.4	4.5	5.9

Table B.5. Effectiveness error Δε (%) for λ=0.08.

Δε (%) @ λ=0.08								
NTU_o	Cr^*	τ_s^*=0.01	τ_s^*=0.02	τ_s^*=0.05	τ_s^*=0.1	τ_s^*=0.2	τ_s^*=0.3	τ_s^*=0.5
1.0	1.0	0.7	1.4	3.6	7.0	13.3	18.0	23.4
1.0	2.0	0.6	1.2	3.1	6.1	11.8	16.2	21.4
1.0	3.0	0.6	1.2	2.9	5.8	11.3	15.6	20.8
1.0	5.0	0.6	1.1	2.8	5.6	10.9	15.1	20.4
1.0	10.0	0.5	1.1	2.7	5.4	10.6	14.8	20.1
2.0	1.0	0.7	1.4	3.4	6.5	11.9	15.7	19.7
2.0	2.0	0.5	1.1	2.6	5.0	9.5	12.7	16.4
2.0	3.0	0.5	0.9	2.3	4.6	8.7	11.8	15.5
2.0	5.0	0.4	0.9	2.1	4.2	8.1	11.1	14.8
2.0	10.1	0.4	0.8	2.0	3.9	7.7	10.6	14.3
5.0	1.0	0.7	1.3	3.2	6.0	10.6	13.5	16.1
5.0	2.0	0.4	0.8	2.1	3.9	7.1	9.2	11.4
5.0	3.0	0.4	0.7	1.7	3.3	6.1	8.1	10.2
5.0	5.0	0.3	0.6	1.5	2.9	5.4	7.2	9.4
5.0	10.0	0.3	0.5	1.3	2.5	4.8	6.6	8.8
7.0	1.0	0.7	1.3	3.2	5.9	10.2	12.8	15.1
7.0	2.0	0.4	0.8	1.9	3.6	6.4	8.3	10.1
7.0	3.0	0.3	0.6	1.6	3.0	5.4	7.1	8.9
7.0	5.0	0.3	0.5	1.3	2.5	4.7	6.3	8.1
7.0	10.0	0.2	0.4	1.1	2.2	4.2	5.7	7.4
10.0	1.0	0.7	1.3	3.1	5.8	9.9	12.2	14.2
10.0	2.0	0.4	0.7	1.8	3.3	5.8	7.4	9.0
10.0	3.0	0.3	0.6	1.4	2.7	4.9	6.3	7.8
10.0	5.0	0.2	0.5	1.2	2.3	4.2	5.5	7.0
10.0	10.0	0.2	0.4	1.0	1.9	3.6	4.9	6.4

Table B.6. Effectiveness error Δε (%) for λ=0.12.

Δε (%) @ λ=0.12								
NTU_o	Cr^*	τ_s^*=0.01	τ_s^*=0.02	τ_s^*=0.05	τ_s^*=0.1	τ_s^*=0.2	τ_s^*=0.3	τ_s^*=0.5
1.0	1.0	0.7	1.4	3.6	7.0	13.3	18.1	23.5
1.0	2.0	0.6	1.3	3.1	6.1	11.8	16.3	21.6
1.0	3.0	0.6	1.2	2.9	5.8	11.3	15.7	21.0
1.0	5.0	0.6	1.1	2.8	5.6	11.0	15.3	20.5
1.0	10.0	0.5	1.1	2.7	5.4	10.7	15.0	20.2
2.0	1.0	0.7	1.4	3.4	6.5	12.0	15.9	20.0
2.0	2.0	0.5	1.1	2.6	5.1	9.6	13.0	16.8
2.0	3.0	0.5	1.0	2.4	4.6	8.9	12.1	15.8
2.0	5.0	0.4	0.9	2.2	4.3	8.3	11.4	15.1
2.0	10.1	0.4	0.8	2.0	4.0	7.8	10.9	14.7
5.0	1.0	0.7	1.3	3.2	6.1	10.9	13.8	16.6
5.0	2.0	0.4	0.9	2.1	4.1	7.4	9.7	12.0
5.0	3.0	0.4	0.7	1.8	3.5	6.4	8.5	10.9
5.0	5.0	0.3	0.6	1.6	3.0	5.7	7.7	10.0
5.0	10.0	0.3	0.6	1.4	2.7	5.2	7.1	9.4
7.0	1.0	0.7	1.3	3.2	6.0	10.5	13.3	15.8
7.0	2.0	0.4	0.8	2.0	3.8	6.8	8.8	10.9
7.0	3.0	0.3	0.7	1.7	3.2	5.8	7.7	9.7
7.0	5.0	0.3	0.6	1.4	2.7	5.1	6.9	8.8
7.0	10.0	0.2	0.5	1.2	2.4	4.6	6.2	8.2
10.0	1.0	0.7	1.3	3.2	5.9	10.2	12.8	15.0
10.0	2.0	0.4	0.8	1.9	3.5	6.3	8.1	9.8
10.0	3.0	0.3	0.6	1.5	2.9	5.3	7.0	8.7
10.0	5.0	0.3	0.5	1.3	2.5	4.6	6.1	7.8
10.0	10.0	0.2	0.4	1.1	2.1	4.1	5.5	7.2

Table B.7. Effectiveness error Δε (%) for λ=0.16

Δε (%) @ λ=0.16								
NTU_o	Cr^*	τ_s^*=0.01	τ_s^*=0.02	τ_s^*=0.05	τ_s^*=0.1	τ_s^*=0.2	τ_s^*=0.3	τ_s^*=0.5
1.0	1.0	0.7	1.5	3.6	7.0	13.4	18.1	23.6
1.0	2.0	0.6	1.3	3.1	6.2	11.9	16.3	21.7
1.0	3.0	0.6	1.2	3.0	5.9	11.4	15.8	21.1
1.0	5.0	0.6	1.1	2.8	5.6	11.0	15.4	20.7
1.0	10.0	0.5	1.1	2.7	5.5	10.8	15.1	20.4
2.0	1.0	0.7	1.4	3.4	6.6	12.1	16.1	20.2
2.0	2.0	0.5	1.1	2.7	5.2	9.8	13.2	17.0
2.0	3.0	0.5	1.0	2.4	4.7	9.0	12.3	16.1
2.0	5.0	0.4	0.9	2.2	4.4	8.4	11.6	15.5
2.0	10.0	0.4	0.8	2.1	4.1	8.0	11.1	15.0
5.0	1.0	0.7	1.3	3.3	6.2	11.1	14.2	17.1
5.0	2.0	0.5	0.9	2.2	4.2	7.7	10.1	12.6
5.0	3.0	0.4	0.8	1.9	3.6	6.7	9.0	11.4
5.0	5.0	0.3	0.7	1.6	3.2	6.0	8.2	10.6
5.0	10.0	0.3	0.6	1.4	2.8	5.5	7.5	10.0
7.0	1.0	0.7	1.3	3.2	6.1	10.8	13.7	16.3
7.0	2.0	0.4	0.9	2.1	4.0	7.1	9.3	11.5
7.0	3.0	0.4	0.7	1.7	3.4	6.2	8.2	10.4
7.0	5.0	0.3	0.6	1.5	2.9	5.5	7.4	9.5
7.0	10.0	0.3	0.5	1.3	2.6	4.9	6.7	8.9
10.0	1.0	0.7	1.3	3.2	6.1	10.5	13.2	15.6
10.0	2.0	0.4	0.8	2.0	3.7	6.7	8.6	10.6
10.0	3.0	0.3	0.7	1.6	3.1	5.7	7.5	9.4
10.0	5.0	0.3	0.6	1.4	2.7	5.0	6.7	8.6

Table B.8. Effectiveness error Δε (%) for λ=0.20

Δε (%) @ λ=0.20								
NTU_o	Cr^*	τ_s^*=0.01	τ_s^*=0.02	τ_s^*=0.05	τ_s^*=0.1	τ_s^*=0.2	τ_s^*=0.3	τ_s^*=0.5
1.0	1.0	0.7	1.5	3.6	7.0	13.4	18.2	23.7
1.0	2.0	0.6	1.3	3.1	6.2	11.9	16.4	21.8
1.0	3.0	0.6	1.2	3.0	5.9	11.5	15.9	21.2
1.0	5.0	0.6	1.1	2.8	5.7	11.1	15.4	20.8
1.0	10.0	0.6	1.1	2.8	5.5	10.8	15.1	20.5
2.0	1.0	0.7	1.4	3.4	6.6	12.2	16.2	20.4
2.0	2.0	0.5	1.1	2.7	5.2	9.9	13.3	17.3
2.0	3.0	0.5	1.0	2.4	4.8	9.1	12.5	16.4
2.0	5.0	0.5	0.9	2.2	4.4	8.6	11.8	15.7
2.0	10.1	0.4	0.8	2.1	4.2	8.2	11.4	15.3
5.0	1.0	0.7	1.4	3.3	6.3	11.2	14.4	17.5
5.0	2.0	0.5	0.9	2.3	4.3	7.9	10.4	13.1
5.0	3.0	0.4	0.8	1.9	3.8	7.0	9.3	12.0
5.0	5.0	0.3	0.7	1.7	3.3	6.3	8.5	11.1
5.0	10.0	0.3	0.6	1.5	3.0	5.8	7.9	10.5
7.0	1.0	0.7	1.3	3.3	6.2	11.0	14.0	16.8
7.0	2.0	0.4	0.9	2.1	4.1	7.4	9.7	12.1
7.0	3.0	0.4	0.7	1.8	3.5	6.5	8.6	11.0
7.0	5.0	0.3	0.6	1.6	3.1	5.8	7.8	10.1
7.0	10.0	0.3	0.6	1.4	2.7	5.2	7.2	9.5
10.0	1.0	0.7	1.3	3.3	6.1	10.7	13.6	16.2
10.0	2.0	0.4	0.8	2.1	3.9	7.0	9.1	11.3
10.0	3.0	0.4	0.7	1.7	3.3	6.1	8.0	10.1
10.0	5.0	0.3	0.6	1.5	2.9	5.4	7.2	9.3

APPENDIX C

THERMODYNAMICS AND PROPERTIES EQUATIONS FOR THE FBR MODEL OF THE DESICCANT-COATED EXCHANGER IN CHAPTER 5

The following table (Table C.1) presents the thermodynamics equations required for the FBR model of the desiccant coated FBRs.

Table C.1. Thermodynamics and properties equations for the FBR model

Equation	Eq. #
$P_g=P_a+P_v$	(C.1)
$P_a=\rho_a R_a T_a$	(C.2)
$P_v=\rho_v R_v T_v$	(C.3)
$\rho_g=\rho_a+\rho_v$	(C.4)
$P_{v,sat}=\exp(F)$	(C.5)
$F=\begin{cases}\frac{C_1}{T}+C_2+C_3T+C_4T^2+C_5T^3+C_6T^4+C_7\ln(T) & 173<T<273K\\ \frac{C_8}{T}+C_9+C_{10}T+C_{11}T^2+C_{12}T^3+C_{13}\ln(T) & 273<T<473K\end{cases}$	(C.6)
$Cp_g=\frac{\rho_a Cp_a+\rho_v Cp_v}{\rho_g}$	(C.7)
$\rho_d=\rho_{d,dry}(1+u)$	(C.8)
$Cp_d=\frac{\rho_{d,dry}\left(uCp_w+Cp_{d,dry}\right)}{\rho_d}$	(C.9)
$\rho_m=\sigma_d\rho_d+\sigma_{Al}\rho_{Al}$	(C.10)
$Cp_m=\frac{\sigma_d\rho_d Cp_d+\sigma_{Al}\rho_{Al}Cp_{Al}}{\rho_m}$	(C.11)
$\sigma_d+\sigma_{Al}=1$	(C.12)

The constants in Eqn. (C.6) are: C_1=-5674.5359, C_2=6.3925247, C_3=-9.677843×10^{-3}, C_4=6.22115701×10^{-7}, C_5=2.0747825×10^{-9}, C_6=-9.484024×10^{-13}, C_7=4.1635019, C_8=-5800.2206, C_9=1.3914993, C_{10}=-4.8640239×10^{-2}, C_{11}=4.1764768×10^{-5}, C_{12}=-1.4452093×10^{-8}, and C_{13}=6.5459673.